USE OF MATHEMATICAL MODELING AND OTHER BIOPHYSICAL METHODS FOR INSIGHTS INTO IRON-RELATED PHENOMENA OF BIOLOGICAL SYSTEMS

A Dissertation

by

JOSHUA D. WOFFORD

Submitted to the Office of Graduate and Professional Studies of
Texas A&M University
in partial fulfillment of the requirements for the degree of

DOCTOR OF PHILOSOPHY

Chair of Committee,	Paul A. Lindahl
Committee Members,	David P. Barondeau
	Simon W. North
	Vishal M. Gohil
Head of Department,	Simon W. North

December 2018

Major Subject: Chemistry

ABSTRACT

Iron is a crucial nutrient in most living systems. It forms the active centers of many proteins that are critical for many cellular functions, either by themselves or as Fe-S clusters and hemes. However, Fe is potentially toxic to the cell in high concentrations and must be tightly regulated. There has been much work into understanding various pieces of Fe trafficking and regulation, but integrating all of this information into a coherent model has proven difficult.

Past research has focused on different Fe species, including cytosolic labile Fe or mitochondrial Fe-S clusters, as being the main regulator of Fe trafficking in yeast. Our initial modeling efforts demonstrate that *both* cytosolic Fe and mitochondrial ISC assembly are required for proper regulation. More recent modeling efforts involved a more rigorous multi-tiered approach. Model simulations were optimized against experimental results involving respiring wild-type and Mrs3/4-deleted yeast. Simulations from both modeling studies suggest that mitochondria possess a "respiratory shield" that prevents a vicious cycle of nanoparticle formation, ISC loss, and subsequent loading of mitochondria with iron.

Work has also been done in understanding an accumulation of Fe in stationary grown yeast cells. This accumulated Fe was found to be localized to the cell wall, and can be used as cells are metabolically reactivating by being placed into fresh media. A maethematical model has been developed to describe the metabolism of oxygen and nutrients in the autocatalytic production of active cells, with subsequent deactivation of cells as nutrients became limiting.

E. coli have similar Fe contents relative to mitochondria, and they also appear to also employ a "respiratory shield". This hypothesis was tested by either inhibiting respiratory complexes with CN, or by growing cells into a metabolically inactive stationary growth state.

The generated nanoparticles were not associated with ferritins, which is surprising given that much of the literature claims that ferritin Fe makes up a large portion of cellular Fe.

The iron content of murine hearts was also studied. Previous work from the Lindahl lab focused on murine brains and livers, which contain ferritin at young and old ages, while losing it in middle age. Hearts differ from these two organs, in that they mainly contain respiratory iron-sulfur clusters, and only gain ferritin as the mice approach old age.

ACKNOWLEDGEMENTS

I dedicate this work, and the time it went into it, to so many people in my life that have supported me in multiple ways that have made my doctorate possible. Firstly, I want to thank Almighty God, for creating the universe we live in, and giving humanity the minds capable of studying it and thinking His thoughts after him. I want to thank my beautiful wife, Elizabeth, who provides daily support and is my partner in life. I want to thank my parents, John and Jennifer, for bringing me up, and encouraging my academic pursuits, even when I didn't want to. I want to thank my siblings, Jacob, Kaitlyn, and Joseph, for being there and giving me healthy competition. I want to thank the members of the Lindahl lab, past and present, for allowing me to learn from them and their assistance in completing this research. I want to thank my collaborators from groups within and without Texas A&M, for allowing me to assist and learn about other research going on around me. I also want to thank the many staff members of the Texas A&M Chemistry department that have assisted with running instruments, navigating paperwork, and fabricating parts that I need, with special thanks to Will Seward, Greg Wylie, Bill Merka, and Sandy Horton. Lastly, I want to thank my advisor, Paul Lindahl, for taking me into his lab and letting me pursue this crazy combination of chemistry, biology, and mathematics.

CONTRIBUTORS AND FUNDING SOURCES

This work was supported by a dissertation committee consisting of Professors Paul A. Lindahl, David P. Barondeau, and Simon W. North of the Department of Chemistry, and Professor Vishal M. Gohil of the Department of Biochemistry and Biophysics.

This research was funded with grants from the National Institutes of Health and the Welch Foundation

NOMENCLATURE

MB	Mössbauer
T_B	Blocking temperature
BPS	Bathophenanthroline disulfonate
DFO	Desferrioxamine
ISC	Iron-Sulfur Cluster
CD	Central Doublet
CIA	Cytosolic Iron-sulfur assembly complex
δ	Isomer shift
ΔE_Q	Quadrupole splitting
Γ	Linewidth
EPR	Electron paramagnetic resonance
LMM	Low molecular mass
$\Delta\Delta$	Mrs3/4$\Delta\Delta$ cells
WT	Wild type
NHHS	Nonheme high-spin
FTS	Flow-through solution
LC-ICP-MS	Liquid chromatography with on-line detection by an inductively coupled plasma mass spectrometer
LIP	Labile iron pool
OXPHOS	Oxidative phosphorylation
TCA	Tricarboxylic acid (cycle)

ROS	Reactive oxygen species
ODE	Ordinary differential equation

TABLE OF CONTENTS

Page

ABSTRACT ……...ii

ACKNOWLEDGMENTS.……iv

CONTRIBUTORS AND FUNDING SOURCES……..….v

NOMENCLATURE……..……..…...vi

TABLE OF CONTENTS……...……..….....viii

LIST OF FIGURES……..…….....xiv

LIST OF TABLES……...……...xviii

CHAPTER I INTRODUCTION ……..……1

Introduction and Instrumentation……..1

Labile Metal Pools……4

Dangers of Fe and the Need for Regulation……..5

Principles of Mössbauer Spectroscopy……..8

Coordination Chemistry of Fe…….10

Types of Fe evident in biological samples……...11

Aggregated Ferric ions……13

Online and Offline LC-ICP-MS……...14

Mathematical Modeling……15

Transition to Projects……16

Modeling Efforts to Determine Regulation Species in S. cerevisiae……17

Recovery of Mitochondrial Iron Contents in Mrs3/4ΔΔ Yeast Cells……21

Multi-Tiered Model……..22

Yeast cell wall acts to store iron for metabolically deactivating cells…….24

E. coli possess a respiratory shield similar to yeast mitochondria……...24

Additional Projects……...28

CHAPTER II MATERIALS AND METHODS……..29

Fe stock prep and Media components……..29

Minimal media…….30

Rich Media……...31

Cell Plates…….31

Cell Stocks……32

Cell Growth……...33

Mitochondria Isolation……..34

Mössbauer Spectroscopy……...36

Liquid Chromatography-Inductively Coupled Plasma-Mass Spectrometry…….39

Electron Paramagnetic Resonance (EPR) Spectroscopy……...40

Mathematical Modeling…….41

CHAPTER III MITOCHONDRIAL IRON-SULFUR CLUSTER ACTIVITY AND CYTOSOLIC IRON REGULATE IRON TRAFFIC IN SACCHAROMYCES CEREVISIAE……42

Summary……42

Introduction……43

Materials and Methods……...52

Results……63

Discussion……..70

Author Contributions……..74

Acknowledgement……..74

Supplemental Material……74

CHAPTER IV RECOVERY OF MRS3ΔMRS4Δ SACCHAROMYCES CEREVISIAE CELLS UNDER IRON-SUFFICIENT CONDITIONS AND THE ROLE OF FE 580……..…90

Summary…….90

Introduction……91

Experimental Procedures…….94

Results…….99

Discussion……..123

Acknowledgements……129

CHAPTER V A MATHEMATICAL MODEL OF IRON IMPORT AND TRAFFICKING IN WT AND MRS3/4ΔΔ YEAST CELLS…….....130

Summary……..130

Introduction……..131

Methods and Results……139

Conclusions……..168

Funding…….171

Acknowledgements……..171

Supplemental Material……..171

CHAPTER VI FERRIC IONS ACCUMULATE IN THE WALLS OF METABOLICALLY INACTIVATING SACCHAROMYCES CEREVISIAE CELLS AND ARE REDUCTIVELY MOBILIZED DURING REACTIVATION……..…...173

Summary…….173

Introduction…….174

Methods……...178

Results and Discussion……181

Conclusions…….223

Acknowledgements…….228

CHAPTER VII CHARACTERIZATION OF THE LABILE IRON POOL IN ESCHERICHIA COLI, AND A "RESPIRATION SHIELD" THAT PROTECTS IT FROM O2 DAMAGE…….…….....229

Summary……....229

Introduction…….....230

Results……235

Discussion……..261

Experimental Procedures……....272

Acknowledgements…….275

Supplemental Information……..276

CHAPTER VIII CONCLUSIONS...…..…….……...284

Dual Regulation Model Characterization of WT and ISC mutants……284

Systems' level understanding of the recovery of ΔMrs3/4 mitochondrial iron and cell growh…….285

Multi-tiered modeling approach to transfer solutions from simpler tiers to more complex……..286
Cell Wall Fe accumulates as multiple forms, is chelatable, and used by cells during metabolic reactivation…….289
E. coli possess similar Fe contents and the means to protect Fe relative to eukaryotic mitochondria……...290
Conclusions……...…...292
REFERENCES……..…293
APPENDIX A: MÖSSBAUER SPECTRA OF MOUSE HEARTS REVEAL AGE-DEPENDENT CHANGES IN MITOCHONDRIAL AND FERRITIN IRON LEVELS……..……..340
Summary……..340
Introduction……..341
Results……..344
Discussion……358
Experimental Procedures…….366
Author Contributions……...368
Acknowledgements…….368
Footnotes…….368
APPENDIX B: STRUCTURES, INTERCONVERSIONS, AND SPECTROSCOPY OF IRON CARBONYL CLUSTERS WITH AN INTERSTITIAL CARBIDE: LOCALIZED METAL CENTER REDUCTION BY OVERALL CLUSTER OXIDATION…….369

Introduction…….369

Physical Measurements……...370

Results and Discussion……....371

Conclusions…….376

LIST OF FIGURES

Page

Figure 1.1: Basic Illustration of Mossbauer splitting, either with an electric field gradient to produce a quadrupole doublet (top), or in the presence of a magnetic field to produce a sextet signal (bottom) ……9

Figure 1.2: Mössbauer spectra of S. cerevisiae whole cells, with simulations of typical species…….. ……...……12

Figure 1.3: Model of regulation of Fe in S. cerevisiae. ……..…19

Figure 3.1: Chemical model of iron trafficking in and regulation in S. cerevisiae…….46

Figure 3.2: Iron regulation pathways in S. cerevisiae. ……..….49

Figure 3.3: Simulated concentrations of iron components in *S. cerevisiae* at increasing concentrations of iron in the growth medium. ..……....60

Figure 3.4: Simulated concentrations of iron components in *S. cerevisiae* at increasing rates by which iron-sulfur clusters and heme centers are synthesized…….….65

Figure 3.5: Selected plots from simulations. ……..68

Figure 4.1: Growth rates of WT (circles) and ΔΔ (triangles) cells. ……99

Figure 4.2: Mössbauer spectra of whole cells (A-H) and isolated mitochondria (I-L). …105

Figure 4.3: The Mrs3/4ΔΔ phenotype. ……...110

Figure 4.4: Electronic absorption spectra of isolated mitochondrial suspensions……..…113

Figure 4.5: EPR spectra of ΔΔ (A-B) and WT (E-H) cells. ……..…..…...114

Figure 4.6: LC-ICP-MS chromatograms of LMM flow-through solutions prepared from the soluble fractions of WT and ΔΔ mitochondrial detergent extracts..……..…119

Figure 4.7: Mn, Zn, and Cu LC-ICP-MS traces of flow-through solutions of soluble extracts of mitochondria isolated from WT and ΔΔ cells. ……..…..121

Figure 5.1: Strategy for optimizing a model of nutrient iron import, trafficking and regulation in growing eukaryotic cells. ……136

Figure 5.2: Plots of growth rate (top), cellular iron concentration (middle), and the rate of iron import into the cell (bottom). ……..143

Figure 5.3: Rates of iron import into the cytosol *only* (A), into the mitochondria (B), and into vacuole (C) according to the C_3 model……....154

Figure 5.4: Simulated concentrations of the iron-containing components in the C_9 version of the model as a function of nutrient iron concentration (in μM). …..…….164

Figure 5.5: "Waterfall" Plots of Mitochondrial oxygen and nanoparticle concentrations (in μM).…….....…...….166

Figure 6.1: Low field (0.05 T) low temperature (5 K) Mössbauer spectra of whole intact fermenting WT cells grown on 57Fe40B0 medium and harvested at different growth stages ……..……182

Figure 6.2: 10 K X-band EPR spectra of whole intact fermenting yeast cells……...185

Figure 6.3: Model of cell growth and O2 consumption in a batch culture of WT fermenting S. cerevisiae. ……187

Figure 6.4: Temperature-dependent Mössbauer spectra of 57Fe-loaded cells (water-washed). ……..192

Figure 6.5: Variable-field 4.2 K Mössbauer spectra of 57Fe-loaded (water-washed) cells……..…193

Figure 6.6: Temperature-dependent EPR spectra of 57Fe-loaded cells (water-washed)……195

Figure 6.7: Iron concentrations in WT post-exponential cells and the corresponding washes and various treatments……...…….197

Figure 6.8: Growth of Fe-loaded or Fe-starved cells after transfer to various media…..……199

Figure 6.9: Mössbauer spectra (5 K, 0.05 T) of whole WT yeast cells before (A) and after (B–E) switching growth media. …….……204

Figure 6.10: Iron concentrations in growth medium before and after inoculation with 57Fe-loaded cells. ……..213

Figure 6.11: Whole-cell Mössbauer spectra (5K, 0.05 T) obtained from the experiment of Fig. 8C……...…….215

Figure 6.12: Mössbauer spectra (5 K, 0.05 T) of 57Fe-loaded cells before (A) and at increasing times after (B–D) transfer to Fe0B100 medium. ……221

Figure 6.13: Western blot showing Fet3p expression levels in WT cells in various media. 223

Figure 6.14: Model for iron accumulation into the cell wall. ……...….224

Figure 7.1: Low-temperature low-field (5 K, 0.05 T) Mössbauer spectra of WT *E. coli* harvested during exponential growth.. …….…….….240 ..

Figure 7.2: Low-temperature X-band EPR spectra of whole packed *E. coli* cells grown on glucose or acetate, and harvested under exponential growth conditions. ……..……..……..244

Figure 7.3: Mössbauer spectra (5 K, 0.05 T) of three separate batches of WT E. coli cells grown in glucose under reduced O_2 conditions. ……..…..246

Figure 7.4: Mössbauer spectra (5 K, 0.05 T) of whole Δ*fur* cells grown on glucose media and harvested during exponential phase….……248

Figure 7.5: Mössbauer spectra (0.05 T) of whole *E. coli* cells grown on MM media, supplemented with 100 μM 57Fe citrate, and harvested during exponential growth and stationary state. …….250

Figure 7.6: Respiratory Shield Model for Mitochondria (top), and for E. coli and other prokaryotes (bottom). ……..…….…….254

Figure 7.7: Mössbauer spectra (5K, 0.05 T) of cyanide-treated E. coli cells. ……..…...256

Figure 7.8: Mössbauer spectra (5 K, 0.05 T) of whole *E. coli* cells, and associated retentate and flow-through solutions. ……..……..…..……258

Figure 7.9: ^{57}Fe-detected LC-ICP-MS chromatograms of flow-through solutions From exponentially grown *E. coli* cells. ……..…260

Figure 7.S1: Low-Field low-temperature (0.05 T, 5 K) Mössbauer spectra of *E. coli* whole cells grown in media containing glucose (A and B) and acetate (C and D). …….....277

Figure 7.S2: High-Field low-temperature (6 T, 4.2 K) Mössbauer spectra of *E. coli* whole cells (A) and flow-through solution (B).. ……..…....278

Figure 7.S3: Individual EPR simulations. …….……279

Figure 7.S4: Mössbauer spectra (5K, 0.05 T) of mitochondria isolated from yeast cells.……280

Figure 7.S5: Mössbauer (5 K, 0.05 T) spectra of whole *E. coli* mutant cells devoid of various ferritin genes.. …..…….281

Figure 7.S6: LC-ICP-MS chromatograms of E. coli flow-through solutions detected by ^{31}P, Mn, Zn, Cu, S, Mo, and Co. ……..……..282

Figure 7.S7: Mössbauer spectra (5 K, 0.05 T) of WT *Bacillus subtilis* harvested during exponential growth conditions. ……..…….283

Figure A.1. Mössbauer spectra of hearts from elderly mice. ……..346

Figure A.2. Mössbauer spectra (5 K) of hearts from young mice. ……..……..…348

Figure A.3. Mössbauer spectra (5 K) of hearts from adult mice. ……..……349

Figure A.4. X-band EPR spectra of heart homogenates from mice of different ages……..356

Figure A.5. Mössbauer spectra of 12 weeks *HFE*-/- hearts and livers *versus* controls……..357

Figure A.6. Heart iron concentrations (excluding blood) as a function of age. ……361

Figure A.7. Illustration of how iron content changes with age in healthy mouse hearts……361

Scheme B.1. Synthesis of the starting $[Fe_6]^{2-}$ cluster 1 (top left), its neutral congener $[Fe_6]^0$ (2, top right), and the closed synthetic loop including the crystallographically defined five-iron clusters $[Fe_5]^n$ (n = 0 or 2–), shown at bottom. ……..…371

Figure B.1. Mössbauer spectrum of a solution of 1a (A) and 2 (B) in frozen THF. ……..…372

Figure B.2. Variable field Mössbauer spectra for a frozen solution of 2 in toluene. ……..375

LIST OF TABLES

Page

Table 3.1. Model reactions and rate expression, including optimized WT parameters ….53

Table 3.S1. Comparison between simulated values and literature data relevant to the model……74

Table 3.S2 Data from previous Mössbauer studies. ……82

Table 3.S3 Optimized Parameters and sensitivities. ……83

Table 4.1. Iron concentrations and iron-containing species in whole cells. ……101

Table 4.2. Iron concentrations and components in isolated mitochondria. …….103

Table 4.3. Copper, manganese, and zinc concentrations in ΔΔ and WT cells and isolated mitochondria. ...…….….116

Table 5.1. Growth rates, iron concentrations, and import rates in ΔΔ and WT cells grown under different nutrient conditions. ……137

Table 5.2. Optimized parameters used in simulations. ……..…….142

Table 5.3. : Estimated concentrations (in μM) of the iron-containing components of the C_9 model ……..……152

Table 5.4. Rates of formation of each component of the C_9 model, for different strains and nutrient concentrations. ……..……159

Table 6.1. Metal concentrations of WT cells grown to exponential and post-exponential phases, and subsequently treated with EDTA or lyticase……...……184

Table 6.2. Model Reactions, Parameters and Sensitivities. …….....189

Table 7.1. Components assumed in simulating Mössbauer spectra of *E. coli* and the percentages of each component included in simulations…….236

Table 7.S1. Selected metal and phosphorus concentrations in exponentially growing *E. coli* cells ……..…….276

Table A.1. Metal concentrations in 57Fe-enriched mouse hearts (and livers), and associated Mössbauer parameters. ……..……...352

Table B.1. Mössbauer and parameters for 1a and 2 derived from low field (0.05 T) measurements at 30 K, as well as DFT calculated charge parameters……...373

CHAPTER I

INTRODUCTION

Introduction and Instrumentation

Iron is a critical nutrient for the proper function of nearly all living systems. Iron and iron-containing proteins participate in enzyme catalysis, electron-transfer reactions, substrate binding, DNA replication/repair, and a multitude of other reactions. In eukaryotic cells, mitochondria are central to Fe trafficking and regulation, as they are the only site of heme synthesis and a major site of Fe-S cluster (ISC) biogenesis **(1)**. Fe is also trafficked through the cytosol to other sites, including ferritin/vacuoles and the nucleus **(2)**. Ferritin is a 24-subunit heteromeric protein complex that is employed by mammalian cells and bacteria for storage of excess Fe **(3)**. Yeast do not have ferritin, but they use vacuole organelles for the same purpose **(4)**.

Environmental Fe is generally present in the insoluble ferric (Fe^{3+}) state **(4)**. Cells have evolved many methods of solubilizing this ferric Fe, either through reduction processes or through chelator complexes called siderophores. Yeast contain both high- and low-affinity Fe uptake pathways. The high-affinity uptake pathway involves the Fet3/Ftr1 heterodimer **(5)**. Fet3 is a multicopper oxidase that oxidizes ferrous ions that are supplied by Fre1 **(6).** Ftr1 is a permease that imports this ferric ion into the cell. Before the ferric ions enter the cytosol, they are reduced to the ferrous state. Fet4 is the low-affinity transporter that also imports other metals besides iron **(7).** Fet4 imports iron

in the absence of oxygen, whereas the high-affinity Fet3 pathway requires oxygen to function.

Once iron is in the cytosol, it is sent to a multitude of locations. As stated previously, one of the main traffic hubs for iron in the eukaryotic cell is the mitochondria, the "powerhouse" of the cell. Iron can presumably cross the outer membrane of the mitochondria through the porin proteins, but there are high-affinity and low-affinity pathways to bring iron across the inner membrane. The high-affinity pathway includes the mitoferrin homolog proteins Mrs3 and Mrs4 **(8,9,10)** whereas Rim2 is used in the low-affinity pathway **(11,12)**. Once in the matrix of the mitochondria, Fe is in a low molecular mass pool (dubbed Fe_{580}) that is implicated in mitochondrial ISC synthesis **(10,13,14)**. This involves the building of a Fe_2S_2 cluster on the ISC scaffold protein. The sulfurs for these clusters originate from cysteine, in a reaction catalyzed by cysteine desulferase Nfs1. Electrons for the process are donated through the Yah1 ferroxidase protein **(15)**. Such clusters are either installed into various target proteins or they are combined with another Fe_2S_2 cluster to form an Fe_4S_4 cluster, and that cluster is installed **(1,3)**.

In the ISC assembly machinery, there is a protein that has had a controversial story as researchers seek to assign a function to it. This protein known as frataxin, and yeast have a homolog known as Yfh1 (Yeast Frataxin Homolog 1) (**16**). This protein has been in search of a function since its discovery. There have been a host of hypothesized functions of this proteins, including iron storage, iron chaperoning to ISC assembly, to stimulating the rest of the ISC machinery for activity **(17, 18)**. No matter what the actual

function of this protein, loss of frataxin in humans leads to the manifestation of a disease known as Friedreich's Ataxia. This disease is manifested as an Fe overload disease, with the accumulated Fe characterized as Fe nanoparticles in the mitochondria. Other symptoms include loss of ISCs and respiratory ability, lethargy, mental retardation, and cardiomyopathy **(19)**. In yeast, the previously discussed ISC mutant phenotype is manifested: a loss of ISCs and hemes, slowed growth, an increase of ROS damage, and an accumulation of Fe in the mitochondria in the form of nanoparticles.

This Fe_{580} pool may also be used in heme synthesis, which are installed, along with ISCs, into the respiratory complexes, which reduce O_2 to water while producing ATP during oxidative phosphorylation **(13)**.

Iron can also be trafficked into the yeast vacuole when cytosolic Fe is found to be in excess. Uptake of Fe into the vacuole is mediated by the Ccc1 protein, and presumably endocytosis **(20,21)**. The iron brought into the vacuole is rapidly oxidized to Fe^{3+}, and can potentially aggregate as Fe-polyphosphate nanoparticles. Vacuoles serve as dynamic storage for the cell. If the cell becomes Fe-deficient, the Fe^{3+} can be reduced to Fe^{2+} through the Fre6 protein **(22)**, and then brought out through the Fet5/Fth1 heterodimer, which is a multicopper oxidase/permease combination **(23)**. The entire pathway is homologous in function to the cytosolic import pathway involving Fre1/Fet3/Ftr1.

Labile Metal Pools

While the previous few paragraphs have looked into the large scale movement of Fe throughout the cell, much research has been done into understanding how the transition metals are moved throughout the organelles and stored. Many labile pools of the biological transition metals have been discovered, but the nature of these pools has provided a challenge for localizing and characterizing the ligand environment of these pools. There have been plenty of groups that have been focused on understanding these groups, and have developed fluorescent chelator probes for the task of locating the labile pools within the cell, to great effect **(24)**. These probes can be tailor made for individual metals and placed in specific locales of the cell. These probes can then fluoresce upon the binding of the desired metal and detected with a high resolution instrument, giving a detailed "map" of metals within the cell **(25)**. However, while these probes have been useful in localizing and detecting various metals, these new chelator probes lose possible information by chelating the metal away from its native ligand. In order to gain valuable insight into the ligand environment of the labile pool in question, separations must be used that preserve the native complex. The Lindahl lab has developed such a methodology that uses LC-ICP-MS (described below) in an anaerobic environment to separate and detect individual metal complexes from biological extracts **(14)**, and efforts are being made to physically characterize them so that the exact identities of the ligands are known.

Dangers of Fe and the Need for Regulation

While Fe may be critical to cell function and survival, Fe can also be lethal. Fe can participate in Fenton chemistry and Haber-Weiss chemistry to produce reactive oxygen species (ROS) and then regenerate the beginning ferrous ion **(26)**. These are shown in reactions 1-3:

$$Fe(II) + H_2O_2 \rightarrow Fe(III) + \mathrm{HO}^- + HO^{\bullet} \quad (1)$$

$$Fe(III) + O_2^{\bullet -} \rightarrow Fe(II) + O_2 \quad (2)$$

Net Reaction

$$O_2^{\bullet -} + H_2O_2 \rightarrow O_2 + \mathrm{HO}^- + HO^{\bullet} \quad (3)$$

These ROS can react rapidly in an indiscriminate manner with proteins, causing misfolding, or DNA, causing gene damage, and ultimately death of the cell. Thus, Fe must be tightly regulated within the cell. This is accomplished in yeast through a number of regulatory pathways which involve Aft1/2 (low iron response) and Yap5 (high iron response) **(27,28)**.

The Aft1/2 transcription factors initiate a Fe-deficient response. When cells are Fe-deficient, Aft1/2 localizes to the nucleus, where they bind the Fe-regulon, which is a set of genes that encode Fe-transport proteins. When Aft1/2 is bound in the nucleus, proteins encoding cellular Fe uptake (Fet3/Ftr1, Fet4) and trafficking (Mrs3/4) to the mitochondria are upregulated **(27)**, and proteins that assist in degrading the vacuolar import proteins (Cth1/2) are also up regulated **(29)**. As cells become Fe-replete, a sulfur containing species (X-S), gets exported from mitochondria by the Atm1 protein **(30)**. This sulfur species is used by the cytosolic ISC assembly complex (CIA) and a 2Fe2S cluster is produced. This cluster binds to the Grx3/4 proteins in a homodimer complex

with the ISC in the middle. In the next step, one of the Grx proteins will be replaced with Fra2 **(28)**. This Grx3/4:Fra2 heterodimer will then interact with Aft1/2 and exchange the Fe_2S_2 cluster. When Aft1/2 is bound with the ISC, it is localized in the cytosol of the cell after being exported from the nucleus by Msn5, though a study where Msn5 was deleted showed healthy Aft1 activity and translocation, so it is possible there is a secondary pathway for Aft1 export from the nucleus **(31)**.

In cases where Fe-trafficking genes in the cell are deleted/mutated, a multitude of phenotypes are evident, with the most common being an overload of Fe and a slow growth rate due to ROS damage. This cell damage can become cumulative and be observed tissues and organs in higher order organisms. Body phenotypes are observed with lethargy, potential mental retardation, and iron overload in organs, leading to cardiomyopathy and other complications **(32)**. Some common Fe-related diseases in which Fe is dysregulated in the cell/body are Friedreich's Ataxia, β-Thalassemia, and Hemochromatosis. Friedreich's Ataxia presents itself when the frataxin protein (Yfh1 in yeast) **(3, 16)**, is mutated or deleted. This protein is involved in mitochondrial ISC assembly, and loss of which leads to loss of assembly, Fe overload localized to the mitochondria, and a large excess of ROS damage in the cell **(33)**. β-Thalassemia is characterized by a malfunction in the production of hemoglobin. This leads to a cascade of problems, stemming from a lack of red blood cells in the body (anemia). This cascade includes a lack of oxygen in parts of the body, pale skin, weakness, fatigue, and a host of additional complications. **(34)** Primary Hemochromatosis is characterized by a loss of the HFE gene, which is involved in Fe regulation in the body. Loss of this leads to iron

overload in the body, and patients need to be able to get rid of this iron, typically through blood transfusions **(35)**. The overall goal of the research performed in the Lindahl laboratory is to understand the biological role of Fe in healthy and diseased cell states, and understand the chemistry involved in the trafficking and regulation of this critical biological metal.

Studying and understanding the roles of Fe in biology in a meaningful way presents an interesting problem, as *in vitro* methods don't necessarily translate to *in vivo* roles, as shown with in vitro studies of the Yfh1 protein demonstrating an iron storage function, where this does not appear to be the case **(17,36)**. In the Lindahl laboratory, a suite of biophysical methods is employed to give a systems' level understanding of Fe metabolism and trafficking in multiple from biological systems while preserving the integrity of these samples **(37)**. Among these are Mössbauer spectroscopy, Electron Paramagnetic Resonance (EPR) spectroscopy, and Liquid Chromatography-Inductively Coupled Plasma Mass Spectrometry (LC-ICP-MS). Among these techniques, Mössbauer spectroscopy has exclusive sensitivity for Fe, specifically ^{57}Fe. This technique can be used to detect ^{57}Fe, regardless of the rest of the sample present. As such, there have been a litany of studies done in biological platforms to study and understand the types of Fe centers present in cells and how they respond to various perturbations **(10,13,15,38,39,40,41)**.

Principles of Mössbauer Spectroscopy

The Mössbauer effect, named after Rudolf Mössbauer, utilizes recoilless nuclear fluorescence of gamma radiation and is the most powerful technique for studying Fe. This is due to the high selectivity for the element that comes from the required energy overlap between source and sample. **(42,43)**. Mössbauer spectroscopy is a nuclear resonance technique, similar to Nuclear Magnetic Resonance (NMR) spectroscopy, except that gamma rays are utilized to excite the nuclear spin as opposed to radio waves. The higher energy radiation is required because Mössbauer transition energies are much greater that NMR transition energies. Protons in the nuclei have a quantum mechanical property called spin angular momentum. These discrete states are called *nuclear spin states* (I). For a single proton, I has the value ½. These states are described by mathematical functions that have solutions only when I and another parameter that reflects magnetic properties, M_I, have specific values. There are two spin functions associated with this I=1/2 state, M_I=+1/2 and -1/2 **(44)**. Assuming a proton in free space, these two functions will be degenerate. When placed in a magnetic field, the energies of these two degenerate functions will split. In NMR spectroscopy, the proton is placed in a magnetic field and exposed to radiation of increasing frequency. When the energy of the radiation matches the transition energy, resonance is achieved, the radiation is absorbed, and the NMR signal is generated/detected. The resonance energy is sensitive to the chemical environment of the proton. This sensitivity makes NMR spectroscopy useful to chemists even though all the activity occurs at the nucleus. The same basic mechanism is occurring in Mössbauer spectroscopy, but more spin states and transitions are involved.

The most common nucleus used in Mössbauer spectroscopy, the ^{57}Fe nucleus contains 26 protons and 31 neutrons, each with their spin angular momenta that either enhance or cancel with each other. This feature results in multiple I values (1/2, 3/2, 5/2…) The I=1/2 state is the lowest in energy and is designated as the ground state. From this, the first level excited state is the I=3/2 state. This first transition (1/2 -> 3/2) is what is detected by Mössbauer spectroscopy. The energy to induce the ^{57}Fe transitions is provided by a ^{57}Co gamma source.

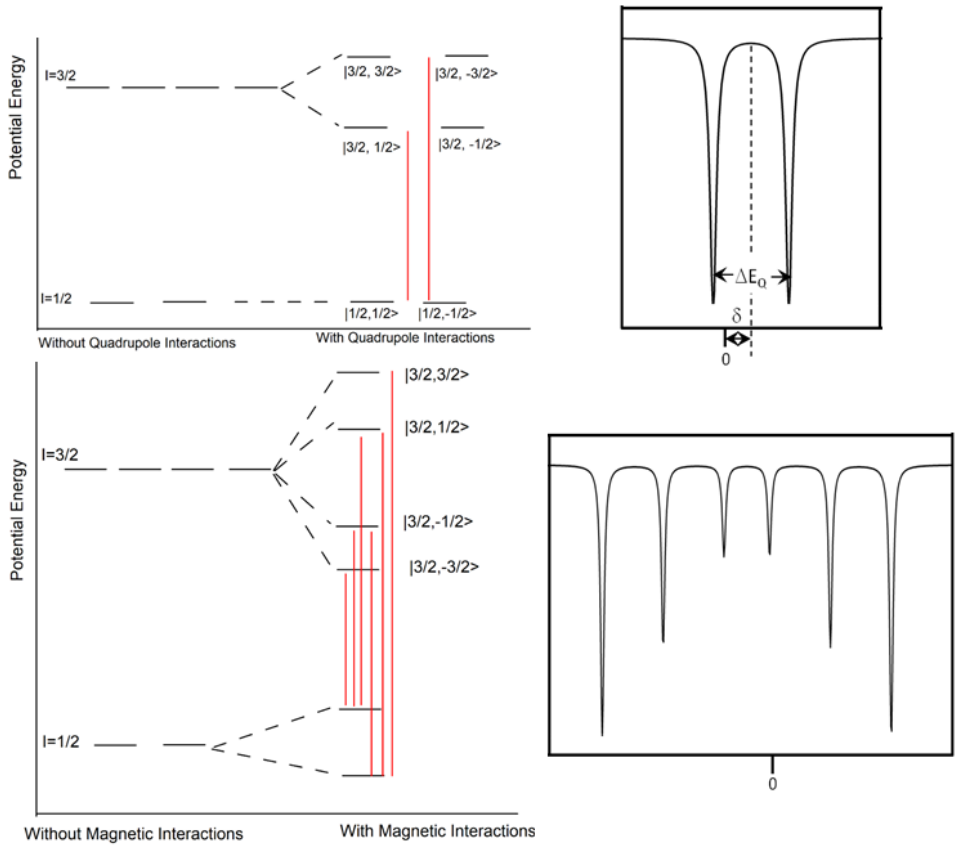

Figure 1.1: Basic Illustration of Mossbauer splitting, either with an electric field gradient to produce a quadrupole doublet (top), or in the presence of a magnetic field to produce a sextet signal (bottom)

Coordination Chemistry of Fe (44,45,46,47)

As a transition metal, Fe is easily found in a variety of oxidation states, with a maximum of 5 electrons able to be removed under physiological conditions. In biological systems, it is fallacious to use the term "free" iron, as at minimum Fe would be found as a hex-aqua complex. Common biological ligands for Fe contain O, N, or S, which contain the capability to "donate" electrons to the metal. Considering this, in proteins with metal centers containing Fe are typically coordinating the metal with amino acids like histidine, cysteine, and aspartic acid; as these contain the required atoms to coordinate Fe. In biology, the most common states of Fe are ferrous and ferric (Fe^{2+} and Fe^{3+} respectively), with the other oxidation states requiring special conditions to obtain in physiological conditions. The 3d orbitals of Fe have interesting shapes, with a node at the nucleus, and lobes along/between the axes. The geometries of orbitals give rise to certain preferences for complex shapes (octahedral, tetrahedral, square pyramidal…). For a free ferrous ion, the 5 3d orbitals are degenerate. Upon complexing the ferrous ion, the degeneracy changes depending on the number of ligands added, as well as the geometry of the molecule. The d orbitals are responsible for the superior catalytic properties of the transition metals, not just Fe. The d orbitals are weakly involved in bonding, allowing them to accept and donate electrons without an effect on stability of the bonds. This allows for weak substrate binding to the metal, which brings substrates close together spatially, increasing the probability of a chemical reaction to occur. All of these properties are what make transition metals such great catalysts, but this is a double edged sword. These metal catalysts can catalyze reactions that produce

ROS, which have deleterious effects on cells **(48,49)**. We can further look at what types of Fe-centers and compounds that are common in biological systems.

Types of Fe evident in biological samples (47)

Almost all known biological Fe centers have been studied by Mössbauer spectroscopy, and a total review of all of them here would require more time and would distract from the goal of this work. Rather, a summary of the Mössbauer characteristics of each major Fe center will be discussed. Heme groups are found in multiple proteins, such as hemoglobin, myoglobin, cytochromes, and mitochondrial respiratory complexes. High spin (HS) and Low Spin (LS) ferrous and ferric hemes are common. Mononuclear ferrous and ferric complexes, typically coordinated by O, N, or S ligands, are also evident. The designation of HS or LS depends on the geometry of the complex and the ligands involved. Also commonly observed are Fe-S clusters. Fe_2S_2, Fe_3S_4, and Fe_4S_4 core structures are found in biology. The overall oxidation state of the cluster is determined by the summation of the oxidation states of the individual Fe's in the cluster (+2 or +3 per Fe) minus the sum of the sulfur charges (-2).

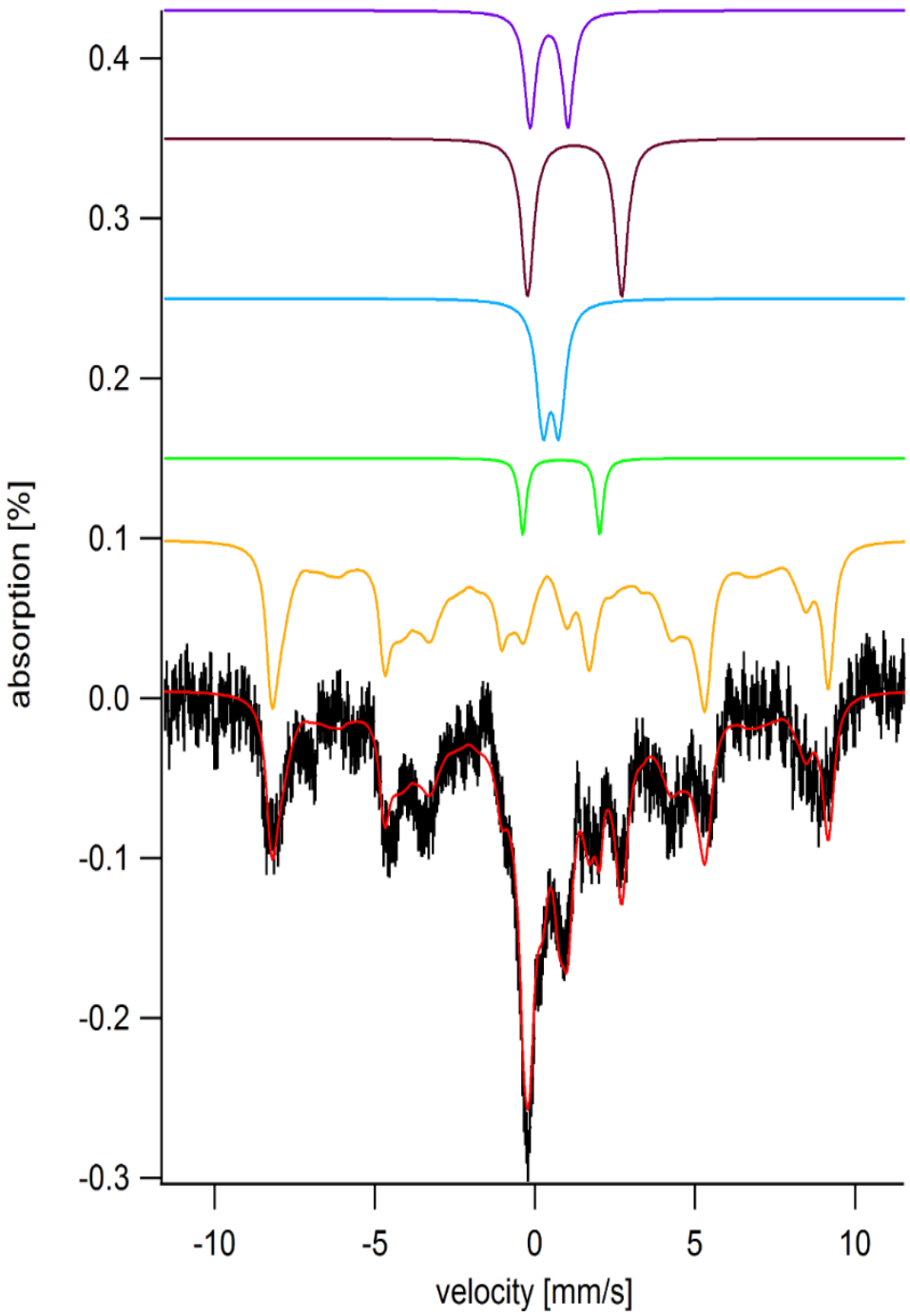

Figure 1.2: Mössbauer spectra of S. cerevisiae whole cells, with simulations of typical species. Gold: NHHS Fe^{3+}, Green: HS Hemes, Cyan: Nanoparticles, Maroon: NHHS Fe^{2+}, Purple: "Central Doublet" comprised of Fe_4S_4 Clusters and Low Spin Hemes

Aggregated Ferric ions

Fe^{3+} aggregates as nanoparticles can be observed with internal magnetic fields that fluctuate and change direction due to thermal excitations **(15,50,51)**. These fluctuations are much faster than the time of measurement by Mössbauer, which shows an average magnetic field of zero, and the resulting spectrum is a doublet. However, the magnetic features can be measured if the temperature is lowered enough. This "blocking Temperature" is the level at which half of the molecules in a population shows magnetic properties and half shows a doublet. This behavior is typical of superparamagnetic behavior. This behavior is observed in the mammalian Fe storage protein, ferritin. This protein is found in the cytosol and is a heterodimer made up of a combination of heavy and light subunits. This spherical protein has an 8 nm diameter core that is filled with Fe-oxyhydroxide nanoparticles as ferrihydrite **(52)**. This material gives a similar signal as hemosiderin, as is discussed below. However, the blocking temperatures of these two materials are vastly different, allowing for characterization of these materials by collecting spectra at various temperatures. Fe-oxyhydroxide nanoparticles are also apparent in yeast **(51)** and human cells **(40)**. These particles have low blocking temperatures (<4.2K), so that even at liquid He temperatures a doublet is evident. This low blocking temperature would indicate that the particles are smaller than in ferritin. This is corroborated by electron microscopy, which revealed an average particle size of 2-4 nm **(51)**.

Online and Offline LC-ICP-MS

LC-ICP-MS is useful for separating out various complexes containing metals. In many studies in the Lindahl laboratory, the low molecular mass (LMM) complexes are studied, as these are thought to be labile metal pools used for trafficking within the cell **(14,53).** In the Lindahl lab, a novel system has been developed that employs a bio-inert HPLC system that is housed in an anaerobic glove box. Samples are separated using an SEC (size exclusion chromatography) column. As analytes elute off the column, they are fed to an ICP-MS. The ICP-MS allows for simultaneous detection of multiple elements, and we are detecting biologically relevant metals (Fe, Cu, Co, Mn, Mo, Zn), as well as P and S. This allows for determination of when complexes containing the desired elements are coming off the columns. By calibrating the system with known standards, a calibration curve can be produced that allows for approximation of the molecular weight of the unknown peak.

Using the ICP-MS alone (called offline mode in the Lindahl lab), absolute concentrations of ^{57}Fe in each sample can be determined. Then by taking the given concentration and applying the dilution factors used to make the sample run on the instrument, one can calculate the absolute concentration of each element of interest in the sample.

Using WMOSS software, we can simulate individual Fe-containing species in the Mössbauer spectra and deconvolute the spectra into percentages of the whole sample. For example, a whole cell sample could be made up of 25% Fe-S clusters, 25% Non-Heme High Spin (NHHS) Fe^{2+}, and 50% NHHS Fe^{3+}. Knowing these, the percentages

can be multiplied by the absolute concentrations obtained through ICP-MS to yield absolute concentrations of the three detected species. There is a synergy of all techniques discussed (Mössbauer spectroscopy, EPR spectroscopy, LC-ICP-MS, and ICP-MS) that allows for a complete picture of the "iron-ome" of a species or cell mutant strain being studied, allowing for a systems level model to be developed.

Mathematical modeling

The above techniques can be used to build Fe-omics studies, studies that characterize the movement, utilization, and regulation of Fe within the system of interest. Many studies done focus on only one part of Fe trafficking and regulation and cannot make insights into the other parts of the cell. One goal of the studies presented in this dissertation is the integration of all of the individual "pieces" into a systems level model. That is, a model that can monitor Fe trafficking and regulation as it is imported into the cytosol, trafficked into organelles and is speciated, either as ISCs, nanoparticles, isolated Fe^{3+}, and so on. This model is implemented in the presented research through a system of ordinary differential equations (ODEs) and will be discussed in further chapters of this dissertation. Due to lack of specific information on certain species/processes as the modeling gets more complex, we rely on mesoscale modeling, and only focus on beginning and end products, for which data is attainable. For example, one may not know the exact details of ISC assembly in mitochondria, but the ISCs themselves, and their reported feedstock pool, can be measured; so one can use a simplified chemical reaction as a surrogate for the actual ISC assembly machinery.

This modeling approach isn't new, as there are many groups out there that have applied modeling approaches to various problems, including Fe. However, this modeling approach claims novelty by grounding the model in experimental data, and allows for computational work to directly communicate to each other. Once a model is sufficiently developed, it can then inform experimental direction, with new data obtained used to augment the model.

Transition to Projects

In this dissertation, multiple studies of Fe-related phenomena are reported, with a goal of understanding the regulation of iron import and trafficking in the cell and its response to various stimuli and perturbations. In the following chapters, the iron contents of *Saccharomyces cerevisiae* and *Escherichia coli,* as well as their responses to various stimuli and genetic perturbations were studied.

In *S. cerevisiae* studies, introduced below, the biophysical data collected from Mössbauer, EPR, and ICP-MS were integrated into an ordinary-differential-equation based model that can model various conditions and genetic strains, including WT cells, a strain in which the high affinity mitochondrial iron trasnporters Mrs3/4 are deleted (Mrs3/4ΔΔ), as well as a strain in which the yeast frataxin homolog (Yfh1) protein is under the control of estradiol. These studies helped to probe the regulatory pathways of yeast, as well as understand the role of oxygen in the ISC phenotype.

E. coli studies, introduced below, WT cells as well as mutants in which the ferric uptake regulator (Fur), and the various ferritins (FtnA, Bfr, and Dps) were deleted, were examined through the same biophysical and bioanalytical methods.

Modeling Efforts to Determine Regulation Species in S. cerevisiae

S. cerevisiae have many homologous systems for transporting metals relative to metals, so they are used as a model system for studying what happens in mammalian systems. Kaplan and co-workers (**54,55**), have monitored the cytosolic Fe species by installing Fe-requiring enzymes into yeast cells. This Erg25 enzyme is inactive under Fe-deficient conditions, but activity develops in cells grown under increasing concentrations of Fe in the growth medium. This would suggest that the cytosolic Fe species qualitatively mirrors the concentration of Fe_{med}. This species is probably not *directly* proportional, as a large concentration of ferrous iron creates the possibility for reactive oxygen species (ROS) damage through Fenton chemistry.

As mentioned above, Fe is toxic to the cell if present in excess concentration through Fenton chemistry and ROS damage. The regulation of this critical, yet dangerous micronutrient has been the subject of study, and some ambiguity. When studies first began on this regulation system, it was thought that Aft1/2 regulated cellular Fe import by "sensing" the cytosolic Fe pool, as it was depleted under Fe deficient conditions, and present under Fe-sufficient/excess conditions (**56,57**). However, studies conducted around 2004 by the Kaplan lab **(54)**, found that a loss of mitochondrial ISC assembly was the main contributor to dysregulation of Fe trafficking and import into *S.*

cerevisiae cells. In a cell strain in which the yeast frataxin homolog (Yfh1) protein was deleted, it was found that cellular iron import was upregulated, yet the cytosolic protein indicated that the cytosol was Fe replete, contradicting the standing model that the Fe regulon was turned on in the absence of the cytosolic Fe pool. This led the Kaplan group to conclude that mitochondrial ISC assembly is the factor that controls Fe regulation through the Aft1/2 transcription factors. Additionally, the Kaplan and Lill labs have found that the transcription factor Yap5 binds ISCs and regulates the "high-iron" genes, such as CCC1, which implicates mitochondrial/cytosolic ISC assembly (**57,58,59**).

An elaborate scenario has developed to explain how a mitochondrial-originated signal can be relayed to Aft1/2. Atm1 is an ATP-binding cassette half-transporter located on the inner membrane of the mitochondria which exports an unidentified sulfur containing molecule that is a byproduct of ISC synthesis (X-S) **(60,61**). X-S provides the required sulfur to cytosolic ISC synthesis and provides indirect control to Aft1/2 activation of the iron regulon. It is thought that the sulfur is used to build a Fe_2S_2 cluster that is used to bridge the Grx3/4 homodimer with the Fe coming from the cytosolic Fe pool **(62**). These glutaredoxin proteins are critical for Aft1/2 dependent regulation, as deletion of these proteins leads to constitutive expression of the iron regulon proteins. Fra2 interacts with the Grx homodier to generate a heterodimer with the Fe_2S_2 bridging **(63.64)**. This heterodimer then interacts with Aft1/2 to donate the Fe_2S_2 cluster, generating an Aft1/2:Fe_2S_2 heterodimer that localizes to the cytosol, which allows for unbinding of the iron regulon and down regulation of associated genes. Since this process appears to involve contributions from both the cytosolic Fe pool and

mitochondrial ISC assembly, it is possible that the cytosolic Fe pool can play a role in Fe regulation of the cell.

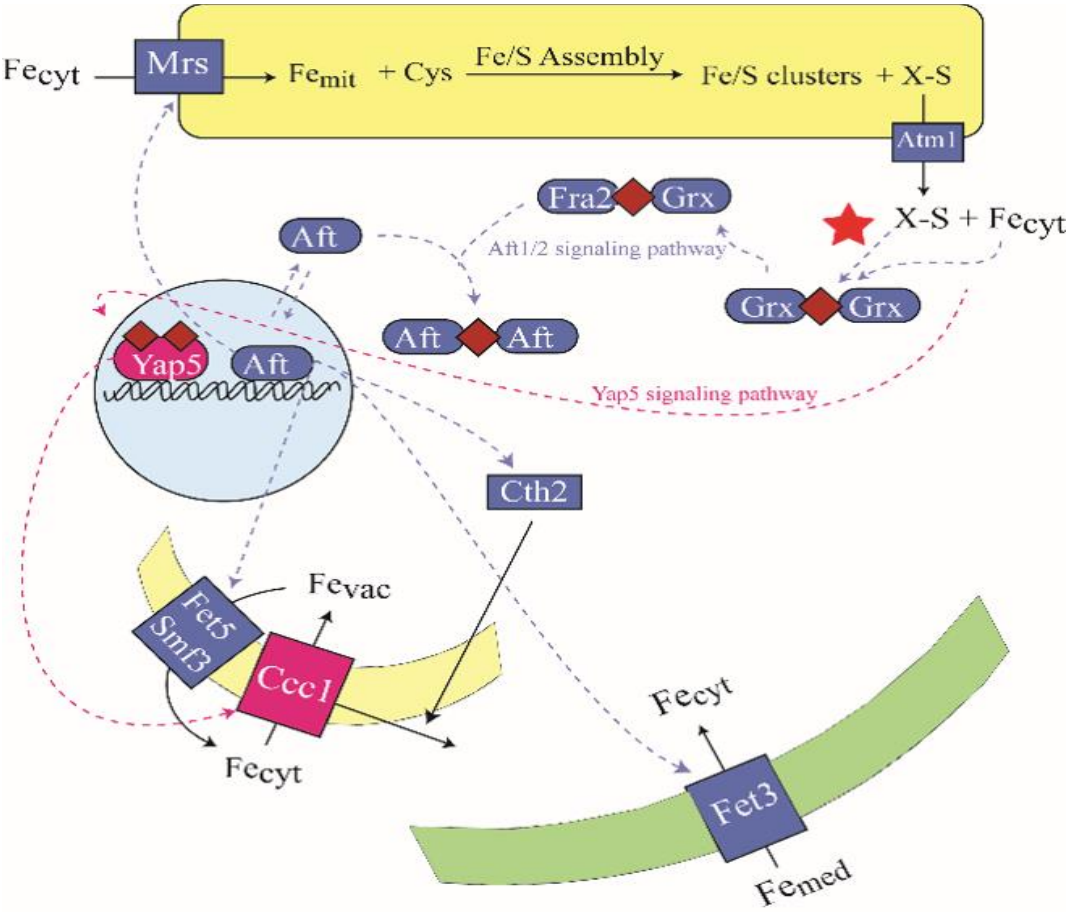

Figure 1.3: Model of regulation of Fe in S. cerevisiae. X-S is generated from mitochondrial ISC assembly, and exported into the cytosol by Atm1 (top of figure). This X-S could then be used to make a Fe2S2 cluster in the cytosol, (red star). This cluster is then picked up and shuttled to the Aft1/2 proteins through the Grx3/4 and Fra2 proteins. From there, depending on whether Aft is bound with the cluster, or bound the Fe regulon, the low Fe response is mediated through the blue arrows leaving the nucleus. It is also conceivable that Yap 5 binds the cytosolic cluster through some yet to be discovered pathway (denoted with red dashed lines).

Multiple nutrient states with wild-type (WT) yeast have been studied. These studies mostly involved changing iron concentration in the growth medium and studying either the whole cell samples, or the isolated organelles that are major Fe traffic hubs (mitochondria, vacuoles) **(65, 66)**. Mutants that attenuate ISC assembly and disrupt healthy Fe distribution in these traffic hubs, and the cell as a whole have also been studied **(50, 51)**. In these cases, whole cell and isolated mitochondria yielded Mössbauer signals in which the majority Fe species were found to be Fe-nanoparticles, with a small portion due to NHHS Fe^{2+}. These *ISC-mutant* phenotypes are characterized with these details, as well as these observations: a decline in both ISCs and hemes in mitochondria, an increase in ROS damage in mitochondria, an absence of vacuolar iron in cells grown on Fe-sufficient media, and an increase of cytosolic iron levels.

While there is much information about the regulatory pathways within S. cerevisiae, little work exists that attempts to integrate all of the pathways together to produce a quantitative model that tracks the concentration and speciation changes of Fe within a cell. It is also unclear exactly what roles cytosolic Fe and mitochondrial ISC assembly play in regards to cellular Fe regulation. In this dissertation, a first generation ordinary-differential-equation (ODE) model that uses surrogate regulation equations to probe the regulatory pathways of S. cerevisiae is presented. This model simulates an exponentially growing cell containing 3 organelles (cytosol, mitochondria, and vacuoles) with Fe flowing in from the growth media. This model was used to understand cases in which more iron was available to the cell (increasing media Fe) as well as understand

genetic mutants in which the mitochondrial ISC machinery, mitochondria import, and vacuolar import was disrupted.

Recovery of Mitochondrial Iron Contents in Mrs3/4ΔΔ Yeast Cells

S. cerevisiae are a workhorse of eukaryotic biochemical studies due to the robust and quick growths of cell cultures relative to human cells, as well as their similarities to human systems. Specifically in the mitochondria, yeast and human mitochondria have conserved high affinity iron importers on the inner membrane. These proteins are known as mitoferrins in humans, and Mrs3/4 in yeast. These transporters are thought to be responsible for bringing in ferrous iron that accumulates in the matrix of the mitochondria as a low molecular mass (LMM) that has been characterized by Mössbauer spectroscopy **(67,68,69,70,71,8,9,13)**.

Single deletions of either Mrs3 or Mrs4 do not yield a phenotype, indicating that they serve redundant functions **(9,13)**. Deleting both genes simultaneously results in a slow growth phenotype when these double mutants are grown in Fe-deficient media. Isolated mitochondria from these conditions contain limited amounts of hemes and ISCs (**9**). Double mutants (ΔΔ) grown in Fe-sufficient conditions rescue in growth rate and presence of hemes and ISCs **(8,9,12,13,71)**. These studies did not provide a satisfactory mechanism to describe the recovery of these mutants under high Fe conditions.

A second phenomenon that arises under Fe sufficient growth is the accumulation of Fe in ΔΔ cells relative to WT, even as growth rate and hemes/ISCs have recovered (**69,9,70**). This would indicate that the iron regulon is activated (of which Mrs4 is

included), and whatever process is responsible for producing X-S is impeded. This accumulated iron is not found in mitochondria, as Mrs3/4 deleted mitochondria have decreased iron uptake and have half the Fe concentration of WT mitochondria. The presence of any Fe at all would indicate a secondary Fe import pathway into mitochondria, of which a candidate protein is Rim2 (**11,12,72**).

The question remains as to where the excess iron accumulates, and previous studies have proposed the vacuoles and cytosol. In ΔΔ cells, the rate of Fe import through the vacuolar Fe transporter Ccc1 is increased **(70)**. Kaplan et al concluded that the activity of Ccc1 is higher due to a proposed signaling pathway between vacuoles and mitochondria that is involved in Ccc1 activity regulation **(73)**.

In this study, Mrs3/4ΔΔ cells were examined using biophysical and bioanalytical methodologies that allow characterization of the iron contents of whole cells and isolated mitochondria. These methods included Mössbauer, EPR, UV-visible spectroscopy, and LC-ICP-MS. The results of these studies help provide insights into a molecular explanation of the recovery of ΔΔ cells when grown in Fe-sufficient media as opposed to Fe-deficient media. They also provide suggestions as to what species of Fe is deficient such that ΔΔ cells are dysregulated, even when grown in high Fe.

Multi-Tiered Model

While applying the original modeling approach to the Mrs3/4ΔΔ strain, it was found that it was insufficient for accurately modeling the experimental data, so we developed a multi-tiered mesoscale model that can transfer fitting parameters from

simpler tiers that have more reliable or "harder" data to more complex tiers in which the data is "softer" as there are more manipulations and assumptions made to arrive at the experimental data one is fitting against at the more complex tier.

The core assumption of our model is that the matrix of the mitochondria is mostly anaerobic under WT conditions, with the respiratory complexes installed at the inner membrane responsible for the reduction of molecular oxygen to water, thereby preventing oxygen from penetrating into the matrix. Although [O2] has not been directly measured for the mitochondrial matrix, there are 3 lines of indirect evidence to support this assumption. First, *in vitro* ISC assembly assays must be done in anaerobic conditions (**74**). Second, numerous enzymes that are present in the mitochondrial matrix are extremely oxygen sensitive (**75, 76**). Third, the nitogenase iron protein, another exquisitely oxygen sensitive protein, is active when expressed in the matrix (**77**). In our model, ISC mutant mitochondria have increased oxygen in the matrix because of a lack of ISCs and hemes, which play a critical role in respiratory complexes.

In this study, an improved ODE-based model of iron trafficking and regulation in yeast is presented. This is accomplished through a multi-tiered examination and solving each model at an expanding steady state to simulate an exponentially growing cell. This novel approach to model building was used to fit WT respiring cells, Mrs3/4ΔΔ respiring cells (**10**) that have been characterized with Mössbauer, EPR, ICP-MS, and LC-ICP-MS. The model is currently being used to quantitatively understand the changes in Yfh1 deficient cells under various conditions (in prep). These Yfh1 cells are being

used as an experimental test of the assumption that oxygen plays a role in the ISC phenotype.

Yeast cell wall acts to store iron for metabolically deactivating cells

The cell wall (CW) is an often ignored organelle of the cell. About 20% of the genes in S. cerevisiae are involved in CW construction and maintenance **(78,79,80,81)**. The cell wall provides more than structural support in the cell, as it is involved in cell reproduction, as well as the virulence of pathogens **(82,83,84,85,86)**. The cell wall also plays a role in Fe metabolism. There are "Facilitator of Iron Transport" proteins (Fit1/2/3) that work to deliver Fe across the cell wall to the plasma membrane **(87)** and these Fit proteins are under the control of the Fe regulon. Data presented in this dissertation indicate the cell wall manifests as another traffic hub (along with cytosol, vacuoles, and mitochondria) of Fe in the cell as the cells transition to stationary state. This cell wall (CW) Fe can then be mobilized, released, and imported by metabolically reactivating cells.

E.coli possess a respiratory shield similar to yeast mitochondria

Escherichia coli (E. coli) is a gram negative, rod-shaped, bacterium that is typically found in the intenstines of warm-blooded organisms. It is also the most well studied microorganism because of its ability to be used to express proteins and quick growth rate. However, the biophysical studies of E. coli have been lacking in consistency of preparation of sample. Many samples were grown to stationary growth

state as opposed to exponential state in the same way as the yeast studies, and the resulting Mössbauer spectra showed a large accumulation of nanoparticles, and many more focus just on isolated proteins rather than look at whole cell samples in a systematic basis.

Under aerobic conditions, E. coli secrete siderophores in the environment that serve to bind the relatively insoluble ferric iron found in abundance. These siderophore-iron chelates are then reimported with specific receptors on the exterior of the E. coli cell **(88,89)**. Under anaerobic conditions, E. coli employ a system for importing ferrous iron (Feo) **(90)**. However, for the studies presented here, the Fec system **(91)** will be the system used for Fe import, as ferric citrate is the primary form of Fe supplied to cultured E. coli. All of these genes are regulated by Fur.

E. coli possess three ferritin-like proteins (FtnA, Bfr, and DPS) **(92,93)**. The main storage protein of these three is FtnA, which binds thousands of iron ions as inert ferric oxy-hydroxide aggregates. Fe-Fur binding leads to production of FtnA and Bfr **(94,95)**, with expression of these proteins increasing as the cell transitions from exponential to stationary phase **(96).**

E. coli are also sensitive to the concentration of available oxygen. The Fnr transcription factor is needed for anaerobic growth **(97)**. Fnr senses O2 and is responsible for regulation the shift between aerobic and anaerobic metabolism. Fnr is responsible for the regulation of ~300 genes, and is sensitive to dissolved [O2] between 0 and 20 μM **(98)**. The "switch" in Fnr is a Fe_4S_4 cluster that is converted to a Fe_2S_2

cluster under oxidizing conditions, which alters DNA binding affinity **(97)**. In anaerobic conditions, FNR retains the Fe_4S_4 cluster and increases expression of Feo.

Fe regulation in E. coli involves a poorly characterized labile Fe species, or pool **(99,100,101)**. This labile Fe pool (LIP), is presumed to be low molecular mass and non-proteinaceous. The LIP is thought to be used in both sensing of Fe levels of the cell, but also metalation of the apo target proteins. Exact chemical characterization of the LIP is difficult due to the fast ligand exchange reactions occurring between the Fe and the weakly bound ligands. Bohnke and Matzanke **(100)** isolated and characterized a non-proteinaceous, negatively charged Fe complex that was accounted as 40 % of the E. coli LIP. This complex possesses a mass of ~2.2 kDa and had potential ligands of pentose, uronic acid, sulfonate, or phosphate esters. Imlay and coworkers used EPR to quantify the LIP, utilizing a membrane-permeable Fe chelator and quantifying the EPR signal associated with the chelate (**101**). The [LIP] was reported to be 15-30 μM in WT and 80 μM in Δfur cells. Hohle and O'Brian reported that the LIP was representative of a maximum of 8% of total iron **(102)**. The size of the LIP has been reported to increase with cyanide treatment and when grown under anaerobic conditions **(103,104,105)**.

There have been a handful of Mössbauer studies performed with E. coli over the past 40 years. Bauminger et al. reported in 1980 that spectra of E. coli exhibited a quadurople doublet with parameters characteristic of magnetically-ordered Fe^{3+} **(106)**. Matzanke reported a second doublet in 1989 which made up 11-56% of the spectral intensity, with parameters matching those of non-heme high spin (NHHS) Ferrous complexes with oxygen and/or nitrogen ligands **(107)**. Hudson reported in 1993 the

decomposition of the NHHS Fe^{2+} doublet into 2 distinct doublets. The Hudson group (**108**) reported that FtnA has a blocking temperature (TB) of 19-22 K, which is significantly different as compared to the magnetically ordered ferric species reported by Bauminger and that ferritin iron was not the source of the magnetically ordered species. Abdul-Tehrani et al **(109)** estimated the [Fe^{2+}] species at ~200 μM. They commented that this was much higher than previous estimates of the LIP in E. coli, and higher than what is implied by the Fe^{2+}-Fur dissociation constant. There have been studies that present even higher [LIP] (300-500 μM), estimated through assaying total acid-soluble non-heme iron in E. coli **(110)**. Abdul-Tehrani et al explains this by concluding that the ferrous species observed in Mössbauer represents a different pool that what is "sensed" by Fur. Hristova et al. **(111)**, reports a fourth doublet, comprising around 60% of the spectra, that is made up of Fe_4S_4 and Fe_2S_2 clusters, LS ferrous hemes, and possibly HS ferric hemes. Beilschmidt et al. described a similar doublet and only hypothesized the doublet to be exclusively due to ISCs **(112)**.

In this dissertation, we present a biophysical study of WT E. coli grown on two carbon sources, glucose and sodium acetate, as well as a mutant in which the ferric uptake regulation (FUR) transcription factor was deleted and grown with glucose exclusively. These cultures were also grown under varying ferric citrate conditions (1, 10, or 100 μM). Experiments were also performed with cyanide treatment, as well as allowing cells to grow into stationary state as a means of studying changes of iron contents, focusing on the LIP. The goal of this study was to provide a systematic Mössbauer analysis of WT E coli, as opposed to using WT simply as a control for

genetic strains being analyzed. In addition to the Mössbauer study, labile metal pools were detected and characterized using LC-ICP-MS. The results presented provide new insights into the iron content of E. coli, and reveal an evolutionary connection between the iron content of E. coli, mitochondria, and perhaps all prokaryotes.

Additional Projects

In addition to the studies presented here, there are also additional studies presented in the appendices. Murine hearts have been examined at various stages of growth, and the iron contents characterized using Mössbauer, EPR, and ICP-MS (Appendix A (**113)**). I also present a study done in collaboration with the Rose group from the University of Texas at Austin in which Fe carbonyl clusters were studied with Mössbauer spectroscopy in the Lindahl lab (Appendix B (**114**)).

CHAPTER II

MATERIALS AND METHODS

Fe stock prep and Media components

^{57}Fe stocks

^{57}Fe powder (isoflex) was weighed and transferred to a small flask. The weigh boat was rinsed with trace metal grade hydrochloric acid (Sigma Aldrich) to ensure complete transfer of the powder. Aqua regia (3:1 TMG Hydrochloric acid and TMG Nitric acid) (Sigma Aldrich) was added to the flask with stirring until the powder was dissolved in acid. This solution was then transferred to a volumetric flask, and diluted to the mark with distilled, deionized water. This 80 mM stock was then aliquoted by 40 mL into 50 mL conical falcon tubes.

^{57}Fe citrate stocks

For the preparation of 40 mM ferric citrate, 3 of the acid stocks prepared above were then thawed and transferred to a graduated cylinder for a starting volume of 120 mL. Deionized, distilled water was added to 200 mL. This solution was then transferred to an Erlenmeyer flask. Sodium citrate (Fisher) was added in 3 molar excess (11.3 grams powder) to this solution and allowed to dissolve. The solution was then buffered to pH 5 using additional sodium citrate. This solution was then transferred back to the graduated cylinder, and diluted to 240 mL with additional distilled, deionized water. This solution was then filter sterilized using a stericup/sterifilter system with a 0.22 µm filter (EMD

Millipore). The same procedure is used to prepare ^{56}Fe citrate, with the exception that ferrous ammonium sulfate power (Fisher) is used in place of the acid stock solutions.

Tryptophan

8 g of tryptophan was dissolved in 1 L of distilled, deionized water. This solution was stirred with a stir bar and stir plate until the tryptophan was thoroughly dissolved, then filter sterilized into a 1 L pre-autoclaved Pyrex bottle using a 0.22 µm sterifilter (EMD Millipore). This solution was used as a stock to add tryptophan to sterilized cell culture media.

$CuSO_4$

10 mM $CuSO_4$ was prepared in distilled, deionized water (.399g in 250 mL). This solution was then filter sterilized with a sterifilter/stericup system in a similar manner to the Fe citrate solution. This solution is used as a stock for providing Cu to sterilized cell culture media.

Minimal media

This is used as a means of knowing the exact chemical make-up of the growth media of the cells. This media is made up with yeast nitogen base (YNB) (1.7 g/L) (MP Bio), Ammonium sulfate (5 g/L) (Fisher Sci), the desired carbon source glucose or galactose (20 g/L) (Fisher Sci) or glycerol ethanol (30 mL/L gly, 10 mL/L EtOH) (Sigma Aldrich gly, Fisher Sci EtOH).

For each strain, the required amino acids to overcome auxotrophies were added. For W303, adenine (50 mg/L), histidine (20 mg/L), uracil (20 mg/L), and leucine (100mg/L) (MPBio) were added. For BY4741 strains, these prior amino acids were added, as well as Methionine (30 mg/L). For YPH499 strains, all the W303 additions were made, as well as Lysine (30 mg/L). The YPH499 strain was the parent to the Gal-YFH1 pGEV strain used in some studies, and all amino acids were added, with the exception of leucine, as it could cause the plasmid to come out.

After this media mixture was autoclaved, the previously mentioned Fe, Cu, and tryptophan stocks were used for addition of those chemicals to the media.

Rich Media

This media (YPAD or YPD) contains plenty of nutrients, but is chemically undefined. YPAD media is made up with yeast extract (10 g/L) (Fisher), peptone (20 g/L) (Fisher), glucose (20 g/L) (Fisher), and adenine (100 mg/L) (MP Bio). YPD is made up in the same manner, but with the exclusion of adenine in the media. Once the media was autoclaved, it was available for ^{57}Fe addition, if the experiment at hand required such addition.

Cell Plates

Yeast

Media plates were made by adding the required ingredients for either minimal or rich (YPAD or YPD) media, then adding 20% w/v agar. This mixture was then

autoclaved for 15 minutes to sterilize the media. Once complete and cool enough to handle, Fe, Cu, and tryptophan was added to the media (minimal media only), and the media was aliquoted into polypropylene petri dishes under sterile conditions and the gel plates were allowed to set up. Once the gel was solid, the plates were inverted, placed into a 30˚C incubator over night to remove excess water. The plates were then wrapped in parafilm and placed into a 4˚C refrigerator until used for cell growth.

E. coli

LB media plates were made using published LB media recipes and adding 10% w/v agar. This mixture was steam sterilized in an autoclave, and plates were poured in the similar manner as above. Once plates were solid and ready, E. coli cells in frozen stock were streaked onto the plate, and the plates were then incubated at 37˚C for 12-16 hours.

Cell Stocks

Yeast

Single colonies from growth plates were inoculated into 50 mL sterile YPAD media in the presence of a Bunsen burner flame to maintain an aseptic environment. These small cultures were grown to high OD, then spun out of media in sterile conical centrifuge tubes. A small volume of sterile 15% glycerol was added to this cell pellet, and aliquots were taken and placed into screw cap vials. These vials were then placed into the -80˚C freezer until cell stocks were needed for cell plate growth.

E. coli

Single colonies were grown in liquid M9 minimal media, then pelleted at 12,000xg. This pellet was suspended in a sterile 50% glycerol solution, and aliquots were added to small (~2 mL) vials and these vials were placed into the -80˚C freezer until these stocks were needed for cell plate growth.

Cell Growth

Yeast

Media plates were brought out of the refrigerator and allowed to come to room temperature. Then cell stocks were brought out of the -80˚C freezer. Using a sterile stick or sterile inoculation loop, stock was scraped out of the bottle and onto the cell plate in an aseptic environment. This initial volume of cells was streaked along the plate with additional sterile loops such that it was diluted out so that single colony growth was obtained. Plates would be placed into a 30˚C incubator for 3-6 days to allow for growth until single colonies were observed on the plate. The plates would be marked with date of inoculation, wrapped in parafilm, and placed into the 4˚C refrigerator until needed for liquid media experiments. Single colonies would be selected using a sterile inoculation loop to inoculate the single colony into a small volume of liquid growth media.

Liquid medium was prepared in either minimal or rich conditions. Rich conditions used either YPD or YPAD containing media, depending on the cell type being grown (BY4741 could be grown in YPD, all other cells required YPAD, as they

would turn pink in YPD, indicating an adenine deficiency). This liquid media was autoclaved, and once cool, filter sterilized $CuSO_4$, Ferric Citrate (56 or 57), and tryptophan were added to the minimal media. Small aliquots (50 mL) were inoculated with single colonies from agar plates. When these cultures were grown to high OD, 1 L cultures were inoculated. If doing whole cell experiments, these cultures would be spun down at 5000x G for Mössbauer, EPR, or ICP-MS analysis. Otherwise, this 1 L culture would be used to inoculate 24 L of media prepared in a 25 L glass fermenter.

E. coli

Cells were maintained in 50% sterilized glycerol stock and plated onto LB media. Cells were grown in liquid M9 minimal medium. The initial culture (50 mL) was grown without added Fe, but ^{57}Fe was added to the final 1 or 2L culture, depending on the experiment being performed.

Mitochondria Isolation

Cells were grown in the method described in **Cell Growth**. Cells were grown in a small (~50 mL) culture, inoculated into a 1 L culture, then finally inoculated into a 24 L culture being maintained in a 25 L glass fermenter. Once cells reached an OD of 0.8 to 1, they were spun down at 5000xG for 5 minutes per spin. This process was repeated around 4 times, as the maximum volume limit per spin was ~ 6 L. The cell pellet was then consolidated into a single centrifuge bottle. All future steps were then done inside an anaerobic, refrigerated glovebox (MBraun).

The cells are washed in Tris buffer, then washed in Tris-DTT buffer (10mM DTT) to start breaking down disulfide bonds in the cell wall. Cells were washing in SP buffer with 1 mM EDTA, then washed in SP-Lyticase to digest and remove the cell wall. The amount of lyticase was calculated such that 1000 units of enzyme were used per gram of cell. This suspension was sealed in a bottle with small aliquots with and without lyticase placed in 2 mL Eppendorf tubes, taken out of the box, and placed in the shaker at 30 C for 30 minutes. The aliquot with lyticase added was measured against the control at 600 nm, and the digestion in lyticase was considered complete when the OD_{600} of the lyticase cells was 30% of the control value. This value requires a 1:100 dilution of the cell solution. The bottle with the majority of cells was then centrifuged at 5000xG for 5 minutes. Cells are washed one more time in SP buffer, then are suspended in a buffer containing 100 mL water, 100 mL 2xSH, and 10 µM PMSF. This suspension was then homogenized using a tight fitting dounce homogenizer for 25 strokes per 40 mL of suspension. This was centrifuged at low speed to get rid of cell debris, homogenized for another 25 strokes, then centrifuged at high speed (12,000x G) to obtain a crude mitochondria pellet. This crude mitochondria was layered on a prepared 15/20% Histodenz gradient prepared in 1xSH, and then spun at 30,000 rpm in the Beckman ultra centrifuge. The mitochondria are then collected from the 15/20% interface, washed in 1x SH buffer, then pelleted into a Mössbauer cup or EPR tube for further analysis.

Mössbauer Spectroscopy

Low Field

Low field (0.05 T) and low temperature spectra were run on a Model MS4 WRC instrument (SEE Co., Edina, MN). These instruments were equipped with heating coils on the sample rods, and were programmed for various temperatures for temperatures higher than ~5 K. The sealed ^{57}Co source was affixed to a driver, where the velocity of the source was controlled using the W302 software (SEE Co.). The detector was controlled using W202 software (SEE Co.)

To put samples into the instrument, helium gas was pumped into the sample space to break the vacuum. The sample rod can then be removed and a cap placed over the opening. The sample can be installed into the sample holder, and the frost from the instrument needs to be dusted off using a Chemwipe. The sample rod can then be reintroduced to the sample chamber while flowing helium at a positive pressure. The set screws on top of the sample rod must then be threaded, then the sample chamber set under vacuum. Once the maximum vacuum is achieved, a small amount of helium is allowed into the sample chamber to allow for heat exchange between the sample and the instrument cold head. The detection windows are then set in the W202 software, the velocity is set in the W302 software, and the spectrum is set to collect.

High field

(0-6 T) spectra were run on a Model LHe6T instrument (See Co., Janis). Use of this instrument requires liquid helium and a procedure to prepare the instrument for use.

The vacuum space of the instrument must be pumped out 5 days before the experiment begins using a turbo pump. 3 days before the experiment, the liquid nitrogen dewar inside the instrument needs to be filled. 2 days before the experiment, the sample space and liquid helium space must be pumped out with a roughing pump. The day before the experiment begins, fill the liquid helium space with liquid nitrogen. Once the sample rod reads liquid nitrogen temperatures, the sample can be introduced in the same manner as with the low field instruments. This method prevents liquid helium loss during the sample introduction if it isn't introduced until after the helium fill. Monitor the signals from the ^{57}Co source in W302. There is enough nitrogen in the helium space when the signals disappear.

The day the experiment begins, before the helium fill, blow the remaining nitrogen out of the helium space with chilled helium gas. The helium gas is chilled using a copper coil submerged in liquid nitrogen. Monitor the signals in W202 to observe their return. Once the nitrogen has been removed, cycle the helium space and sample space with vacuum and chilled helium gas twice. Then pull vacuum on both spaces for approximately 20 minutes. Then fill the helium space with chilled helium gas. Once this is done, the helium fill can begin. This requires using the liquid helium transfer line to transfer helium from the liquid helium tank into the helium dewar inside the instrument. For the initial fill, there is an initial fill port on the instrument that has a tube going to the bottom of the dewar, ensuring an initial fill. As the instrument is cooled, the resistance at the instrument magnet can be measured. Once the resistance is at 5000 Ω, there is liquid helium on the magnet. Then monitor the helium level until it reaches about 75% full.

Then release the helium pressure, remove the transfer line, and cap the initial fill port, and attach a tygon tube line to the refill port as a vent for the gaseous helium escaping from the helium dewar.

The magnet can be charged after 8 hrs. Turn on the magnet power supply, and allow 30 minutes for it to warm up. Then press the "PSH on" button to connect the power supply to the magnet. After the connection is established, charge the magnet by increasing the field. This is accomplished by pressing "output settings" then inputting the desired field. Wait for the power supply to ramp up the current to the desired setting, then press "PSH off". This has disconnected the power supply from the magnet, and the power supply can be ramped down and shut off. To change the magnet field, the power supply is turned back on, ramped up to the previous field, reconnected with PSH on, and then change to the next desired field using output settings.

Monitor the helium levels, and either refill the helium dewar when the level is at 30%, or reconnect to the magnet and ramp the field back to 0 T. If the helium level decreases past 30%, it becomes likely that the magnet field becomes inhomogenous and the magnet could quench. If the refill is desired, use the helium transfer line and introduce the helium through the refill port on the instrument.

Sample data collection is accomplished in the same way as described for the low field instruments. The windows are set in W202 software, and the sample velocity is set and data collection is accomplished with W302 software. Sample changes are done in the same way, by flowing chilled helium gas into the sample space to break the vacuum, the rod is removed, samples changed out of the holder, and the sample rod replaced

while flowing chilled helium gas to give positive pressure. Then set the windows and reset the spectrum. Sample changes should be done with purpose, as heat exchange between the chilled helium in the sample space and the helium dewar leads to increased consumption of liquid helium during this time.

Liquid Chromatography-Inductively Coupled Plasma-Mass Spectrometry (LC-ICP-MS)

Online

Cell extracts were prepared in a 2% Triton X-100 detergent mixed with 20 mM ammonium bicarbonate buffered to pH 8.5. The extracts were then passed through an Amicon filtration system with a 10 kDa cutoff membrane that has been soaked in buffer or in distilled, deionized, distilled water (DDD H_2O). Argon gas was used to pressurize the chamber, and the extract was stirred while the flow through solution FTS was obtained. The FTS was then run through the size exclusion chromatography (SEC) column with 20 mM ammonium bicarbonate at pH 8.5 as the mobile phase, and the eluents were detected using the ICP-MS instrument (Agilient 7700X).

Offline

Packed cell/mitochondria pellets were obtained by spinning samples in short (3”) quartz EPR tubes. The pellet heights were marked on the tube, and pellets were removed with a known volume of DDD H_2O. The tubes were filled with water to the mark, and this amount of water was removed and massed to determine pellet volume. Pellet

volumes were corrected with the packing efficiency of whole cells or mitochondria **(41)**. The cell samples were digested in acid, and triplicate samples were made from this "master mix" and diluted to a known volume with DDD H_2O.

These samples were then placed on an automatic sampler. The ICP-MS was tuned, then standards (Inorganic Ventures) were made in serial dilutions as a calibration curve to approximate the concentration of the various analytes in the unknown samples. The true concentrations can be calculated by applying the various dilution factors (water to remove from tube, added acid, final water dilution) from digestion on to the ICP-MS analysis.

Electron Paramagnetic Resonance (EPR) Spectroscopy

Samples were prepared in 7.25" precision quartz EPR tubes (Wilmad Lab Glass). The samples were diluted in the minimal amount of Distilled, Deionized H_2O and spun at 4000x G in a custom designed rotor to obtain a packed sample pellet. The samples were then analyzed using an X-band Elexsys spectrometer (Bruker Biospin Corp., Billerica, MA). Samples were introduced to the instrument in the following way: The chamber valve was closed, allowing helium flow. The brass cap was removed, and the sample was quickly wiped to remove any frost/water to keep from potentially icing the instrument. Once the sample was introduced, the valve was reopened to allow vacuum to be re-established in the sample chamber.

Once the sample was in the chamber, the instrument was then tuned using the Bruker X EPR software. After tuning, the instrument was ready for operation. Typical

settings involved a frequency of 9.38 GHz, attenuation of 30 dB, .2 mW power, 300 s sweep time, 298 ms conversion time, 10 G modulation amplitude, 2550 G center field, and a 5000 G sweep width. The center field and sweep width could be adjusted to focus in on desired regions of the full sweep spectrum. If the sample was too concentrated, the attenuation needed to be increased to decrease the power, or the attenuation decreased if the sample was too dilute.

Mathematical Modeling

Models were written in either Mathematica 9 or Mathematica 10 software (wolfram.com). Ordinary differential equations were written into the notebook files as described in further chapters (**154**). The ODE's written were solved to steady state conditions by solving over long times using the NDSolve routine and over multiple nutrient Fe conditions, as well as other conditions using the Table routine. Parameters were optimized using an error function that compared values simulated in the model to experimental data values obtained from offline ICP-MS and Mössbauer spectroscopy.

CHAPTER III

MITOCHONDRIAL IRON-SULFUR CLUSTER ACTIVITY AND CYTOSOLIC IRON REGULATE IRON TRAFFIC IN SACCHAROMYCES CEREVISIAE*

Summary

An ordinary differential equation-based mathematical model was developed to describe trafficking and regulation of iron in growing fermenting budding yeast. Accordingly, environmental iron enters the cytosol and moves into mitochondria and vacuoles. Dilution caused by increasing cell volume is included. Four sites are regulated, including those in which iron is imported into the cytosol, mitochondria, and vacuoles, and the site at which vacuolar Fe^{2+} is oxidized to Fe^{3+}. The objective of this study was to determine whether cytosolic iron (Fe_{cyt}) and/or a putative sulfur-based product of iron-sulfur cluster (ISC) activity was/were being sensed in regulation. The model assumes that the matrix of healthy mitochondria is anaerobic, and that in ISC mutants, O_2 diffuses into the matrix where it reacts with nonheme high spin Fe^{2+} ions, oxidizing them to nanoparticles and generating reactive oxygen species. This reactivity causes a further decline in ISC/heme biosynthesis, which ultimately gives rise to the diseased state. The ordinary differential equations that define this model were numerically integrated, and

---

*This work was originally published in the Journal of Biological Chemistry. Joshua D. Wofford, Paul A. Lindahl, Mitochondrial iron-sulfur cluster activity and cytosolic iron regulate iron traffic in Saccharomyces cerevisiae, 2015, Volume 290, 26968-29677.

concentrations of each component were plotted *versus* the concentration of iron in the growth medium and *versus* the rate of ISC/heme biosynthesis. Model parameters were optimized by fitting simulations to literature data. The model variant that assumed that both Fe_{cyt} and ISC biosynthesis activity were sensed in regulation mimicked observed behavior best. Such "dual sensing" probably arises in real cells because regulation involves assembly of an ISC on a cytosolic protein using Fe_{cyt} and a sulfur species generated in mitochondria during ISC biosynthesis and exported into the cytosol.

Introduction

Iron is a critical component of virtually all living systems; it participates in enzyme catalysis, electron-transfer reactions, substrate binding, DNA replication and repair, and many other types of reactions. In eukaryotic cells, iron-rich respiratory complexes in mitochondria are filled with hemes and iron-sulfur clusters (ISCs). (**115**) Environmental iron is imported into cells where it is trafficked to various cellular compartments. How this traffic is regulated remains an enigma despite extensive investigations (**28**). Here, we use mathematical modeling to better understand iron regulation in yeast cells.

Environmental iron is generally present as poorly soluble Fe^{3+} that is reduced to Fe^{2+} before it enters the cell (**115**). Iron enters through various importers, including a high affinity importer consisting of a permease (Ftr1) and a multicopper oxidase (Fet3). Imported iron is released into the cytosol, probably in the Fe^{2+} state. Little is known about cytosolic iron (Fe_{cyt}) because no trafficking species has been isolated or

characterized. This is unfortunate because Fe_{cyt} plays an essential role in iron trafficking, and it cannot be ignored in developing a mathematical model of iron trafficking and regulation.

Kaplan and co-workers (**54, 55**) have indirectly monitored the concentration of Fe_{cyt} by genetically installing iron-requiring enzymes into *Saccharomyces cerevisiae*. In iron-deficient cells, the heterologously expressed enzymes are inactive because they lack iron at their active sites. The enzymes develop activity in cells grown on medium containing iron (Fe_{med}) at high concentrations. These reporter proteins develop activity at rates and to extents that are proportional to [Fe_{med}]. These and other experiments suggest that in WT cells, [Fe_{cyt}] qualitatively mirrors the concentration of [Fe_{med}]. We will assume this here, but not that [Fe_{med}] and [Fe_{cyt}] are *directly*proportional; [Fe_{cyt}] is expected to be tightly regulated such that it changes modestly as [Fe_{med}] changes dramatically.

Mitochondria are the major iron traffic hubs in eukaryotes. The organelle from *respiring* yeast cells grown in iron-sufficient medium contains 500–800 μM iron, most of which is present as Fe_4S_4 clusters and heme centers housed in respiration-related proteins (**65**). $[Fe_2S_2]^{1+/2+}$ clusters and Fe^{3+} phosphate oxyhydroxide nanoparticles are also present. Mitochondria from iron-sufficient *fermenting* cells contain iron at a similar concentration but in a different distribution; the concentration of iron associated with respiratory complexes is reduced ~3-fold (implying a decline from ~600 to 200 μM in iron). In contrast, the concentrations of nonheme high spin (NHHS) Fe^{2+} ions, NHHS Fe^{3+}ions, and Fe^{3+} phosphate oxyhydroxide nanoparticles are increased to ~130, 100,

and 200 μM, respectively. These latter three pools are probably related through redox and ligand exchange reactions.

Vacuoles are another iron traffic hub in yeast. These acidic organelles dynamically store and mobilize iron. They are devoid of iron under iron-deficient conditions. Vacuoles from cells grown on iron-sufficient medium contain high concentrations of a NHHS Fe^{3+} complex in which the coordinating ligands are closely related to polyphosphate (**66**). A NHHS Fe^{2+} species evident in Mössbauer spectra of adenine-deficient whole cells may also be located in vacuoles (**116**). Under adenine-sufficient conditions in which the vacuolar iron importer Ccc1 is either absent or overproduced, high levels of Fe^{2+} are present (**66**).

Mössbauer spectra of whole yeast cells exhibit major contributions from both traffic hubs (**13**). In iron-sufficient WT cells, vacuolar iron exhibits a sextet that accounts for ~70% of spectral intensity. Much of the remaining intensity arises from mitochondrial iron, including a central quadrupole doublet that arises from $[Fe_4S_4]^{2+}$ clusters and low spin Fe^{2+} hemes and quadrupole doublets that arise from high spin Fe^{2+} heme and NHHS Fe^{2+} ions. The intensity of the NHHS Fe^{2+} doublet in whole cell spectra is greater than can be accounted for by Fe^{2+} ions in mitochondria alone; Fe^{3+}_{cyt} and vacuolar Fe^{2+} ions probably also contribute.

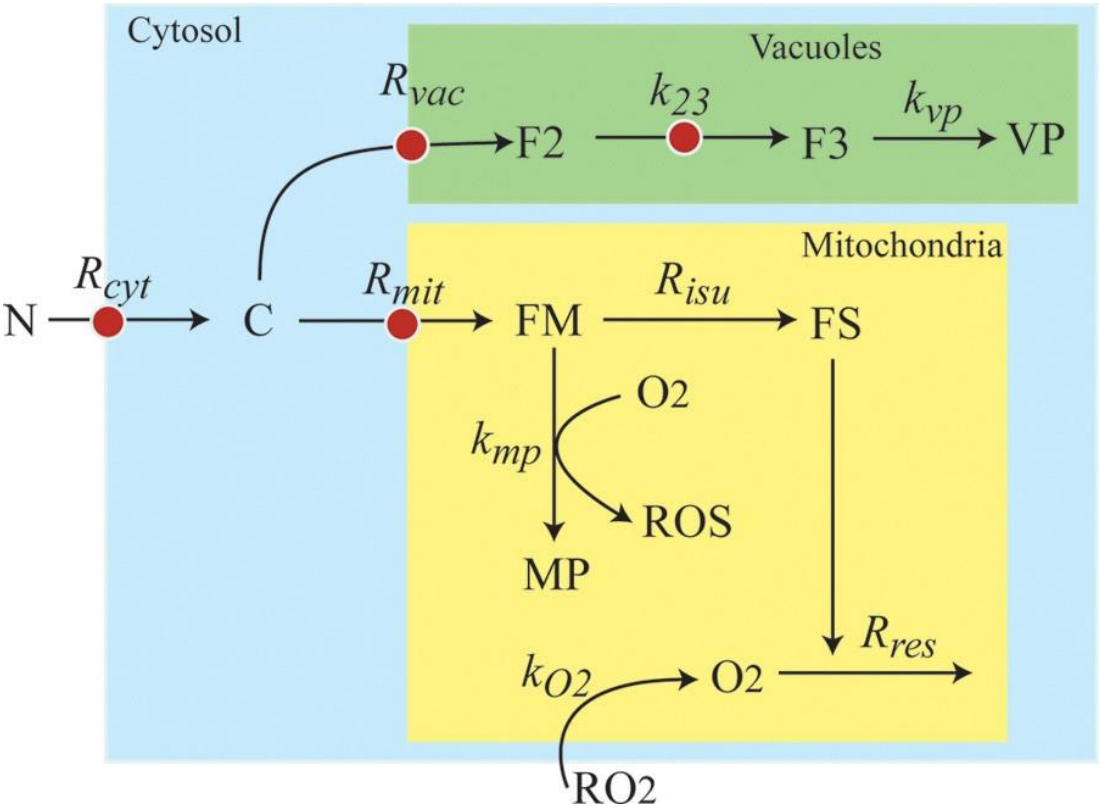

Figure 3.1: Chemical model of iron trafficking in and regulation in S. cerevisiae. Nutrient Fe^{3+} citrate (N) becomes cytosolic Fe^{2+} (C) as it enters the cell. C moves into the vacuole forming F2 (Fe^{2+}), which oxidizes to Fe^{3+} (F3) and converts into nanoparticles (VP). C also moves into mitochondria, forming FM (Fe^{2+}), which is used to generate FS. This component symbolizes ISCs and heme centers. FS is inserted into respiratory complexes, which function to maintain an O_2-free environment in healthy mitochondria. Some O2 that diffuses into the matrix reacts with FM to generate mitochondrial nanoparticles and ROS. *Red dots* indicate the four regulated sites.

We define *iron-deficient* conditions as minimal medium supplemented with bathophenanthroline disulfonate and 1 μM $^{57}Fe^{3+}$ citrate. We define *iron-sufficient*conditions as the same medium supplemented with 10–40 μM $^{57}Fe^{3+}$ citrate, and *iron excess* conditions as the medium supplemented with ≥100 μM $^{57}Fe^{3+}$ citrate.

Other researchers might use different media and supplement with Fe^{2+} rather than Fe^{3+} ions, making quantitative comparisons difficult.

In our studies, the overall concentration of iron in cells grown on iron-deficient, iron-sufficient, and iron excess conditions is ~ 200, 400, and 600 μM iron, respectively. Iron-deficient cells are largely devoid of vacuolar iron; their Mössbauer spectra are dominated by the central doublet and an unusually strong NHHS Fe^{2+} doublet (**65**). Mitochondria isolated from iron-deficient cells contain less iron than do mitochondria from iron-sufficient or iron-excess ones (~400 μM *versus* 700–800 μM), but they contain similar levels of respiration-related ISCs and heme centers. This has ramifications for the mechanism of iron regulation.

Fe_{cyt} is trafficked into the mitochondria via two paralogous inner membrane transporters, namely Mrs3 and Mrs4 (Mrs3/4) (**69, 9**). Imported mitochondrial NHHS Fe^{2+} ions are primarily used for heme and ISC biosynthesis. At higher [Fe_{med}], Fe_{cyt} is also trafficked into vacuoles through the Ccc1 importer (**117, 21**). These are the major iron traffic patterns in a yeast cell (Fig. 1). There are other secondary import and trafficking pathways but they will be ignored here.

The best studied mechanism of iron regulation in *S. cerevisiae* involves Aft1 and Aft2 (**56,57,118,119**). These transcriptional activators control expression of 20–30 genes known as the "iron regulon," including, but not limited to genes *FET3*, *FTR1*, *FET5*, *FTH1*, *SMF3*, *ISU1*, *GRX4*, *MRS4*, and *CTH2*. Aft1 and Aft2 have slightly different functions (**56, 120**), but these differences will be ignored here. In iron-deficient cells, Aft1/2 monomers are located in the nucleus (**121**) where they are bound

to promotor sites and serve to activate the iron regulon. Under iron-sufficient and iron-excess conditions, Aft1/2 release from these sites, exit the nucleus, and dimerize, thereby deactivating the iron regulon. Aft1/2 dimers bind a Fe_2S_2 cluster that bridges the two subunits (**122**). These events are part of a signal transduction regulatory pathway that originates in mitochondria (Fig. 2).

The form of iron sensed by Aft1/2 has been considered since the mid 1990s, when Yamaguchi-Iwai *et al.* (**56, 57**) monitored Aft1 activity using Fet3 expression as a reporter. Fet3 expression increases under iron-deficient conditions relative to iron-sufficient ones (supplemental Table S1 and Ref. **137**). The Aft1/2-dependent regulatory system was initially assumed to sense Fe_{cyt} (**117,21,56,57**), but the situation changed starting in circa 2004 when Kaplan, Winge, and co-workers (**54**) determined that Aft1/2-dependent iron regulation was sensitive to ISC biosynthesis in the matrix of mitochondria rather than to Fe_{cyt}.

Deleting proteins that are involved in mitochondrial ISC biosynthesis, such as Yfh1, Atm1, and Yah1, affords an unusual phenotype that has been characterized extensively and has been used to probe the mechanism of Aft1/2-based regulation (**16,15,51,123**). The so-called *ISC mutant phenotype* includes: (*a*) increase of cytosolic and mitochondrial iron import rates, (*b*) accumulation of Fe^{3+} phosphate oxyhydroxide nanoparticles in mitochondria, (*c*) decline of both ISCs and hemes in mitochondria, (*d*) increase of ROS damage in mitochondria, (*e*) absence of vacuolar iron in cells grown on iron-sufficient media, and (*f*) increase of cytosolic iron levels.

These effects are absent when ISC mutant cells are grown anaerobically (**15, 51**). The iron regulon is active in such mutant cells, even when grown on high [Fe_{med}]. The discovery that [Fe_{cyt}] is not low in ISC mutant cells (**123**) raised the possibility that Fe_{cyt} may not be sensed in cellular iron regulation.

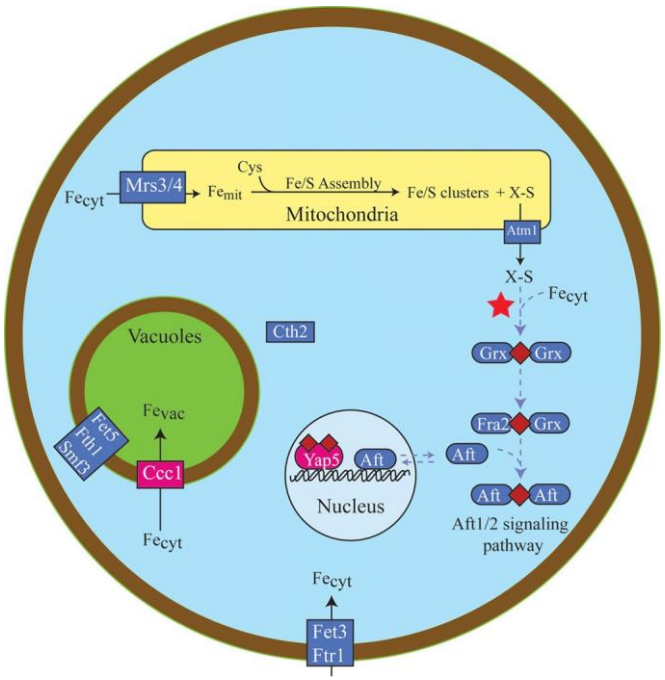

Figure 3.2: Iron regulation pathways in S. cerevisiae. ISC assembly in mitochondria is thought to generate a sulfur-based species called X-S that is exported from the organelle, possibly through Atm1. X-S and Fecyt combine in the cytosol to generate a Fe2S2 cluster bridged between two glutaredoxin monomers (*red star*). This reaction is proposed to be the origin of Dual regulation. In the Aft1/2 signaling pathway (*purple symbols*) and under iron-sufficient conditions, the cluster is passed to Aft1/2 (via Fra2), which prevents activation of the iron regulon in the nucleus. Under iron-deficient conditions, cluster-free monomeric Aft1/2 activates the iron regulon including the Fet3/Ftr1 importer on the plasma membrane. Cth2, Fet5, and Smf3 are also regulated to control vacuole iron levels. Less is known about Yap signaling pathway (*red symbols*). An ISC is likely built on an unknown protein and transferred eventually to Yap5. Cluster-bound Yap5 activates Ccc1, which imports cytosolic iron into the vacuoles.

An elaborate scenario has developed to explain how a signal originating in mitochondria can be relayed to Aft1/2 in the nucleus (Fig. 2). Atm1, an ATP-binding cassette half-transporter on the inner membrane of mitochondria, is thought to export a sulfur-containing by-product of ISC assembly called "X-S" (**60, 61**). The identity of X-S is unknown, but it is thought to pass through a cavity sized for a small metabolite such as glutathione persulfide (**124**). X-S provides the sulfur required for cytosolic ISC biosynthesis and indirectly controls Aft1/2 activity and the iron regulon. The sulfur is probably used to build the Fe_2S_2 cluster that bridges a homodimer of Grx3/4 in the cytosol (**62**). These monothiol glutaredoxins are critical for Aft1/2-dependent regulation. The absence of Grx3/4 activates the iron regulon **(63)** as this disrupts the signal transduction pathway. Fra2 reacts with the Grx·Fe_2S_2·Grx homodimer to generate a Grx·Fe_2S_2·Fra2 heterodimer (**122, 63, 64**). This heterodimer donates its Fe_2S_2cluster to two Aft1/2 monomers to generate the Aft·Fe_2S_2·Aft homodimer, titrating away apo-Aft1/2 monomers that would otherwise bind tightly to iron regulon promotor sites on DNA. In this way, ISC biosynthesis in mitochondria controls the activity of the iron-regulon in the nucleus.

Iron traffic into and out of vacuoles is also highly regulated, with Yap5 playing the dominant role (**125**). This iron-sensitive transcription factor is constitutively expressed in the nucleus where it is bound to the promoters of *CCC1* (and other genes) to regulate expression (Fig. 2). Earlier studies suggested that Yap5 senses Fe_{cyt} (**58**), but a later study (**55**) found that it senses mitochondrial ISC synthesis activity. When ISC synthesis is blocked, Yap5 transcription levels decline, and vacuoles no longer fill with

iron (**58**). However, Yap5 is not controlled by Aft1/2, and the Yap5 signaling pathway does not involve Grx proteins. Yap5 contains seven cysteine residues that are used in iron sensing. Under high iron conditions, Yap5 uses them to bind two Fe_2S_2 clusters (**59**). This alters the conformation of the protein such that it binds DNA and promotes *CCC1*expression.

Fet5 and Fth1, respective homologs of Fet3 and Ftr1, are also involved in regulating vacuolar iron. The Fet5·Fth1 complex on the vacuolar membrane exports iron to the cytosol. Expression levels of *FET5* and *FTH1* increase under iron-deficient conditions because they are part of the iron regulon (**23**). Smf3 is another iron exporter on the vacuolar membrane and is also part of the Aft1/2 system (**118**). Aft1/2-dependent activation under extreme iron-deficient conditions increases expression of *CTH2* (**58**). Cth2 binds to and destabilizes *CCC1* mRNA transcripts (**126**) preventing vacuoles from importing Fe_{cyt}.

Iron traffic into mitochondria is also regulated. Deleting *MRS3/4* affords mitochondria with reduced ISC and heme activities and lower iron concentrations (**9, 69**). Although the exact species imported by Mrs3/4 is/are unknown, members of this family transport small metabolites and cofactors (**127**). Δ*MRS3/4* cells acquire more than normal amounts of iron because the Aft1/2-dependent iron regulon is activated due to low ISC activity (**9, 69**). Mrs4 expression in Δ*YFH1* cells is higher than in WT cells, indicating an up-regulation of mitochondrial iron import under ISC mutant conditions. Activating Aft1/2 under iron-deficient conditions also enhances MRS4 expression (**120**).

Cells lacking Ccc1 are sensitive to high iron levels in the medium because Fe_{cyt}, which most likely engages in ROS-generating chemistry, is probably present at higher than normal concentrations. Overexpressing Mrs3/4 suppresses that sensitivity probably because it imports more Fe_{cyt} into mitochondria (**70**). Cells lacking Mrs3/4 up-regulate Ccc1 activity—evidence of what Kaplan calls a "mitochondrial vacuolar" signaling pathway (**70**).

Materials and Methods

A chemical model was developed to describe trafficking and regulation of iron in yeast cells (Fig. 1); reactions and rate expressions are listed in Table 1. Relevant data were obtained from WT and ISC mutant cells grown in batch culture under iron-deficient, iron-sufficient, and iron excess conditions (supplemental Tables S1 and S2). Cells in these studies were generally harvested during exponential phase.

Table 3.1: Model reactions and rate expression, including optimized WT parameters

Reactions and Optimized Parameters	Rate Expressions
$N \longrightarrow C$ R_{cyt} = 410 µM·hr^{-1} K_{cyt} = 14 µM $[C]_{spcyt}$ = 27 µM *csencyt* = 5 $[FS]_{spcyt}$ = 190 µM *fssencyt* = 9	$\frac{R_{cyt}\cdot[N]}{K_{cyt}+[N]}\frac{1}{1+\left(\frac{[C]}{[C]_{spcyt}}\right)^{csencyt}}\frac{1}{1+\left(\frac{[FS]}{[FS]_{spcyt}}\right)^{fsencyt}}$
$C \longrightarrow FM$ R_{mit} = 900 µM·hr^{-1} K_{mit} = 12 µM $[C]_{spmit}$ = 80 µM *csenmit* = 5 $[FS]_{spmit}$ = 200 µM *fssenmit* = 4	$\frac{R_{mit}\cdot[C]}{K_{mit}+[C]}\frac{1}{1+\left(\frac{[C]}{[C]_{spmit}}\right)^{csenmit}}\frac{1}{1+\left(\frac{[FS]}{[FS]_{spmit}}\right)^{fsenmit}}$
$C \longrightarrow F2$ R_{vac} = 1500 µM·hr^{-1} K_{vac} = 5.5 µM $[C]_{spvac}$ =1.2 µM *csenvac* = 3 $[FS]_{spvac}$ = 190 µM *fssenvac* = 8	$\frac{R_{vac}\cdot[C]}{K_{vac}+[C]}\left(1-\frac{1}{1+\left(\frac{[C]}{[C]_{spvac}}\right)^{csenvac}}\right)\left(1-\frac{1}{1+\left(\frac{[FS]}{[FS]_{spvac}}\right)^{fsenvac}}\right)$
$F2 \longrightarrow F3$ k_{23} = 7.3 hr^{-1} $[C]_{sp23}$ =2 µM *csen23* = 10 $[FS]_{sp23}$ = 210 µM *Fssen23* = 10	$k_{23}[F2]\left(1-\frac{1}{1+\left(\frac{[C]}{[C]_{sp23}}\right)^{csen23}}\right)\left(1-\frac{1}{1+\left(\frac{[FS]}{[FS]_{sp23}}\right)^{fsen23}}\right)$
$FM \longrightarrow FS$ R_{isu} = 250 µM·hr^{-1} K_{isu} = 610 µM	$\frac{R_{isu}[FM]}{K_{isu}+[FM]}$
$O2 \longrightarrow$ k_{res} = 150 hr^{-1} K_{res} = 9 µM	$\frac{k_{res}[FS][O2]}{K_{res}+[O2]}$
$FM + O_2 \longrightarrow MP + ROS$ k_{mp} = 0.18 µM^{-1}hr^{-1}	$k_{mp}[FM][O2]$
$F3 \longrightarrow VP$ k_{vp} = 0.02 hr^{-1}	$k_{vp}[F3]$
$O_{2(cytosol)} \longrightarrow O_{2(matrix)}$ k_{O2} = 52 hr^{-1} $[RO2]$ = 100 µM	$k_{o2}\left([RO2]-[O2]\right)$

The concentrations of iron-containing components in exponentially growing cells should be invariant with time. In an expanding steady state, the increase in cellular iron caused by iron influx is counterbalanced by the dilution of cellular iron caused by increasing cell volume. The exponential growth rate of the cell, defined as $\alpha = (1/V) \times (dV/dt)$, is an essential aspect of our model. When cells grow exponentially, α is constant which makes it particularly easy to evaluate. Assuming that the optical density of cells is proportional to cell volume, α equals the slope of the straight line that results when the natural logarithm of A_{600} is plotted *versus* time ($\ln OD_t = \ln OD_0 + \alpha t$).

Modeling homeostatic regulatory systems that control cytosolic, mitochondrial, and vacuolar iron import on the molecular level is currently not feasible because many critical details remain unknown. Our goal was merely to explore essential aspects of the regulation at four key traffic sites. To do this, we used surrogate mathematical expressions—called "Reg functions"—to mimic regulatory behavior (**66, 128**). Reg functions can be viewed as valves that dynamically adjust between closed and fully opened to smoothly regulate traffic flow through a site. These functions are characterized by the iron species that they sense (S), the set point concentration at which the valve is half-opened ($[S]_{sp}$), and the sensitivity of the response (*sen*). There are two types of Reg functions, called Reg_{-S} and Reg_{+S}, defined as follows.

$$Reg_{-S} = \frac{1}{1+\left(\frac{[S]}{[S]_{sp}}\right)^{sen}}; \quad Reg_{+S} = 1 - Reg_{-S}$$

When [S] > $[S]_{sp}$, the Reg_{-S} valve closes and cell growth dilutes S toward $[S]_{sp}$. When [S] < $[S]_{sp}$, the Reg_{-S} valve opens to achieve the same effect. Reg_{+S} behaves the same as Reg_{-S} but in the opposite direction (closing the valve when [S] is low and opening it when [S] is high). A Reg_{-S} function should be used when the homeostatic response *opposes* the perturbation. Thus, if the concentration of the sensed species is too high, the response of Reg_{-S} would be to decrease flow. A Reg_{+S} function should be used when the homeostatic response reinforces the perturbation; if the concentration of the sensed species is too high, Reg_{+S} increases the flow.

In addition to including regulation at the site of iron import into the cytosol, and at the two sites through which iron moves into mitochondria and vacuoles, the model includes a fourth regulatory site in which vacuolar Fe^{2+} (called F2) is oxidized to Fe^{3+}(F3). There are a number of conditions and genetic strains (iron-deficient, adenine-deficient, *ΔCCC1*, and *CCC1* overexpression) in which F3 levels are low and F2 levels are high relative to iron-sufficient adenine-sufficient WT conditions (Refs. **65,66,116** and supplemental Table S1). The model regulates the rate of this oxidation to recreate the effect.

We wanted to evaluate whether Fe_{cyt} (called C in our model) or mitochondrial ISC activity (proportional to the concentration of FS in our model) was sensed in regulation. To do this, three model variants were considered. The *C-Reg* variant assumes that all four regulatory valves exclusively sense C. For rates associated with importing iron into the cytosol (R_{cyt}) and into mitochondria (R_{mit}), Reg_{-C} functions shut down

import when [C] is too high. For rates associated with importing C into vacuoles (R_{vac}) or oxidizing F2 to F3 (R_{23}), Reg_{+C} functions are needed.

The FS-Reg variant exclusively senses the activity of ISC assembly in the mitochondria, which in our model generates FS (a substitute for X-S). $Reg_{–FS}$ functions regulate $R_{cyt}$and R_{mit}, whereas Reg_{+FS} functions regulate R_{vac} and R_{23}. The Dual-Reg variant assumes that both C and FS are sensed at all four regulation sites. To control the rates of R_{cyt} and R_{mit}, we used the product of two $Reg_{–S}$ functions (see supplemental information for a derivation). A similar $\{Reg_{+C} \cdot Reg_{+FS}\}$ product function was used to control R_{vac} and R_{23}.

Inferring the appropriate Reg functions to describe the regulation of vacuolar iron requires some consideration. At the transcriptional level, *CCC1* expression is regulated by Yap5 activity. The response to high [C] and/or [FS] is to increase flow into vacuoles, implying that Reg_{+C} and Reg_{+FS} functions should be used. At the translational level, *CCC1* mRNA is degraded by Cth2 which is regulated, in turn, by Aft1/2. The cell response to low [C] and/or [FS] is to decrease flow through Ccc1 (via increasing Cth2-associated Ccc1 degradation). This effect again implies use of Reg_{+} functions. Deleting Mrs3/4 causes Ccc1 activity to increase (**70**); thus Mrs3/4 can be viewed as inhibiting Ccc1—analogous to the overall effect of Cth2—again implying use of Reg_{+} functions. Finally, Smf3 and Fet5 export vacuolar iron into the cytosol, and an increase in either protein (which are both controlled by the Aft1/2-dependent iron regulon and thus are up-regulated under iron-deficient conditions) causes loss of vacuolar iron. This has the same net effect as inhibiting *CCC1* expression. In summary, although Yap5, Cth2, Mrs3/4,

Smf3, and Fet5 regulate vacuolar iron by different mechanisms, their effects can be collectively simulated using Reg_{+} functions.

The model presumes a cell encapsulated by a semipermeable membrane surrounded by an environment containing Fe^{3+} citrate (N) and molecular oxygen (RO2). The *in silico*cell is composed exclusively of cytosol, mitochondria, and vacuoles such that $V_{cell} = V_{cyt} + V_{vac} + V_{mit}$. The model involves seven chemical components that contain iron and four that do not (Fig. 1). In addition to F2 and F3, vacuoles contain nanoparticles (*VP*). In addition to FS, mitochondria contain *FM* (NHHS Fe^{2+}) and *MP* (mitochondrial nanoparticles). Other non-iron species include O_2 and *ROS* in the mitochondrial matrix. Mass balance of iron requires that

$$[Fe]_{cell} = f_{cyt}[C] + f_{vac}\{[F2]+[F3]+[VP]\} + f_{mit}\{[FM]+[FS]+[MP]\} \quad [1]$$

where f_{vac}, f_{mit}, and f_{cyt} are fractional volume ratios (volume of the designated compartment divided by the volume of the cell). The ordinary differential equations that define the Dual-Reg variant of the model are given by the following equations.

$$\frac{d[C]}{dt} = \frac{R_{cell}[N]}{K_{cell}+[N]}\mathrm{Re}g_{-C}\cdot\mathrm{Re}g_{-FS} - \frac{V_{mit}}{V_{cyt}}\frac{R_{mit}[C]}{K_{mit}+[C]}\mathrm{Re}g_{-C}\cdot\mathrm{Re}g_{-FS} - \frac{V_{vac}}{V_{cyt}}\frac{R_{vac}[C]}{K_{vac}+[C]}\mathrm{Re}g_{+C}\cdot\mathrm{Re}g_{+FS} - \alpha[C] \quad [2]$$

$$\frac{d[FM]}{dt} = \frac{R_{mit}[C]}{K_{mit}+[C]}\mathrm{Re}g_{-C}\cdot\mathrm{Re}g_{-FS} - \frac{R_{isu}[FM]}{K_{isu}+[FM]} - k_{mp}[FM][O2] - \alpha[FM] \quad [3]$$

$$\frac{d[F2]}{dt} = \frac{R_{vac}[C]}{K_{vac}+[C]}\mathrm{Reg}_{+C}\cdot\mathrm{Reg}_{+FS} - k_{23}[F2]\cdot\mathrm{Reg}_{+C}\cdot\mathrm{Reg}_{+FS} - \alpha[F2] \quad [4]$$

$$\frac{d[FS]}{dt} = \frac{R_{isu}[FM]}{K_{isu}+[FM]} - \alpha[FS] \quad [5]$$

$$\frac{d[MP]}{dt} = k_{mp}[FM][O2] - \alpha[MP] \quad [6]$$

$$\frac{d[F3]}{dt} = k_{23}[F2] \cdot \mathrm{Reg}_{+C} \cdot \mathrm{Reg}_{+FS} - k_{vp}[F3] - \alpha[F3] \quad [7]$$

$$\frac{d[VP]}{dt} = k_{vp}[F3] - \alpha[VP] \quad [8]$$

$$\frac{d[O2]}{dt} = k_{o2}\left([RO2] - [O2]\right) - k_{mp}[FM][O2] - \frac{R_{res}[FS][O2]}{K_{O2} + [O2]} \quad [9]$$

$$\frac{d[ROS]}{dt} = k_{mp}[FM][O2] - \alpha[ROS] \quad [10]$$

Ordinary differential equations for the C-Reg and FS-Reg variants were identical except that they lacked FS-sensed and C-sensed *Reg* functions, respectively. The model included 30 floating and 9 fixed parameters (Table 1 and supplemental Table S3). The exponential growth rate for cells that were transitioning smoothly from healthy to diseased state, for any point *i* along that transition, was calculated by solving

$$\frac{[FS]_{health} - [FS]_i}{[FS]_{health} - [FS]_{disease}} = \frac{\alpha_{health} - \alpha_i}{\alpha_{health} - \alpha_{disease}} \quad [11]$$

for $\alpha_{current}$ using the FS concentration from the previous point in the transition. Connecting growth rate to [FS] makes sense because FS represents mitochondrial respiratory complexes and hemes. These complexes control cellular energy and perhaps growth rate.

The overall change in cellular iron is given by the following equation (see supplemental information for derivation).

$$\frac{d[Fe_{cell}]}{dt} = f_{cyt} \frac{\mathrm{R}_{cell} \cdot [N]}{K_{cell} + [N]} \mathrm{Reg}_{-C} \cdot \mathrm{Reg}_{-FS} - \alpha \cdot [Fe_{cell}] \quad [12]$$

The iron importers that contribute to the import rate R_{cyt} were viewed as a single collective Michaelis-Menten enzyme acting on substrate *N*. For cells in an expanding steady state,

$$[Fe_{cell}] = \frac{f_{cyt}}{\alpha} \frac{R_{cell} \cdot [N]}{K_{cell} + [N]} \mathrm{Reg}_{-C} \cdot \mathrm{Reg}_{-FS} \qquad [13]$$

For R_{cyt}, f_{cyt}, *N*, α, K_{cyt}, Reg_{-C}, and Reg_{-FS} values of 410 μM/h, 0.65, 40 μM, 0.2 h^{-1}, 14 μM (Table 1), 1, and 0.4, respectively, the concentration of cellular iron would be ~400 μM.

Oxygen plays a major role in the ISC mutant phenotype, but how it acts on the molecular level remains uncertain. We hypothesize that the matrix of healthy mitochondria is nearly anaerobic and that $[O_2]$ in the matrix is higher in ISC mutants. Because of the activity of cytochrome *c* oxidase on the inner membrane, the concentration of O_2 in the matrix of healthy mitochondria must be lower than in the cytosol (**129**). However, the magnitude of this difference is uncertain, and $[O_2]$ in the matrix has not been measured. ISC assembly assays require anaerobic conditions (**130**), as do a number of enzymes in the matrix, including aconitase (**131**), biotin synthase (**132**), and lipoic acid synthase (**133**), supporting our hypothesis.

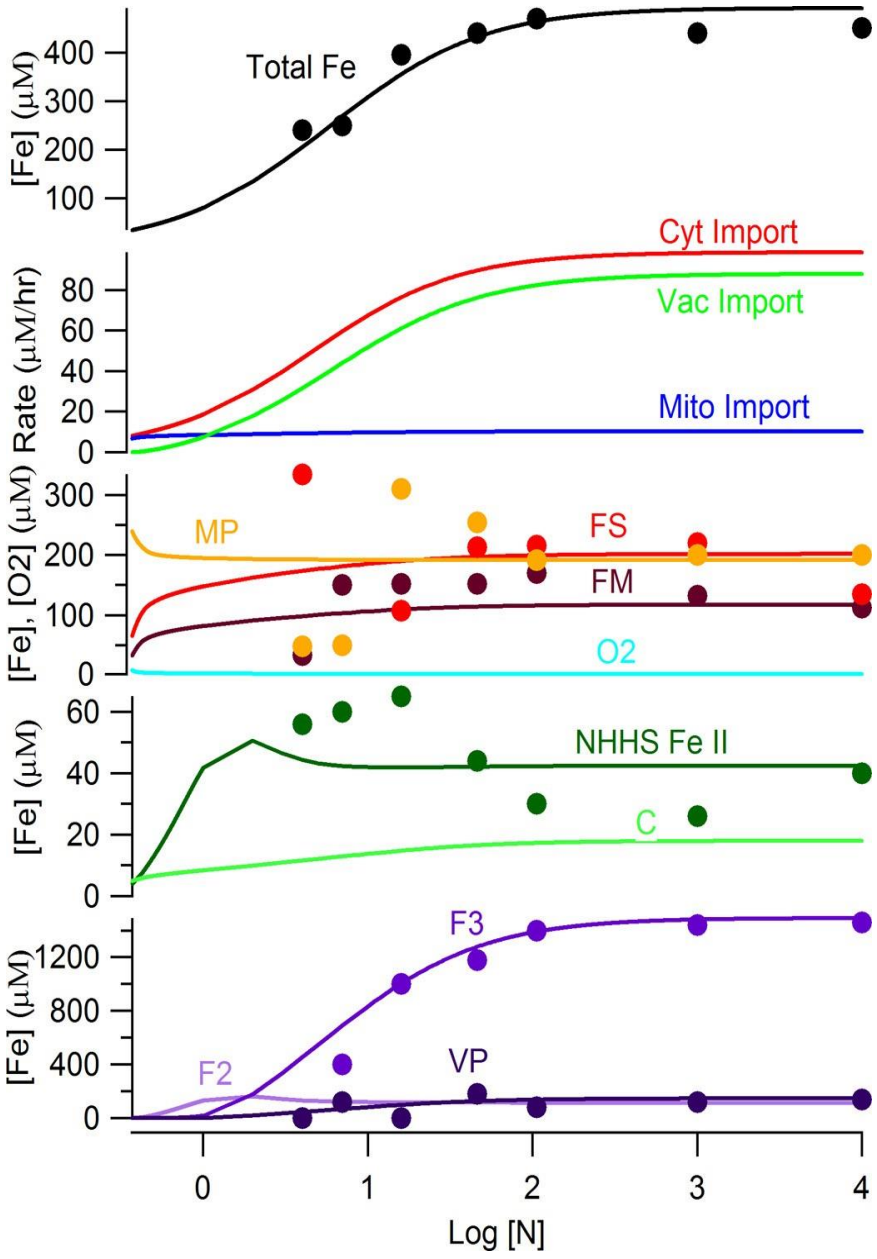

Figure 3.3: Simulated concentrations of iron components in *S. cerevisiae* at increasing concentrations of iron in the growth medium. The Dual-Reg variant was assumed. The trace of [C] has been multiplied by 5 for ease of viewing.

Our model implies that anaerobic conditions arise in healthy mitochondria because most of the O_2 that diffuses across the IM is rapidly reduced by the respiratory complexes. ISC mutants contain fewer functional respiratory complexes such that more O_2 diffuses into the matrix. Once in the matrix, O_2 reacts with a pool of NHHS Fe^{2+} (FM) that is used as feedstock for ISC biosynthesis (**13, 134**). Reaction of O_2 with FM not only depletes a reagent needed for ISC biosynthesis; it also generates nanoparticles and ROS. The O_2-dependent loss of FM reduces [FS] further, which causes more O_2 to penetrate the mitochondrial inner membrane. A "disease spiral" results, transforming healthy mitochondria into the ISC mutant diseased state. All of these events are choreographed by our model. This disease spiral would occur regardless of the particular role served by the deleted protein in ISC biosynthesis; the only requirement is that loss of the protein leads to a decline in ISC activity. This situation is indeed observed in that the losses of various proteins, each with different functions in ISC biosynthesis, exhibit the same iron accumulation phenotype.

Ordinary differential Equations 3–11 were coded into Mathematica 9 (Wolfram, Champaign, IL) and numerically integrated using the NDSolve routine and the parameters listed in Table 1. The large number of parameters precluded a rigorously systematic optimization of parameter space. Moreover, the data used in fitting (supplemental Tables S1 and S2) were sparse and had large uncertainties. Thus, parameters were initially adjusted at will to achieve the following desired qualitative behavior. Because [N] increased from iron-deficient conditions, we wanted [C] to increase modestly, [FS] and [FM] to increase quickly and then plateau, vacuolar iron to

increase once [N] reached iron-sufficient levels, and [F2] to increase initially and then be replaced by F3 whose concentration would increase sharply at higher [N]. We wanted mitochondrial and vacuolar nanoparticles, and mitochondrial ROS and O_2 to remain at low concentrations throughout the entire range of [N]. In the ISC mutant state (created by lowering R_{isu}), we wanted [MP] to increase dramatically, vacuolar iron to empty, and [C] to remain relatively invariant. Considerable efforts were made to achieve this group of behaviors for each variant.

We then optimized parameters of the Dual-Reg variant by minimizing the following function,

$$RMSD = \sum_{i=Table\ X\ entries} wf_i \sum_{j=C,FM,FS,MP\ etc} \frac{\left|[Sim]_{i,j} - [Dat]_{i,j}\right|}{[Fe]_{cell,i}} + \sum_{m=Table\ X\ entries} \frac{\left|[Sim]_m - [Dat]_m\right|}{\left(\frac{[Sim]_m + [Dat]_m}{2}\right)} \quad [14]$$

where $[S]_{i,j}$ and $[D]_{i,j}$ are the simulated and experimental concentrations, respectively, for six components (j = *F3*, *VP*, *FM*, *FS*, *MP*, and *NHHS*, Fe^{2+}) measured for experiments i = 1–18 involving WT, ISC mutant, ΔCCC1, and CCC1-UP fermenting cells (supplemental Table S2). Weighting factors wf_i equaled 1 for each experiment except for that involving an ISC mutant. In this case, wf_i equaled 10 so as to emphasize the ISC phenotype relative to other experiments. $[Fe]_{cell,i}$ is the whole-cell iron concentration for experiment i. The second term refers to the 43 comparisons listed in supplemental Table S1. Overall, there were 151 comparisons between experiment and simulation, with six comparisons weighted by 10 (205 comparisons with these weights included).

For fitting, each modeling parameter was increased and decreased while all others were held fixed. The minimum RMSD obtained was called $RMSD_{min}$. Optimized simulation values are given in Table 1. To evaluate sensitivities, RMSDs obtained when a given parameter was 10% greater ($RMSD_{+}$) and 10% lesser ($RMSD_{-}$) than its optimal value were averaged and divided by $RMSD_{min}$ (supplemental Table S3). Once the Dual-Reg variant was optimized, the C-reg and FS-reg versions were generated by removing the appropriate Reg functions.

Results

The optimized Dual-Reg variant simulated iron import and trafficking in exponentially growing fermenting WT cells with relatively high fidelity; $RMSD_{min}$ was 0.33, nearly half of that obtained using the FS-Reg variant ($RMSD_{min}$ = 0.54) and four times less than obtained using the C-Reg variant ($RMSD_{min}$ = 1.3). The total iron concentration in simulated cells ranged from ~60 μM at [N] = 0.37 μM to ~450 μM at [N] > 100 μM. This is similar to iron concentrations in real cells. The rate of iron import into mitochondria was nearly constant over the entire range of [N], and at low [N] this rate dominated cellular iron traffic flow (Fig. 3). Vacuoles were largely devoid of iron at [N] < 1 μM, but they were half-filled at [N] = ~10 μM and completely filled by [N] = ~40 μM. At [N] > 5 μM, the flow of iron into vacuoles exceeded that into mitochondria. The simulated concentrations of mitochondrial iron species FM and MP were relatively invariant over the considered range of [N]; [FS] was similarly invariant except for a decline at low [N]. At [N] > 10 μM, the concentrations of all three mitochondrial iron-

containing species plateaued near the means of highly scattered experimental values. In simulated healthy cells, mitochondrial O_2 and ROS levels were near 0 throughout the range of [N] (not shown). Simulated vacuolar iron levels were near to experimental values over all [N] (Fig. 3). At low [N], F2 dominated vacuolar iron, but most of this oxidized to F3 at [N] > ~5 μM. [VP] was near 0 at low [N], but it gradually increased as [N] increased. Simulated concentrations of C increased from 2.3 to 3.5 μM as [N] increased from ~0.37 to 30 μM. At higher [N], [C] plateaued at ~3.5 μM. We regard this as well regulated, in that an 80-fold change of [N] resulted in a ~1 μM change in [C]. The collective NHHS Fe^{2+} species (0.65[C] + 0.1[FM] + 0.25[F2]) increased to ~50 μMnear [N] = 5 μM (mostly because of the accumulation of F2). At higher [N], these species collectively declined to ~40 μM (mainly because of a shift from F2 to F3). This behavior is similar to what is observed experimentally.

To simulate the ISC phenotype, we incrementally reduced the rate of ISC synthesis (R_{isu}) from 250 μM/h, the rate for healthy cells, to 15 μM/h. The concentration plots of all species changed significantly at $30 < R_{isu} < 100$ μM/h (Fig. 4). In this regime [FS] declined and [FM] increased more dramatically than at higher R_{isu} rates. These changes are easily rationalized, because R_{isu} is the rate by which FM converts to FS. Other observed changes are secondary effects caused by shifts in regulation due to declining [FS]. These include a decline in vacuolar iron levels and increases in the rates of iron import into the cytosol and into mitochondria.

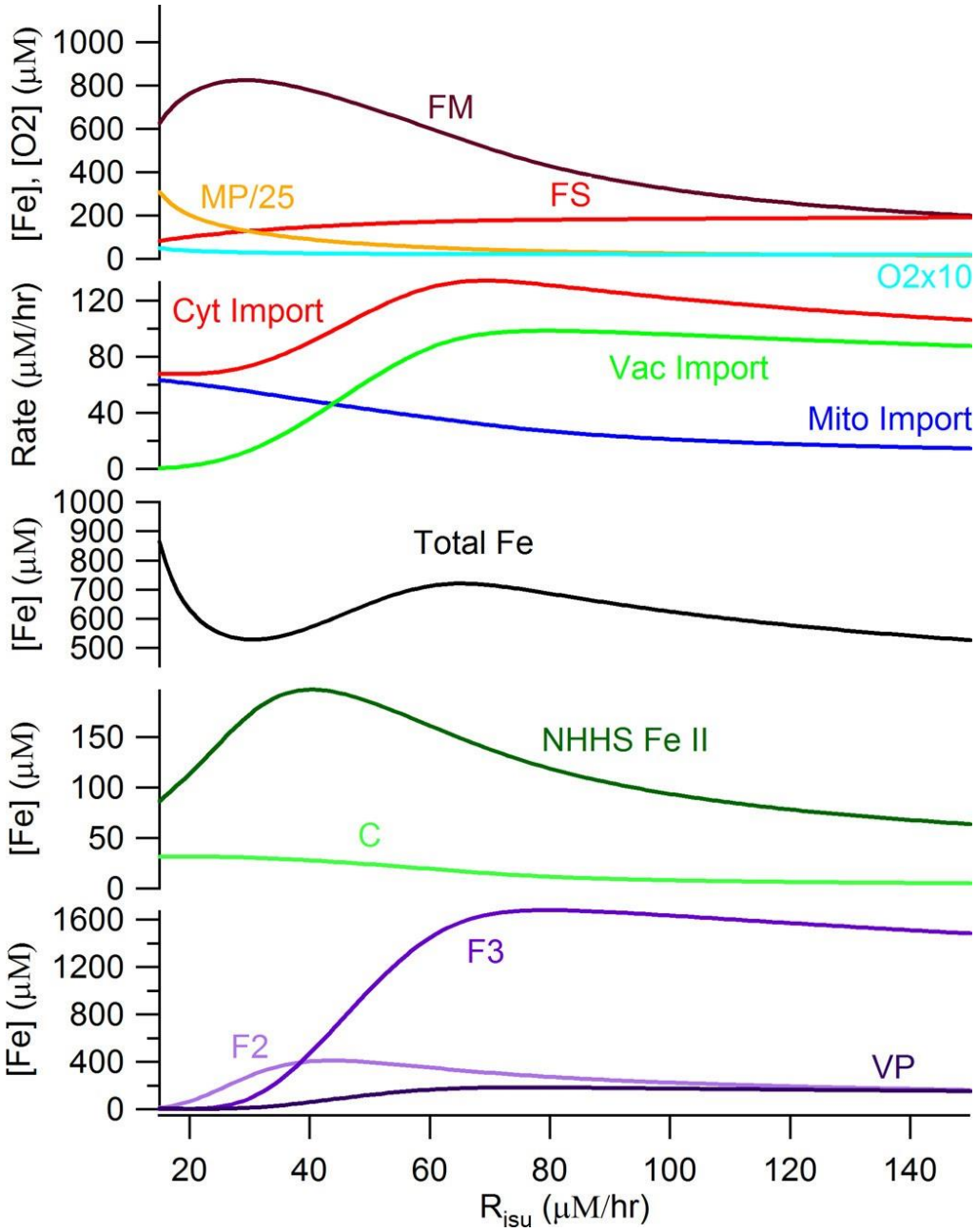

Figure 3.4: Simulated concentrations of iron components in *S. cerevisiae* at increasing rates by which iron-sulfur clusters and heme centers are synthesized. The Dual-Reg model variant is assumed along with [N]=40 µM.The diseased state is on the *left*; the healthy state is on the *right*.

At R_{isu} < 30 μM/h, even more dramatic changes occurred, all associated with the ISC disease spiral. The primary event causing these changes was a decline of [FS] to concentrations below those required to maintain the matrix in an anaerobic state. The O_2 that penetrates the matrix under these conditions reacts with FM, causing its decline, as well as an increase in ROS and MP concentrations. The loss of FM slows the rate of FS production further, leading to the spiraling effect. The decline in [FS] also causes cytosolic and mitochondrial import valves to open (and the vacuolar iron import valve to close) such that iron rushes into the cytosol, out of the vacuole and into mitochondria where it accumulates as MP. Some FM is not consumed in the ISC diseased state, such that the steady state ratio of [FM]/[Fe_{mit}] is ∼7%. This is similar to the Mössbauer spectral intensity of mitochondria isolated from ISC mutant cells, which exhibit features of NHHS Fe^{2+} in addition to the dominating nanoparticles (**15, 51**). The origin of this NHHS Fe^{2+} as an expanded FM pool had been unexplained prior to this model.

The disease spiral is delayed and moderated under micro-erophilic conditions (RO2 = 1 μM) (Fig. 5*A*). When the system lacks O_2, FM cannot convert into nanoparticles, and [FS] only declines marginally. At R_{isu} < 40 μM/h, low [FS] and an assumed low growth rate result in higher iron levels in the cell and mitochondria, such that [FM] increases dramatically, reaching 6 mM at R_{isu} = 20 μM/h. Thus, the model predicts that the iron content of mitochondria isolated from ISC mutant cells grown under anaerobic condions will be dominated by NHHS Fe^{2+} rather than by nanoparticles. We are examining this prediction experimentally.

Most component traces of the C-Reg variant were similar to those of the Dual-Reg variant, but vacuolar iron in the C-Reg variant did not empty as [FS] declined in simulating the ISC mutant state (Fig. 5*B*). Cellular iron in C-Reg cells increased largely because the growth rate declined, and vacuoles imported that iron because they could not sense the decline of [FS] in mitochondria. There was also no increase in the rate of iron import into mitochondria during formation of the ISC diseased state (Fig. 5*C*), in contrast to what is observed.

The FS-Reg variant exhibited acceptable behavior overall except that [C] increased to exceedingly high (mM) levels under ISC mutant conditions (Fig. 5*B*). Such unrealistically high concentrations arise because there is no Reg_{-C} valve to curtail the flow of iron in slowly growing cells in which the Reg_{-FS} valve is fully opened.

We next examined the ability of the Dual-Reg variant to reproduce the phenotype of nine genetic strains including ΔYFH1, ΔMRS3/4, Mrs3/4 overexpression, ΔCCC1, CCC1 overexpression, $Aft1/2{-}1^{UP}$, ΔYFH1:ΔMRS3/4, ΔYFH1:MRS3/4 overexpression, and ΔCCC1:ΔMRS3/4 (supplemental Tables S1 and S2). We simulated each strain by only adjusting the rate(s) in our model that was(were) associated with the particular genetic modification. Rates for deletion strains were not assigned exactly to 0 because the cells contain secondary pathways that remain operational despite the deletion. The model implicitly includes all pathways of iron into the cytosol, into mitochondria and vacuoles, whereas the genetic strains perturb only a particular pathway.

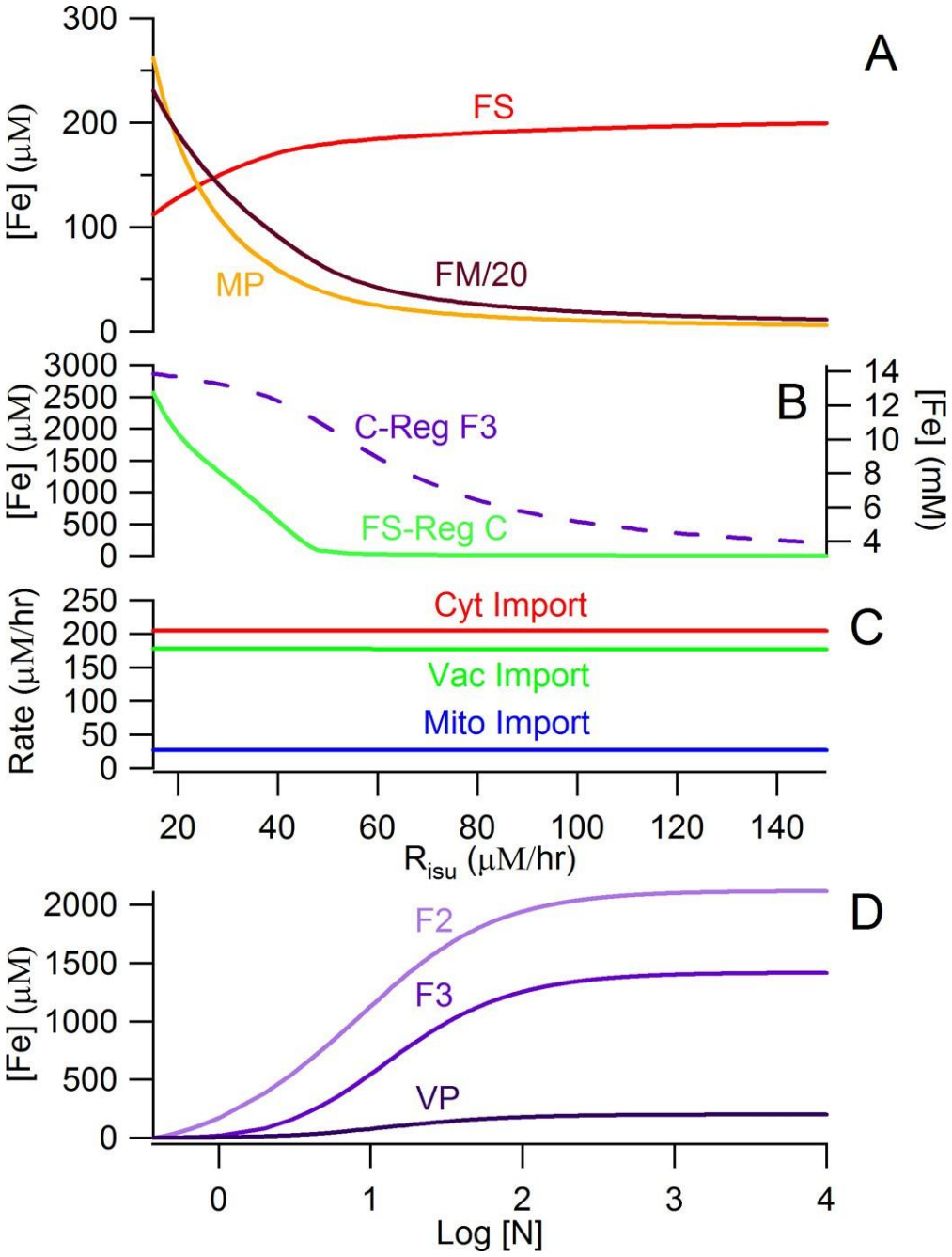

Figure 3.5: Selected plots from simulations. *A*, concentrations of mitochondrial iron species under anaerobic growth conditions assuming the Dual-Reg variant. In the diseased state, [FM] is_20-fold higher than [MP]. *B*, [F3] (*dashed purple line*, *right axis*) simulated by the C-Reg variant does not decline in the diseased state. [C] (*green line*, *left axis*) simulated by the FS-Reg variant increases to unrealistically high concentrations in the diseased state. *C*, import rates simulated by the C-Reg variant are invarient in the diseased state: no accumulation of iron in mitochondria. *D*, simulation of [F2] and [F3] by the Dual-Reg variant in CCC1-UP cells that are adenine-deficient. [F2] is
subtantially higher than [F3] as observed.

The most unusual simulated behavior was that of CCC1-UP, which showed high [F2] and low [F3] under conditions where the WT strain is dominated by F3 (Fig. 5*D*). This shift was due to a down-regulation of k_{23} in the simulated CCC1-UP strain, attributed to a more reducing vacuolar environment. In ~65% of all literature cases reported in supplemental Table S1, model simulations "trended" in the observed direction and had reasonable quantitative agreement. Model simulations fitted even better to the Mössbauer-based data of supplemental Table S2. This overall ability to reproduce observed behaviors from the literature and from previous studies in our lab, although not uniformly successful, suggests that many aspects of this simple model are correct.

Finally, we evaluated the sensitivity of model parameters (supplemental Table S3). The rate of iron import into mitochondria was the most sensitive parameter, followed by rate constants for O_2 reacting with FM, for respiration and for nanoparticle formation. The rate of ISC/heme biosynthesis was also sensitive. The model was sensitive to the set point concentrations of FS and to Michaelis-Menten K_m terms involving the import of cytosolic iron into mitochondria, the conversion of FM into FS, and the reduction of O_2 in respiration.

The optimized setpoint concentration for FS, averaged for all four sites, was 170 ± 30 μM. This was comparable to the average concentrations of FS in mitochondria (~200 μM), and it suggests that the FS-Reg valves were opening and closing as designed. The average *sen* factor for FS-Reg functions was 8 ± 2, indicating the need for sensitive regulation.

In contrast, the model was relatively insensitive to parameters associated with C regulation. Set point concentrations for C were highly variable, including values of 27, 80, 1.2, and 2 μM for cytosolic iron import, mitochondrial iron import, vacuolar iron import, and vacuolar Fe^{2+} oxidation, respectively. Those for cytosolic and mitochondrial iron import differed from the simulated range of C concentrations (2–4 μM). This means that under most circumstances, the C-Reg valves "controlling" import into the cytosol and mitochondria were fully opened such that these import rates were essentially controlled only by [FS]. C-regulation played a stronger role in vacuolar iron import and oxidation, especially with variations in [N].

Discussion

Immediately following the discovery of Aft1-dependent regulation in 1995, cytosolic iron was commonly assumed to be the sensor of a classic homeostatic regulatory system for controlling iron import and trafficking in yeast cells. This assumption was based on the response of healthy WT cells to changes in the iron concentration of the growth medium. Starting in the early 2000s, cellular iron overload caused by defects in mitochondrial ISC activity revealed the importance of this activity in cellular iron regulation. The classic model predicted that the massive import of iron into ISC-defective mitochondria resulted from an iron-deficient cytosol, which stimulated iron import by activating the iron regulon. Unexpectedly, evidence suggested that the cytosol in ISC mutant cells is iron-replete.

Once it was established that events in the mitochondria impacted those in the nucleus, focus shifted to how such information was transferred from mitochondria to nucleus. In the last decade, many details regarding this mitochondrial → nuclear signal transduction pathway have been established.

Included in this intellectual journey was the conclusion that cytosolic iron is NOT sensed in regulation. However, our study suggests that both cytosolic iron and mitochondrial ISC activity are sensed. Fe_{cyt}-sensing plays an important regulatory role when healthy cells are grown in iron-deficient, iron-sufficient, and iron excess medium (especially with regard to vacuolar iron import and oxidation). In these cases, the level of ISC assembly is relatively constant, such that the rates of iron import into the cytosol and mitochondria are largely invariant. This leads to the observed relative invariance of iron content in mitochondria. On the other hand, when mitochondrial ISC activity is attenuated or halted, FS-based regulation controls these iron import rates.

Both Fe_{cyt} and mitochondrial ISC activity could be regulatory sensors if both were required to generate a single downstream signal for the mitochondrial-nuclear signal transduction pathway. This requirement would be fulfilled if Fe_{cyt} reacted in the cytosol with X-S that had been exported from the mitochondria to generate the Fe_2S_2cluster in the Grx·Fe_2S_{2c}Grx homodimer (see red star in Fig. 2). When Fe_{cyt} is limiting and X-S abundant, [Grx·Fe_2S_2·Grx] would be limited, which would activate the iron regulon. In this circumstance, Fe_{cyt} would play the dominant regulatory role. On the other hand, when X-S is limiting and Fe_{cyt} is abundant, [Grx·Fe_2S_2·Grx] would also be limiting, and the iron regulon would again be activated. However, [X-S] would play the

dominant regulatory role. It is only when Fe_{cyt} AND X-S are both abundant (relative to the amount of Grx available) that the iron regulon would not be activated. This is the situation found in healthy WT cells grown on iron-sufficient (or iron excess) conditions. These considerations were assumed in deriving the product function used in the Dual-Reg variant.

Remarkably, dual regulation was proposed in 2003 by Mühlenhoff *et al.* (**9**) based on their perceptive observation that both deletion and overexpression of Mrs3/4 activated the iron regulon. They posited that deleting Mrs3/4 caused low levels of ISC biosynthesis (thereby stimulating the iron regulon), whereas overexpressing Mrs3/4 caused low levels of Fe_{cyt} (also stimulating the iron regulon). Kaplan and co-workers (**117, 21, 70**) also interpreted particular experiments assuming that both cytosolic iron and ISC activity regulate iron traffic in yeast.

ISC biosynthesis activity might regulate iron trafficking to help mitochondria import more iron when cells transition from fermentation to respiration. In the late 1980s, Raguzzi, Lesuisse, and Crichton (**135**) hypothesized that vacuolar iron is mobilized during this metabolic transition. Respiring cells contain approximately three times the concentration of mitochondria as fermenting cells, indicating that the metabolic shift involves mitochondriogenesis (**136**). Some of the iron for this process comes from mobilized vacuolar iron. The trigger for mitochondriogenesis (perhaps low glucose levels) may not be perfectly coordinated to an increase in the rate of iron import into mitochondria. In this case, growing and dividing mitochondria might experience a transitory period in which insufficient ISCs are made. This might be sensed by a lower

than set point concentration of X-S in the cytosol, which might stimulate the ISC mutant phenotype (importing more iron into the cell, exporting vacuolar iron into the cytosol, and importing more Fe_{cyt} into mitochondria). The essential difference is that in healthy respiring cells, the imported iron *can* be used to make ISCs, whereas in ISC mutant cells, it cannot. Accordingly, the up-regulation of iron import, which generates nanoparticle iron in ISC mutant cells, is "earmarked" for ISC biosynthesis in healthy cells. In healthy cells, once sufficient ISCs are made, the signal (X-S) indicating this would attenuate further iron import and allow vacuolar iron stores to be replenished. In contrast, ISC mutant cells cannot use that iron to make ISCs, and so X-S is not made in sufficient amounts to shut down the coordinated import of iron into mitochondria; thus, vacuoles remain devoid of iron, whereas excessive iron pours into mitochondria, generating large amounts of nanoparticles and ROS as it reacts with O_2. This leads to the iron accumulation phenotype that defines ISC-associated diseases.

Mathematical models of biochemical processes in cells become increasingly insightful as the complexity of such processes and the amount of relevant information increases. Such models have the unique ability to integrate the pieces of the puzzle and allow the entire process to be viewed from a systems' level perspective. Modeling the progression from healthy to diseased states is a powerful way to understand the mechanism of diseases and to evaluate the efficacy of different treatments. We hope that further developments of this model will clarify the complex chemical relationships that collectively cause Friedreich's ataxia and other iron accumulation diseases and that such models might promote more effective treatments.

Author Contributions

J. D. W. helped develop the model, wrote the software code, and executed all simulations. P. A. L. designed the model, provided advice, and wrote most of the paper. Both authors reviewed and approved the final version of the manuscript.

Acknowledgement

We thank Dr. Zhigang Zhang for advice in designing the model.

Supplemental Material

Table 3.S1: Comparison between simulated values and literature data relevant to the model. Unless otherwise indicated, [N] = 40 μM and $\alpha = 0.2\ hr^{-1}$.

Experimental Condition (Ref)	Experimental Measurement	Experimental Result	Simulation Details	Simulation vs. Experiment
WT at Fe-deficient, Fe-sufficient (9)	FET3 expression	4-5↑at Fe-deficient vs. Fe sufficient	$[Fe]_{med}$ = 4, 40	$S_1 = \frac{(\text{Reg}_{\text{-C}} \cdot \text{Reg}_{\text{-FS}} \cdot R_{cell})_{N=4}}{(\text{Reg}_{\text{-C}} \cdot \text{Reg}_{\text{-FS}} \cdot R_{cell})_{N=40}} = 1.6$ $D_1 = 4.5$
ΔYfh1				
ΔYfh1 (23, 121)	Fermenting $[Fe]_{mit}$	5-15 time higher than WT	R_{isu} = 15 μM/hr α = 0.07 hr^{-1}	$S_2 = \left(\frac{[Fe_{mit}]_{\Delta Yfh1}}{[Fe_{mit}]_{WT}} \right)_{N=40} = 16$ $D_2 = 10$
ΔYfh1 (23)	mRNA levels of Mrs4	Levels were ~ 2.5 times increased relative to WT (Fig 1A, p 24476)	R_{isu} = 15 μM/hr α = 0.07 hr^{-1}	$S_3 = \frac{(\text{Reg}_{\text{-C}} \cdot \text{Reg}_{\text{-FS}} \cdot R_{mit})_{\Delta\text{Yfh1}}}{(\text{Reg}_{\text{-C}} \cdot \text{Reg}_{\text{-FS}} \cdot R_{mit})_{\text{WT}}} = 1.8$ $D_3 = 2.5$

Table 3.S1 Continued

Experimental Condition (Ref)	Experimental Measurement	Experimental Result	Simulation Details	Simulation vs. Experiment
ΔYfh1 (23)	$[^{55}Fe_{mit}]$, $[^{55}Fe_{super}]$	Mitochondria from ΔYfh1 contained 40%-45% of cellular ^{55}Fe; mitochondria from WT cells contained 5 – 10% of cellular ^{55}Fe. (Ratio is ca. 42/7.5 = 5.7)	R_{isu} = 15 μM/hr α = 0.07 hr^{-1}	$S_4 = \frac{([Fe_{mit}]/[Fe_{cell}])_{\Delta Yfh1}}{([Fe_{mit}]/[Fe_{cell}])_{WT}} = 8.2$ $D_4 = 5.7$
ΔYfh1 (23)	Aconitase and COX activities	Aconitase activity was 41% of WT COX activity was 74% of WT Ave = 58%	R_{isu} = 15 μM/hr α = 0.07 hr^{-1}	$S_5 = \frac{[FS]_{\Delta Yfh1}}{[FS]_{WT}} = 0.52$ $D_5 = 0.58$
Cu treatment to mimic ISC mutant (136)	Mrs4 expression	2.1↑ vs. WT	R_{isu} = 15 μM/hr α = 0.07 hr^{-1}	$S_6 = \frac{(\mathrm{Reg}_{\text{-C}} \cdot \mathrm{Reg}_{\text{-FS}} \cdot R_{mit})_{Cu}}{(\mathrm{Reg}_{\text{-C}} \cdot \mathrm{Reg}_{\text{-FS}} \cdot R_{mit})_{WT}} = 1.8$ $D_6 = 2.1$
ΔMrs3/4				
ΔMrs3/4 (23)	$[^{55}Fe_{mit}]$,$[^{55}Fe_{super}]$	Total cellular Fe was about 1.7 times that of WT cells.	R_{mit} = 180 μM/hr	$S_7 = \frac{[Fe_{cell}]_{\Delta Mrs3/4}}{[Fe_{cell}]_{WT}} = .88$ $D_7 = 1.7$
ΔMrs3/4 (23)	$[Fe]_{mit}$	Percentage of cellular iron in mito was 2.5% for ΔMrs3/4 and 4.0% for WT; the ratio was 0.62	R_{mit} = 180 μM/hr	$S_8 = \frac{([Fe_{mit}]/[Fe_{cell}])_{\Delta Mrs3/4}}{([Fe_{mit}]/[Fe_{cell}])_{WT}} = 1.0$ $D_8 = 0.62$
ΔMrs3/4 (23)	Aconitase and COX activities	Aconitase activity was 60% of WT COX activity was 59% of WT Ave = 60%	R_{mit} = 180 μM/hr	$S_9 = \frac{[FS]_{\Delta Mrs3/4}}{[FS]_{WT}} = 0.82$ $D_9 = 0.60$
ΔMrs3/4 (126)	FET3 expression FTR1 expression	FET3 = 2.2↑ vs. WT FTR1 = 1.9 ↑vs. WT (microarray)	R_{mit} = 180 μM/hr	$S_{10} = \frac{(\mathrm{Reg}_{\text{-C}} \cdot \mathrm{Reg}_{\text{-FS}} \cdot \mathrm{R}_{\text{cell}})_{\Delta Mrs3/4}}{(\mathrm{Reg}_{\text{-C}} \cdot \mathrm{Reg}_{\text{-FS}} \cdot \mathrm{R}_{\text{cell}})_{WT}} = .89$ $D_{10} = 2.0$

Table 3.S1 Continued

Experimental Condition (Ref)	Experimental Measurement	Experimental Result	Simulation Details	Simulation vs. Experiment
ΔMrs3/4 (126)	[hemes], [Bio2] aconitase, SDH	Hemes: 1.4↓ vs. WT (was 2-fold down in Fe-starved cells) Bio2: 2.5↓ vs. WT (was 1.7 fold lower in Fe-depleted mitos) Aconitase unchanged SDH unchanged (Ave ca. 1.5 fold down)	R_{mit} = 180 μM/hr $[Fe]_{med}$ = 4	$S_{11} = \left(\frac{[FS]_{\Delta Mrs3/4}}{[FS]_{WT}} \right)_{[Femed]=4} = 0.82$ $D_{11} = 0.67$
ΔMrs3/4 (126)	Aconitase and SDH activities	In mito preparations, no significant differences in the activities of aconitase and SDH.	R_{mit} = 180 μM/hr	$S_{12} = \left(\frac{[FS]_{\Delta Mrs3/4}}{[FS]_{WT}} \right)_{[Femed]=40} = 0.82$ $D_{12} = 1.0$
ΔMrs3/4 (126)	$[Fe]_{mit}$	Mitochondria had 2.1 fold less Fe than WT mitochondria	R_{mit} = 180 μM/hr $[Fe]_{med}$ = 4	$S_{13} = \left(\frac{[Fe_{mit}]_{\Delta Mrs3/4}}{[Fe_{mit}]_{WT}} \right)_{[Femed]=4} = 0.89$ $D_{13} = 0.48$
ΔMrs3/4 (126)	$[Fe]_{mit}$	In mitochondria, no substantial changes in iron accumulation relative to WT; heme formation was similar to WT	R_{mit} = 180 μM/hr	$S_{14} = \left(\frac{[Fe_{mit}]_{\Delta Mrs3/4}}{[Fe_{mit}]_{WT}} \right)_{[Femed]=40} = 0.89$ $D_{14} = 1.0$
ΔMrs3/4 (127)	FET3, FRE1, FTR1 expression	FET3 = 4.7↑ vs. WT FRE1 = 4.1↑ vs. WT FTR1 =3.5↑ vs. WT Ave = 4.1	R_{mit} = 180 μM/hr	$S_{15} = \frac{(\mathrm{Reg}_{\text{-C}} \cdot \mathrm{Reg}_{\text{-FS}} \cdot R_{cell})_{\Delta Mrs3/4}}{(\mathrm{Reg}_{\text{-C}} \cdot \mathrm{Reg}_{\text{-FS}} \cdot R_{cell})_{WT}} = .89$ $D_{15} = 4.1$
ΔMrs3/4 (127)	$[Fe]_{cell}$	2.8↑ vs. WT	R_{mit} = 180 μM/hr	$S_{16} = \frac{[Fe_{cell}]_{\Delta Mrs3/4}}{[Fe_{cell}]_{WT}} = .89$ $D_{16} = 2.8$

Table 3.S1 Continued

Experimental Condition (Ref)	Experimental Measurement	Experimental Result	Simulation Details	Simulation vs. Experiment
ΔMrs3/4 (127)	$[Fe]_{vac}$	4.0↑ vs. WT	R_{mit} = 180 μM/hr	$S_{17} = \frac{[Fe_{vac}]_{\Delta Mrs3/4}}{[Fe_{vac}]_{WT}} = .84$ $D_{17} = 4.0$
ΔMrs3/4 (127)	FET3 expression Iron uptake	FET3: 8.0↑ vs. WT Iron uptake: 14.8 times WT Ave: 11.4	R_{mit} = 180 μM/hr	$S_{18} = \frac{(\mathrm{Reg}_{\text{-C}} \cdot \mathrm{Reg}_{\text{-FS}} \cdot R_{cell})_{\Delta Mrs3/4}}{(\mathrm{Reg}_{\text{-C}} \cdot \mathrm{Reg}_{\text{-FS}} \cdot R_{cell})_{WT}} = .89$ $D_{18} = 11.4$
ΔMrs3/4 (127)	$[Fe]_{cell}$	2.0↑ vs. WT	R_{mit} = 180 μM/hr	$S_{19} = \frac{[Fe_{cell}]_{\Delta Mrs3/4}}{[Fe_{cell}]_{WT}} = .89$ $D_{19} = 2.0$
ΔMrs3/4 (127)	Aconitase activity	0.25 times WT	R_{mit} = 180 μM/hr	$S_{20} = \frac{[FS]_{\Delta Mrs3/4}}{[FS]_{WT}} = 0.82$ $D_{20} = 0.25$
MRS3/4 Overexpression				
MRS3/4-over (126)	FET3 expression FTR1 expression	FET3 = 2.8↑ vs. WT FTR1 = 2.5↑ vs. WT (microarray)	R_{mit} = 2340 μM/hr $[Fe]_{med}$ = 4	$S_{21} = \frac{(\mathrm{Reg}_{\text{-C}} \cdot \mathrm{Reg}_{\text{-FS}} \cdot R_{cell})_{\mathrm{Mrs3/4over}}}{(\mathrm{Reg}_{\text{-C}} \cdot \mathrm{Reg}_{\text{-FS}} \cdot R_{cell})_{WT}} = 0.61$ $D_{21} = 2.6$
MRS3/4-over (126)	[hemes], [ISC] aconitase, SDH	Hemes: 1.7↑ vs. WT ISCs: 2↑ vs. WT Aconitase unchanged SDH unchanged	R_{mit} = 2340 μM/hr	$S_{22} = \left(\frac{[FS]_{Mrs3/4over}}{[FS]_{WT}} \right)_{[Femed]=4} = 1.1$ $D_{22} = 1.8$
MRS3/4-over (126)	$[Fe]_{mit}$	2.5↑ vs. WT	R_{mit} = 2340 μM/hr $[Fe]_{med}$ = 4	$S_{23} = \left(\frac{[Fe_{mit}]_{Mrs3/4over}}{[Fe_{mit}]_{WT}} \right)_{[Femed]=4} = 1.2$ $D_{23} = 2.5$

Table 3.S1 Continued

Experimental Condition (Ref)	Experimental Measurement	Experimental Result	Simulation Details	Simulation vs. Experiment
MRS3/4-up (127)	$[Fe]_{cell}$	$[Fe]_{cell}$ = 40% of WT	R_{mit} = 2340 μM/hr	$S_{24} = \frac{[Fe_{cell}]_{Mrs3/4UP}}{[Fe_{cell}]_{WT}} = 0.55$ $D_{24} = 0.40$
ΔCcc1				
ΔCcc1 (127)	FET3 expression Iron uptake	FET3: 0.67 times WT Iron uptake: 0.75 times WT Ave: 0.7	R_{vac} = 510 μM/hr	$S_{25} = \frac{(\text{Reg}_{\text{-C}} \cdot \text{Reg}_{\text{-FS}} \cdot R_{cell})_{\Delta CCC1}}{(\text{Reg}_{\text{-C}} \cdot \text{Reg}_{\text{-FS}} \cdot R_{cell})_{WT}} = 0.60$ $D_{25} = 0.70$
ΔCcc1 (127)	$[Fe]_{cell}$	0.59 times WT	R_{vac} = 510 μM/hr	$S_{26} = \frac{[Fe_{cell}]_{\Delta CCC1}}{[Fe_{cell}]_{WT}} = 0.60$ $D_{26} = 0.59$
ΔCcc1 (127)	Aconitase activity	1.5 times WT	R_{vac} = 510 μM/hr	$S_{27} = \frac{[FS]_{\Delta CCC1}}{[FS]_{WT}} = 1.1$ $D_{27} = 1.5$
ΔCcc1 (127)	$[Fe_{vac}]$	27% of WT value	R_{vac} = 510 μM/hr	$S_{28} = \frac{[Fe_{vac}]_{\Delta CCC1}}{[Fe_{vac}]_{WT}} = 0.54$ $D_{28} = 0.27$
Ccc1 overexpression				
Ccc1 over (120)	$[Fe_{vac}]$	2.2 times greater than in WT vacuoles	R_{vac} = 20,000 μM/hr	$S_{29} = \frac{[Fe_{vac}]_{CCC1over}}{[Fe_{vac}]_{WT}} = 2.2$ $D_{29} = 2.2$
Ccc1 overexpression (120)	Aconitase activity	Reduced relative to WT	R_{vac} = 20,000 μM/hr	$S_{30} = \frac{[FS]_{CCC1over}}{[FS]_{WT}} = 0.79$ $D_{30} = 0.8$
Aft1/2-1^{UP}				

Table 3.S1 Continued

Experimental Condition (Ref)	Experimental Measurement	Experimental Result	Simulation Details	Simulation vs. Experiment
Aft1-1^{up} (21) Aft2-1^{up} ΔAft1ΔAft2	FET3 expression FTR1 expression	FET3: (25.2+3.7) ↑ Up vs. Δ FTR1: (5+2.6) ↑ Up vs. Δ FRE1: (4+3.5) ↑ Up vs. Δ Ave = 7.3	$[Fe]_{med}$ = 0.4 and 10,000	$S_{31} = \frac{\left(\mathrm{Reg}_{\text{-C}} \cdot \mathrm{Reg}_{\text{-FS}} \cdot R_{cell}\right)_{N=0.4}}{\left(\mathrm{Reg}_{\text{-C}} \cdot \mathrm{Reg}_{\text{-FS}} \cdot R_{cell}\right)_{N=10,000}} = 2.7$ $D_{31} = 7.3$
Aft1-1^{up} (117) Aft2-1^{up} ΔAft1ΔAft2	Mrs4 expression	3.5 ↑ Up (ave) vs. Δ	$[Fe]_{med}$ = 0.4 and 10,000	$S_{32} = \frac{\left(\mathrm{Reg}_{\text{-C}} \cdot \mathrm{Reg}_{\text{-FS}} \cdot R_{mit}\right)_{N=0.4}}{\left(\mathrm{Reg}_{\text{-C}} \cdot \mathrm{Reg}_{\text{-FS}} \cdot R_{mit}\right)_{N=10,000}} = 2.0$ $D_{32} = 3.5$
Aft1-1^{up} (117) Aft2-1^{up} ΔAft1ΔAft2	FET5 expression SMF3expression	~ 2.6↑ Up (ave) vs. Δ (Fet5) ~ 2↑ Up (ave) vs. Δ (Smf3)	$[Fe]_{med}$ = 0.4 and 10,000	$S_{33} = \frac{\left(\mathrm{Reg}_{\text{-C}} \cdot \mathrm{Reg}_{\text{-FS}} \cdot R_{vac}\right)_{N=10,000}}{\left(\mathrm{Reg}_{\text{-C}} \cdot \mathrm{Reg}_{\text{-FS}} \cdot R_{vac}\right)_{N=0.4}} = 574$ $D_{33} = 2.3$
ΔYfh1ΔMrs3/4				
ΔYfh1ΔMrs3/4 (23)	$[^{55}Fe_{mit}]$, $[^{55}Fe_{super}]$	Mitochondrial iron concentration is decreased to almost WT levels (Ratio is ca. 1.0)	R_{isu} = 15 μM/hr R_{mit} = 180 μM/hr α = 0.07 hr^{-1}	$S_{34} = \frac{[Fe_{mit}]/[Fe_{cell}]_{\Delta Yfh1\Delta Mrs3/4}}{[Fe_{mit}]/[Fe_{cell}]_{WT}} = 7.1$ $D_{34} = 1.2$
ΔYfh1ΔMrs3/4 (23)	$[^{55}Fe_{mit}]$, $[^{55}Fe_{super}]$	Mitochondrial iron concentration is 13% of cellular Fe.	R_{isu} = 15 μM/hr R_{mit} = 180 μM/hr $[Fe_{med}]$ = 10000 μM α = 0.07 hr^{-1}	$S_{35} = \frac{[Fe_{mit}]_{\Delta Yfh1\Delta Mrs3/4}}{[Fe_{cell}]_{\Delta Yfh1\Delta Mrs3/4}} = 0.83$ $D_{35} = 0.13$
ΔYfh1ΔMrs3/4 (23)		Cellular Fe is about 3.5 times WT cellular iron level	R_{isu} = 15 μM/hr R_{mit} = 180 μM/hr $[Fe_{med}]$ = 10000 μM α = 0.07 hr^{-1}	$S_{36} = \frac{[Fe_{cell}]_{\Delta Yfh1\Delta Mrs3/4}}{[Fe_{cell}]_{\Delta Yfh1\Delta Mrs3/4}} = .49$ $D_{36} = 3.5$

Table 3.S1 Continued

Experimental Condition (Ref)	Experimental Measurement	Experimental Result	Simulation Details	Simulation vs. Experiment
ΔYfh1ΔMrs3/4 (23)	Aconitase and COX activities	Aconitase activity was 16% of WT COX activity was 45% of WT Ave = 30%	R_{isu} = 15 μM/hr R_{mit} = 180 μM/hr α = 0.07 hr^{-1}	$S_{37} = \frac{[FS]_{\Delta Yfh1\Delta Mrs3/4}}{[FS]_{WT}} = 0.06$ $D_{37} = 0.3$
ΔYfh1; MRS3/4over				
ΔYfh1;MRS3/4over (127)	$[Fe]_{mit}$	2.5 ↑ vs. ΔYfh1	R_{isu} = 15 μM/hr R_{mit}=4000 μM/hr α = 0.07 hr^{-1}	$S_{38} = \frac{[Fe_{mit}]_{\Delta Yfh1-Mrs3/4UP}}{[Fe_{mit}]_{\Delta Yfh1}} = 2.3$ $D_{38} = 2.5$
ΔCcc1;ΔMrs3/4				
ΔCcc1;ΔMrs3/4 (127)	FET3, FRE1, FTR1 expression	FET3: 0.978 vs. WT FRE1: 1.374 vs WT FTR1: 0.834 vs. WT Ave: 1.1	R_{vac} = 510 μM/hr R_{mit} = 180 μM/hr	$S_{39} = \frac{(\mathrm{Reg}_{\text{-C}} \cdot \mathrm{Reg}_{\text{-FS}} \cdot R_{cell})_{\Delta CCC1\Delta Mrs3/4}}{(\mathrm{Reg}_{\text{-C}} \cdot \mathrm{Reg}_{\text{-FS}} \cdot R_{cell})_{WT}} = .24$ $D_{39} = 1.1$
ΔCcc1;ΔMrs3/4 (127)	FET3 expression Iron uptake	FET3: 4 times vs. WT Iron uptake: 3.4 times vs. WT Ave: 3.7 times vs. WT	R_{vac} = 510 μM/hr R_{mit} = 180 μM/hr	$S_{40} = \frac{(\mathrm{Reg}_{\text{-C}} \cdot \mathrm{Reg}_{\text{-FS}} \cdot R_{cell})_{\Delta CCC1\Delta Mrs3/4}}{(\mathrm{Reg}_{\text{-C}} \cdot \mathrm{Reg}_{\text{-FS}} \cdot R_{cell})_{WT}} = .24$ $D_{40} = 3.7$
ΔCcc1;ΔMrs3/4 (127)	Whole cell iron	1.6 times vs. WT	R_{vac} = 510 μM/hr R_{mit} = 180 μM/hr	$S_{41} = \frac{[Fe_{cell}]_{\Delta Yfh1\Delta Ccc1}}{[Fe_{cell}]_{WT}} = .46$ $D_{41} = 3.7$
ΔCcc1;ΔMrs3/4 (127)	$[Fe_{vac}]$	2 times vs. WT vacuoles	R_{vac} = 510 μM/hr R_{mit} = 180 μM/hr	$S_{42} = \frac{[Fe_{vac}]_{\Delta Yfh1\Delta Ccc1}}{[Fe_{vac}]_{WT}} = 0.35$ $D_{42} = 2.0$

Table 3.S1 Continued

Experimental Condition (Ref)	Experimental Measurement	Experimental Result	Simulation Details	Simulation vs. Experiment
ΔCcc1;ΔMrs3/4 (127)	Aconitase activity	0.81 times vs. WT	R_{vac} = 510 μM/hr R_{mit} = 180 μM/hr	$S_{43} = \frac{[FS]_{\Delta Yfh1\Delta Ccc1}}{[FS]_{WT}} = 0.84$ $D_{43} = 0.81$

Table 3.S2: Data from previous Mössbauer studies (All numbers are referenced from (**66**) and the references therein with the exception of ISC40)

Experiment	[N]	[C] (S only)	[F2] (S only)	[F3]	[VP]	[FM]	[FS]	[MP]	[O2] (S only)	[ROS] (S only)	Fe^{2+}	Total Fe	RMSD
BPS	4	2.31	132	452 S 1 D	44.5 S 1 D	98.3 S 33.6 D	173 S 334 D	192 S 48 D	2.17	192.22	44.3 S 56.0 D	205 S 153 D	5.72
WT1	7	2.58	121	688 S 400 D	67.5 S 120 D	103 S 150 D	181 S 550 D	191 S 50 D	2.06	192	42.2 S 60.0 D	268 S 250 D	3.66
WT10	16	2.95	116	1004 S 1000 D	98.3 S 1 D	109 S 152 D	289 S 107 D	192 S 310 D	1.96	192	41.8 S 65.0 D	366 S 395 D	.931
WT40	46	3.30	114	1277 S 1180 D	125 S 180 D	114 S 152 D	197 S 213 D	192 S 254 D	1.87	192	42.0 S 44.0 D	412 S 440 D	.616
WT100	106	3.45	114	1390 S 1400 D	136 S 80 D	115 S 170 D	199 S 215 D	192 S 192 D	1.84	192	42.2 S 30.0 D	463 S 470 D	.319
WT1000	1006	3.57	113	1480 S 1440 D	144 S 120 D	117 S 132 D	201 S 220 D	192 S 200 D	1.82	192	42.3 S 26.0 D	488 S 455 D	.279
WT10000	10006	3.59	113	1491 S 1460 D	146 S 140 D	117 S 112 D	201 S 135 D	192 S 200 D	1.81	192	42.3 S 40.0 D	490 S 440 D	.262
ISC40 (20)	46	31.5	56.9	7.19 S 0 D	16.8 S 0 D	803 S 370 D	103 S 0 D	7013 S 7030 D	3.68	7013	115 S 20 D	833 S 1000 D	.668
DelC1	7	3.02	61.3	110 S 36 D	33.1 S 36.0 D	56.8 S 388 D	221 S 388 D	83.7 S 242 D	1.63	83.7	22.9 S 27.0 D	89.2 S 150 D	4.92
DelC10	16	3.32	92.9	178 S 212 D	53.2 S 40.0 D	58.2 S 340 D	227 S 340 D	83.5 S 212 D	1.58	83.6	31.2 S 54.0 D	120 S 209 D	2.84
DelC20	26	3.46	109	215 S 316 D	63.9 S 92.0 D	58.9 S 311 D	228 S 311 D	83.5 S 193 D	1.57	83.5	35.4 S 98.0 D	136 S 284 D	2.24
DelC40	46	3.58	124	249 S 456 D	74.1 S 244 D	59.4 S 316 D	231 S 316 D	83.5 S 197 D	1.56	83.5	39.3 S 107 D	181 S 357 D	2.52
Cup1	7	1.71	944	192 S 176 D	274 S 184 D	83.1 S 118 D	149 S 118 D	194 S 73.6 D	2.59	194	245 S 128 D	396 S 250 D	1.64
Cup10	16	1.87	1362	347 S 372 D	495 S 516 D	88.1 S 141 D	157 S 141 D	193 S 87.4 D	2.43	193	351 S 305 D	596 S 565 D	.472
Cup20	26	1.96	1574	433 S 608 D	618 S 1400 D	90.3 S 266 D	161 S 266 D	193 S 166 D	2.36	193	404 S 407 D	702 S 981 D	1.29
Cup40	46	2.04	1769	515 S 1480 D	736 S 2088 D	92.3 S 437 D	164 S 437 D	193 S 271 D	2.31	193	453 S 828 D	801 S 1838 D	1.84
Cupade1	7	1.87	53.2	602 S 156 D	659 S 168 D	87.9 S 130 D	157 S 130 D	193 S 80.5 D	2.44	193	23.3 S 269 D	373 S 385 D	3.55
Cupade40	46	2.63	16.4	1043 S 1872 D	1139 S 1204 D	104 S 233 D	182 S 233 D	192 S 145 D	2.04	192	16.2 S 187 D	599 S 1019 D	1.27

Table 3.S3: Optimized Parameters and sensitivities.

Parameter	Optimized Value	Unit	Sensitivity
R_{mit}	900	$\mu M \cdot hr^{-1}$	1.15
$R_{mit(\Delta Mrs3/4)}$	180	"	1.00
$R_{mit(Mrs3/4\text{-}UP)}$	2340	"	1.00
$R_{mit(\Delta Yfh1;Mrs3/4\text{-}UP)}$	4000*	"	1.04
k_{O2}	52	hr^{-1}	1.08
k_{res}	150	hr^{-1}	1.07
k_{mp}	0.18	$\mu M^{-1}hr^{-1}$	1.06
K_{mit}	12	µM	1.08
K_{O2}	9	"	1.07
K_{isu}	610	"	1.07
K_{cell}	14	"	1.00
K_{vac}	5.5	"	1.00
$[FS]_{spcell}$	190	µM	1.08
$[FS]_{spmit}$	200	"	1.09
$[FS]_{spvac}$	190	"	1.02
$[FS]_{spvac(\Delta Ccc1)}$	170*	"	1.00
$[FS]_{spvac(CCC1\text{-}UP)}$	170	"	1.00
$[FS]_{spvac(UP+Ad)}$	145	"	1.01
$[FS]_{sp23}$	210	"	1.00
$[FS]_{sp23(\Delta Ccc1)}$	110	"	1.00
$[FS]_{sp23(CCC1\text{-}UP)}$	150	"	1.00

Table 3.S3 Continued

Parameter	Optimized Value	Unit	Sensitivity
$[FS]_{sp23(CCC1\text{-}UP+Ad)}$	190	"	1.01
$[C]_{spcell}$	27	µM	1.05
$[C]_{spmit}$	80*	"	1.00
$[C]_{spvac}$	1.2	"	1.00
$[C]_{spvac(\Delta Ccc1)}$	4.2	"	1.00
$[C]_{spvac(CCC1\text{-}UP)}$	0.2	"	1.00
$[C]_{spvac(CCC1\text{-}UP+Ad)}$	.5*	"	1.00
$[C]_{sp23}$	2	"	1.02
$[C]_{sp23(\Delta Ccc1)}$	2.3	"	1.00
$[C]_{sp23(CCC1\text{-}UP)}$	0.14	"	1.00
$[C]_{sp23(CCC1\text{-}UP+Ad)}$	2	"	1.05
fssenmit	4	none	1.03
fssencell	9	"	1.00
fssenvac	8	"	1.00
fssenvac(ΔCcc1)	7	"	1.00
fssenvac(CCC1-up)	10	"	1.00
fssenvac(UP+Ad)	10	"	1.00
fssen23	10	"	1.00
fssen23(ΔCCC1)	10	"	1.00
fssens23(CCC1-UP)	10	"	1.00
fsens23(UP+Ad)	7	"	1.01
csenmit	5	none	1.00

Table 3.S3 Continued

Parameter	Optimized Value	Unit	Sensitivity
csencell	5	"	1.00
csenvac	3	"	1.00
csenvac(ΔCcc1)	5	"	1.00
csenvac(CCC1-up)	4	"	1.00
csenvac(UP+Ad)	4	"	1.00
csen23	10	"	1.00
csen23(ΔCCC1)	2	"	1.00
csens23(CCC1-UP)	5	"	1.00
csens23(UP+Ad)	10	"	1.01
R_{vac}	2200	$\mu M \cdot hr^{-1}$	1.01
$R_{vac(\Delta ccc1)}$	825 (748?)	"	1.00
$R_{vac(CCC1\text{-}UP)}$	7920	"	1.00
$R_{vac(CCC1\text{-}UP+Ad)}$	2200	"	1.00
$R_{vac(litdelta)}$	510	"	1.01
$R_{vac(litup)}$	20,000*	"	1.00
R_{cell}	410	$\mu M \cdot hr^{-1}$	1.00
R_{isu}	520	$\mu M \cdot hr^{-1}$	1.00
R_{isu}(ΔYfh1)	15	"	1.03
k_{23}	7.3	hr^{-1}	1.00
$k_{23(\Delta Ccc1)}$	0.74	"	1.00

Table 3.S3 Continued

Parameter	Optimized Value	Unit	Sensitivity
$k_{23(CCC1\text{-}up)}$	0.20	"	1.00
$k_{23(CCC1\text{-}UP+Ad)}$	66	"	1.00
k_{vp}	0.02	hr^{-1}	1.00
$k_{vp(\Delta Ccc1)}$	0.06	"	1.00
$k_{vp(Ccc1\text{-}UP)}$	0.29	"	1.00
$k_{vp(Ccc1\text{-}UP+Ad)}$	0.22	"	1.00
k_{ros}	0.014	$\mu M^{-1}hr^{-1}$	Fixed
RO2 (aerobic)	100	µM	Fixed
RO2 (anaerobic)	1	µM	Fixed
$\alpha_{healthy}$	0.2	hr^{-1}	Fixed
$\alpha_{diseased}$	0.07	hr^{-1}	Fixed
f_{cyt}	0.65	none	Fixed
f_{mit}	0.10	none	Fixed
f_{vac}	0.25	none	Fixed

A. Derivation of Product Reg Functions

This derivation assumes that X-S and Fe_{cyt} react to generate the Grx[Fe_2S_2]Grx homodimer, and that only the apo-form of Grx is active. Following the nomenclature in the text, X-S = FS and Fe_{cyt} = C. Also, A = the active form of Aft1/2; inactive forms include AC, AFS and AFSC. We assume that either substrate can bind first and that the binding strength does not change when the other substrate is bound. The dissociation equilibrium expressions for these binding events are…

$$AC \rightleftarrows A + C \quad K_C = \frac{A \cdot C}{AC}$$

$$AFS \rightleftarrows A + FS \quad K_{FS} = \frac{A \cdot FS}{AFS}$$

$$AFSC \rightleftarrows AFS + C \quad K_C = \frac{AFS \cdot C}{AFSC}$$

$$AFSC \rightleftarrows AC + FS \quad K_{FS} = \frac{AC \cdot FS}{AFSC}$$

The fraction of A_{tot} that is active depends on these binding constants and the concentrations of FS and C, as follows.

$$A_{tot} = A + AFS + AC + AFSC$$

$$A_{tot} = A + \frac{A \cdot FS}{K_{FS}} + \frac{A \cdot C}{K_C} + \frac{AFS \cdot C}{K_C}$$

$$A_{tot} = A + \frac{A \cdot FS}{K_{FS}} + \frac{A \cdot C}{K_C} + \frac{A \cdot C \cdot FS}{K_C \cdot K_{FS}}$$

$$A_{tot} = A\left(1 + \frac{FS}{K_{FS}} + \frac{C}{K_C} + \frac{C \cdot FS}{K_C \cdot K_{FS}}\right)$$

$$A_{tot} = A\left(1 + \frac{FS}{K_{FS}}\right)\left(1 + \frac{C}{K_C}\right)$$

$$\frac{A}{A_{tot}} = \frac{1}{\left(1 + \frac{FS}{K_{FS}}\right)} \frac{1}{\left(1 + \frac{C}{K_C}\right)}$$

$$\frac{A}{A_{tot}} = \mathrm{Re}\, g_{-FS} \cdot \mathrm{Re}\, g_{-C}$$

B. Derivation of cellular iron concentrations

Multiply the ODEs associated with each of the 7 Fe-containing species in the model ([2] – [8]) by the fractional volume associated with each species whose concentration-change is described by the ODE. For example, both sides of ODE [2] are multiplied by fractional cytosolic volume (V_{cyt}/V_{cell}) because the component described by that ODE, namely C, is found in the cytosol. We have…

$$\frac{V_{cyt}}{V_{cell}}\frac{d[C]}{dt}=\frac{V_{cyt}}{V_{cell}}\frac{\mathrm{R}_{cell}[N]}{K_{cell}+[N]}\mathrm{Re}\,g_{-C}\cdot\mathrm{Re}\,g_{-FS}-\frac{V_{mit}}{V_{cell}}\frac{R_{mit}[C]}{K_{mit}+[C]}\mathrm{Re}\,g_{-C}\cdot\mathrm{Re}\,g_{-FS}-\frac{V_{vac}}{V_{cell}}\frac{R_{vac}[C]}{K_{vac}+[C]}\mathrm{Re}\,g_{+C}\cdot Re\,g_{+FS}-\frac{V_{cyt}}{V_{cell}}\alpha[C]$$

$$\frac{V_{mit}}{V_{cell}}\frac{d[FM]}{dt}=\frac{V_{mit}}{V_{cell}}\frac{R_{mit}[C]}{K_{mit}+[C]}\mathrm{Re}\,g_{-C}\cdot\mathrm{Re}\,g_{-FS}-\frac{V_{mit}}{V_{cell}}\frac{R_{isu}[FM]}{K_{isu}+[FM]}-\frac{V_{mit}}{V_{cell}}k_{mp}[FM][O2]-\frac{V_{mit}}{V_{cell}}\alpha[FM]$$

$$\frac{V_{vac}}{V_{cell}}\frac{d[F2]}{dt}=\frac{V_{vac}}{V_{cell}}\frac{R_{vac}[C]}{K_{vac}+[C]}\mathrm{Reg}_{+C}\cdot\mathrm{Reg}_{+FS}-\frac{V_{vac}}{V_{cell}}k_{23}[F2]\mathrm{Reg}_{+C}\cdot\mathrm{Reg}_{+FS}-\frac{V_{vac}}{V_{cell}}\alpha[F2]$$

$$\frac{V_{mit}}{V_{cell}}\frac{d[FS]}{dt}=\frac{V_{mit}}{V_{cell}}\frac{R_{isu}[FM]}{K_{isu}+[FM]}-\frac{V_{mit}}{V_{cell}}\alpha[FS]$$

$$\frac{V_{mit}}{V_{cell}}\frac{d[MP]}{dt}=\frac{V_{mit}}{V_{cell}}k_{mp}[FM][O2]-\frac{V_{mit}}{V_{cell}}\alpha[MP]$$

$$\frac{V_{vac}}{V_{cell}}\frac{d[F3]}{dt}=\frac{V_{vac}}{V_{cell}}k_{23}[F2]\mathrm{Reg}_{+C}\cdot\mathrm{Reg}_{+FS}-\frac{V_{vac}}{V_{cell}}k_{vp}[F3]-\frac{V_{vac}}{V_{cell}}\alpha[F3]$$

$$\frac{V_{vac}}{V_{cell}}\frac{d[VP]}{dt}=\frac{V_{vac}}{V_{cell}}k_{vp}[F3]-\frac{V_{vac}}{V_{cell}}\alpha[VP]$$

The sum of these terms on the left-hand-side of the ODEs is

$$\frac{V_{cyt}}{V_{cell}}\frac{d[C]}{dt}+\frac{V_{mit}}{V_{cell}}\frac{d[FM]}{dt}+\frac{V_{mit}}{V_{cell}}\frac{d[FS]}{dt}+\frac{V_{mit}}{V_{cell}}\frac{d[MP]}{dt}+\frac{V_{vac}}{V_{cell}}\frac{d[F2]}{dt}+\frac{V_{vac}}{V_{cell}}\frac{d[F3]}{dt}+\frac{V_{vac}}{V_{cell}}\frac{d[VP]}{dt}$$

This is identical to the derivative of the overall mass balance equation [1].

$$\frac{d[Fe_{cell}]}{dt} = \frac{V_{cyt}}{V_{cell}}\frac{d[C]}{dt} + \frac{V_{mit}}{V_{cell}}\frac{d[FM]}{dt} + \frac{V_{mit}}{V_{cell}}\frac{d[FS]}{dt} + \frac{V_{mit}}{V_{cell}}\frac{d[MP]}{dt} + \frac{V_{vac}}{V_{cell}}\frac{d[F2]}{dt} + \frac{V_{vac}}{V_{cell}}\frac{d[F3]}{dt} + \frac{V_{vac}}{V_{cell}}\frac{d[VP]}{dt}$$

Indicating that the left-hand-side of the ODEs is equal to $\frac{d[Fe_{cell}]}{dt}$.

The sum of the last terms of the right-hand-side of the ODEs affords

$$-\frac{V_{cyt}}{V_{cell}}\alpha[C] - \frac{V_{mit}}{V_{cell}}\alpha[FM] - \frac{V_{mit}}{V_{cell}}\alpha[FS] - \frac{V_{mit}}{V_{cell}}\alpha[MP] - \frac{V_{vac}}{V_{cell}}\alpha[F2] - \frac{V_{vac}}{V_{cell}}\alpha[F3] - \frac{V_{vac}}{V_{cell}}\alpha[VP]$$

Simplifying yields

$$-\alpha\left(\frac{V_{cyt}}{V_{cell}}[C] + \frac{V_{mit}}{V_{cell}}[FM] + \frac{V_{mit}}{V_{cell}}[FS] + \frac{V_{mit}}{V_{cell}}[MP] + \frac{V_{vac}}{V_{cell}}[F2] + \frac{V_{vac}}{V_{cell}}[F3] + \frac{V_{vac}}{V_{cell}}[VP]\right)$$

The sum of the terms within the parentheses is identical to the right-hand-side of [1], such that we can simply to $-\alpha \cdot [Fe_{cell}]$. Most (but not all) of the remaining terms of the summed ODEs cancel, finally yielding the equation

$$\frac{d[Fe_{cell}]}{dt} = \frac{V_{cyt}}{V_{cell}}\frac{\mathrm{R}_{cell} \cdot [N]}{K_{cell} + [N]}\mathrm{Re}\, g_{-C} \cdot \mathrm{Re}\, g_{-FS} - \alpha \cdot [Fe_{cell}]$$

CHAPTER IV

RECOVERY OF MRS3ΔMRS4Δ SACCHAROMYCES CEREVISIAE CELLS UNDER IRON-SUFFICIENT CONDITIONS AND THE ROLE OF FE 580[*]

Michael J. Moore[†], Joshua D. Wofford[†], Andrew Dancis[¶], and Paul A. Lindahl [†,§,*]

[†]Department of Chemistry, Texas A&M University, College Station, TX 77843 USA

[¶]Department of Medicine, Division of Hematology-Oncology, Perelman School of Medicine, University of Pennsylvania, Philadelphia, PA, 19104 USA

[§]Department of Biochemistry and Biophysics, Texas A&M University, College Station, TX 77843 USA

Summary

Mrs3 and Mrs4 are mitochondrial inner membrane proteins that deliver an unidentified cytosolic iron species into the matrix for use in iron-sulfur-cluster (ISC) and heme biosynthesis. The Mrs3/4 double-deletion strain (ΔΔ) grew slowly in iron-deficient glycerol/ethanol medium but recovered to WT rates in iron-sufficient medium. ΔΔ cells grown under both iron-deficient and iron-sufficient respiring conditions accumulated large amounts of iron relative to WT cells, indicating iron homeostatic dysregulation regardless of nutrient iron status. Biophysical spectroscopy (including Mössbauer, EPR, and electronic absorption) and bioanalytical methods (liquid chromatography with online

[*] Reprinted with permission from Biochemistry. Michael J. Moore, Joshua D. Wofford, Andrew Dancis, and Paul A. Lindahl, Recovery of mrs3Δmrs4Δ Saccharomyces cerevisiae Cells under Iron-Sufficient Conditions and the Role of Fe 580, 2018, Volume 57, 672-683.

ICP-MS detection) were used to characterize these phenotypes. Anaerobically isolated mitochondria contained a labile iron pool composed of a nonheme high-spin Fe^{2+} complex with primarily O and N donor ligands, called Fe_{580}. Fe_{580} likely serves as feedstock for ISC and heme biosynthesis. Mitochondria from respiring ΔΔ cells grown under Fe-deficient conditions were devoid of Fe_{580}, ISCs, and hemes; most iron was present as Fe^{3+} nanoparticles. O_2 likely penetrates the matrix of slow-growing poorly respiring iron-deficient ΔΔ cells and reacts with Fe_{580} to form nanoparticles, thereby inhibiting ISC and heme biosynthesis. Mitochondria from iron-sufficient ΔΔ cells contained ISCs, hemes, and Fe_{580} at concentrations comparable to those of WT mitochondria. The matrix of these mutant cells was probably sufficiently anaerobic to protect Fe_{580} from degradation by O_2. An ~1100 Da manganese complex, a ~1200 Da zinc complex, and a ~5000 Da copper species were also present in ΔΔ and WT mitochondrial flow-through solutions. No copper complex of lower mass was evident.

Introduction

Mitochondria are the major site of iron-sulfur-cluster (ISC) biosynthesis in eukaryotes, and the only site for the iron-insertion step of heme biosynthesis; thus, large amounts of iron must be imported into the organelle. **(67,68)** Mrs3 and Mrs4 (Mrs3/4) in *Saccharomyces cerevisiae* are paralogous mitochondrial inner membrane proteins that deliver cytosolic iron into the matrix, presumably for use in both processes **(69,9,70,71,8).** Mammals have homologs of Mrs3/4 called *mitoferrin1/2* **(138,139)**. The

iron species imported by these proteins is unknown, but the narrow channels in these proteins imply a small coordination complex **(9,140,141)**.

Mössbauer spectra of anaerobically isolated mitochondria reveal a pool of non-heme high-spin (NHHS) Fe^{2+} in the organelle **(13)**. The concentration of iron in this pool ranges from 60 - 200 μM whereas the overall iron concentration in mitochondria ranges from 400 – 800 μM **(142, 65)**. The Fe^{2+} complex that composes this pool is selectively chelated when isolated mitochondria are treated with membrane-soluble 1,10-phenanthroline **(13)**. The same treatment inhibits ISC biosynthesis **(143,144,134)** suggesting that the Fe^{2+} complex is feedstock for ISC (and perhaps heme) biosynthesis **(53)**.

Size-exclusion chromatograms of low-molecular-mass (LMM) mitochondrial flow-through solutions (defined as solutions that pass through a 10 kDa cutoff membrane) from exponentially growing fermenting yeast cells exhibit a single iron-associated peak of mass ~ 580 Da **(53,14)**. The concentration of the so-called Fe_{580} complex is of the same order-of-magnitude as the NHHS Fe^{2+} pool, raising the intriguing possibility that this complex comprises the pool and is the iron-containing substrate for ISC and heme biosynthesis. Flow-through solutions from mammalian mitochondria contain Fe_{580} along with a few other LMM iron species **(14)**. Mitochondrial flow-through solutions from fermenting yeast cells harvested under stationary-state conditions exhibit a LMM iron species of mass ~ 1100 Da called Fe_{1100}. Anaerobic incubation of such flow-through solutions for a few days causes Fe_{1100} to disappear and Fe_{580} to appear; thus, the two species appear to be related **(14)**.

Deleting either *MRS3* or *MRS4* does not afford a growth phenotype, indicating that the two proteins possess redundant functions **(69,9)**. However, deleting both genes simultaneously results in a strain (called ΔΔ) that exhibits a slow-growth phenotype when grown in iron-deficient media. Mitochondria from iron-deficient ΔΔ cells contain low concentrations of hemes and ISC-containing enzymes **(9)**. ΔΔ cells in iron-sufficient medium grow at WT rates and exhibit normal activities of ISC-containing enzymes **(69,9,8,12)**. The molecular-level details of how such cells recover remain a puzzle.

A second puzzle is why ΔΔ cells grown under both iron-deficient and iron-sufficient conditions accumulate large amounts of iron relative to WT cells grown under the same conditions **(69,9,70)**. Such iron accumulation indicates that the *Iron Regulon* is activated and that cellular iron is dysregulated in ΔΔ cells. The iron regulon consists of 20 – 30 genes, including *MRS4*, that are involved in iron import, trafficking, and regulation. It is activated when WT cells are iron-starved (e.g. grown with the chelator bathophenanthroline disulfonate (BPS) in the medium) or in mutant cells in which mitochondrial ISC biosynthetic activity is defective **(67,68)**. In WT cells, the iron regulon is deactivated under iron-sufficient conditions whereas in ISC-mutant cells (e.g. *yfh1Δ*), it is activated *regardless of the concentration of iron in the medium* **(54)**. This results in a massive accumulation of Fe^{3+} phosphate oxyhydroxide nanoparticles in mitochondria.[22,23] Iron also accumulates in ΔΔ cells, but not in mitochondria, as the absence of Mrs3/4 impedes iron import into this organelle **(9,70)**. The iron concentration in ΔΔ mitochondria is reportedly ca. *half* of that in WT mitochondria **(9,70)**. The presence of iron in mitochondria from ΔΔ cells implies the existence of an alternative

iron import pathway that does not involve Mrs3/4. This pathway may involve Rim2 **(12,54,11)**.

Vacuoles are acidic organelles in yeast that store and sequester iron; they are another "hub" of iron trafficking and regulation. Ccc1 is the only known vacuolar iron importer of cytosolic iron **(21)**. In ΔΔ cells, the rate of vacuolar iron import through Ccc1 is greater than in WT cells, despite lower-than-WT concentrations of the Ccc1 protein **(70)**. Kaplan and co-workers concluded that Ccc1 *activity* is higher in ΔΔ cells than in WT cells due to a proposed signaling pathway between mitochondria and vacuoles that regulates Ccc1 activity **(70,73)**.

In this study, we examined ΔΔ cells using powerful biophysical and bioanalytical methods that allow in-depth characterization of iron content. These methods included Mössbauer (MB), EPR, and electronic absorption spectroscopies, as well as liquid chromatography linked to an online inductively coupled plasma mass spectrometer (LC-ICP-MS). These results help explain, on a molecular level, how iron-deficient Mrs3/4 ΔΔ cells recover in terms of growth and mitochondrial function when placed in iron-sufficient medium. They also suggest how iron might remain dysregulated in ΔΔ cells even under iron-sufficient conditions for which they grow at WT rates. Collectively, this study provides new insights into iron trafficking and regulation in eukaryotic cells.

Experimental Procedures

A gamma construct was designed to knockout *MRS3* in which 200 base pairs (bp) of the flanking 5' and 3' regions of the *MRS3* coding sequence were juxtaposed on

either side of a BamHI site in the polylinker of vector pRS403. The plasmid was linearized with BamHI and transformed into W303 (MAT alpha ade2-1 his3-1,15 leu2-3,112, trp1-1 ura3-1) selecting for histidine prototrophy. The correctness of the insertion was confirmed by colony PCR with primers (012302A 5' aggcgattaagttgggtaac) from the vector and 022314A (5' gcaatcattaagcaattgggcc) from the *MRS3* flanking region generating the expected product of 435 bp. In a second step, 200 bp of 5' and 3' flanking regions of MRS4 were juxtaposed on either side of a BamHI site in the polylinker of vector pRS405. The vector was linearized with BamHI and transformed into the Δmrs3 strain, selecting for leucine prototrophy. The correctness of the insertion was confirmed by colony PCR with primers 012302A from the vector and 122314B (5' tagttattgggtggcatatggg) from the MRS4 flanking region, generating the expected product of 247 bp.

The double ΔMrs3ΔMrs4 deletion strain (ΔΔ) was identified and further characterized phenotypically. Deletion of *MRS3* and *MRS4* was confirmed via PCR analysis. To confirm that iron homeostasis was perturbed, non-repressing ferric reductase activity was assessed using a soft agar overlay assay. Strains were streaked on YPAD agar with 50 μM copper added, incubated overnight, and then 0.8% soft agar containing 1 mM BPS and 1 mM ferric ammonium sulfate was overlaid. The red color due to the $Fe^{2+}(BPS)_3$ complex developed rapidly and was markedly enhanced in the ΔΔ strain compared with W303 parent or Δmrs3 and Δmrs4 single mutants.

WT and ΔΔ cells were grown on YPAD agar plates for 3 days at 30 °C. Cells were taken from plates and grown under respiring conditions in liquid minimal medium

containing 3% (v/v) glycerol, 1% (v/v) ethanol, 5 g/L ammonium sulfate, 1.7 g/L YNB, which lacked ammonium sulfate and copper sulfate, 100 mg/L leucine, 50 mg/L adenine hemisulfate dihydrate, 20 mg/L histidine, 20 mg/L uracil, 50 mg/L tryptophan, and 1 μM copper sulfate. A 40 mM stock solution of $^{57}Fe^{3+}$ citrate (pH ~5) was prepared as described[14] and added to the growth medium. For BPS-treated medium, BPS was added to a final concentration of 25 μM, followed by supplementation with 1 μM (final concentration) of $^{57}Fe^{3+}$ citrate.

Fifty mL and 1 L cell cultures were grown in baffled flasks at 30 °C with constant shaking. Cell growth was monitored by the optical density at 600 nm (OD_{600}). For all experiments, single colonies from YPAD plates were inoculated into 50 mL of minimal medium. 50 mL cultures were grown to OD_{600} = 0.8 and immediately transferred into 1 L of minimal medium. Growth was measured from the time of inoculation (t = 0) until cells reached stationary phase. Mutant and WT whole-cell samples were harvested at OD_{600} = 0.8 by centrifugation at 5000*g* for 5 min. Cells were washed 3× with unbuffered 1 mM EGTA and then 3× with distilled water. Cells were subsequently packed by centrifugation into EPR tubes and Mössbauer cups, and then frozen in liquid N_2 for later analysis.

To prepare mitochondrial samples, 1 L cell cultures (OD_{600}= 0.8) were used to inoculate 24 L of minimal medium in a custom-built iron-free glass/titanium bioreactor at 30 °C with O_2 gas bubbled through the medium (~1 L/min). Once OD_{600} = 0.8, they were harvested and mitochondria were isolated anaerobically in a refrigerated N_2-atmosphere glove box (MBraun, ~10 °C, ~ 5 ppm of O_2) as described **(146,147,14)**.

Isolated mitochondria were packed into EPR tubes or Mössbauer cups as above. For UV-Vis studies, mitochondrial samples were thawed anaerobically inside glove boxes and loaded into 2 mm path-length custom quartz cuvettes (NSG Precision Cells, Inc.) as described **(66)**.

Metal concentrations of whole cells or mitochondria were analyzed by ICP-MS (Agilent Model 7700x). After collecting Mössbauer spectra, samples were thawed and packed into EPR tubes to measure sample volumes (ca. 200 – 300 μL). Samples were then diluted with 250 μL of high purity double-distilled-and-deionized water generated using a Teflon sub-boiling still (Savillex DST-1000). Fifty, 75, and 100 μL aliquots from the resulting suspensions were transferred to 15 mL screw-top polypropylene Falcon tubes, digested with 250 μL of concentrated trace-metal-grade nitric acid, and heated ~16 hr at 90 $^{\circ}$C. Digested samples were diluted with high purity double-distilled-and-deionized H_2O to a final volume of 8.0 mL. Reported metal concentrations of whole cells and mitochondria were calibrated as described **(14)** and corrected using packing efficiencies of 0.70 for whole cells and 0.77 for mitochondria **(50)**.

For electronic absorption experiments, solutions of isolated mitochondria were packed under anaerobic conditions into EPR tubes by centrifugation, and the volume of packed organelles in each sample was determined. Packed mitochondria were diluted 1:1 with SH buffer (0.6 M sorbitol, 20 mM HEPES, pH= 7.4) and transferred into cuvettes. Cuvettes were sealed with a rubber septum, removed from the glove box, and spectra were obtained at RT using a Hitachi U-3310 spectrometer with a Head-on photomultiplier tube. Mössbauer spectra were obtained using an MS4 WRC

spectrometer (SEE Co., Edina, MN), simulated with WMOSS software, and calibrated at RT with α-iron foil **(50)**. Applied magnetic fields were parallel relative to the γ-radiation. EPR spectra were collected using an X-band Elexsys spectrometer (Bruker Biospin Corp., Billerica, MA).

For LC-ICP-MS experiments, mitochondrial samples were manipulated anaerobically in refrigerated N_2 atmosphere glove boxes. Isolated mitochondria were washed twice with 20 mM ammonium bicarbonate pH 8.5 and solubilized with 2% (w/v) Triton X-100 in the same buffer. The resulting suspension was vortexed for 20 min, followed by centrifugation at 12000*g* for 15 min. The soluble mitochondrial extract was passed through a 10 kDa cutoff membrane in an Amicon stirred cell concentrator, and then the flow-through solution was injected onto two Superdex peptide 10/300GL columns (GE Healthcare Life Sciences) connected in series and equilibrated with 20 mM ammonium bicarbonate pH 8.5. Buffer was pumped through the columns at a flow rate of 0.350 mL/min for 166 min using an Agilent Bioinert HPLC (Tokyo, Japan). Chromatograms were acquired and analyzed, and columns were calibrated and cleaned as described **(14)**.

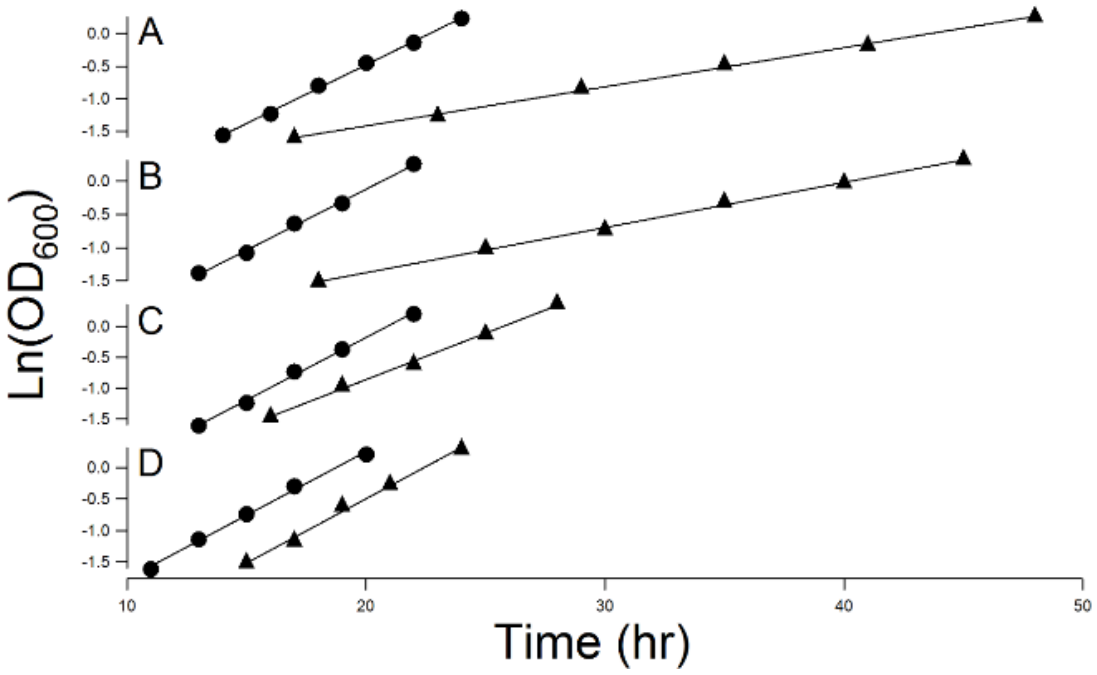

Figure 4.1: Growth rates of WT (circles) and ΔΔ (triangles) cells. A, $WT1_{BPS}$ and $\Delta\Delta1_{BPS}$; B, WT1 and ΔΔ1; C, WT10 and ΔΔ10; D, WT40 and ΔΔ40. Growth rates α in units of hr^{-1} (Table 1) are the slopes of the plotted lines.

Results

The Slow-Growth Phenotype of ΔΔ cells.

ΔΔ and WT cells were grown in minimal medium containing 1, 10, or 40 μM $^{57}Fe^{3+}$ citrate. Some batches containing 1 μM $^{57}Fe^{3+}$ citrate were pre-treated with BPS to chelate endogenous iron and increase iron deficiency. We will refer to these cells as *ΔΔ1* and *WT1*, *ΔΔ10* and *WT10*, *ΔΔ40* and *WT40*, and $\Delta\Delta1_{BPS}$ and $WT1_{BPS}$, respectively. The numbers refer to the concentration of nutrient ^{57}Fe (in μM) in the medium and BPS indicates the presence of the chelator. ^{57}Fe was added to BPS-treated media to enrich

cells with this Mössbauer-active isotope. Glycerol/ethanol was exclusively used as the carbon source to force the cells to respire. Cells were harvested while growing exponentially. Exponential growth rates (α) were defined as the slopes of $\ln(OD_{600})$ vs. time plots.

Under iron-deficient conditions, $\Delta\Delta$ cells grew substantially slower than WT cells, whereas under iron-sufficient conditions, they grew at WT rates (Fig. 1 and Table 1). Thus, the slow-growth phenotype of $\Delta\Delta$ cells recovered as the iron concentration of the growth medium increased.

Table 4.1. Iron concentrations and iron-containing species in whole cells. Concentrations are in μM. Iron concentrations and growth rates are averages of two independent experiments. Simulation parameters were (δ, ΔE_Q, and Γ units in mm/s): NHHS Fe^{3+} sextet in ΔΔ spectra; δ = 0.54 ± 0.05, ΔE_Q = 0.62 ± 0.08, D = 0.3 ± 0.1 cm^{-1}, E/D = 0.29 ± 0.02, η =1.5 ± 1, A_{iso} = -220 ± 8 kG, and Γ = 0.8 ± 0.2; NHHS Fe^{3+} sextet in WT spectra: δ = 0.56 ± 0.03, ΔE_Q = 0.42 ± 0.05, D = 0.5 cm^{-1}, E/D = 0.33 ± 0.01, η =1.8 ± 0.5, A_{iso} = -228 ± 3 kG, and Γ = 0.4; CD: δ = 0.45 ± 0.01, ΔE_Q = 1.11 ± 0.05, and Γ = 0.50 ± 0.15; NHHS Fe^{2+} doublet: δ = 1.23 ± 0.06, ΔE_Q = 3.07 ± 0.17, and Γ = 0.59 ± 0.16; high spin Fe^{2+} Heme Doublet: δ = 0.87 ±0.11, ΔE_Q = 2.22 ± 0.04, and Γ= 0.49 ± 0.19; $[Fe_2S_2]^{2+}$ Doublet: δ = 0.30 ± 0.04, ΔE_Q = 0.44 ± 0.07, and Γ = 0.48 ± 0.19; Fe^{3+} nanoparticles: δ = 0.50 ± 0.05, ΔE_Q = 0.50 ± 0.06, and Γ = 0.4 ± 0.04. The sum of all percentages of Mössbauer components was forced to equal 100%; however, 10% - 15% of spectral intensities were typically unaccounted for by these components.

Sample	Growth Rate α	[Fecell]	Sextet from High-Spin Fe3+ mainly in vacuoles		Doublet due to [Fe4S4]2+ clusters and Low-Spin Fe2+ hemes in mito. and cyt.		Doublet due to NHHS Fe2+ pools in cytosol, mitochondria, and/or vacuoles		Doublet due to High-Spin Fe2+ Hemes in mitochondria and cytosol		Doublet due to [Fe2S2]2+ clusters mainly in mitochondria		Doublet due to Fe3+ nano-particles in mitochondria, vacuoles, and or cytosol	
	hr-1	[μM]	%	[μM]	%	[μM]	%	[μM]	%	[μM]	%	[μM]	%	[μM]
WT1BPS	0.181	120 ± 20	0	0	69	84	12	14	12	14	7	8		---
WT1	0.184	200 ± 20	39	78	39	78	10	20	4	8	8	16		---
WT10	0.203	480 ± 30	39	190	39	190	11	50	5	20	6	30		---
WT40	0.202	880 ± 70	52	460	25	220	8	70	6	50	9	80		---
ΔΔ1BPS	0.060	360 ± 30	11	40	25	90	47	170	6	20	---	---	11	40
ΔΔ1	0.068	680 ± 70	50	340	16	110	20	140	3	20	---	---	11	70
ΔΔ10	0.150	2160 ± 60	50	1080	9	190	5	110	5	110	---	---	31	670
ΔΔ40	0.204	3920 ± 80	57	2230	4	160	3	120	3	120	---	---	33	1290

Iron concentrations in ΔΔ cells

We determined the absolute iron concentration in ΔΔ and WT cells ($[Fe_{cell}]$) to help quantify the iron-dependent growth phenotype. These determinations are more difficult than measuring the ratio of iron concentration divided by protein concentration, as is typically reported. To determine absolute concentrations, known volumes of packed cells must be quantitatively transferred, dilution factors must be carefully measured, and packing efficiencies need to be measured and included in calculations **(146)**. However, absolute concentrations once determined allow a more in-depth analysis than is possible using concentration ratios.

Table 4.2. Iron concentrations and components in isolated mitochondria. Data are from a single preparation for each strain and condition. Other conditions are described in Table 1.

Sample	[Femit]	Sextet: NHHS Fe^{3+}		Central Doublet: $[Fe_4S_4]^{2+}$ clusters and Low-Spin Fe^{2+} hemes		Doublet: NHHS Fe^{2+}		Doublet: high-spin Fe^{2+} hemes		Doublet: $[Fe_2S_2]^{2+}$ clusters		Doublet: Fe^{3+} nanoparticles	
	[μM]	%	[μM]	%	[μM]	%	[μM]	%	[μM]	%	[μM]	%	[μM]
WT1	430	15	60	42	180	18	80	4	20	21	90	---	---
WT40	690	0	0	57	390	30	210	2	10	11	80	---	---
ΔΔ1	690	9	60	6	40	8	60	---	---	---	---	77	530
ΔΔ40	740	0	0	63	475	15	110	11	80	---	---	10	75

[Fe_{cell}] in ΔΔ cells was substantially higher than in WT cells grown on the same medium (Table 1). This iron-overload phenotype was observed for all nutrient conditions examined, including those for which the growth rate of ΔΔ cells matched that of WT cells. The iron content of isolated mitochondria was also determined (Table 2). Isolated ΔΔ mitochondria were not iron-overloaded relative to the huge accumulation observed in ISC mutant cells **(145,51)**. This indicates that the excess iron in ΔΔ cells accumulates in *non-mitochondrial* locations such as vacuoles and/or cytosol.

The massive accumulation of iron in ΔΔ cells suggests that the iron regulon is activated *under both iron-deficient and iron-sufficient conditions*. Ironically, iron-overloaded ΔΔ cells "feel" iron deficient. To explain how the iron regulon might be

active in ΔΔ cells under iron-sufficient conditions, we reasoned that the vast majority of accumulated iron must not be "sensed" by the cell or be part of the iron regulation mechanism. We further reasoned that the concentration of the sensed species in iron-sufficient ΔΔ cells, whatever it is, must be *below* its "set-point" concentration. One objective of this study was to identify iron-containing species present at sub-WT concentrations in ΔΔ cells under all growth conditions; this species might sense iron status and be used in cellular iron regulation.

Mössbauer (MB) spectra of whole cells and isolated mitochondria

We turned to MB spectroscopy to determine the forms of iron that accumulated in ΔΔ cells. The low-temperature low-field MB spectrum of $WT1_{BPS}$ cells was dominated by the *Central Doublet* (CD) (Fig. 2B, simulated by the green line). The CD arises from $[Fe_4S_4]^{2+}$ clusters and low-spin Fe^{2+} hemes; the two types of centers cannot be resolved by MB spectroscopy **(147)**.

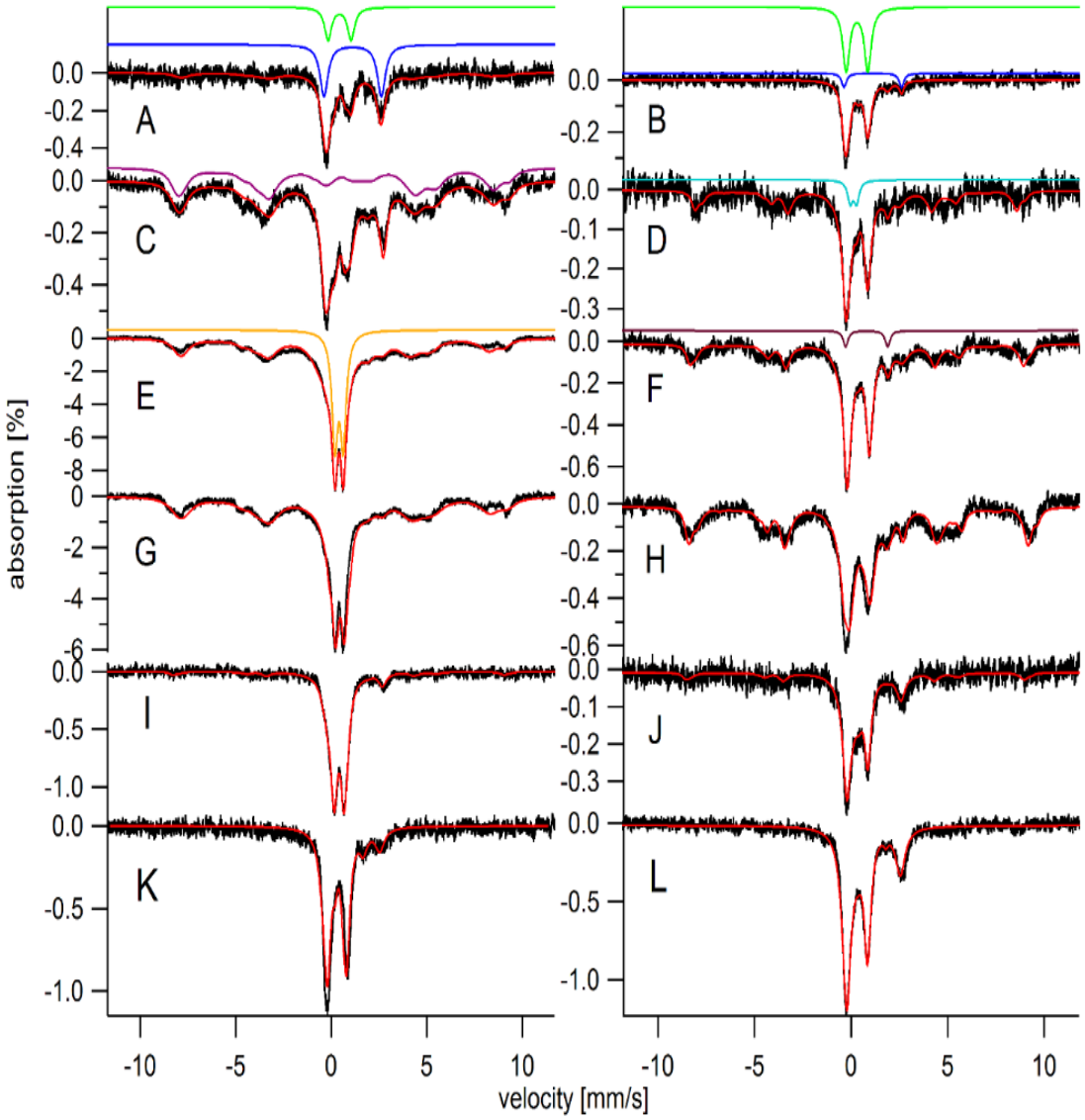

Figure 4.2: Mössbauer spectra of whole cells (A – H) and isolated mitochondria (I – L). A, $\Delta\Delta1_{BPS}$; B, $WT1_{BPS}$; C, $\Delta\Delta1$; D, WT1; E, $\Delta\Delta10$; F, WT10; G, $\Delta\Delta40$; H, WT40; I, $\Delta\Delta1$; J, WT1; K, $\Delta\Delta40$; L, WT40. Solid lines are simulations for the Central Doublet (green), NHHS Fe^{2+} doublet (blue), vacuolar high spin Fe^{3+} sextet (purple), Fe^{3+} oxyhydroxide nanoparticles (gold), $[Fe_2S_2]^{2+}$ doublet (teal), and high spin Fe^{2+} heme doublet (brown). The temperature was 5 K and a field of 0.05 T was applied parallel to the gamma rays. The solid red lines are composite simulations assuming the area percentages listed in Tables 1 and 2.

A minor quadrupole doublet with parameters typical of NHHS Fe^{2+} was also evident; this feature is simulated by the blue line. All components and parameters used in simulations are listed in Table 1. MB spectra of respiring mitochondria are dominated by the CD. This feature dominates because respiratory complexes and respiration-related proteins (e.g. aconitase and cytochrome c) contain numerous ISCs and heme centers, and these complexes are highly expressed in respiring cells **(142)**. Fe_2S_2 clusters are also prevalent in respiring mitochondria; they contribute a shoulder on the CD **(65)**.

We have previously assumed that *all* of the CD intensity in whole-cell MB spectra arose from *mitochondrial* ISCs and low spin Fe^{2+} hemes **(13)**. However, non-mitochondrial $[Fe_4S_4]^{2+}$ clusters, assembled by the CIA (cytosolic iron-sulfur cluster assembly system) **(67,68)** *must* contribute to the CD in whole-cell MB spectra – the only issue is how much. Our current MB spectra suggest that they contribute a quarter to a half of the overall CD intensity in the $WT1_{BPS}$ spectrum. A proportion of this magnitude is required to explain the presence of central-doublet-like intensity in the MB spectra of iron-deficient ΔΔ cells (Fig. 2, A and C) even though the spectra of iron-deficient ΔΔ mitochondria (see later) are largely devoid of the CD. We have included formation of cytosolic ISCs in the summary mechanistic model of Fig. 3. CIA activity is reduced in ΔΔ cells under iron-deficient conditions **(9)** suggesting that this activity is related to the *severity* of iron-deficiency. The stronger-than-expected CD doublet in the MB spectra of our iron-deficient cells may be due to the inclusion of 1 μM ^{57}Fe in the medium which may have been sufficient for normal CIA activity.

That a significant portion of the CD intensity in the $WT1_{BPS}$ and $\Delta\Delta1_{BPS}$ spectra is due to cytosolic $[Fe_4S_4]^{2+}$ clusters is also consistent with the distribution of ISCs in human cells **(148)**. Human cells contain ~70 proteins housing $[Fe_4S_4]^{2+}$ and/or $[Fe_2S_2]^{2+}$ clusters. If each ISC-containing protein were expressed at the same level (and if the distribution in human and yeast were similar), we calculate from published data **(148)** that ~40% of the iron associated with such clusters should be located in mitochondria, and ~60% in the cytosol and nucleus (combined). Although our assumptions may not be strictly correct, the calculated 40:60 distribution is remarkably similar to that needed to interpret our MB spectra.

The MB spectrum of $\Delta\Delta1_{BPS}$ cells (Fig. 2A) was dominated by the same two doublets, albeit with different relative intensities. On a percentagewise basis, the CD was about a third as intense as it was in the $WT1_{BPS}$ spectrum (Table 1). However, similar CD concentrations are suggested based on absolute iron concentrations. In such cases of apparent discrepancy, we rely in our analysis more heavily on percentage differences, since fitting MB spectra has fewer sources of error relative to absolute concentration determinations.

Since the MB spectrum of $\Delta\Delta1$ mitochondria (Fig. 2I) was largely devoid of the CD, we conclude that most ISCs exhibited by the $\Delta\Delta1_{BPS}$ whole-cell spectrum are non-mitochondrial. The model of Fig. 3 suggests that the absence of Mrs3/4 should cause NHHS Fe^{2+} species to accumulate in the cytosol of $\Delta\Delta1_{BPS}$ cells and cause greater-than-WT rates of cytosolic ISC production. The same blockage would cause a deficiency of ISCs and hemes within mitochondria.

The MB spectrum of WT1 cells (Fig. 2D) exhibited two major features, including the CD and a sextet due to vacuolar NHHS Fe^{3+} **(149)**. More intense sextets are evident in the spectrum of WT10 and WT40 cells (Fig. 2, F and H). This component is simulated by the purple line above the spectrum of Fig. 2C. Confirming earlier reports **(65)**, the MB spectrum of mitochondria isolated from WT1 cells (Fig. 2J) was dominated by the CD. As mentioned above, we assumed that about half of the CD in the whole-cell WT1 spectrum originates from ISCs in mitochondria and half from ISCs in the cytosol (and nucleus). The MB spectrum of WT1 cells also exhibited a NHHS Fe^{2+} doublet and a minor sextet suggesting a small amount of NHHS Fe^{3+} in WT1 mitochondria. Previous spectra of iron-deficient WT mitochondria also included a semi-resolved doublet due to $[Fe_2S_2]^{2+}$ clusters **(65)**. Such a doublet (simulated by the solid teal line) fits nicely into this spectrum.

The MB spectrum of ΔΔ1 cells (Fig. 2C) was dominated by an intense NHHS Fe^{3+} sextet, indicating that the vacuoles are essentially filled with iron under these conditions. On a percentagewise basis, the intensity of the CD in the ΔΔ1 spectrum was 2.4-times *lower* than in the WT1 spectrum, while that of the NHHS Fe^{2+} doublet was 2 times higher. Again, comparison of absolute concentrations differed slightly, with the CD concentration in both ΔΔ1 and WT1 cells similar (and that of the NHHS Fe^{2+} doublet for ΔΔ1 cells 7 times higher than in WT1 cells). According to the model of Fig. 3, cytosolic iron should accumulate in ΔΔ1 cells at the expense of mitochondrial ISCs. Higher-than-normal concentrations of cytosolic iron would also be expected to stimulate iron import into the vacuoles, (and stimulate cytosolic ISC production) consistent with

the spectrum. The central region of the ΔΔ1 spectrum was poorly resolved, but the absorption that remained after removing known features was a doublet with parameters typical of Fe^{3+} oxyhydroxide nanoparticles.

The MB spectrum of mitochondria isolated from ΔΔ1 cells also exhibited a doublet due to such nanoparticles (Fig. 2I). A low-intensity NHHS Fe^{2+} doublet was also present *but no CD was evident*. This indicates that few $[Fe_4S_4]^{2+}$ clusters and/or low spin Fe^{2+} hemes were present in ΔΔ1 mitochondria, and it suggests that most of the CD in the ΔΔ1 whole-cell MB spectrum (Fig. 2C) was due to non-mitochondrial ISCs assembled by the CIA. Similarly, the strong intensity of the NHHS Fe^{2+} doublet in the ΔΔ1 whole-cell spectrum is incompatible with NHHS Fe^{2+} species being located in ΔΔ1 mitochondria (too little is present in the mitochondria spectrum for this species to make a significant contribution to the NHHS Fe^{2+} doublet in the whole-cell spectrum).

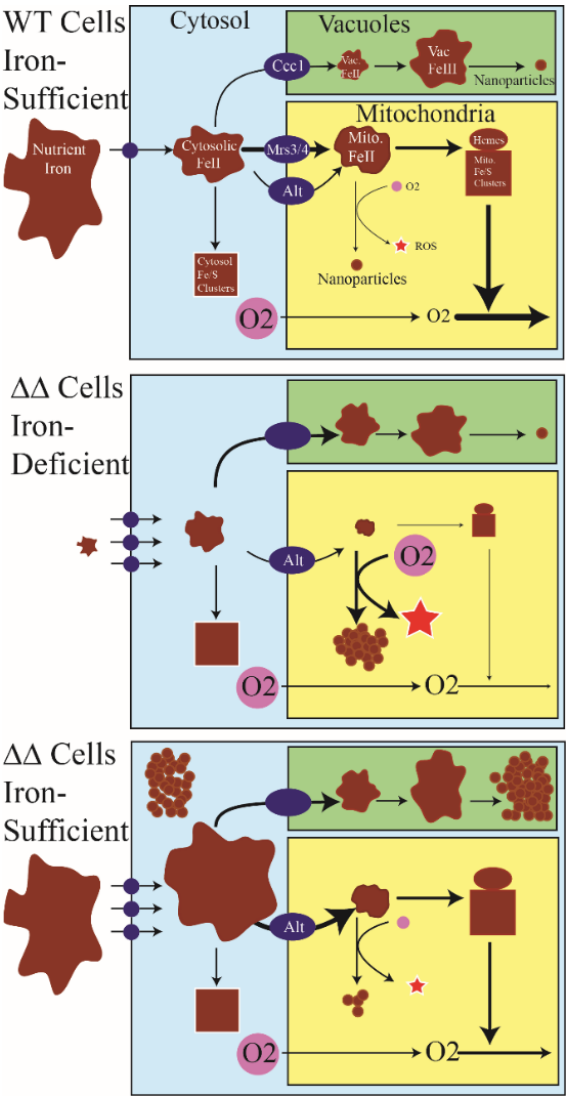

Figure 4.3: The Mrs3/4ΔΔ phenotype. Nutrient iron enters the cell and becomes cytosolic Fe^{2+}. Cytosolic Fe^{2+} can enter vacuoles where most of vacuolar Fe^{2+} oxidizes to Fe^{3+}. In WT cells, a small portion converts into nanoparticles. Some cytosolic Fe^{2+} converts into cytosolic $[Fe_4S_4]^{2+}$ clusters. The remaining cytosolic Fe^{2+} enters WT mitochondria through the Mrs3/4 import pathway and through a slow alternative pathway, where it becomes the mitochondrial Fe^{2+} pool. Cytosolic Fe^{2+} can only enter ΔΔ mitochondria through the alternative pathway. Mitochondrial Fe^{2+} is feedstock for the biosynthesis of ISCs and heme centers, the majority of which are installed in respiratory complexes which catalyze the reduction of O_2 to water. O_2 is constantly diffusing into the matrix. In healthy WT cells, the activity of the respiratory complexes is sufficiently high to prevent O_2 from diffusing in, but in iron-deficient ΔΔ cells, the activity is too low to prevent penetration. In that case, O_2 reacts with the Fe^{2+} pool to generate mitochondrial nanoparticles. The cell responds by increasing the expression of iron importers on the plasma membrane. Under iron-sufficient conditions, cytosolic Fe^{2+} concentration is high, allowing sufficient iron to enter mitochondria and generate sufficient respiration activity to re-establish anaerobic conditions in the matrix. However, the size of the mitochondrial Fe^{2+} pool remains sub-normal such that the iron regulon remains activated.

These results again support the model of Fig. 3 in which iron accumulates in the cytosol of ΔΔ1 cells; the unusually high cytosolic iron concentration should increase the rate of iron import into vacuoles, and indeed the concentration of vacuolar Fe^{3+} in ΔΔ1 cells is 4-times that for WT1 cells. Most iron in ΔΔ1 mitochondria are present as Fe^{3+} nanoparticles. The presence of some CD intensity in the whole-cell ΔΔ1 MB spectrum suggests that cytosolic ISC assembly is functioning in ΔΔ mutant cells grown under our iron-deficient conditions. Although ΔΔ1 cells were iron-overloaded relative to WT1 cells, ΔΔ1 mitochondria contained about the same concentration of iron as in WT1 mitochondria. Thus, the excess iron that flowed into ΔΔ1cells did not localize to the mitochondria but rather remained in the cytosol or flowed into vacuoles.

The WT10 cell spectrum (Fig. 2F) was dominated by the CD and the Fe^{3+} sextet; minor doublets due to high spin Fe^{2+} hemes and NHHS Fe^{2+} species were also evident. The corresponding ΔΔ10 whole-cell spectrum (Fig. 2E) was far more intense, reflecting a higher iron concentration in the cell (Table 1). The spectrum was dominated by the Fe^{3+} sextet and nanoparticle doublet. The composite simulation of the ΔΔ10 spectrum included intensity due to the CD, but this doublet was not resolved which made quantification difficult.

The MB spectrum of WT40 cells (Fig. 2H) was similar to that of WT10 cells, except that the sextet was more intense and the CD was poorly resolved. The spectrum of mitochondria isolated from WT40 cells (Fig. 2L) exhibited a strong CD and NHHS Fe^{2+} doublet. The spectrum is generally consistent with previous reports, but the NHHS

Fe^{2+} doublet is more intense than in previous MB of *respiring* mitochondria **(13,142)**. We previously reported that the size of the NHHS Fe^{2+} pool was smaller in respiring WT mitochondria than in the organelle from fermenting WT cells; however, the intensity of the NHHS Fe^{2+} doublet in spectra of recently prepared mitochondria from respiring WT cells is similar to that from fermenting cells.

The MB spectrum of ΔΔ40 cells (Fig. 2G) was nearly identical to that of ΔΔ10 cells, again indicating the accumulation of nanoparticles and NHHS Fe^{3+}. Surprisingly, the spectrum of ΔΔ40 mitochondria (Fig. 2K) was devoid of nanoparticles but rather exhibited an intense CD. Thus, the nanoparticles and NHHS Fe^{3+} in ΔΔ40 whole cells must be in a non-mitochondrial location. The spectrum of ΔΔ40 mitochondria also exhibited significant intensity due to the NHHS Fe^{2+} pool (and perhaps some high spin Fe^{2+} hemes), but it was only about half as intense as in the WT40 mitochondria spectrum (Fig. 2L). We conclude that *ΔΔ40 mitochondria* have returned to a "healthy" state (at least from an iron-centric perspective). On the other hand, ΔΔ40 *cells* accumulated excessive iron, implying that the iron regulon was activated even though ΔΔ40 mitochondria exhibited a CD with roughly the same intensity as in WT mitochondria. This was unexpected because the iron regulon is regulated by the ISC activity in mitochondria **(67,68)**. Here, the ISC level is near normal yet the iron regulon appears to be activated.

We hypothesize that the slow-growth phenotype of ΔΔ1 cells is due to the absence of respiratory complexes in mitochondria and that the WT growth rate of ΔΔ40 cells is due to their presence. How this transformation occurs simply by increasing the

nutrient iron concentration is puzzling, as is the reason why the cells continue to be iron dysregulated even though ISC levels are largely recovered. We investigated these issues further using electronic absorption and EPR spectroscopies.

Electronic absorption and EPR spectra

Mitochondria isolated from WT1 and WT40 cells exhibited Soret bands at ~ 400 nm and α and β bands between ca. 500 – 600 nm (Fig. 4, A and C, respectively). These features are characteristic of cytochromes *a*, *b* and *c*. Mitochondria isolated from ΔΔ40 cells exhibited similar features (Fig. 4D), albeit with about half of WT intensity.

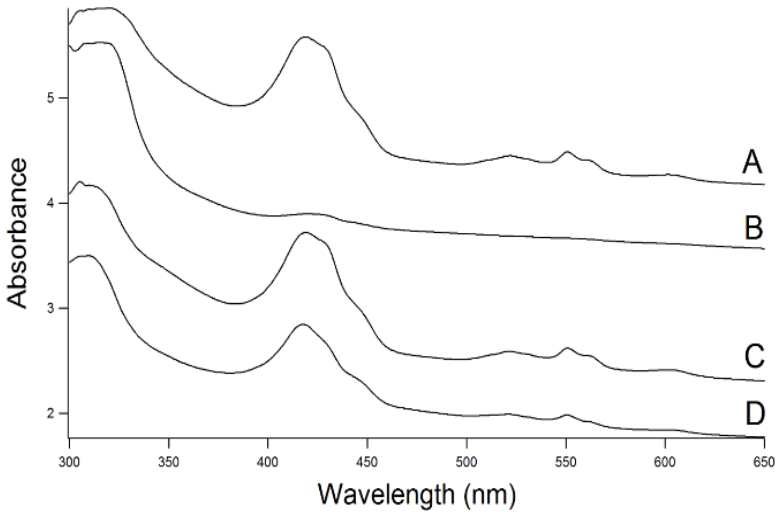

Figure 4.4: Electronic absorption spectra of isolated mitochondrial suspensions. Mitochondria were isolated anaerobically from A, WT1; B, ΔΔ1; C, WT40; and D, ΔΔ40 cells. Packed mitochondria were diluted 1:1 with buffer, transferred to a 2 mm pathlength quartz cuvette, sealed with a stopper, removed from the box, and spectra were collected. We estimate a protein concentration of ca. 80 mg/mL in the sample based on previous results.[13] Spectra have been offset for viewing.

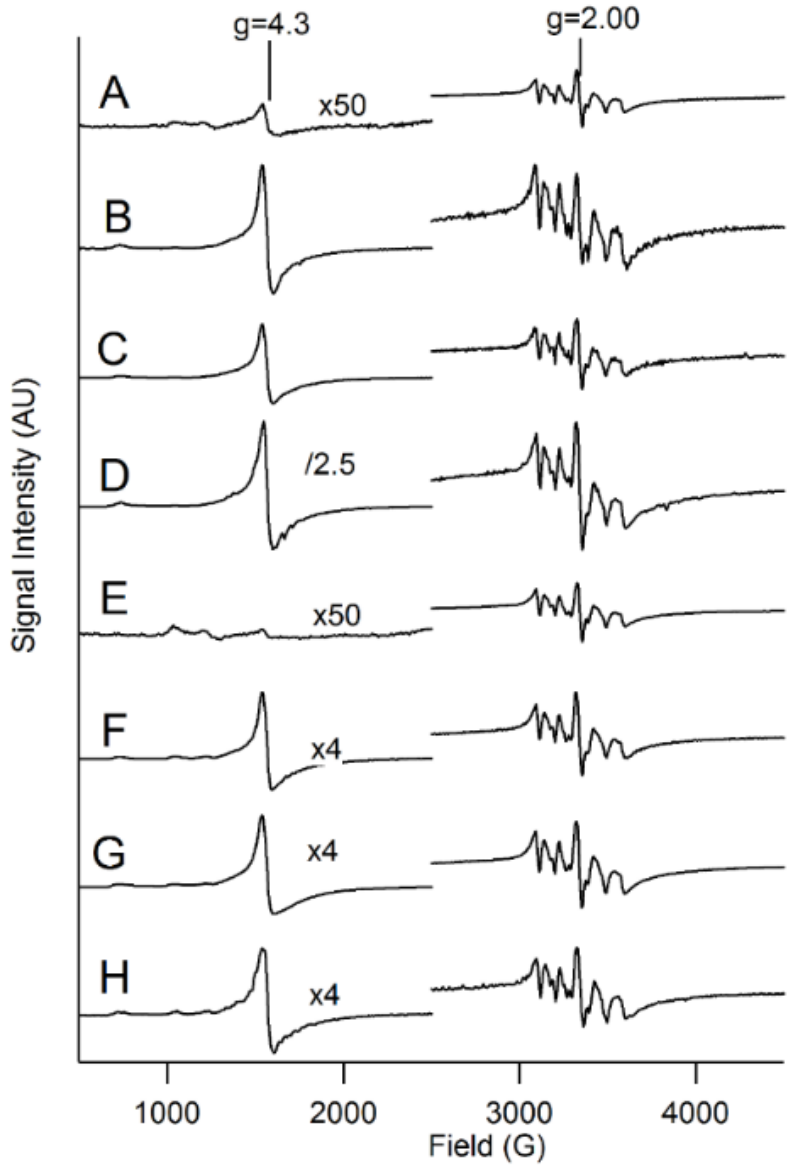

Figure 4.5: EPR spectra of ΔΔ (A – B) and WT (E - H) cells. A, $\Delta\Delta1_{BPS}$; B, ΔΔ1; C, ΔΔ10; D, ΔΔ40; E, $WT1_{BPS}$; F, WT1; G, WT10, and H, WT40. Temperature in A, C, E, and G were 10 K while that in others was 4.2 K; intensities were temperature-adjusted to allow comparisons. Other parameters: average microwave frequency, 9.373 ± 0.003 GHz; microwave power, 0.2 mW; modulation amplitude, 10 G; Gain, 1000; conversion time, 0.3 sec. Displayed intensities on the left were adjusted as indicated for ease of viewing. None of the spectra on the right side was adjusted

Mitochondria from ΔΔ1cells (Fig. 4B) were devoid of such features. This indicates that hemes were not synthesized by ΔΔ cells grown under iron-limited conditions, but *were* synthesized by such cells under iron-sufficient conditions. Low-temperature X-band EPR spectra of ΔΔ and WT whole cells (Fig. 5) were dominated in the g = 2 region by a hyperfine split signal due to mononuclear S = 5/2 Mn^{2+} species. This signal has been observed previously in spectra of yeast cells **(65)**, and was found to arise from most of the Mn in the cell (quantified here at ~ 30 μM, see Table 3). The presence or absence of Mrs3/4 did not influence the shape or intensity of that signal, consistent with the absence of an observed effect of Mrs3/4 deletion on cellular Mn concentration.

Table 4.3. Copper, manganese, and zinc concentrations in ΔΔ and WT cells and isolated mitochondria. Details as in Table 2.

Sample	[Copper], µM		[Manganese], µM		[Zinc], µM	
	cell	mito	cell	mito	Cell	mito
WT1BPS	120 ± 10	---	21 ± 4	---	310 ± 65	---
WT1	140 ± 20	110	24 ± 6	22	300 ± 20	250
WT10	130 ± 10	---	29 ± 3	---	315 ± 60	---
WT40	140 ± 20	89	31 ± 11	27	330 ± 60	320
WT Ave	130 ± 8	100 ± 15	26 ± 5	24 ± 4	310 ± 10	280 ± 50
ΔΔ1BPS	290 ± 10	---	32 ± 5	---	240 ± 45	---
ΔΔ1	280 ± 30	63	25 ± 14	31	200 ± 50	180
ΔΔ10	320 ± 40	---	39 ± 8	---	190 ± 30	---
ΔΔ40	320 ± 10	48	29 ± 7	34	250 ± 25	210
ΔΔ Ave	300 ± 20	56 ± 11	31 ± 6	32 ± 2	220 ± 30	200 ± 20

Overlapping the Mn-based signal in all spectra was an isotropic S = ½ signal at g = 2.00. This signal was not assigned to a particular radical species, as there were too many candidates. Surprisingly, no g = 1.94 type signals from S = ½ $[Fe_2S_2]^{1+}$ or $[Fe_4S_4]^{1+}$ clusters were observed. Along with our MB spectra, this demonstrates that *the vast majority of such clusters in whole yeast cells are in the oxidized S = 0* $[Fe_2S_2]^{2+}$ *and* $[Fe_4S_4]^{2+}$ *states*. Similarly, there were no EPR signals from low-spin Fe^{3+} hemes, suggesting that the majority of such centers in exponentially growing cells are in the Fe^{2+} state. Some WT EPR spectra exhibited low-intensity signals between g = 4 - 6 (weak features between 1000 – 1300 G in Fig. 5) which probably arise from cytochrome c oxidase **(147)**.

The most prominent signal in the low-field region was at g = 4.3 arising from high-spin S = 5/2 Fe^{3+} species with a rhombicity parameter E/D ~ 1/3. This signal arises from vacuolar Fe^{3+}**(149)**. Its intensity in WT cells increased as nutrient iron increased, consistent with increasing amounts of cellular iron being stored in vacuoles. The intensity of the g = 4.3 signal exhibited by ΔΔ cells was substantially higher than in spectra from comparable WT cells, consistent with the differences observed by MB. The intensity of the g = 4.3 signal from ΔΔ40 cells was defined as 100%. The average intensities of the g = 4.3 signal from $\Delta\Delta1_{BPS}$, ΔΔ1, and ΔΔ10 cells were 2%, 34%, and 53%, respectively. For comparison, the intensities of the same signal in $WT1_{BPS}$, WT1, WT10, and WT40 cells were lower (0%, 9%, 8%, and 14%, respectively). We conclude that ΔΔ cells contain substantially more vacuolar Fe^{3+} than in comparable WT cells, consistent with our MB analysis (Table 1).

LC-ICP-MS of Mitochondrial Flow-Through-Solutions

We initially hypothesized that the Fe_{580} complex passes intact from the cytosol through Mrs3/4 and into the matrix. Thus, we expected to observe Fe_{580} in flow-through solutions of WT1 and WT40 mitochondria, but not in ΔΔ1 or ΔΔ40 mitochondria samples. Fe_{580} was indeed observed in flow-through solutions of WT1 and WT40 mitochondrial extracts (Fig. 6, top panel, A and D), and not in ΔΔ1 extracts (Fig. 6, top panel, B; two independent trials are shown). Unexpectedly, Fe_{580} was also observed in the ΔΔ40 trace (Fig. 6, top panel, C), albeit with a lower intensity than in the WT40 trace sample, indicating a lower concentration. Quantification of areas indicates an [Fe_{580}] concentration of 180 μM in WT40 mitochondria and 100 μM in ΔΔ40 mitochondria. The presence of Fe_{580} in ΔΔ40 mitochondria supports the idea that ΔΔ40 mitochondria have recovered under iron-sufficient conditions and are "healthy" from an iron perspective. The trace of the ΔΔ1 flow-through solution exhibited two weak LMM iron peaks, at 2700 and 2100 Da. These species were not investigated further.

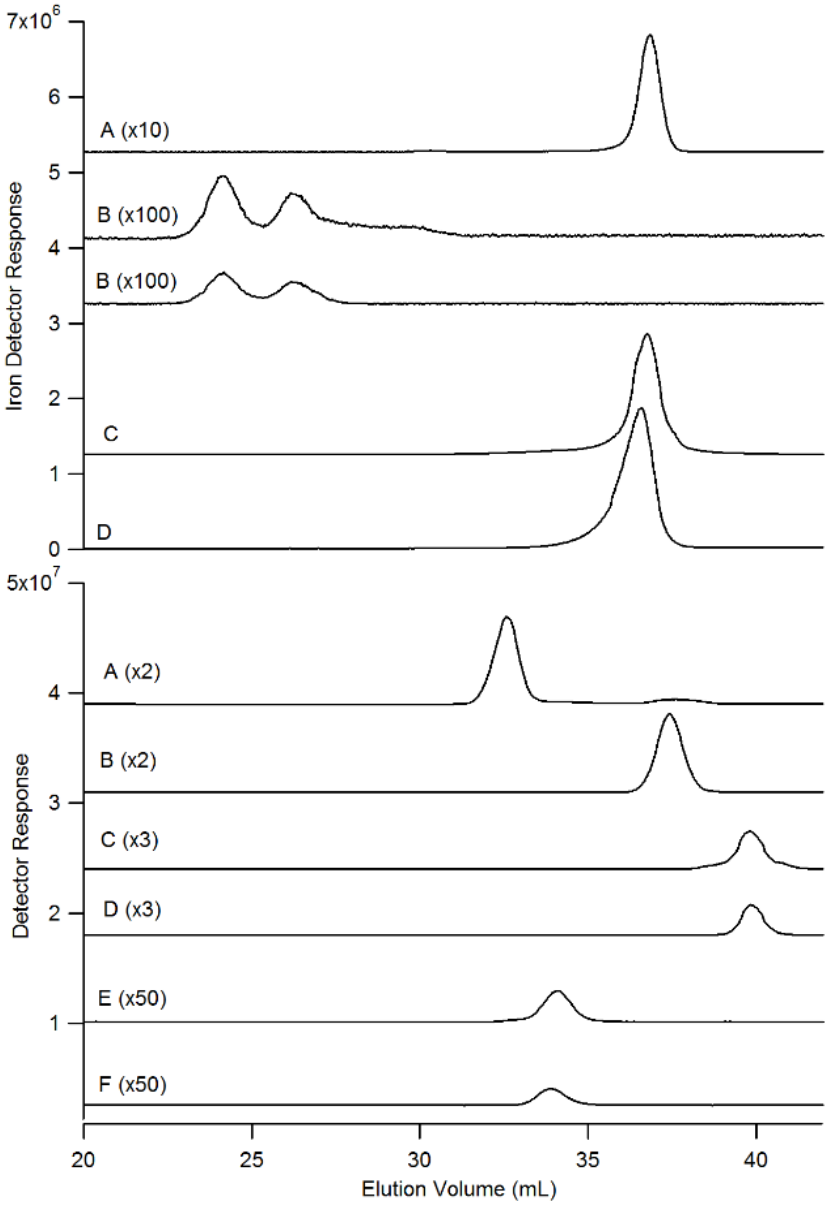

Figure 4.6: LC-ICP-MS chromatograms of LMM flow-through solutions prepared from the soluble fractions of WT and ΔΔ mitochondrial detergent extracts. Top panel, ^{56}Fe detection: A, WT1; B, ΔΔ1 (replicate runs); C, ΔΔ40; D, WT40. Trace intensities were adjusted as indicated for ease of viewing. Bottom panel, ^{56}Fe (A and B), ^{34}S (C and D), and ^{31}P (E and F) detection of flow-through solutions from mitochondria harvested from WT40 cells harvested as cells were transitioning to stationary state: Traces A, C, and E were fresh, while traces B, D, and F were after 5-day incubation in a refrigerated glove box.

Relationship of Fe_{1100} to Fe_{580}

Mitochondrial extracts from fermenting yeast harvested at or near stationary-state contain an iron species called Fe_{1100} **(14)**. This species converts into Fe_{580} in mitochondrial extracts that are allowed to sit in a refrigerated anaerobic glove box for 5 days. The same phenomenon occurred in our current studies involving respiring yeast cells. One batch was harvested at OD_{600} = 1.0 (typically we harvest at OD_{600} = 0.8). The higher OD suggests that cells were transitioning from exponential to stationary state when they were harvested. The resulting LC-ICP-MS trace of the flow-through solution from mitochondria isolated from these cells was dominated by Fe_{1100} (Fig. 6, lower panel, A); some minor Fe_{580} intensity is evident. After 5 days in a refrigerated box, the same solution exhibited a strong Fe_{580} peak and no Fe_{1100} peak (Fig. 6, lower panel, B). This behavior indicates that the two LMM iron species are related – perhaps Fe_{1100} is a dimer of Fe_{580}. Corresponding S and P traces did not exhibit peaks that comigrated with either iron peak (Fig. 6, lower panel, C - F) indicating that neither P nor S are associated with either iron complex. The coordinating atoms to the iron ions in these complexes are probably O and/or N.

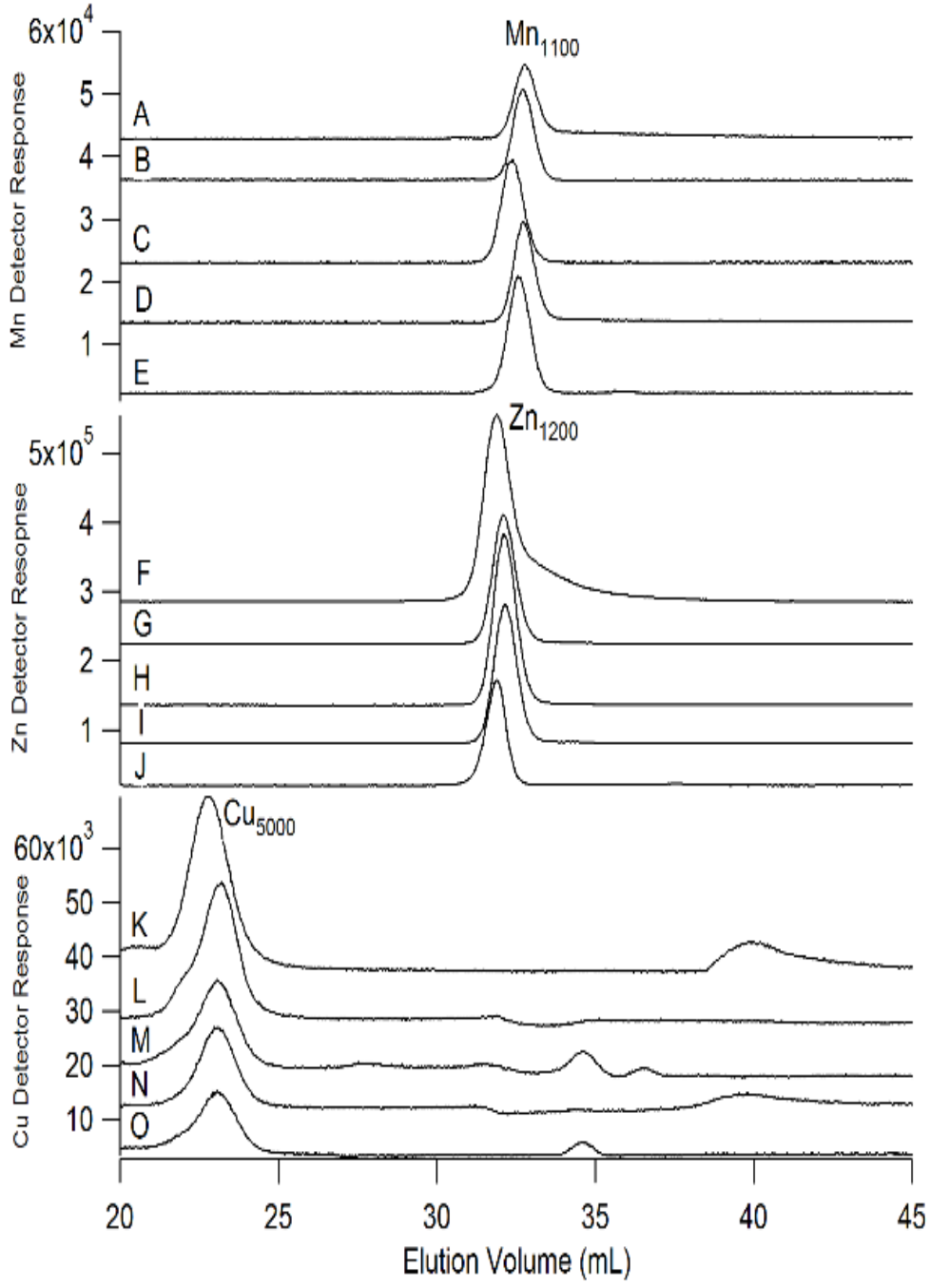

Figure 4.7: Mn, Zn, and Cu LC-ICP-MS traces of flow-through solutions of soluble extracts of mitochondria isolated from WT and ΔΔ cells. Traces A – E detected Mn, traces F – J detected Zn, and traces K - O detected Cu. Traces A, F, and K were from WT1 mitochondria. Traces B, G, and L were from WT40 mitochondria. Traces C, H, and M were from ΔΔ1 mitochondria. Traces D, I, and N were from a different batch of ΔΔ1 mitochondria. Traces E, J, and O were from ΔΔ40 mitochondria.

Effect of Deleting Mrs3/4 on Copper, Manganese, and Zinc

The average copper concentration in ΔΔ cells was 2.3 fold higher that in WT cells (Table 3), regardless of the iron concentration in the medium. The average manganese and zinc concentrations in ΔΔ cells showed little difference, relative to WT cells, across a range of nutrient iron concentrations; no trends were evident.

In contrast, the average copper concentration in ΔΔ mitochondria was about *half* of that in WT mitochondria. This suggests that copper is dysregulated in ΔΔ cells, and that *a deficiency of copper in ΔΔ mitochondria either increases the rate of copper import into the cell or decreases the rate of copper export.*

LC-ICP-MS traces of flow-through solutions from mitochondria isolated from *respiring* WT and ΔΔ cells exhibited the same LMM copper, manganese, and zinc species as reported previously from mitochondrial flow-through solutions from *fermenting* cells **(14)**, including Cu_{5000}, Mn_{1100}, and Zn_{1200} (Fig. 7). These species are probably involved in metallating apo-metalloproteins in the mitochondria **(14,150)** and are generated at relatively constant levels regardless of metabolic state.

Cu_{5000} intensities were reduced in ΔΔ traces, relative to what they were in WT traces, consistent with the lower copper concentration in ΔΔ mitochondria. Minor copper species with masses between 200 - 2000 Da were present sporadically in some traces but not in others (Fig. 7, bottom panel, elution volumes between 27 – 42 mL), suggesting that they are isolation artefacts.

The vast majority of copper in mitochondria has been proposed to be in the form of a labile nonproteinaceous LMM copper species called Cu_L **(151)**. Cu_L is thought to be

imported from the cytosol through Mrs3 and another IM protein (Pic2) **(152)**. Cu_L is thought to be stored in the matrix, and trafficked back to the IMS through an unidentified copper exporter on the IM. Our results provide no evidence supporting this concept. We are currently trying to identify Cu_{5000} and probe its physiological function.

Discussion

In this study, we used biophysical and bioanalytical methods to help understand the phenotype of yeast cells in which Mrs3 and Mrs4, the high-affinity iron importers on the mitochondrial IM, were both deleted. Under iron-deficient conditions, ΔΔ cells grew slowly relative to WT cells, whereas under iron-sufficiency, they grew at WT rates. Our results can be explained using the model of Figure 3. Accordingly, under iron-deficiency, the rate of iron import into mitochondria is too slow to prevent O_2 from diffusing into the matrix. This is caused by an insufficiently large Fe^{2+} pool in the matrix which causes an insufficient quantity of ISCs, hemes, and thus respiratory complexes to be assembled. Insufficient respiratory complexes allow diffusing cellular O_2 to penetrate the matrix. Once in the matrix, the O_2 reacts with the Fe^{2+} pool to generate Fe^{3+} nanoparticles and ROS, thereby reducing the size of the pool further. This leads to a vicious cycle culminating in ROS-damaged mitochondria that contain few active holo-respiratory complexes, and iron mostly in the form of nanoparticles. Mitochondrial membrane potential is probably also affected.

In iron-sufficient ΔΔ cells, the process reverses. Higher cytosolic iron concentrations increase the rate of iron import into mitochondria through the alternative

iron import pathway. This increases the size of the Fe^{2+} pool and the rate of ISC and heme biosynthesis. This allows respiratory complexes to be metallated and active. Normal respiratory activity returns, blocking O_2 from entering the matrix. The anaerobicity of the matrix and membrane potential are re-established. Viewed from a broader biological context, our results illustrate the complex interrelationships between iron metabolism, oxygen, and respiration.

Our results also offer some new insights as to why the iron regulon is activated in ΔΔ cells under iron *sufficient* conditions, even though such cells grow at normal rates and their mitochondria appear relatively "healthy" (from an iron-centric perspective). According to regulatory control theory, the cell should contain a molecular sensor that monitors the iron status and controls cellular iron import **(157,158)**. The concentration of the sensor should be *below* its normal set-point concentration under conditions when the rate of iron import into the cell is faster than normal. Since we observed greater-than-WT iron import rates in ΔΔ cells grown under *both* iron-deficient and iron-sufficient conditions, the sensor (whatever it is) should be *below* its WT concentration in these mutant cells grown under both conditions.

Thus, we sought to identify iron species whose concentration was lower in mutant cells than in WT cells grown under equivalent conditions. We can eliminate nanoparticles as the sensor because they are present at higher-than-WT levels in mutant cells. Similarly, cytosolic iron concentrations in mutant cells appear to be higher than in WT cells, as evidenced by more intense NHHS Fe^{2+} quadrupole doublet in comparative Mössbauer spectra.

The most popular view is that the sensor is a sulfur-containing species called X-S that reflects the level of ISC activity in mitochondria. We previously used the concentration of mitochondrial ISCs as a proxy for X-S in our previous model of iron regulation **(153)**. However, our current results do not favor using mitochondrial ISCs as a proxy for X-S-based regulation because mutant mitochondria isolated from ΔΔ cells grown under high iron conditions contained near normal levels of ISCs.

The only Fe-containing species (observable in our investigation) at lower-than-WT concentrations in mutant cells were the mitochondrial Fe^{2+} pool and mitochondrial heme centers. We favor the mitochondrial NHHS Fe^{2+} pool as being the regulatory sensor but cannot exclude heme. The Fe^{2+} pool could conceivably work together with X-S as a regulatory sensor (e.g. as substrates for the Fe_2S_2 cluster that eventually is transferred onto Aft1/2). In this way, either Fe^{2+} or X-S could regulate the assembly of clusters. We previously proposed a similar situation, except that cytosolic (rather than mitochondrial) Fe^{2+} was considered to be the sensor **(151)**. Our current results dis-favor this because cytosolic Fe^{2+} concentration in ΔΔ cells are probably higher than in WT cells. Viewed from a broader biological context, understanding iron regulation in eukaryotic cells is extremely important because dysregulation is associated with numerous diseases.

Composition of the Mitochondrial NHHS Fe^{2+} Pool

Our results provide strong evidence that the mitochondrial NHHS Fe^{2+} pool in exponentially growing yeast cells is composed *exclusively* of Fe_{580} (no other LMM Fe

complex was present). This species also appears to be present in mitochondria from mammalian sources **(14)**. The iron concentration associated with the Fe^{2+} pool in yeast mitochondria ranges from 60 - 200 μM (Table 1), depending on strain and growth conditions. We previously estimated the concentration of Fe_{580} in mitochondria to be in the same ballpark, ca. 100 μM **(14)**.

Our current results suggest that the irons of Fe_{580} and Fe_{1100} are coordinated mainly by O and/or N donor ligands, not by S. In support of this, the ΔE_Q and δ of the NHHS Fe^{2+} doublet in MB spectra of isolated mitochondria (3.07 mm/s and 1.23 mm/s, respectively) are typical of Fe^{2+} complexes with 4 - 6 O and 0 – 2 N donor ligands **(155)**. These parameters are *not* typical of Fe^{2+} complexes with sulfur-based ligands.

Mechanisms of Iron Passage through Importers

We suggest two possible mechanisms by which cytosolic iron might pass into the mitochondrial matrix. In the "*intact channeling*" mechanism, Fe_{580} in the cytosol passes intact through Mrs3/4 channels. In the "*unwrapping/rewrapping*" mechanism, cytosolic iron enters the IMS through porins on the outer membrane and then docks on Mrs3/4. The iron dissociates from its coordinating ligands and the bare Fe^{2+} ion passes through the Mrs3/4 channels. Indeed, there are three conserved histidine residues in Mrs3/4 which seem poised to transport such an ion **(156)**. When the Fe^{2+} ion reaches the end of the channel on the matrix side, it coordinates with other ligands to generate the Fe_{580} complex.

If intact channeling were operative, Fe_{580} should not have been observed in the flow-through solution of ΔΔ40 mitochondria (but it was). If Fe_{580} was also channeled intact through the alternative import transporter, then Fe_{580} should have been present in the flow-through solution of ΔΔ1 mitochondria (but it was not). One complication is that loss of membrane potential in ΔΔ1 mitochondria might have prevented Fe_{580} import through the alternative importer; thus the intact channeling mechanism cannot be eliminated cleanly. However, we find it unlikely that both Mrs3/4 and the alternative iron import pathway import the same complex (since different proteins would have different channels). Also, the specificity implied by intact channeling seems contradicted by the ability of simple hexaqua Fe^{2+} ions to enter isolated mitochondria and be used for heme and ISC biosynthesis **(71,8)**.

The unwrapping/rewrapping mechanism implies the opposite in terms of specificity (i.e. any Fe^{2+} complex could serve as Fe^{2+} donor as long as the coordinating ligands were not bound so tightly that they could not dissociate within a reasonable timeframe). Whether Fe_{580} assembles in the matrix upon exiting the channel should depend, according to the unwrapping/rewrapping mechanism, on the *metabolic state* of the organelle. Fe_{580} may not form if the matrix is devoid of the appropriate coordinating ligand(s), or if the matrix region is not sufficiently anaerobic to maintain the Fe^{2+} state. Under stationary-state conditions, the metabolic state of the matrix may be different than under exponential growth conditions (e.g. the concentrations of potential coordinating ligands might vary) such that Fe_{1100} (or Fe_{2700} or Fe_{2100}) might form instead of Fe_{580}.

Viewed collectively, these considerations support the unwrapping/rewrapping mechanism, but further studies are required to establish either mechanism.

Physiological Function of the Fe_{580} Mitochondrial Fe^{2+} pool

Our results confirm and extend previous studies showing that there is a pool of NHHS Fe^{2+} in mitochondria **(13)**, that this pool is feedstock for ISC and heme biosynthesis in the organelle **(143,144,134)**, and that Fe_{580} comprises this pool **(53,14)**. Although iron accumulates in mitochondria of cells in which *YFH1* is deleted **(145)**, iron does not accumulate in mitochondria of cells in which *YFH1*, *MRS3*, and *MRS4* have all been deleted **(69,9,71,8)**. This strongly suggests that the iron which accumulates in mitochondria of Friedreich's Ataxia patients (deficient in frataxin, the human homolog of Yfh1) passes through mitoferrins1/2 (the human homologs of Mrs3/4). The iron oxidation state in nanoparticles is Fe^{3+} whereas that for the mitochondrial iron pool is Fe^{2+}. This implies that Fe_{580} is an Fe^{2+} complex that reacts with O_2 (in diseased mitochondria) to generate nanoparticles.

Nanoparticles are often described as toxic to the cell, since ROS is formed in association with them. However, from a chemical perspective, nanoparticles should be benign and unreactive with O_2. The reaction of Fe_{580} with O_2 is more likely to be toxic and to generate ROS. Thus, the reaction chemistry of Fe_{580} is probably critical for understanding the pathophysiology of Friedreich's Ataxia and perhaps other iron-associated mitochondrial diseases. Our study is significant because it further

characterizes Fe_{580} and provides evidence for a model in which O_2 is of critical importance for the iron-related reaction chemistry of mitochondria.

Acknowledgements: This work was supported by the National Institutes of Health (GM084266) and the Robert A. Welch Foundation (A1170).

CHAPTER V

A MATHEMATICAL MODEL OF IRON IMPORT AND TRAFFICKING IN WT AND MRS3/4ΔΔ YEAST CELLS*

Joshua D. Wofford and Paul A. Lindahl

Summary

Iron plays crucial roles in the metabolism of eukaryotic cells. Much iron is trafficked into mitochondria where it is used for iron-sulfur cluster assembly and heme biosynthesis. A yeast strain in which Mrs3/4, mitochondrial high-affinity iron importer proteins on the inner membrane, are deleted exhibits a slow-growth phenotype when grown under iron-deficient conditions. However, these cells grow at WT rates under iron-sufficient conditions. The object of this study was to develop a math model that could explain this recover on the molecular level. A multi-tiered strategy was used to solve an ordinary-differential-equations-based mathematical model of iron import, trafficking, and regulation in growing *Saccharomyces cerevisiae* cells. At the simplest level of modelling, all iron in the cell was presumed to be a single species and the cell was considered to be a single homogeneous volume. Optimized parameters associated with the rate of iron import and the rate of dilution due to cell growth were determined. At the next level of complexity, the cell was divided into three regions, including cytosol, mitochondria, and vacuoles, each of which was presumed to contain a single

* This work has been submitted to BMC Systems Biology and is awaiting review.

form of iron. Optimized parameters associated with import into these regions were determined. At the final level of complexity, nine components were assumed within the same three cellular regions. Parameters obtained at simpler levels of complexity were used to help solve the more complex versions of the model; this was advantageous because the data used for solving the simpler model variants were more reliable and complete relative to those required for the more complex variants. The optimized full-complexity model simulated the observed phenotype of WT and Mrs3/4ΔΔ cells with acceptable fidelity, and the model exhibited some predictive power. The developed model highlights the importance of an Fe^{2+} mitochondrial pool and the necessary exclusion of O_2 in the mitochondrial matrix for eukaryotic iron-sulfur cluster metabolism. Similar multi-tiered strategies could be used for any micronutrient in which concentrations and metabolic forms have been determined for different organelles within a growing eukaryotic cell.

Introduction

The complexity of biochemical processes as they occur in growing eukaryotic cells is enormous, often rendering the corresponding genetic phenotypes difficult to understand at the chemical level. One means of analyzing such systems is to develop ordinary-differential-equation (ODE^4)-based kinetic models **(159,160,161)**. In principle, such models can reveal on a quantitative basis whether observed phenotypic behavior could emerge from a proposed system of reacting chemical players and using a particular set of kinetic and thermodynamic parameters. This is a huge advantage relative to the

common practice of describing complex biochemical processes as a cartoon or scheme. Another advantage of math-based kinetic models is that all assumptions are explicit and available for public inspection; cartoons and schemes generally include hidden assumptions. The major *disadvantage* of math-based kinetic models is that a complete and accurate dataset, including rate-law expressions, rate-constants, and reactant concentrations, are required to solve them and endow them with predictive power. Rarely is all such information available, and available information is often less quantitative than desired.

A common approach to circumventing this problem is to employ *simplistic* models (in terms of numbers of components and reactions) that nevertheless remain capable of generating observed cellular behavior and of explaining genetic phenotypes. Designing such models involves deciding which species and reactions to include, which to leave out, and which to combine into groups. Such decisions often boil-down to whether including an additional component or reaction is "worth" (in terms of generating the desired behavior) an additional adjustable parameter. Simple models with few adjustable parameters simplify realty but they can also provide fundamental insights into reality - by penetrating through the entangled and bewildering complexity of a highly complex system.

Iron is critical for all eukaryotic cells **(28,67)**. It is present in many forms including hemes, iron-sulfur clusters (ISCs), nonheme mononuclear species, and iron-oxo dimeric centers. Such centers are commonly found in the active-sites of metalloenzymes. Iron plays a major role in energy metabolism; e.g. there are iron-rich

respiratory complexes located on the inner membrane of mitochondria. Mitochondria are the primary site in the cell where ISCs are assembled, and the only site where iron is installed into porphyrins during heme biosynthesis. For these reasons, mitochondria are a major 'hub' for iron trafficking.

The cytosol also plays an important role in iron trafficking, in that nutrient iron enters this region prior to being distributed to the organelles. Most of the iron that enters the cytosol is probably in the Fe^{2+} state, but neither the oxidation state nor the concentration of cytosolic Fe has been established **(162)**. The vacuoles are another trafficking 'hub' in yeast, as much of the iron imported into these cells (when grown on iron-sufficient media) is stored in these acidic organelles **(70,135)**. Vacuolar iron is predominately found as a mononuclear nonheme high spin (NHHS) Fe^{3+} species, probably coordinated to polyphosphate ions **(149)**.

Iron is tightly regulated in cells, and some insightful math models involving iron metabolism, trafficking and regulation have been developed. Twenty years ago, Omholt et al. designed and analyzed a model of the IRP/IRE iron regulatory system in mammalian cells **(163)**. More recently, Mobilia developed a similar model that assumed scarce or unavailable data; they developed new methods to represent data by constrained inequalities **(164,165)**. Chifman and coworkers developed a logical-rule-based math model of iron homeostasis in healthy mammalian cells, and a similar model for iron dysregulation in cancer cells in which the roles of the IRP-based regulation, the iron storage protein ferritin, the iron export protein ferroportin, the labile iron pool, reactive oxygen species, and the cancer-associated Ras protein were emphasized **(166,167)**.

Mitchell and Mendes used ODE's to model iron metabolism and regulation in a liver cell and its interaction with blood plasma **(168)**. They emphasized the role of iron-regulating hormone hepcidin and the regulatory and storage systems mentioned above, and they simulated the effects of iron-overload disease. Their model was complex- involving 66 adjustable parameters many of which were not experimentally determined. None of the above models included iron-sulfur cluster (ISC) synthesis, the role of mitochondria (or other organelles), and none modeled the cells as growing. In terms of biological emphasis, the model of Achcar et al. **(169)** is most relevant to the current study. They developed a model of iron metabolism and oxidative stress in yeast cells using a Boolean approach in which reactions were weighted. Their model included ISC assembly, as well as organelles such as mitochondria, vacuoles, cytosol, and nucleus. Their model was exceeding complicated (642 components and 1007 reactions) and was not ODE based **(169)**. They modeled the development of Fe^{3+} (phosphate) oxyhydroxide nanoparticles in mitochondria of mutant cells lacking ISC assembly proteins (e.g. Yfh1, the yeast frataxin homolog), similar to the emphasis of our previous model **(154)**. They included a reaction in which an unidentified species X converted nanoparticles into free iron, and hypothesized that X might be glutathione. Our model emphasized the role of oxygen in controlling nanoparticle formation.

The iron content of yeast cells and the major organelles involved in iron trafficking have been analyzed using Mössbauer (MB) spectroscopy, the most powerful spectroscopic tool for interrogating the iron content of biological samples **(44)**. If the absolute iron concentration of ^{57}Fe-enriched cells and organelles are known, the absolute

concentrations of major groups of iron-containing species in such cells can be calculated using percentages obtained by MB. Such data is used here to develop an advanced math model of iron import and trafficking in eukaryotic cells.

In WT cells, much iron enters mitochondria through Mrs3 and Mrs4, paralogous inner-membrane proteins **(69,68)**. These "high affinity" iron-importers contain a small channel that allows a low-molecular-mass cytosolic iron species to enter the matrix. We have recently discovered a low-molecular mass species in mitochondria, designed Fe_{580}, which might serve as feedstock for ISC assembly **(14)**. Iron can enter mitochondria through alternative pathways, including one that involves Rim2 **(12)**.

Iron import in yeast is regulated according to the ISC activity occurring in mitochondria **(54)**. When this activity is attenuated, for example by mutations in the ISC assembly machinery, the rate of nutrient iron imported increases. In yeast, iron regulation involves the *Iron Regulon*, a group of 20-30 genes whose expression is controlled by transcription factors Aft1/2 **(122,120)**. This includes the Fet3/Ftr1 complex on the plasma membrane through which much cellular iron is imported.

Yfh1 helps catalyze ISC assembly in mitochondria **(170)**. This and other ISC mutant cells accumulate large quantities of iron in the form of Fe^{3+} nanoparticles **(145, 51)**. These cells import excessive iron because the iron regulon is activated in response to insufficient mitochondrial ISCs. Excess iron (in the form of nanoparticles) accumulates in mitochondria because the rate of iron import into the organelle increases due to activation of the iron regulon. The *net* rate of iron import into vacuoles is reduced such that these organelles contain little iron in ISC mutants. Actually, the iron export

rate is probably increased in these mutants. This is because the vacuolar membrane contains an iron-export complex (Fet5/Fth1) that is homologous to the Fet3/Ftr1 iron import complex on the plasma membrane, and both are controlled by the iron regulon **(23)**.

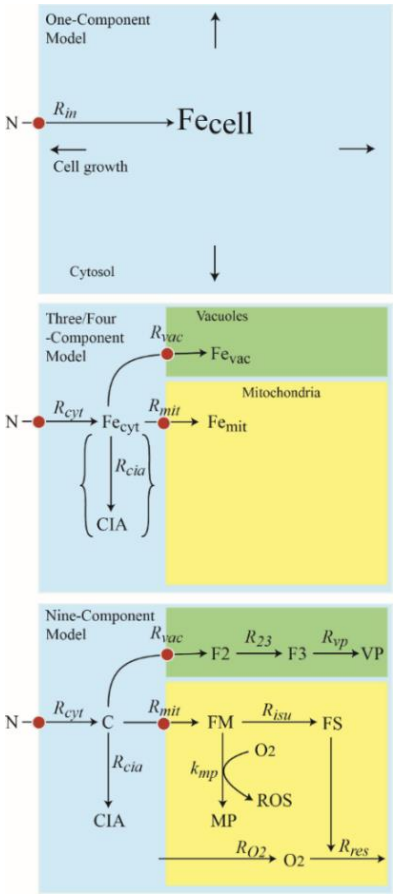

Figure 5.1: Strategy for optimizing a model of nutrient iron import, trafficking and regulation in growing eukaryotic cells. Top panel: C_1 model in which all iron in the cell is treated as a single species and the cell is considered to be homogeneous. Middle panel: C_3 model in which the cell is divided into three regions and each region is assumed to contain a single type of iron species. C_4 model includes the reaction forming *CIA*. Bottom panel: C_9 model in which the cell remains divided into 3 regions but the number of iron-containing species is expanded to 8.

Table 5.1. Growth rates, iron concentrations, and import rates in ΔΔ and WT cells grown under different nutrient conditions. [N] refers to the μM concentration of iron in the respiring medium, as described **(10)**. The untreated medium was assumed to contain 1 μM of endogenous iron. For each entry, the top number is datum or data-based estimates ($R_{...\text{-}dat}$) and the bottom number is the corresponding simulated value ($R_{...\text{-}sim}$). Concentrations are in units of μM, rates are in units of μM/hr, and α_{cell} is in units of hr^{-1}. Data for α_{cell} and $[Fe_{cell}]$ have been published **(10)** whereas $[Fe_{cyt}]$, $[Fe_{mit}]$, and $[Fe_{vac}]$ were estimated as described in the text.

[N]	α_{cell}	$[Fe_{cell}]$	R_{cell}	$f_{cyt}\cdot[Fe_{cyt}]$	$f_{mit}\cdot[Fe_{mit}]$	$f_{vac}\cdot[Fe_{vac}]$	$R_{cyt} - R_{mit} - R_{vac}$	R_{mit}	R_{vac}
WT									
1	0.18 0.18	120 60	22 10	79 22	41 22	0 16	18 5.0	9.2 4.9	0 3.7
2	0.18 0.19	200 190	37 35	75 76	43 35	82 81	17 18	9.9 8.4	19 19
11	0.20 0.20	480 810	97 160	200 180	56 66	220 560	52 45	14 17	56 140
41	0.20 0.20	880 900	180 180	310 180	69 69	500 640	77 46	18 18	130 160
ΔΔ									
1	0.06 0.05	360 540	22 27	110 240	69 74	180 230	8.1 13	5.2 3.9	14 12
2	0.068 0.069	680 1,100	46 90	130 380	69 77	480 660	11 33	5.9 6.6	41 58
11	0.15 0.15	2,200 2,300	320 360	280 280	72 71	1,800 1,900	52 53	13 13	340 360
41	0.20 0.19	3,900 2,000	800 390	230 230	74 61	3,600 1,800	59 54	19 14	920 410

We have developed a simple model (Figure 1, bottom panel) to illustrate the changes in iron import and trafficking that occur in ISC mutants relative to in WT cells **(154)**. The core assumption of the model is that the matrix of healthy WT mitochondria is largely anaerobic, due to the ability of the respiratory complexes on the IM to quickly reduce much of the O_2 that would otherwise diffuse into the matrix. Although dissolved

[O_2] concentrations in the mitochondrial matrix have not been measured directly, three lines of evidence indicate that this space is anaerobic. Firstly, *in vitro* ISC assembly assays must be performed anaerobically **(74)**. Secondly, numerous enzymes in the matrix, including aconitase, biotin synthase, and lipoic acid synthase are O_2-sensitive **(75,76)**. Thirdly, the nitrogenase iron protein which is exquisitely O_2-labile remains active when installed in the mitochondrial matrix **(77)**. According to our model, in ISC mutant mitochondria, the lack of ISCs and hemes cause a deficiency of respiratory complexes, and this allows O_2 to diffuse into the matrix and react with a pool of Fe^{2+}, forming nanoparticles.

Relative to WT cells, Mrs3/4ΔΔ cells (to be called **ΔΔ**) grow slowly under iron-deficient conditions but at WT rates in iron-sufficient media **(69,67,68)**. The iron concentration of ΔΔ cells is higher than in comparable WT cells, indicating that the iron regulon is activated. We recently found that mitochondria from iron-deficient ΔΔ cells is dominated by nanoparticles whereas the iron content of mitochondria from iron-sufficient ΔΔ cells are quite similar to WT mitochondria – i.e. dominated by the ISC and heme centers that are found in respiratory complexes, and containing a substantial amount of a NHHS Fe^{2+} that might arise from Fe_{580} **(10)**. Fe_{580} is present in mitochondria from iron-replete ΔΔ and both iron-deficient and iron-replete WT cells. However, our previous model **(154)** was unable to reproduce the ΔΔ phenotype.

In this paper, we present an improved ODE-based model of iron trafficking and regulation in yeast, and use a multi-tiered strategy to solve it at an expanding steady-

state. This model was able to explain both the ΔΔ phenotype *and* the ΔYfh1 phenotype while also requiring fewer adjustable parameters relative to our previous model.

Methods and Results

As is typical of modeling biochemical processes within cells, the challenge was to generate a useful and insightful model despite sparse and imperfect data **(164,165)**. Our strategy for doing this was to optimize the model at different levels of complexity. Model variants ranged from one that consisted of a single iron species and no cellular compartments to one that involved nine species in three cellular compartments. The parameters used to optimize the simpler variants were transferrable to the more complex models. This was an important insight because the data needed to solve simpler systems tend to be more reliable and complete relative to those required to solve more complex variants. A similar strategy could be applied for models involving the trafficking of other micronutrients. The only requirements are that the concentrations and metabolic forms of the micronutrient in the cell and in major organelles be known (at some reasonable level of accuracy) for different growth conditions and/or genetic strains.

The complete chemical model is shown in Figure 1, bottom panel. We initially solved this model (to be referred to as $\boldsymbol{C_9}$, the nine-component model, including components *C*, *CIA*, *F2*, *F3*, *VP*, *FM*, *FS*, *MP*, and O_2) at three simpler levels of complexity called $\boldsymbol{C_1}$ (the one-component model, with component Fe_{cell}), $\boldsymbol{C_3}$ (the three-component model, including Fe_{cyt}, Fe_{mit}, and Fe_{vac}), and $\boldsymbol{C_4}$ (the four-component model, including *C*, *CIA*, Fe_{vac}, and Fe_{mit}). These model variants are illustrated in Figure 1, top

and middle panels. We solved the C_9 model in this way because the data that were required to solve the simpler versions were more reliable and complete than those required to solve the C_9 variant. Importantly, *the parameters that were optimized using the simpler versions could be transferred to the more complex variants*. This minimized the number of adjustable parameters that had to be assigned using less reliable or incomplete data. As far as we are aware, this multi-tiered modeling strategy has not been employed previously within the context of ODE-based models involving the trafficking of iron or any micronutrient within a growing eukaryotic cell. Code for all model variants was written using *Mathematica 10* software (wolfram.com). ODEs were solved to steady-state using the NDSolve routine.

Development of the C_1 model

Consider a population of cells growing exponentially on a nutrient form of iron called *N* which enters the cell through a transporter on the plasma membrane (Figure 1, top panel, red circle). Let V_{cell} represent the collective cell volume (within a culture) at time *t*. When cells are growing exponentially, V_{cell} will increase according to the relationship

$$\frac{dV_{cell}}{dt} = \alpha_{cell} \cdot V_{cell} \tag{1}$$

where α_{cell} is the growth rate. During exponential growth α_{cell} will be constant in time. The optical density at 600 nm of an exponentially growing culture is proportional to V_{cell} such that the slope of the {ln(OD_{600}) vs. time} plot affords α_{cell}. This parameter has been

determined for WT and ΔΔ cells grown in medium containing 4 different concentrations of nutrient iron [N] = 1, 2, 11, and 41 μM (**(10)**and Table 1). The 8 "data-based" determinations of α_{cell} will be called $\alpha_{cell-dat}$. For simulations, a continuous α function between N = 1 – 41 μM was required, so we optimized

$$\alpha_{cell-sim} = \frac{\alpha_{\max}[N]}{K_{\alpha} + [N]} \tag{2}$$

by fitting against the $\alpha_{cell-dat}$ values using the error function

$$ERR = \frac{1}{4} \sum_{N=1,2,11,41} \frac{2 \cdot \left| \alpha_{cell-sim,N} - \alpha_{cell-dat,N} \right|}{\alpha_{cell-sim,N} + \alpha_{cell-dat,N}} \tag{3}.$$

Best-fit $\alpha_{\max}$ and K_{α} values are given in Table 2, and plots of α_{cell} are shown in Figure 2 (top). The plots show that the simulated growth rates of WT and ΔΔ cells increased as the concentration of iron in the medium [N] increases, mirroring the experimental growth rates with acceptable fidelity (apart from the point associated with ΔΔ cells at [N] = 41 μM).

Table 5.2. Optimized parameters used in simulations.

Parameter	Value (strain)	units	Sens.
C_1			
$R_{cell\text{-}max}$	180 (WT) 390 (ΔΔ)	μM hr^{-1}	1.021 1.049
K_N	4	μM	1.062
sens	2	none	1.043
α_{max}	0.204	hr^{-1}	1.068
K_α	0.13(WT) 3.9 (ΔΔ)	hr^{-1}	1.047 1.029
C_3			
R_{cyt}	230 (WT) 480 (ΔΔ)	μM hr^{-1}	1.011 1.024
$k_{mit(C3)}$	2.8(WT) 1.6 (ΔΔ)	hr^{-1}	1.001 1.000
$R_{vac\text{-}max}$	1140	μM hr^{-1}	1.000
K_{vac}	11	μM	1.001
nvac	3	none	1.001
C_4			
$R_{cia\text{-}max}$	56	μM hr^{-1}	1.001
K_{cia}	3.8	μM	1.000
ncia	3	none	1.000
C_9			
k_{mit}	5.5(WT) 1.2 (ΔΔ)	hr^{-1}	1.000 1.000
$R_{isu\text{-}max}$	180	μM hr^{-1}	1.005
K_{isu}	220	μM	1.021
nisu	2.3	none	1.106
k_{vp}	1.10×10^{-7} (WT) 2.37×10^{-7} (ΔΔ)	$\mu M^{1\text{-}nvp}$ hr^{-1}	1.000 1.000
nvp	2.4	none	1.001
k_{23}	5.2	hr^{-1}	1.000
$[FS]_{sp}$	370	μM	1.000
n23	1.6	none	1.000
k_{mp}	0.09	μM^{-1} hr^{-1}	1.013
k_{O2}	25	hr^{-1}	1.008
k_{res}	9	μM^{-1} hr^{-1}	1.010

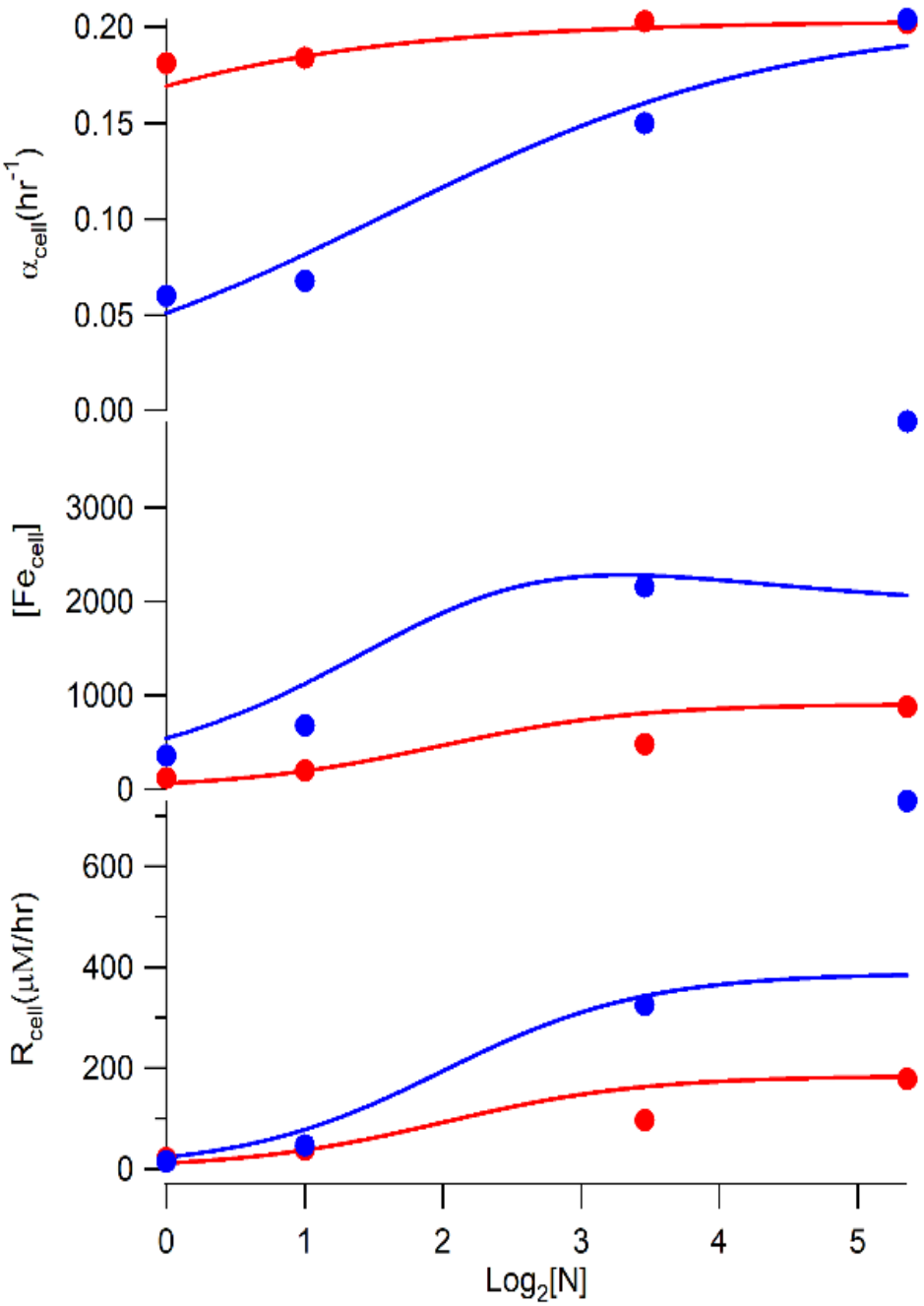

Figure 5.2: Plots of growth rate (top), cellular iron concentration (middle), and the rate of iron import into the cell (bottom). Red circles and lines indicate data-based and simulated WT cells. Blue circles and lines indicate ΔΔ cells. Data-based values and corresponding simulation values are given in Table 1.

In the C_1 model, all iron in the cell is considered to be a single component called Fe_{cell}. The concentration [Fe_{cell}] is a function of moles (n_{Fecell}) and V_{cell}, namely [Fe_{cell}] = n_{Fecell}/V_{cell}. Since the cell is growing as chemistry is occurring, the time-dependent change of [Fe_{cell}] is given by the partial derivative

$$\left\{\begin{array}{l} \dfrac{d[Fe_{cell}]}{dt} = \dfrac{\partial[Fe_{cell}]}{\partial n_{Fecell}} \cdot \dfrac{dn_{Fecell}}{dt}\Big|_{\text{constant V}} + \dfrac{\partial[Fe_{cell}]}{\partial V_{cell}} \cdot \dfrac{dV_{cell}}{dt}\Big|_{\text{constant n}} \\ \dfrac{d[Fe_{cell}]}{dt} = \dfrac{1}{V_{cell}} \dfrac{dn_{Fecell}}{dt}\Big|_{\text{constant V}} - \dfrac{n_{Fecell}}{(V_{cell})^2} \cdot \dfrac{dV_{cell}}{dt}\Big|_{\text{constant n}} \\ \dfrac{d[Fe_{cell}]}{dt} = \dfrac{d[Fe_{cell}]}{dt}\Big|_{\text{constant V}} - \dfrac{1}{V_{cell}} \cdot \dfrac{dV_{cell}}{dt}[Fe_{cell}]\Big|_{\text{constant n}} \\ \dfrac{d[Fe_{cell}]}{dt} = R_{cell} - \alpha_{cell} \cdot [Fe_{cell}] \end{array}\right\} \quad (4).$$

The first term on the right-hand-side of the last equation of (4) describes the rate of iron import at constant volume ($N \xrightarrow{R_{cell}} Fe_{cell}$) – i.e. for chemistry in a no-growth cell. The second term reflects dilution due to the growth of cells at constant moles of Fe_{cell} - .i.e. for a growing cell devoid of chemistry. Under the *expanding-steady-state* condition, as would exist for a population of exponentially growing cells, [Fe_{cell}] is constant and the import rate R_{cell} equals the dilution rate,

$$R_{cell} = \alpha_{cell} \cdot [Fe_{cell}] \quad (5).$$

[Fe_{cell}] was measured in WT and ΔΔ cells grown under the four concentrations of [N] **(10)**, and the product of this and corresponding $\alpha_{cell-dat}$ values afforded the "data-based" $R_{cell\text{-}dat}$ values listed in Table 1 and shown as the circles in Figure 2 bottom panel.

We next assigned a rate-law expression to R_{cell} that depended solely on [N], such that a continuous $R_{cell\text{-}sim}$ function could be generated at all [N]. The iron-importer on the

plasma membrane of yeast cells is saturatable by nutrient iron **(5)**, and so we assigned the rate-law for $R_{cell\text{-}sim}$ to the Michaelis-Menten function

$$R_{cell-sim} = \frac{R_{\text{cell-max}}[N]^{sens}}{K_N{}^{sens} + [N]^{sens}} \quad (6)$$

where *sens* is a sensitivity factor allowing for cooperative iron import. $R_{cell\text{-}sim}$ was optimized by minimizing an ERR function similar to equation (3). The resulting optimized $R_{cell\text{-}sim}$ simulation parameters are given in Tables 1 and 2. Optimized $R_{cell\text{-}sim}$ was used to generate an ODE (based on the last equation in (4)) that could be used in kinetic modeling (see (S1) and (S2)). However, the current study focuses on the expanding steady-state condition, and so the ODEs were solved at infinitely long times for [N] ranging from 1 – 41. Plots of steady-state $R_{cell\text{-}sim}$ vs. $\log_2$[N] are shown in Figure 2 bottom panel. As expected, the simulated rate of iron import increased in both WT and ΔΔ cells as the concentration of iron in the medium increased, with higher rates for ΔΔ cells since they accumulate more iron. The [N]-dependent increase in iron import rate is counterbalanced by the [N]-dependent increase in cell growth rate.

Development of the C_3 model

We next subdivided the cell volume into mitochondria, vacuoles and all remaining compartments, such that

$$V_{cell} = V_{cyt} + V_{mit} + V_{vac} \quad (7).$$

Here, "*cyt*" refers to cytosol *plus* all organelles besides mitochondria and vacuoles; there is insufficient published information to justify subdividing cyt into

additional cellular compartments. This collective compartment includes the iron content of the nucleus which contains a significant number of [Fe_4S_4] containing proteins **(148)**. Topologically, cyt was treated as though it was exclusively cytosol i.e. surrounding mitochondria and vacuoles and being surrounded by the plasma membrane.

Each cellular compartment in C_3 was presumed to contain a single iron species, called Fe_{cyt}, Fe_{mit}, and Fe_{vac}. The conservation of matter requires that

$$[Fe_{cell}] = f_{cyt} \cdot [Fe_{cyt}] + f_{mit} \cdot [Fe_{mit}] + f_{vac} \cdot [Fe_{vac}] \quad (8)$$

where f_{cyt}, f_{mit}, and f_{vac} are fractional volumes e.g. $f_{mit} = V_{mit}/V_{cell}$. In an expanding steady-state, these fractional volumes will be constant such that

$$\frac{d[Fe_{cell}]}{dt} = f_{cyt} \cdot \frac{d[Fe_{cyt}]}{dt} + f_{mit} \cdot \frac{d[Fe_{mit}]}{dt} + f_{vac} \cdot \frac{d[Fe_{vac}]}{dt} \quad (9).$$

For the C_3 model, N is imported into the cytosol forming Fe_{cyt} ($N \xrightarrow{R_{cyt}} Fe_{cyt}$). Some Fe_{cyt} is imported into mitochondria ($Fe_{cyt} \xrightarrow{R_{mit}} Fe_{mit}$) and some into vacuoles ($Fe_{cyt} \xrightarrow{R_{vac}} Fe_{vac}$). The rest remains in cyt. Based on this scheme, the time-dependent changes of the concentrations of the Fe species in each region are

$$\left\{ \begin{array}{l} \frac{d[Fe_{cyt}]}{dt} = R_{cyt} - R_{mit} - R_{vac} - \frac{1}{V_{cyt}} \frac{dV_{cyt}}{dt} [Fe_{cyt}] \\ \frac{d[Fe_{mit}]}{dt} = \frac{f_{cyt}}{f_{mit}} R_{mit} - \frac{1}{V_{mit}} \frac{dV_{mit}}{dt} \cdot [Fe_{mit}] \\ \frac{d[Fe_{vac}]}{dt} = \frac{f_{cyt}}{f_{vac}} R_{vac} - \frac{1}{V_{vac}} \frac{dV_{vac}}{dt} \cdot [Fe_{vac}] \end{array} \right\} \quad (10).$$

Fraction volume ratios in the second and third equations of (10) are required to conserve mass as Fe_{cyt} moves from one region to another. Under an expanding steady-state,

$$\left\{\begin{array}{l} R_{cyt} = R_{mit} + R_{vac} + \dfrac{1}{V_{cyt}}\dfrac{dV_{cyt}}{dt}[Fe_{cyt}] \\ R_{mit} = \dfrac{1}{V_{cyt}}\dfrac{dV_{mit}}{dt}\cdot[Fe_{mit}] \\ R_{vac} = \dfrac{1}{V_{cyt}}\dfrac{dV_{vac}}{dt}\cdot[Fe_{vac}] \end{array}\right\} \quad (11).$$

The growth rate of each cellular region will equal the growth rate of the cell multiplied by the fractional volume of that compartment,

$$\left\{\begin{array}{l} \dfrac{dV_{cyt}}{dt} = f_{cyt}\dfrac{dV_{cell}}{dt} \\ \dfrac{dV_{mit}}{dt} = f_{mit}\dfrac{dV_{cell}}{dt} \\ \dfrac{dV_{vac}}{dt} = f_{vac}\dfrac{dV_{cell}}{dt} \end{array}\right\} \quad (12).$$

Substituting (12) into (11) affords

$$\left\{\begin{array}{l} R_{cyt} = R_{mit} + R_{vac} + \alpha_{cell}\cdot[Fe_{cyt}] \\ R_{mit} = \dfrac{V_{mit}}{V_{cyt}}\alpha_{cell}\cdot[Fe_{mit}] \\ R_{vac} = \dfrac{V_{vac}}{V_{cyt}}\alpha_{cell}\cdot[Fe_{vac}] \end{array}\right\} \quad (13).$$

Published fractional volumes were used to help solve these equations. The cellular content of fermenting (exponentially growing, nonbudding) *S. cerevisiae* was reconstructed in 3D and volume fractions were determined **(171)**. Mitochondria and vacuoles occupied 1.7% and 5.8% of cell volume, respectively. Another study reported that the same two organelles occupied 1.6% and 7.8%, respectively **(172)**. In a third study, vacuoles in yeast strain W303 (the same as used in our studies) accounted for 10% of cell volume **(173)**. And in *respiring* yeast cells, mitochondrial volume was 10-12% of cell volume **(174)**. Since the model developed here is of iron trafficking in respiring W303 yeast cells, we assumed $f_{mit} = 0.1$, $f_{vac} = 0.1$, and $f_{cyt} = 0.8$.

The relationships given in (13) are connected to (5). Substituting the last two equations of (13) into the first, and then simplifying and comparing to (5) affords the relationship

$$R_{cyt} = \frac{1}{f_{cyt}} R_{cell} \qquad (14).$$

This equation connects C_1 and C_3 models. The rate of iron import into cyt (R_{cyt}) equals the data-based rate of Fe import into the cell (R_{cell}) divided by the volume fraction f_{cyt}. (Note that these rates describe the change of iron *concentrations* within the cell or cytosol, not the change in the number of moles of N imported. Since $V_{cyt} < V_{cell}$, $[Fe_{cyt}]$ will increase faster than $[Fe_{cell}]$ (in proportion to the ratio V_{cell}/V_{cyt}) even though the same number of moles of iron per hour are imported.) The rate-law expression for $R_{cyt\text{-}sim}$ should also involve a Michaelis-Menten expression, with the same K_N and *sens* as in (6) but with a maximal velocity that is 1.25-times ($1/f_{cyt}$) faster.

The C_3 model could not be solved fully until [Fe_{cell}] was separated into [Fe_{cyt}], [Fe_{mit}], and [Fe_{vac}] components for each of the 8 growth/strain conditions investigated. To do this, we relied on conservation of matter equation (8) but also used published MB spectra and iron concentrations for WT and ΔΔ cells and organelles **(10, 65)**. The spectra were separated into contributions from the eight iron-containing components specified by the C_9 model. Then we combined particular components into cytosol, mitochondria, or vacuoles locations (as dictated by the model of Figure 1). Finally, we summed the iron concentrations for all of the components assigned to each compartment to afford [Fe_{cyt}], [Fe_{mit}], and [Fe_{vac}]. Results are given in Table 1.

Development of the C_9 model

Before explaining how MB spectra were decomposed, we introduce the components of the C_9 model. Component *C* represents cytosolic Fe, presumed to be a NHHS Fe^{2+} complex. This component can move into vacuoles and mitochondria, but it can also stay in cyt and react to form component *CIA*. *CIA* represents the sum of the ISCs and low-spin Fe^{2+} hemes in this collective compartment. Numerous ISCs are found in the cytosol and nucleus **(171,175)**, justifying the inclusion of CIA in the model. *FM* represents the pool of NHHS Fe^{2+} ions in mitochondria, *FS* represents ISCs and heme centers in the organelle, and *MP* refers to mitochondrial nanoparticles. Components *FM*, *FS*, and *MP* have all been characterized experimentally. *F2* and *F3* are NHHS Fe^{2+} and Fe^{3+} species in vacuoles, and *VP* represent vacuolar nanoparticles; they have also been characterized experimentally **(149,116)**. When *C* enters the vacuoles, this component

becomes *F2* some of which oxidizes to *F3*. Some *F3* converts into *VP*. When *C* enters mitochondria, it converts into *FM*, which serves as feedstock for *FS*. The *FS* metal centers are viewed as being installed into the respiratory complexes on the inner membrane, which then catalyze the reduction of O_2 to water. *FM* can also react with O_2 in the matrix to generate *MP* and ROS. ROS exhibits the exact behavior of *MP* so is not formally included in the model.

Decomposing MB features into Modeling Components

MB spectroscopy detects all of the ^{57}Fe in samples. However, resolution is limited so the spectra under consideration were subdivided into just four groups of iron centers, including NHHS Fe^{3+}, NHHS Fe^{2+}, the central doublet (CD), and Fe^{3+} oxyhydroxide nanoparticles. The CD represents $[Fe_4S_4]^{2+}$ clusters and low-spin Fe^{2+} heme centers; the two cannot be resolved. Other minor spectral features (HS Fe^{2+} hemes and $[Fe_2S_2]$ clusters) can be resolved and quantified, but we decided to bundle them with the CD since they are not individually represented in the model. The absolute concentrations associated with each group were obtained by multiplying the associated percentages by $[Fe_{cell}]$. The conservation of mass requires that

$$\left\{\begin{array}{l}[Fe_{cell}]=[Fe^{II}{}_{cell}]+[CD_{cell}]+[NP_{cell}]+[Fe^{III}{}_{cell}]\\ [Fe_{mit}]=[Fe^{II}{}_{mit}]+[CD_{mit}]+[NP_{mit}]+[Fe^{III}{}_{mit}]\end{array}\right\} \quad (15).$$

These MB features were assigned to the following combinations of modeling components.

$$\left\{\begin{array}{l}[Fe^{II}{}_{cell}] = f_{cyt}\cdot[C] + f_{mit}\cdot[FM] + f_{vac}\cdot[F2]\\ [CD_{cell}] = f_{cyt}\cdot[CIA] + f_{mit}\cdot[FS]\\ [NP_{cell}] = f_{mit}\cdot[MP] + f_{vac}\cdot[VP]\\ [Fe^{III}{}_{cell}] = f_{vac}\cdot[F3]\\ [Fe^{II}{}_{mit}] = [FM]\\ [CD_{mit}] = [FS]\\ [NP_{mit}] = [MP]\\ [Fe^{III}{}_{mit}] = [MP]\end{array}\right\} \quad (16).$$

Then these species were organized into the three cellular compartments by summing contributions as described by (17).

$$\left\{\begin{array}{l}[Fe_{cyt}] = [C] + [CIA]\\ [Fe_{mit}] = [FM] + [FS] + [MP]\\ Fe_{vac}] = [F2] + [F3] + [VP]\end{array}\right\} \quad (17).$$

The one component of the C_9 model that could not be determined in this way with reasonable accuracy was *C*. Thus, we relied on published reports to estimate the concentration of cytosolic Fe^{2+}. Petrat et al. **(176)** used a fluorescent chelator to quantify the concentration of labile iron in hepatocytes and liver endothelial cells at 5 – 7 μM, and we assumed similar values for iron-sufficient WT yeast cells. We further assumed that the concentration of cytosolic Fe^{2+} increases with increasing nutrient iron concentrations, and that [C] in iron-sufficient ΔΔ cells is higher than in WT cells (because the absence of

Mrs3/4 should block import of *C* into mitochondria). Within these constraints, we assigned the concentrations of *C* to those listed in Table 3. MB spectral

decompositions, along with these relationships and assumptions, were sufficient to generate concentrations for all other modeling components (Table 3).

Table 5.3: Estimated concentrations (in μM) of the iron-containing components of the C_9 model. For each entry, the top number is data-based while the bottom number is the corresponding simulated value. The sum of these concentrations, after multiplying each by their respective fractional volume, approximately equals [Fe_{cell}]. The sum of the concentrations of each species located in each compartment (cyt, mitochondria, and vacuoles) approximately equals [Fe_{cyt}], [Fe_{mit}], and [Fe_{vac}], respectively.

[N]	[C]	[CIA]	[FM]	[FS]	[MP]	[F2]	[F3]	[VP]
WT								
1	2.5 1.5	92 16	60 110	320 160	0 90	60 14	0 85	0 0
2	3 2.7	84 79	80 190	290 380	60 62	96 43	780 590	0 2.6
11	4 5.6	250 210	140 430	380 730	30 71	320 250	1900 540	0 320
41	5 6.0	380 220	210 470	480 750	0 75	450 290	4600 5200	0 440
ΔΔ								
1	3 2.6	130 310	60 3.6	40 0.8	530 580	140 2,300	400 57	0 0.6
2	4 4.3	160 470	60 100	40 350	530 140	1,300 180	3,400 4,600	170 2,000
11	8 8.6	340 340	85 150	300 330	300 70	950 1,200	11,000 11.000	6,400 7,500
41	10 9.2	280 280	110 140	560 260	80 71	1,000 1,600	22,000 10,000	13,000 5,700

Solving the C_3 model:

Once [Fe_{cyt}], [Fe_{mit}] and [Fe_{vac}] were determined, we determined rates of import into each compartment, R_{cyt}, R_{mit}, and R_{vac} as defined by (13). Data-based import rates $R_{cyt\text{-}dat}$, $R_{mit\text{-}dat}$, and $R_{vac\text{-}dat}$ for the 8 conditions are shown as circles in Figure 3 and are tabulated in Table 1. The rate of iron import into "cyt" but not exported into mitochondria or vacuoles equals $R_{cyt} - R_{mit} - R_{vac}$. According to these rates, iron flows faster into the cyt of ΔΔ cells, and slower into their mitochondria, relative to in WT cells. This makes sense because the absence of Mrs3/4 in ΔΔ cells should hinder Fe_{cyt} from entering mitochondria.

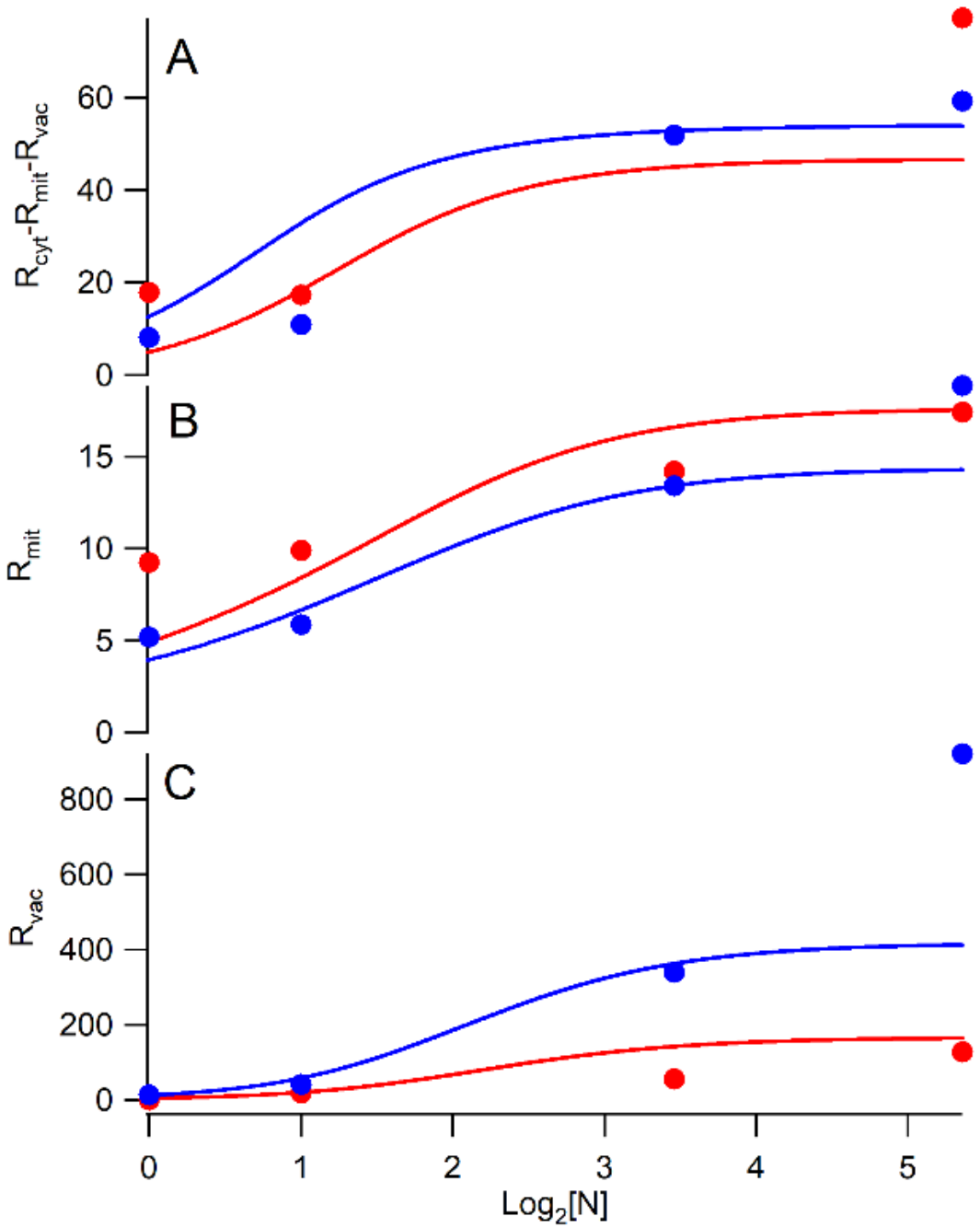

Figure 5.3: Rates of iron import into the cytosol *only* (A), into the mitochondria (B), and into vacuole (C) according to the C_3 model. Color coding is the same as in Figure 2.

We next assigned rate-law expressions to $R_{mit\text{-}sim}$ and $R_{vac\text{-}sim}$. We considered two forms for rate-laws, namely a mass-action form $R_i = k_i[*]^n$ and a Michaelis-Menten form $V_i[*]^n/\{K_M+[*]^n\}$ where [*] indicates the concentration of one or more of the C_9 modeling components. The latter form was used only if the simpler mass-action form was unable to generate reasonable simulations to the relevant data-based rates. The simple mass-action form was acceptable for $R_{mit\text{-}sim}$ whereas $R_{vac\text{-}sim}$ required a Michaelis-Menten term. The terms were optimized using an ERR function. One complication was that we used C rather than Fe_{cyt} as substrate for these processes. This was done so that the resulting rates would not change when solving the C_9 model. The following rate-law expressions were ultimately selected.

$$\left\{\begin{array}{l} R_{mit-sim} = k_{mit}[C] \\ R_{vac-sim} = \dfrac{R_{vac-\max}[C]^{nvac}}{K_{vac}^{nvac}+[C]^{nvac}} \end{array}\right\} \quad (18).$$

Optimized $R_{mit\text{-}sim}$ and $R_{vac\text{-}sim}$ values were used along with $R_{cyt\text{-}sim}$ (obtained from C_1 model), to construct a full set of ODEs (equations (S3) – (S5)) describing the C_3 model. Once combined in this way, all of the parameters associated with the three rates $R_{cyt\text{-}sim}$, $R_{mit\text{-}sim}$, and $R_{vac\text{-}sim}$ were re-optimized against data-based rates using an ERR function. To do this, each parameter was increased and decreased by 10% as all other parameters were fixed; candidate values that lowered ERR were then fixed as the next parameter on the list was varied. The process was repeated for a second round except that each parameter was adjusted ± 5%. In the third and final round, each parameter was adjusted ± 1%. The final plots are shown in Figure 3.

The C_4 model

We next solved the C_4 model which is identical to the C_3 model except that [Fe_{cyt}] is separated into [CIA] and [C] components. To obtain [CIA], we subtracted the values of [C] given in Table 3 from [Fe_{cyt}], resulting in the *CIA* concentrations listed in Table 3. These values were multiplied by α_{cell} to generate $R_{cia\text{-}dat}$. We assumed a Michaelis-Menten expression to generate an $R_{cia\text{-}sim}$ function that minimized differences with $R_{cia\text{-}dat}$ with acceptable fidelity.

Solving the C_9 model

The C_9 model could now be solved. The derivative of (17) is

$$\left\{\begin{array}{l} \dfrac{d[Fe_{cyt}]}{dt} = \dfrac{d[C]}{dt} + \dfrac{d[CIA]}{dt} \\ \dfrac{d[Fe_{mit}]}{dt} = \dfrac{d[FM]}{dt} + \dfrac{d[FS]}{dt} + \dfrac{d[MP]}{dt} \\ \dfrac{d[Fe_{vac}]}{dt} = \dfrac{d[F3]}{dt} + \dfrac{d[VP]}{dt} \end{array}\right\} \qquad (19).$$

According to the mechanism of Figure 1, bottom panel, the rates of change in the concentrations of the two cyt iron species are

$$\left\{\begin{array}{l} \dfrac{d[C]}{dt} = R_{cyt} - R_{mit} - R_{vac} - R_{cia} - \alpha_{cell}[C] \\ \dfrac{d[CIA]}{dt} = R_{cia} - \alpha_{cell}[CIA] \end{array}\right\} \qquad (20).$$

Adding the two equations of (20) affords the first equations of (19) and (10). The rate of change of the concentrations of the iron-containing species in the mitochondria is given by (21).

$$\left\{\begin{array}{l}\dfrac{d[FM]}{dt}=\dfrac{V_{cyt}}{V_{mit}}R_{mit}-R_{isu}-R_{mp}-\alpha_{cell}[FM]\\ \dfrac{d[FS]}{dt}=R_{isu}-\alpha_{cell}[FS]\\ \dfrac{d[MP]}{dt}=R_{mp}-\alpha_{cell}[MP]\end{array}\right\} \quad (21).$$

Summing the equations of (21) affords the second equations of (19) and (10). Similarly for vacuoles,

$$\left\{\begin{array}{l}\dfrac{d[F2]}{dt}=\dfrac{V_{cyt}}{V_{vac}}R_{vac}-R_{23}-\alpha_{cell}[F2]\\ \dfrac{d[F3]}{dt}=R_{23}-R_{vp}-\alpha_{cell}[F3]\\ \dfrac{d[VP]}{dt}=R_{vp}-\alpha_{cell}[VP]\end{array}\right\} \quad (22).$$

Summing the equations of (22) affords the third equations of (19) and (10). Thus, the ODE system for the iron-components of the C_9 model "collapses" down to that of the C_3 model when the components of the three regions are summed appropriately. In an expanding steady state, the left-hand-sides of (20), (21), and (22) equal zero such that

$$\left\{\begin{array}{l} R_{cyt} = R_{mit} + R_{vac} + R_{cia} + \alpha_{cell}[C] \\ R_{mit} = \dfrac{V_{mit}}{V_{cyt}}\left(R_{isu} + R_{mp} + \alpha_{cell}[FM]\right) \\ R_{vac} = \dfrac{V_{vac}}{V_{cyt}}\left(R_{23} + \alpha_{cell}[F2]\right) \\ R_{cia} = \alpha_{cell}[CIA] \\ R_{isu} = \alpha_{cell}[FS] \\ R_{vp} = \alpha_{cell}[VP] \\ R_{23} = R_{vp} + \alpha_{cell}[F3] \\ R_{mp} = \alpha_{cell}[MP] \end{array}\right\} \qquad (23).$$

Data-based and simulation-based values of R_{cyt}, R_{mit}, R_{vac}, and R_{cia} have already been obtained. Using the experimental values of α_{cell} and the values of model-component concentrations listed in Table 3, we constructed data-based rates for the formation of each C_9 component using data from the 4 nutrient conditions in WT and ΔΔ cells. $R_{vp\text{-}dat}$ was then used along with α_{cell} and [F3] to generate $R_{23\text{-}dat}$ as defined in (23). The next step was to assign a rate-law expression to each of the remaining rates associated with the C_9 model as listed in (23) – expressions that depended solely on other C_9 components. Once assigned, a system of ODEs could be defined in these terms (S6) – (S14) and integrated numerically to afford our final simulations.

Table 5.4: Rates of formation of each component of the C_9 model, for different strains and nutrient concentrations. Data-based rates are the top entries; simulated rates are bottom entries.

[N]	R_C	R_{CIA}	R_{isu}	R_{F3}	R_{VP}	R_{FM}	R_{FS}	R_{MP}
WT								
1	0.45 0.26	17 3.0	52 29	0 15	0 0	11 19	58 29	0 16
2	0.55 0.52	15 15	53 73	140 110	0 0.5	15 36	53 73	11 12
11	0.81 1.1	50 43	78 150	390 910	0 65	29 87	78 150	6.1 14
41	1.0 1.2	76 44	97 150	930 1000	0 89	42 95	91 150	0 15
ΔΔ								
1	0.12 0.11	8.0 13	2.4 0.014	24 0.75	0 0	3.6 0.13	2.4 0.01	32 24
2	0.28 0.29	11 33	2.7 27	230 320	12 140	4.1 7.2	2.7 27	36 7.1
11	1.2 1.3	51 52	45 50	1,600 1,600	960 1,100	13 22	45 50	45 11
41	1.9 1.7	57 52	110 48	4,500 2,000	2,600 1,100	22 27	110 48	15 13

We first assigned rate-law expressions for the remaining C_9 components that did not involve O_2, namely R_{vp} and R_{isu}. The expressions k_{vp}·[F3] and k_{isu}·[FM] were sufficient to simulate $R_{vp\text{-}dat}$ and $R_{isu\text{-}dat}$ with acceptable fidelity. The simple rate-law $R_{23\text{-}sim} = k_{23}$·[F2] was unable to simulate the data. The problem was that cells grown under low-iron conditions have an unusually high concentration of NHHS Fe^{2+}, only a small percentage of which can be assigned to *FM* in mitochondria. Under these conditions, it seemed unlikely that this Fe^{2+} could be cytosolic, as there should be low concentrations of [C] (as given in Table 3). The only remaining option (in our model) to could account

for the extra Fe^{2+} was component *F2* in vacuoles. As cells become iron-sufficient, this effect disappears as [F3] increases. We presumed that the extra *F2* converted into *F3* under these conditions. To coordinate this behavior with increasing cellular iron-sufficiency, we incorporated a Reg_{+FS} into the $R_{23\text{-}sim}$ rate-law expression, as we have done previously **(154)**. In summary, the following rate-law expressions were used in solving the C_9 model.

$$\left\{\begin{array}{l} R_{cia} = \dfrac{R_{cia-\max}[C]^{ncia}}{K_{cia}^{ncia} + [C]^{ncia}} \\ R_{isu} = \dfrac{R_{isu-\max}[FM]^{nisu}}{K_{isu}^{nisu} + [FM]^{nisu}} \\ R_{vp} = k_{vp}[F3]^{nvp} \\ R_{23} = k_{23}[F2]\left(\dfrac{1}{1+\left(\dfrac{[FS]_{sp}}{[FS]}\right)^{n23}}\right) \end{array}\right\} \quad (25).$$

Effect of O_2

O_2 plays a critical role in the C_9 model as it reacts with *FM* to generate *MP*. O_2 is constantly diffusing into the matrix (in accordance with rate R_{O2}) and is reduced to H_2O by cytochrome c oxidase on the inner membrane. We used [FS] as a proxy for oxidase activity such that the rate of respiration (R_{res}) was assumed to be proportional to both [FS] and [O_2]. Collectively, these processes determine the dissolved O_2 concentration in the matrix, as described by

$$\frac{d[O_2]}{dt} = R_{O2} - R_{mp} - R_{res} - \alpha_{cell}[O_2] \quad (26).$$

Under an expanded steady-state condition

$$R_{O2} = R_{mp} + R_{res} + \alpha_{cell}[O_2] \quad (27).$$

R_{O2} was presumed to be proportional to the *difference* in the O_2 concentration in the cytosol (called $[O_2]_{cyt}$ – assumed to be fixed at 100 μM) and the concentration of O_2 in the matrix ($[O_2]$). With rate-law expressions included, (27) becomes

$$k_{O2}([O_2]_{cyt} - [O_2]) = k_{mp}[FM][O_2] + k_{res}[FS][O_2] + \alpha_{cell}[O_2] \quad (28).$$

Rearrangement yields

$$[O_2] = [O_2]_{cyt} \frac{k_{O2}}{k_{O2} + k_{mp}[FM] + k_{res}[FS] + \alpha_{cell}} \quad (29).$$

Since all numbers in (29) are positive, the term in the numerator serves to increase $[O_2]$ while those of the denominator serve to decrease it. [FM], [FS], and α_{cell} are controlled by other aspects of the model, and so those parameters were not altered in order to generate the behavior desired for $[O_2]$ vs [N] in WT vs. ΔΔ cells. This behavior was essentially controlled by the three unassigned parameters, k_{O2}, k_{res}, and k_{mp} contained in equation (29).

The overall objective of the model was to assess, on a quantitative basis, the ability of the model of Figure 1 to explain how ΔΔ mitochondria transition from a diseased state (dominated by nanoparticles, *MP* in the model) when cells are grown in low-iron media, to a healthy state (dominated by ISCs and hemes, *FS* in the model)

when they are grown in high-iron media. We also wanted WT mitochondria to be healthy regardless of the iron concentration in the growth medium. The only molecular-level difference between WT and ΔΔ cells should be the rates at which iron enters the mitochondria (R_{mit}) and cells (R_{cyt}) – which have already been set by solving the simpler versions of the model. The key to achieving this desired behavior, according to our model, was to vary the concentration of O_2 in the matrix. In WT mitochondria, [O_2] should be low at all [N] whereas in ΔΔ mitochondria, [O_2] should be high at low [N] and low at high [N]. We needed to generate an abrupt decline of [O_2] in ΔΔ mitochondria as [N] increases while keeping [O_2] low in WT mitochondria at all [N]. *And* we needed to make this happen only by adjusting k_{O2}, k_{res}, and k_{mp}.

The [O_2] concentration in the matrix has not been measured directly. We estimated [O_2] to be in the ballpark of 1 – 10 μM for iron-sufficient WT mitochondria as this value is similar to the K_M for O_2 reduction by cytochrome c oxidase **(177)**. We had [MP] vs. [N] data that could be used to help optimize these parameters (especially k_{mp}), but they were insufficient.

We also considered the known behavior of ΔYfh1 cells, which we have explained using a similar model **(154)**. ΔYfh1 mitochondria contain excessive levels of nanoparticles. The previous model explained the excessive nanoparticles as being due to a lack of *FS* (respiratory complexes), which allows for O_2 to diffuse into the matrix, react with *FM*, and generate *MP*. This behavior (obtained by setting $R_{isu} = 0$) provided another constraint on possible solutions for the current problem. Another consideration

was that respiring WT cells grown at all [N] do not accumulate *MP* in their mitochondria.

After extensive trials, we obtained values of k_{O2}, k_{res}, and k_{mp} (listed in Table 2) that generated the best overall behavior. However, despite our efforts to satisfy all of these constraints, we could not completely eliminate the formation of *MP* in WT mitochondria while also having *MP* accumulate at high levels in ΔYfh1 mitochondria. Two additional changes were required, namely to increase k_{mit} of WT cells 2-fold and decrease k_{mit} of ΔΔ cells 1.3-fold, both relative to the values obtained by solving the simpler C_3 version of the model. The adjustment of k_{mit} in ΔΔ cells was minor whereas the adjustment for WT cells implies that the concentration of iron in WT mitochondria is actually 2-fold higher than given by the data used for simulations.

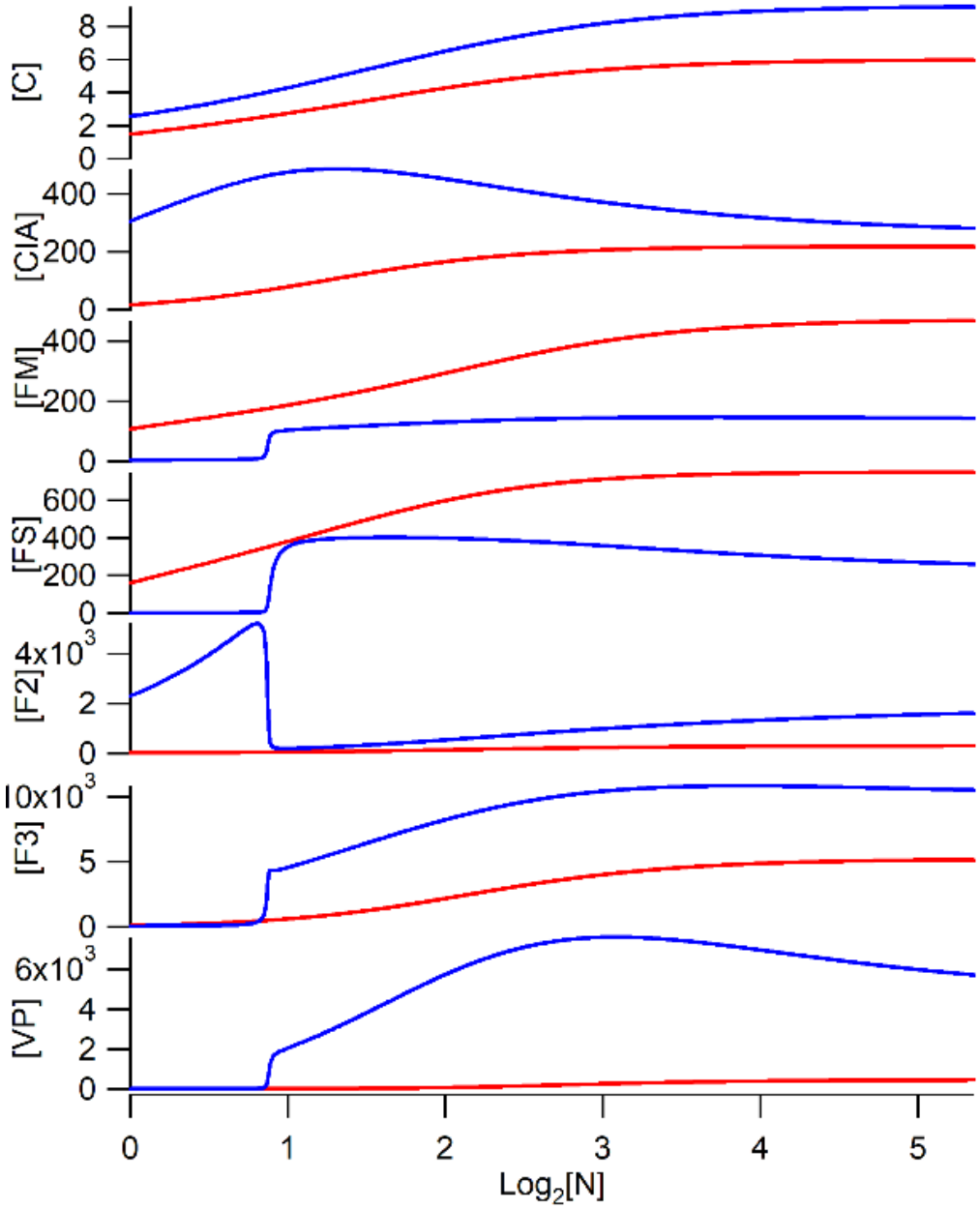

Figure 5.4: Simulated concentrations of the iron-containing components in the C_9 version of the model as a function of nutrient iron concentration (in μM). Blue, ΔΔ cells; Red, WT cells. The component plotted is indicated near to the trace.

Final Optimization and sensitivity analysis

Once each parameter was optimized individually as described above, we re-optimized the entire system by changing one component at a time while holding the others fixed, as described above. For the C_1, C_3/C_4, and C_9 model variants, the best-fit ERR values were 0.32, 0.39, and 0.72, respectively. A sensitivity analysis was performed for each parameter by taking the average of the ± 1% ERR values, and normalizing the average to the optimal ERR for that parameter **(154)**. Highest sensitivity values (Table 2) indicate which parameters have the greatest impact on the overall fit of the model; *nisu* (Hill coefficient for ISC assembly), α_{max} (growth rate), and K_N (K_M for nutrient iron import) were the most sensitive.

Simulation plots showing the concentrations of each iron-containing component of the C_9 model (except for nanoparticles) is shown in Figure 4. In line with expectations, simulated concentrations of most components increased as the nutrient iron concentration increased. Simulated concentrations of cytosolic and vacuolar components in ΔΔ cells were higher than in WT cells, whereas the simulated concentrations of mitochondrial components *FS* and *FM* in ΔΔ cells were lower than in WT cells. Vacuolar iron is dominated by *F2* under iron-deficient conditions and by *F3* under iron-sufficient conditions.

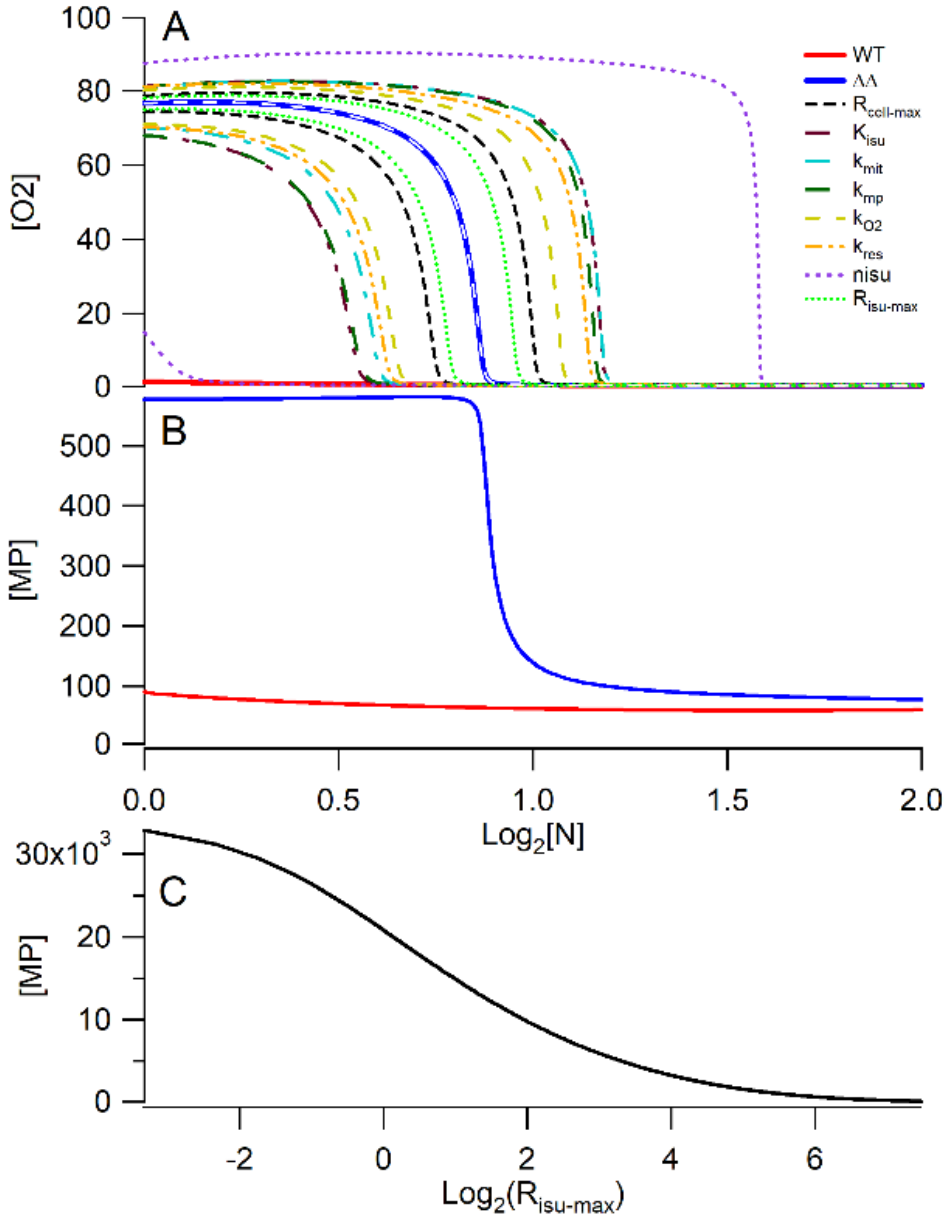

Figure 5.5: "Waterfall" Plots of Mitochondrial oxygen and nanoparticle concentrations (in μM). Optimized simulated [O_2] (in panel A) and [MP] (in panel B) in mitochondria of ΔΔ (solid blue line) and WT (solid red line) cells, plotted against the nutrient iron concentration (Log_2[N]). Only certain parameters affected curve shape, as illustrated by the other traces in which the indicated parameters were altered ± 10% of their optimized values while holding all other parameters fixed. Changing other parameters yields traces (e.g. k_{23} in the white dashed line) that had no effect on the plots. Panel C is a plot of [MP] vs. $R_{isu\text{-}max}$, the maximum rate of *FS* formation. Low $R_{isu\text{-}max}$ values simulate the slow rate of ISC assembly in yfh1Δ cells, while higher values reflect WT conditions.

Waterfall Effect on O_2 and nanoparticles

Simulations of mitochondrial O_2 and nanoparticle concentrations are shown in the "waterfall" plots of Figure 5. This nonlinear effect simulates the observed behavior of ΔΔ mitochondria. Mitochondria from iron-deficient ΔΔ cells contain mostly nanoparticles and are responsible for the slow-growth defect. However, mitochondria from these cells recover when ΔΔ cells are grown in iron-sufficient medium. The plot simulates this recovery. As [N] increases, [O_2] levels decline because increasing concentrations of respiratory complexes (*FS*) prevent O_2 from diffusing into the matrix and reacting with *FM*. This allows more *FS* to be made with allows even less O_2 into the matrix. This vicious cycle leads to the observed nonlinear behavior. The same behavior is observed for the formation of nanoparticles (Figure 5, panel B). Other traces to either side of the best-fit [O_2] trace represent the effect of increasing/decreasing one parameter while keeping all others fixed. Since the percentage change for each parameter was the same, the parameters that influence the shape of the "waterfall" more dramatically are located on the extremes. A similar waterfall effect is obtained by lowering R_{isu} (Figure 5, panel C) which simulates the effect of lowering the Yfh1 concentration in yeast mitochondria (or the frataxin concentration in human mitochondria). WT mitochondria do not exhibit the waterfall effect because they can exclude O_2 from the matrix at all [N] considered.

Conclusions

Comparison to Previous Model

The model developed here represents a major advance relative to our previous model **(154)**. Both simulate iron import and trafficking in a growing yeast cell, both include the three regions (cytosol, mitochondria, and vacuoles), and both involve the import of a single nutrient iron form *N*. The major difference between the two models is their complexity level, method of optimization, and predictive power. The previous model included ~ 35 adjustable parameters (Table S2 of **(154)**) whereas the current model includes only 23 (Table 2). The previous model was optimized by guessing an initial set of values and minimizing an error function. However, the most important difference is that *the previous model does not predict the waterfall behavior described above*.

Our current model was solved at different levels of complexity. We solved the simpler variants first, and discovered that the parameters obtained could be transferred to the more complex variants. This multi-tiered strategy was helpful because the parameters obtained by fitting the simpler models used more reliable data. Another strategic difference in modeling approaches was that we excluded all but one Reg function in the current model. This made the current model more responsive to changing parameters and allowed better comprehension of inherent behavior.

In the end, only four parameters differed between ΔΔ and WT simulations, namely $R_{cyt\text{-}max}$, k_{mit}, k_{vp}, and K_{α}. *All other assigned parameter values were identical between the two genetic strains.* The ability of the model to reproduce ΔΔ and WT

behavior with such few differences is remarkable. Moreover, we can easily rationalize why at least half of these parameters should be different. A 4.6-fold reduction of k_{mit} for ΔΔ cells makes sense because Mrs3/4, the high-affinity importers into mitochondria are deleted in this strain. $R_{cyt\text{-}max}$ is 2-times higher for ΔΔ cells because iron is dysregulated in these cells so expression of the Ftr1/Fet3 complex on the plasma membrane should be higher. Explaining why K_α should be 30-times higher in ΔΔ cells is more difficult. K_α is a K_M-like parameter which reflects the sensitivity of the growth rate to changes in the nutrient iron concentration [N]. For some reason, the growth of iron-deficient ΔΔ cells is 30 times less sensitive to increases in [N] than are comparable WT cells. Perhaps this reflects difficulties in flowing sufficient iron into iron-deficient ΔΔ mitochondria to support robust respiratory cell growth. Why k_{vp} is 2-fold higher in ΔΔ cells is even more difficult to explain; it implies that the rate of vacuolar nanoparticle formation is faster in ΔΔ cells than in WT cells. But why? The actual mechanism of vacuolar nanoparticle formation is undoubtedly more complicated than is represented in our current model. However, it is a tribute to the model that it has the ability to highlight this effect.

Predictive Power of the model

Mathematical models *might* have predictive power, but this is not guaranteed. This ability is related to how close the assumed mechanism and assigned kinetic parameters correspond to reality. We have attempted to make our model predictive by keeping it simple and well-grounded experimentally. This was a challenge given the

complexity of the process under investigation and the limited amount of relevant data available.

Our model can be used to predict the effect of O_2 on iron metabolism in yeast cells. It predicts that the iron in mitochondria of Yfh1-deficient cells that have been grown under microaerophilic conditions should predominantly be *FM* (i.e. NHHS Fe^{2+}). We are currently examining a Yfh1-deficient strain of yeast, and found that this is indeed the case (data not shown). Our model also predicts that O_2 should not affect vacuolar iron (it should still be present mainly as *F3* (Fe^{3+}) under microaerophilic conditions). However, this prediction is not realized by our current experiments, highlighting a deficiency in this particular aspect of the model. We believe that this iterative approach of prediction→testing→remodeling will yield major new insights in understanding iron import, trafficking, and regulation in eukaryotic cells. We are currently using this approach in our studies of the Yfh1-deficient strain.

Finally, the same strategy could be applied to model the import and trafficking of any micronutrient. The concentration of the nutrient (or its derivatives) in whole cells and in various organelles and cytosol should be known as should exponential growth rates. Obvious candidates include other metals such as Cu, Mn, Zn, Mo, Co. The same approach could be used to examine the import and trafficking of Pt anticancer drugs into human cells. A better understanding of how such drugs are trafficked intracellularly might provide new insights for treating cancer.

Funding: This work was supported by the National Institutes of Health (GM127021) and the Robert A. Welch Foundation (A1170).

Acknowledgements: We thank Ivan V. Surovtsev (Yale University) for suggesting equation (12).

Supplemental Material

ODE for the C_1 Model:

$$\frac{d[Fe_{cell}]}{dt} = \frac{R_{\text{cell-max}}[N]^{sens}}{K_N^{\ sens} + [N]^{sens}} - \alpha_{cell}[Fe_{cell}] \qquad (S1)$$

$$\alpha_{cell} = \frac{\alpha_{\max}[N]}{K_\alpha + [N]} \qquad (S2)$$

ODEs for the C_3 Model:

$$\frac{d[Fe_{cyt}]}{dt} = \frac{R_{\text{cyt-max}}[N]^{sens}}{K_N^{sens} + [N]^{sens}} - k_{mit}[C] - \frac{R_{\text{vac-max}}[C]^{nvac}}{K_{vac}^{nvac} + [N]^{nvac}} - \alpha_{cell}[Fe_{cyt}] \qquad (S3)$$

$$\frac{d[Fe_{mit}]}{dt} = \frac{f_{cyt}}{f_{mit}} k_{mit}[C] - \alpha_{cell}[Fe_{mit}] \qquad (S4)$$

$$\frac{d[Fe_{vac}]}{dt} = \frac{f_{cyt}}{f_{vac}} \frac{R_{\text{vac-max}}[C]^{nvac}}{K_{vac}^{nvac} + [N]^{nvac}} - \alpha_{cell}[Fe_{vac}] \qquad (S5)$$

ODEs for the C_9 Model:

$$\frac{d[C]}{dt} = \frac{k_{cyt}[N]^{sens}}{K_N^{sens} + [N]^{sens}} - \frac{k_{vac}[C]^{nvac}}{K_{vac}^{nvac} + [C]^{nvac}} - k_{mit}[C] - \frac{k_{cia-\max}[C]^{ncia}}{K_{cia}^{ncia} + [C]^{ncia}} - \alpha_{cell}[C] \qquad (S6)$$

$$\frac{d[CIA]}{dt} = \frac{k_{cia-\max}[C]^{ncia}}{K_{cia}^{ncia} + [C]^{ncia}} - \alpha_{cell}[CIA] \qquad (S7)$$

$$\frac{d[F2]}{dt} = \frac{f_{cyt}}{f_{vac}} \frac{R_{vac-\max}[C]^{nvac}}{K_{vac}^{nvac} + [C]^{nvac}} - k_{23}[F2]\left(\frac{1}{1+\left(\frac{[FS]_{sp}}{[FS]}\right)^{n23}}\right) - \alpha_{cell}[F2] \qquad (S8)$$

$$\frac{d[F3]}{dt} = k_{23}[F2]\left(\frac{1}{1+\left(\frac{[FS]_{sp}}{[FS]}\right)^{n23}}\right) - k_{vp}[F3]^{nvp} - \alpha_{cell}[F3] \qquad (S9)$$

$$\frac{d[VP]}{dt} = k_{vp}[F3]^{nvp} - \quad a_{cell}[VP] \qquad (S10)$$

$$\frac{d[FM]}{dt} = \frac{f_{cyt}}{f_{mit}} k_{mit}[C] - \frac{R_{isu-\max}[FM]^{nisu}}{K_{isu}^{nisu} + [FM]^{nisu}} - k_{mp}[FM][O2] - \alpha_{cell}[FM] \qquad (S11)$$

$$\frac{d[FS]}{dt} = \frac{R_{isu-\max}[FM]^{nisu}}{K_{isu}^{nisu} + [FM]^{nisu}} - \alpha_{cell}[FS] \qquad (S12)$$

$$\frac{d[MP]}{dt} = k_{mp}[FM][O2] - \alpha_{cell}[MP] \qquad (S13)$$

$$\frac{d[O2]}{dt} = k_{O2}(100 - [O2]) - k_{mp}[FM][O2] - k_{res}[FS][O2] - \alpha_{cell}[O2] \qquad (S14)$$

CHAPTER VI

FERRIC IONS ACCUMULATE IN THE WALLS OF METABOLICALLY INACTIVATING SACCHAROMYCES CEREVISIAE CELLS AND ARE REDUCTIVELY MOBILIZED DURING REACTIVATION*

Summary

Mössbauer and EPR spectra of fermenting yeast cells before and after cell wall (CW) digestion revealed that CWs accumulated iron as cells transitioned from exponential to post-exponential growth. Most CW iron was mononuclear nonheme high-spin (NHHS) Fe^{3+}, some was diamagnetic and some was superparamagnetic. A significant portion of CW Fe was removable by EDTA. Simulations using an ordinary-differential-equations-based model indicated that cells accumulate Fe as they become metabolically inactive. When dormant Fe-loaded cells were metabolically reactivated in Fe-deficient bathophenanthroline disulfonate (BPS)-treated medium, they grew using Fe that had been mobilized from their CWs AND using trace amounts of Fe in the Fe-deficient medium. When grown in Fe-deficient medium, Fe-starved cells contained the lowest cellular Fe concentrations reported for a eukaryotic cell. During metabolic reactivation of Fe-loaded dormant cells, Fe^{3+} ions in the CWs of these cells were mobilized by reduction to Fe^{2+}, followed by release from the CW and reimport into the cell. BPS short-circuited this process by chelating mobilized and released Fe^{2+} ions

---

* This work was originally published in Metallomics, reproduced from Ref # **288** with permission from the Royal Society of Chemistry

before reimport; the resulting $Fe^{2+}(BPS)_3$ complex adsorbed on the cell surface. NHHS Fe^{2+} ions appeared transiently during mobilization, suggesting that these ions were intermediates in this process. In the presence of chelators and at high pH, metabolically inactive cells *leached* CW Fe; this phenomenon probably differs from metabolic mobilization. The iron regulon, as reported by Fet3 levels, was not expressed during post-exponential conditions; Fet3p was maximally expressed in exponentially growing cells. Decreased expression of the iron regulon and metabolic decline combine to promote CW Fe accumulation.

Introduction

Although commonly considered an *extracellular* structure, the cell wall (CW) is actually an *intracellular* component of fungal cells **(78,79,80,81)**. It is synthesized from cellular components that are under the genetic control of the cell - about 20% of the genes in *Saccharomyces cerevisiae* affect CW construction **(178,179)** – and the CW contributes to the cell's ability to survive and flourish. The CW provides structural support and rigidity, and it allows the cell to withstand high osmotic pressure. The CW allows cells to adhere to each other and to solid supports, and is involved in mating and morphogenesis **(80)**. It affects the virulence of pathogenic fungi and thus has biomedical importance **(180,83-86)**.

The CW of budding yeast *S. cerevisiae* consists of an inner glucan frame linked to an outer layer of mannose-based glycoproteins **(181-184)**. The frame includes chitin and β-1,3-glucans. Numerous mannose-based glycoproteins are in the outer layer, most

of which have N-linked glycosidic bonds anchored to the frame via β-1,6-glucan glycosylphosphatidylinositol (GPI) phosphodiester linkages **(179)**. Mature GPI-CW proteins are linked to the frame via their C-termini. Their N-termini extend outward into the environment due to extensive glycosylation of serine and threonine residues in this region.

About 80% of the proteins in the CW can be solubilized using SDS, implying that such proteins are not covalently linked to the frame **(78-81,178-179)**. Most covalently linked manno-proteins are solubilized by gluconase. Other CW proteins are attached to the frame via poorly defined "alkali-sensitive linkages"; these proteins dissociate from the frame under alkali conditions.

The CW constantly remodels as cells grow and divide, and its composition changes with the phase of the cell cycle and growth conditions. The CW acts like a filter to limit access of environmental species to cellular regions within the plasma membrane. Cell *porosity* refers to the degree to which such species pass through the CW and into the cytosol. CW porosity maximizes in the early-exponential phase of growth, and declines dramatically during post-exponential growth **(79)**. Declining porosity is associated with increasing densities of mannan side-chains and disulfide bonds of the gluconase-solubilizable proteins of the outer layer. Porosity is not affected by the more abundant SDS-solubilizable mannoproteins.

From the energy-dispersive TEM spectrum, Vainshtein *et al.*identified iron-containing nanoparticles associated with the CW of yeast cells grown on medium containing high concentrations of iron **(185)**. X-ray microanalyses suggested that these

particles are ferric oxides. To the best of our knowledge, this is the only published physical characterization of CW iron in yeast. Philpott and coworkers determined that ca. 40% of cellular iron is released upon treatment with Zymolyase **(87)**, a mixture of β-1,3-gluconase and proteases that catalyzes the disassembly of the CW and releases mannoproteins **(186)**. This implies that a large percentage of cellular Fe can be found in the CW. The pH of the growth medium influences the amount and speciation of metals that accumulate in the CW **(187)**.

The only *S. cerevisiae* CW proteins known to be involved in Fe metabolism are the "Facilitator of Iron Transport" mannoproteins Fit1, Fit2 and Fit3 **(87)**. These proteins are secreted by the cell and bound to the frame by β-1,6-glucan units through GPI anchors. They contain numerous serine and threonine residues that are heavily glycosylated. FIT1/2/3 genes are part of the Aft1/2-associated *Iron Regulon* **(28)**. These genes are transcribed under Fe-deficient growth conditions but not under Fe-rich ones. Their expression levels change dramatically (60 to 230 fold) depending on the concentration of Fe in the medium **(87)**. Strains lacking these proteins have difficulty importing Fe^{3+} siderophores whereas the import rates of other Fe^{3+} complexes are unaffected. Thus, the Fit1/2/3 proteins facilitate import of *specific* siderophores, rather than all Fe-species that enter the cell. Fit1/2/3-deficient strains behave as though they are Fe-deficient even in Fe-replete medium, another indication that these proteins help import Fe. Less CW Fe is found in Fit-deficient strains, again suggesting that the Fit proteins are involved in Fe import **(87)**. However, other Fe import proteins must also be involved. Fit proteins apparently do not affect CW porosity.

Fe is an essential component of all eukaryotic cells. In yeast cells, environmental Fe must pass through the CW on its way to the cell interior. Much cytosolic Fe is trafficked to the mitochondria where it is used in the biosynthesis of iron-sulfur clusters (ISCs) and heme centers **(1)**. Many such centers are installed into respiratory complexes contained within that organelle. Under Fe-sufficient and Fe-excess conditions, Fe traffics into vacuoles for storage **(55)**. Mitochondria and vacuoles are the two established "hubs" of Fe trafficking in yeast **(65)**.

We recently reported that glucose-grown *S. cerevisiae* cells accumulate Fe in post-exponential stages of growth **(128)**. Based on the spectral characteristics of the Fe that accumulated, we hypothesized that this Fe localized in vacuoles and/or mitochondria as mononuclear nonheme high-spin (NHHS) Fe^{3+} species and nanoparticles. At that time, we were unaware that the CW accumulates Fe. Once aware of this, we wondered whether the accumulated Fe in post-exponential cells might have actually localized in the CW rather than (or in addition to) vacuoles. In this paper, we show that this is indeed the case. Our results suggest that there are multiple types of Fe^{3+} species in the CW, and that CW Fe accumulates when metabolic activity is declining. CW Fe^{3+} is reductively mobilized and released from metabolically reactivated cells. Some of the resulting Fe^{2+} ions are reimported into such cells to support growth. The concentration of CW Fe is high, far greater than that found within the cytosol and internal organelles, indicating that the CW is a third "hub" in fungal iron trafficking.

Methods

Yeast Strain and Media

W303-1B (*MATα, ura3-1, ade2-1, trp1-1, his3-11,15, leu2-3,112*) cells were grown from frozen stocks on standard YPAD agar plates for 3-4 days. The medium contained 1% yeast extract, 2% peptone, 2% (w/v) glucose and 40 mg/L adenine hemisulfate dihydrate. Single colonies were used to inoculate YPD medium. YPD-grown cells were used to inoculate synthetic minimal medium (*MM*) prepared as described **(41)** with 40 μM $^{57}Fe^{3+}$ citrate added **(128)**. We will refer to this medium as $^{57}Fe_{40}B_0$, where the superscript indicates the Fe isotope used, the first subscript indicates the final concentration of added Fe-citrate in μM, and the last subscript indicates the final concentration (also in μM) of added bathophenanthroline disulfonate (BPS). The Fe^{2+} chelator BPS is commonly used to generate Fe-deficient medium. Other MM-based media used include $^{56}Fe_{40}B_0$, $^{57}Fe_1B_{21}$, Fe_0B_{30}, Fe_0B_{100}, Fe_0B_0, and Fe_0B_{100}-*NAB* (Table S1). *NAB* indicates medium prepared with No Amino acids or Bases. Sterile deionized water (DW) was also used as a medium into which cells were inoculated.

Fe-loaded and Fe Starved Cells

A colony was used to inoculate 50 mL of YPD medium, and cells were grown in a shaker at ~ 150 rpm and 30 °C until OD_{600} = 1.0. An aliquot was transferred to $^{57}Fe_{40}B_0$ medium, achieving OD_{600}= 0.01. Cells grown for 5 days will be called *Fe-loaded* or *post-exponential*. Another aliquot was added to $^{57}Fe_1B_{21}$ medium, again

attaining OD_{600} = 0.01. Cells harvested after 15 hrs (OD_{600}≈ 1.0) or 5 days will be called *Fe-starved*.

Cell manipulations and spectroscopy

Cells were harvested by spinning at 2,500×g for 5 min. Cells were washed 3 times with chilled 100 μM EDTA in 150 μM Tris pH 8.0 followed by 3 washings with chilled DW. Resulting cells were packed into 5 mm OD tubes by centrifugation at 4,000×g for 5 min using an ultracentrifuge (Beckman Coulter Optima L-90K) and swinging-bucket rotor (SW 32 Ti). For metal analysis, packed cells were resuspended with an equal volume of DW. Resulting suspensions were incubated overnight in 200 μL of 30% trace-metal grade HNO_3 (Fisher Scientific) at 95 °C, and then diluted with DW before analysis. Fe concentrations were measured by ICP-MS (Agilent 7700×) as described **(146)**. A cell packing efficiency of 70% was used **(50)**. Western Blots were performed as described **(128)**.

For Mössbauer (MB) studies, cells were loaded into MB cups by centrifugation at 5,000×g for 5 min and frozen in liquid N_2. MB spectra were collected on either a model MS4 WRC or LHe6T spectrometer (SEE Co., Edina, MN). Both instruments were calibrated using α-Fe foil at RT. For UV-vis studies, packed cells were diluted with an equal volume of DW and then transferred to a 2 mm pathlength quartz cuvette (NSG Precision Cells, Inc.). Spectra were recorded on a Hitachi 3010 spectrometer possessing a Head-On photomultiplier tube. Absorbances were measured 6 times and results were

averaged and multiplied by 5 to yield the value expected if a 10 mm rather than a 2 mm path-length cuvette had been used.

Dissolved O_2 concentrations

An O_2 probe (24″ long FOXY-T-1000-RTD, Ocean Optics Inc, Dunedin FL) was placed in an iron-free custom glass/titanium bioreactor filled with 24 L of $^{57}Fe_{40}B_0$ medium at 30 °C. The reactor was inoculated with cells that had been grown overnight in YPAD similarly supplemented. Standard purity O_2 gas was bubbled into the bioreactor at a fixed rate of ca. 500 mL/min. The paddle stir-rate was ca. 100 RPM.

Measuring CW Fe release

Cells were grown in the bioreactor for 5 days and then centrifuged and washed twice with water to remove residual medium. Cells were resuspended in water and aliquots were transferred into 50 mL plastic screw-top vials. The vials were centrifuged to yield pellets the volumes of which (ca. 5 mL) were determined from the height of the pellet and the mass of water needed to fill the vial to that height (after the experiment). The volume of the pellet was corrected for packing efficiency. Various treatment buffers (40 mL) were added to each tube at time 0, including: water, 100 μM EDTA (prepared in 150 μM Tris buffer pH 8.0), and 100 μM EDTA plus lyticase (Sigma; 1000 U of lyticase activity per gram of wet packed cell in tube) in SP buffer (1.2 M sorbitol in 50 mM potassium phosphate pH 7.4). At 10 min intervals, 2 mL of solution were removed from each tube and transferred to microfuge tubes and centrifuged. Supernatants were saved

for metal analysis and pellets were washed twice with triple-distilled water or SP buffer (lyticase samples) that lacked chelators or lyticase. The volumes of these pellets and supernatants were measured, and Fe, Mn, Cu, and Zn concentrations were determined. At each buffer condition, the relationship V_{pell}•[Fe_{pell}] + V_{sup}•[Fe_{sup}] equalled a constant number of moles at each time point within an error of ± 10%.

Results and Discussion

Mössbauer and EPR characterization of iron-loaded post-exponential cells before and after CW digestion

Iron accumulates in glucose-grown yeast cells as they transition from exponential to post-exponential growth **(128)**. To test whether that Fe accumulated in the CW, we grew WT cells in $^{57}Fe_{40}B_0$medium and harvested them during exponential (OD_{600} = 0.2, 0.4, and 0.7) and post-exponential (OD_{600} = 1.5, 5 days after inoculating) growth phases. Cells were washed 3 times with water, 100 μM EDTA, or EDTA plus lyticase, an enzyme that, like zymolyase, digests CWs.

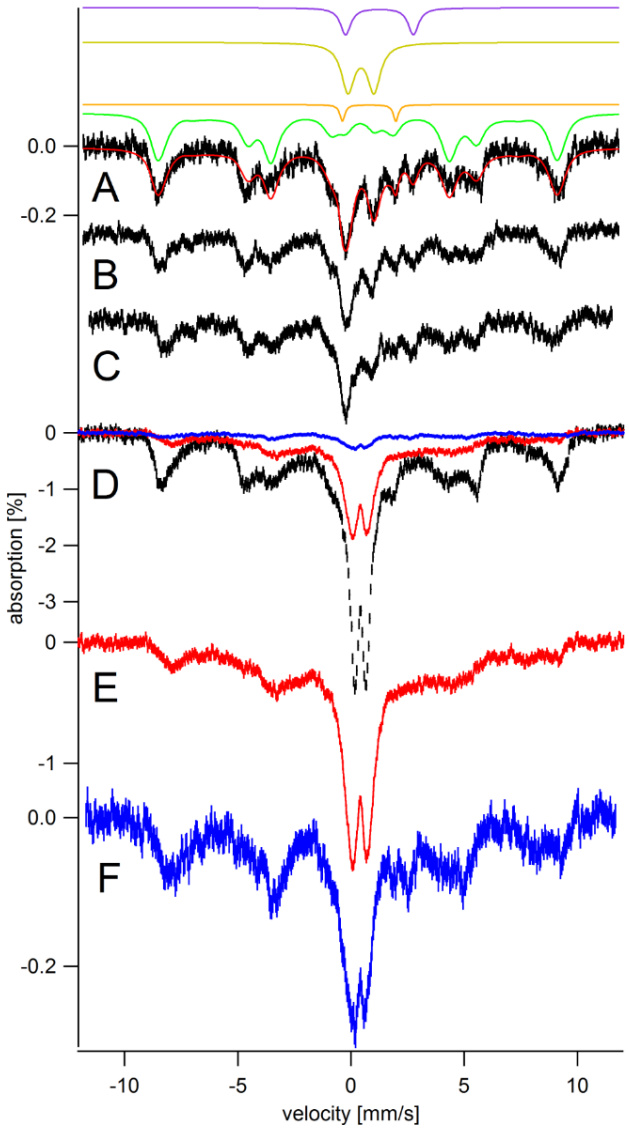

Figure 6.1: Low field (0.05 T) low temperature (5 K) Mössbauer spectra of whole intact fermenting WT cells grown on 57Fe40B0 medium and harvested at different growth stages. (A) Harvested at OD600 = 0.4 (exponential stage) and washed with water; (B) harvested at OD600 = 0.7 (exponential stage) and washed with water; (C) same as B except treated with lyticase/EDTA; (D) black trace, harvested at OD600 = 1.5 (postexponential stage; 5 days) and water washed; (E) same as D except washed with EDTA; (F) same as D and E except treated with lyticase/EDTA. Red and blue trace in D are the same spectra as shown in E and F, respectively, scaled to the spectrum in black. Solid red line in A is a simulation consisting of NHHS S = 5/2 Fe3+ from vacuoles (green line; 74%; δ= 0.52 mm s^{-1}; DEQ = 0.38 mm s^{-1}; Aiso/gnbn = _228 kG; D = 0.5 cm^{-1}; E/D = 0.33; Z = 3; Γ=0.7mms^{-1}), HS Heme Fe2+ (orange line: δ=0.8mms^{-1}; ΔEQ=2.4mms^{-1}; G = 0.3 mm s^{-1}), central doublet (gold line: δ = 0.45 mm s^{-1}; ΔEQ = 1.15 mm s^{-1};Γ= 0.7mm s^{-1}), and NHHS Fe2+ (purple line: δ = 1.26 mm s^{-1}; ΔEQ = 3.0 mm s^{-1}; Γ = 0.6 mm s^{-1}). The Y-axis scale for A, B, and C are the same.

Low-temperature (5 K), low-field (0.05 T) MB spectra of cells harvested at different times during exponential phase and washed in water (Figure 1, A and B) were similar to each other and to previous spectra of cells harvested in this growth phase **(128)**. Exponential cells washed with EDTA exhibited similar spectra (data not shown). Spectra were dominated by a sextet due to NHHS Fe^{3+} in the vacuole (Figure 1, green line) followed by a central quadrupole doublet (gold line) due mainly to $[Fe_4S_4]^{2+}$ clusters and LS Fe^{2+} heme centers in mitochondria **(13)**. Minor quadrupole doublets due to HS Fe^{2+} heme (orange line) and NHHS Fe^{2+} (purple line) were also evident. The average concentration of Fe in these samples was 370 ± 170 μM. Cellular Mn, Cu and Zn concentrations were also determined (Table 1). A portion of freshly harvested exponentially grown cells were treated with lyticase, but this had no significant effect on the spectrum (Figure 1C), suggesting that little if any Fe accumulated in the CWs of exponentially growing cells.

Table 6.1. Metal concentrations of WT cells grown to exponential and post-exponential phases, and subsequently treated with EDTA or lyticase. Concentrations are in μM. The MB spectrum of cells harvested 5 days after inoculation, in post-exponential mode, exhibited a percent effect 10-times greater than that of cells harvested during exponential growth (Figure 1D, black trace). Subsequent ICP-MS analysis indicated that such cells were indeed loaded with Fe (Table 1). Cells from the same harvest but treated with lyticase/EDTA and then washed 3 times with SP buffer afforded a MB spectrum (Figure 1, D and F, blue traces) that was only ca. 10% as intense as that of water-washed cells. Similar cells treated with EDTA alone exhibited a spectrum (Figure 1, D and E, red line) that was less intense than water-washed cells but more intense than those washed with lyticase/EDTA

OD_{600}	Treatment	[Fe]	[Mn]	[Cu]	[Zn]
0.2	Water	230	14	22	320
0.4	Water	190	12	24	440
0.7	Water	590	10	24	560
0.7	Lyticase/EDTA	480	13	21	420
1.5	Water	7400	12	32	620
1.6	EDTA	4400	9	24	510
1.5	Lyticase/EDTA	1800	8	30	600

After the MB spectra of Figure 1 (and Figures 4 and and 5 see below) were collected, samples were pulverized and packed into EPR tubes while being kept in or directly above liquid N_2. The 10 K X-band EPR spectrum of post-exponential cells showed dramatic changes upon lyticase/EDTA treatment (Figure 2, A vs. C). The spectrum of the water-washed sample (Figure 2A) exhibited intense features at g = 4.3 and in the g = 2 region. The g = 4.3 signal is typical of paramagnetic NHHS Fe^{3+} species with rhombic symmetry. The signal in the g = 2 region was unusually broad as is typical

of Fe^{3+} oxyhydroxide nanoparticles found in mitochondria of yeast that are defective in ISC-related processes **(188,15,51)**. The intensity at g = 4.3 was significantly diminished and the broad g = 2 signal was absent in the spectrum of the lyticase/EDTA-treated sample (Figure 2C). The EPR spectrum of the sample treated only with EDTA (Figure 2B) was also devoid of the broad g = 2 signal and the integrated intensity of the sharper g = 4.3 derivative signal was reduced relative to that in the spectrum of water-washed cells. The decline in the intensity of these signals upon lyticase treatment suggests that CW Fe is heterogeneous, with mononuclear NHHS Fe^{3+} affording the g = 4.3 signal and superparamagnetic Fe^{3+}nanoparticles affording the broad g = 2 signal.

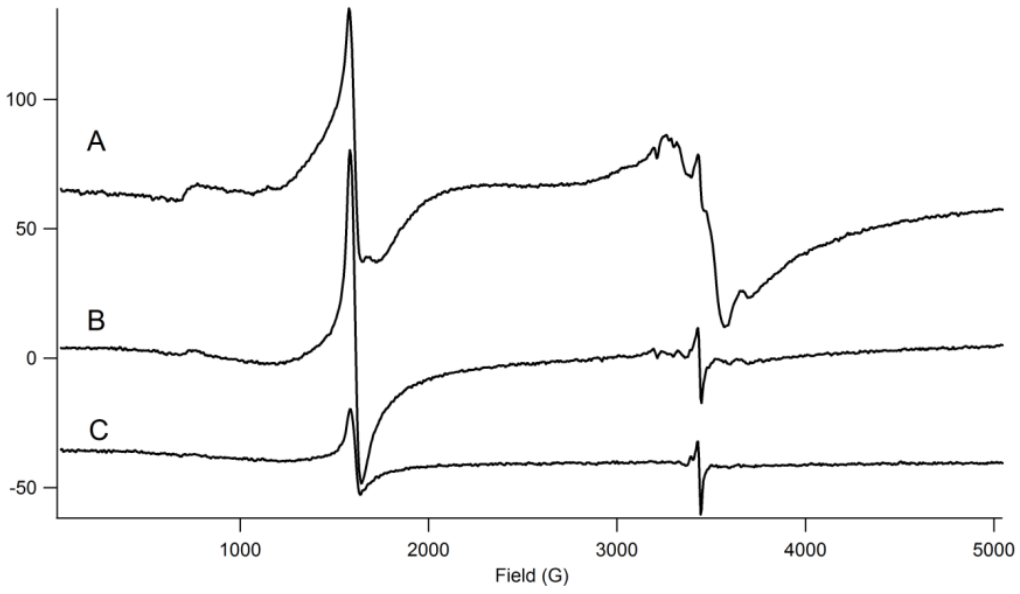

Figure 6.2: 10 K X-band EPR spectra of whole intact fermenting yeast cells. (A) Treated with water; (B) treated with EDTA; (C) treated with EDTA/lyticase. Other EPR conditions: microwave power, 0.2 mW; microwave frequency, 9.645 GHz; modulation amplitude, 9.2 G; sweep time, 160 s. Samples were the same as those used to generate Fig. 1D, E, and F, respectively, obtained by transferring samples from MB holder to EPR tubes while maintained near 77 K.

The concentration of cellular Fe after lyticase-treatment was about 24% of that in water-washed cells (Table 1). Interestingly, the concentrations of Mn, Cu, and Zn did *not* increase in post-exponential cells, relative to concentrations of the same metals in exponential cells, and the concentrations of the same metals did not decline upon lyticase treatment. We conclude that *Fe (but not Cu, Mn, or Zn) accumulates in the CW of post-exponential (but not exponential) cells and that the majority (75% - 90%) of the Fe in those cells is located in the CW.*

Rate of O_2-dependent metabolism declines in post-exponential cells

To evaluate whether post-exponential cells are metabolically active, we simultaneously measured cell density, as reported by OD_{600}, and dissolved [O_2] in the growth medium *vs*. time after inoculating 24 L of minimal medium with cells that had been grown overnight in YPAD. [O_2] consumption was used as a reporter of metabolic activity. O_2 gas was bubbled into the bioreactor at a fixed rate, with temperature and stir conditions also fixed. The resulting OD_{600}trace (Figure 3, green dots) exhibited a lag phase followed by exponential growth and then a transition into the post-exponential state. The corresponding traces of dissolved [O_2] (Figure 3, red dots) began high (because the reactor contained few cells and the bubbling rate was fast) and then declined as the concentration of cells and O_2 consumption increased (overpowering the fixed bubbling rate). Towards the end of the experiment, dissolved [O_2] gradually returned to near its initial concentration.

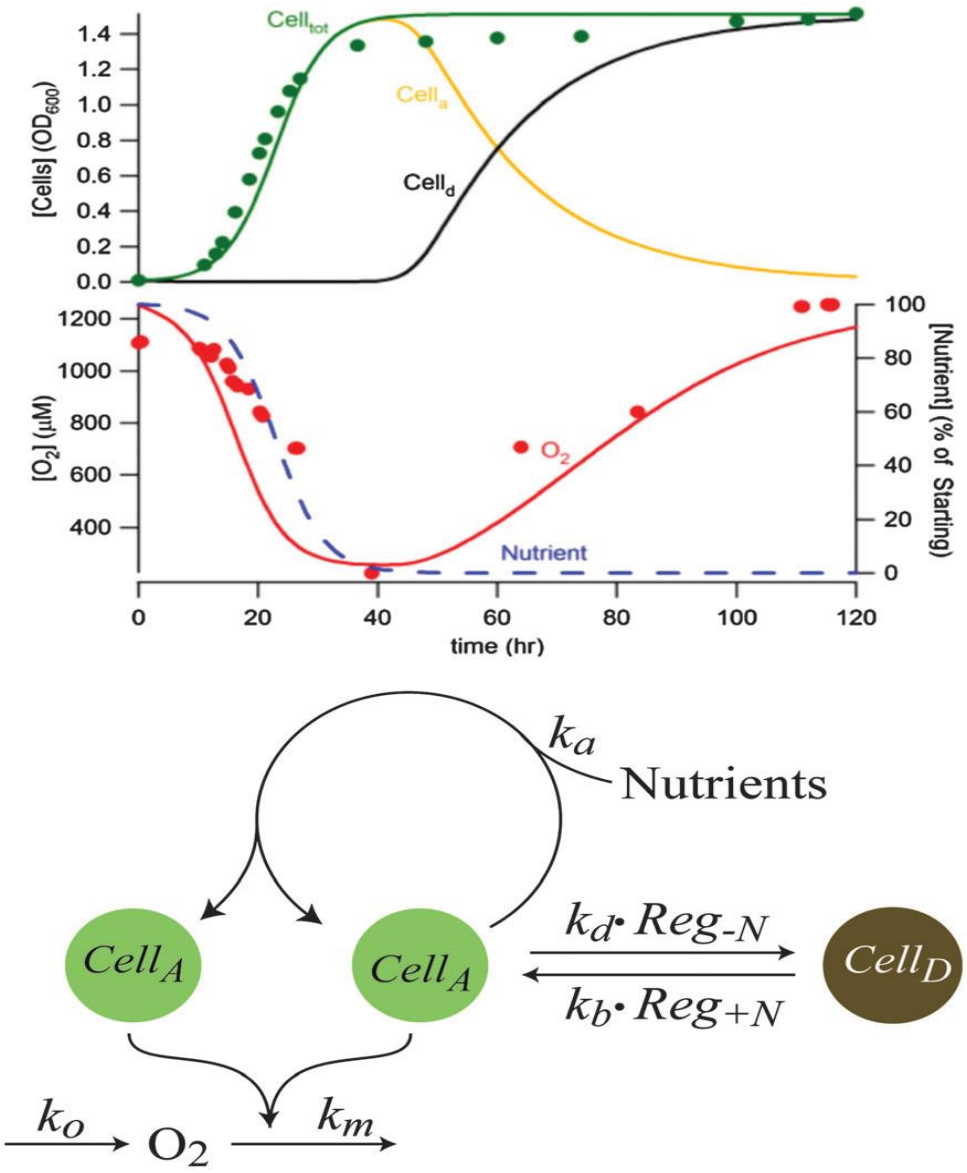

Figure 6.3: Model of cell growth and O2 consumption in a batch culture of WT fermenting S. cerevisiae. Upper panel: Plots of OD600 and [O2] in 57Fe40B0 medium vs. time after inoculation. Data are solid green (OD600) and red (O2) circles. Simulations are green (total cells), yellow (active cells), black (dormant cells), blue (nutrient concentration) and red (O2 concentration) lines. Lower panel: Chemical model showing generation of O2, consumption of O2 by active cells, self-replication of active cells, and interconversion of active and dormant cells as regulated by the nutrient concentration.

This final return of $[O_2]$ to near its initial concentration indicated that metabolically active cells converted into an inactive dormant state when nutrients became scarce. We assumed this in a chemical model (Figure 3, bottom and Table 2) in which metabolically active cells ($Cell_A$) self-replicate and metabolize O_2 along with a hypothesized nutrient N. Dormant cells ($Cell_D$) were assumed only to convert into active cells when [N] levels were sufficiently high. This model was translated into ordinary differential equations (ODEs) [1] – [4].

$$\frac{d[Cell_A]}{dt} = k_A[N][Cell_A] - k_D \cdot \left(\frac{1}{1+\left(\frac{[N]}{[N]_{sp}}\right)^{sen}} \right) \cdot [Cell_A] + k_b \left(1 - \frac{1}{1+\left(\frac{[N]}{[N]_{sp}}\right)^{sen}} \right) \cdot [Cell_D] \qquad [1]$$

$$\frac{d[Cell_D]}{dt} = k_D \cdot \left(\frac{1}{1+\left(\frac{[N]}{[N]_{sp}}\right)^{sens}} \right) \cdot [Cell_A] - k_b \left(1 - \frac{1}{1+\left(\frac{[N]}{[N]_{sp}}\right)^{sens}} \right) \cdot [Cell_D] \qquad [2]$$

$$\frac{d[O2]}{dt} = RO2 \cdot (1256 - [O2]) - k_m[Cell_A][O2] \qquad [3]$$

$$\frac{d[N]}{dt} = -k_A[N][Cell_A] \qquad [4]$$

Reg.$_N$ functions **(154)** were used to regulate the rate at which metabolically active cells became dormant and dormant cells became active. Selecting initial parameters was complicated because the concentration of total cells at each time was unknown, as were the identity and concentration of *N*. For simplicity, we assigned cell concentration to units of OD_{600}, such that the initial cell concentration was taken as 0.01 (the OD_{600} at the time of inoculation) and the final concentration was taken as 1.4 (OD_{600} at the time of harvesting). Given the assumed stoichiometry that 1 *N*is required to generate 1

$Cell_A$ (Table 2) and the need for a dramatic decline in [N] to prompt the conversion from $Cell_A \rightarrow Cell_D$, we selected initial $[N]_0 = 1.5$, just greater than the final OD_{600}. This concentration was high enough to generate all of the cells in the experiment but low enough to decline dramatically (percentagewise) during the time-course of the experiment.

Table 6.2. Model Reactions, Parameters and Sensitivities. Sensitivities were determined as described (**154**).

Reaction	Rate Expression	Parameter	Sens.
$N \xrightarrow{R_a} Cell_A$	$k_a \cdot [N] \cdot [Cell_A]$	k_a = 0.18 hr^{-} ^{1}ANU^{-1}	1.08
$O2 \xrightarrow{R_m}$	$k_m \cdot [O2] \cdot [Cell_A]$	k_m = 690 hr^{-} ^{1}OD^{-1}	1.04
$Cell_A \xrightarrow{R_d} Cell_D$	$k_d \cdot \left(\frac{1}{1+\left(\frac{[N]}{[N]_{sp}}\right)^{sen}} \right) [Cell_A]$	k_d = 0.072 hr^{-1} $[N]_{sp}$ = 0.01 ANU *Sen* = 6.6	1.01 1.00 1.00
$\xrightarrow{R_o} O2$	$k_o \cdot (1250 - [O2])$	k_o = 220 hr^{-1}	1.01
$Cell_D \xrightarrow{R_b} Cell_A$	$k_b \cdot \left(1 - \frac{1}{1+\left(\frac{[N]}{[N]_{sp}}\right)^{sen}} \right) [Cell_D]$	k_b = 0.33 hr^{-1} $[N]_{sp}$=0.01 ANU *Sen* = 6.6	1.00 1.00 1.00

ODEs [1] – [4] were numerically integrated using the NDSolve routine in *Mathematica 9* (http:\\www.wolfram.com). The model was optimized by adjusting parameters k_a, k_b, k_d, k_m, k_o, $[N]_{sp}$, and *sen* (Table 2), minimizing the RMSD function defined in Appendix A (Electronic Supplementary Information) to the value 0.016. Simulations (Figure 3, upper panel, solid lines) fit the data acceptably well. The cells used to inoculate the culture were assumed to be dormant ($Cell_D$), so that their conversion to active cells ($Cell_A$) could generate the observed lag phase that preceded exponential growth. Self-replication of active cells and the consumption of O_2 were the most sensitive reactions of the model, whereas the activation of dormant cells was the least sensitive (Table 2). The increase of dormant cells correlated well with the accumulation of large quantities of CW Fe. We conclude that *cells accumulate Fe in their walls as they become metabolically inactive*.

Cell wall iron consists of a heterogeneous distribution of Fe^{3+} species

To characterize CW iron further, we collected MB spectra of Fe-loaded dormant cells at 5, 15, 25, 50, 75, 100, and 150 K (all at 0.05 T parallel-applied magnetic field, Figure 4, A - G) and at perpendicular-applied magnetic fields of 0, 0.75, 1.5, 3, and 6 T (all at 4.2 K, Figure 5). We also collected X-band EPR spectra of such cells at 10, 20, 40 and 80 K (Figure 6, red, yellow, green, and blue lines, respectively). MB spectra were composed of sextet and doublet species, with the sextet representing the majority. Given the results of Figure 1 and Table 1, we presumed that all of the spectral absorption was due to CW Fe, and that the sextet and doublet arose from a paramagnetic S = 5/2

Fe^{3+} species and a diamagnetic S = 0 species, respectively. A small contribution to the sextet intensity was probably due to *vacuolar* mononuclear NHHS Fe^{3+} (S = 5/2) but this contribution could not be distinguished from the dominating CW Fe^{3+}. A small contribution to the doublet intensity was probably due to superparamagnetic Fe^{3+} oxyhydroxide nanoparticles. (A portion of the doublet intensity could have arisen from an integer spin species with a very small hyperfine field, but this seems unlikely.) Any central doublet due to mitochondrial $[Fe_4S_4]^{2+}$ clusters and LS Fe^{2+} hemes was undetectable due to the dominance of the CW Fe and so we made no attempt to take this feature into account. The high-energy line due to HS Fe^{2+} heme, representing a few percent of the overall spectral absorption, was observed at low temperatures, but this was also ignored in fitting.

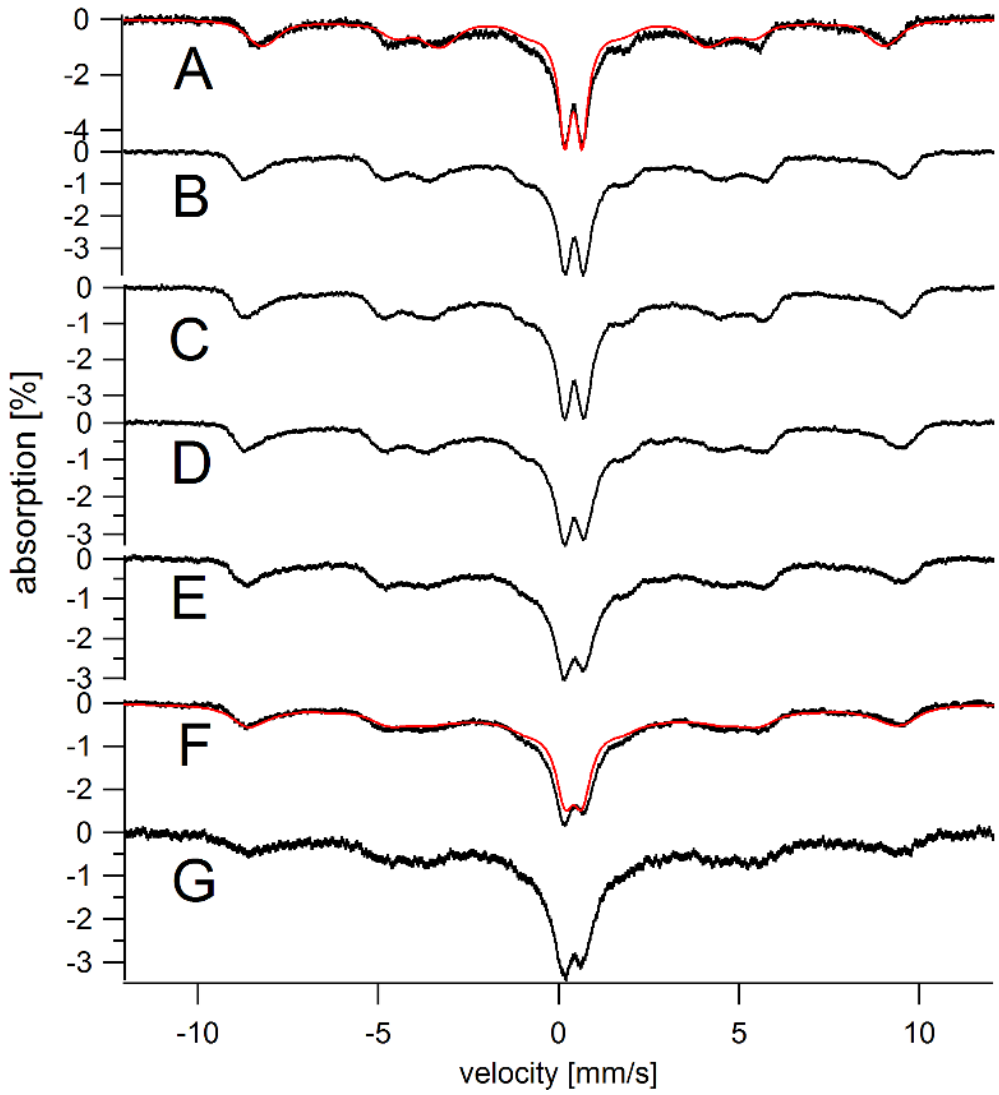

Figure 6.4: Temperature-dependent Mössbauer spectra of 57Fe-loaded cells (water washed). (A) 5; (B) 15; (C) 25; (D) 50; (E) 75; (F) 100; (G) 150 (all in K). A field of 0.05 T was applied parallel to the gamma radiation. The sample used was the same as in Fig. 1D. Overall simulations (red lines in A and F) were the sum of two simulated spectra, including an S = 5/2 species (Aiso/gnbn = -226 ±2 kG, D = 0.001 ±0.04 cm^{-1}, E/D=0.26± 0.06, δ=0.52mms^{-1}, ΔEQ=0.3±0.1mm s^{-1}, η = 1–5 and Γ = 0.4–1.0 mm s^{-1}) representing 60–70% of spectral intensity, and an S = 0 species (δ = 0.52mm s^{-1}, ΔEQ = 0.47 mm s^{-1} and Γ =0.4–0.6 mm s^{-1} representing 25–36% of spectral intensity. With increasing temperature, spectral features broadened.

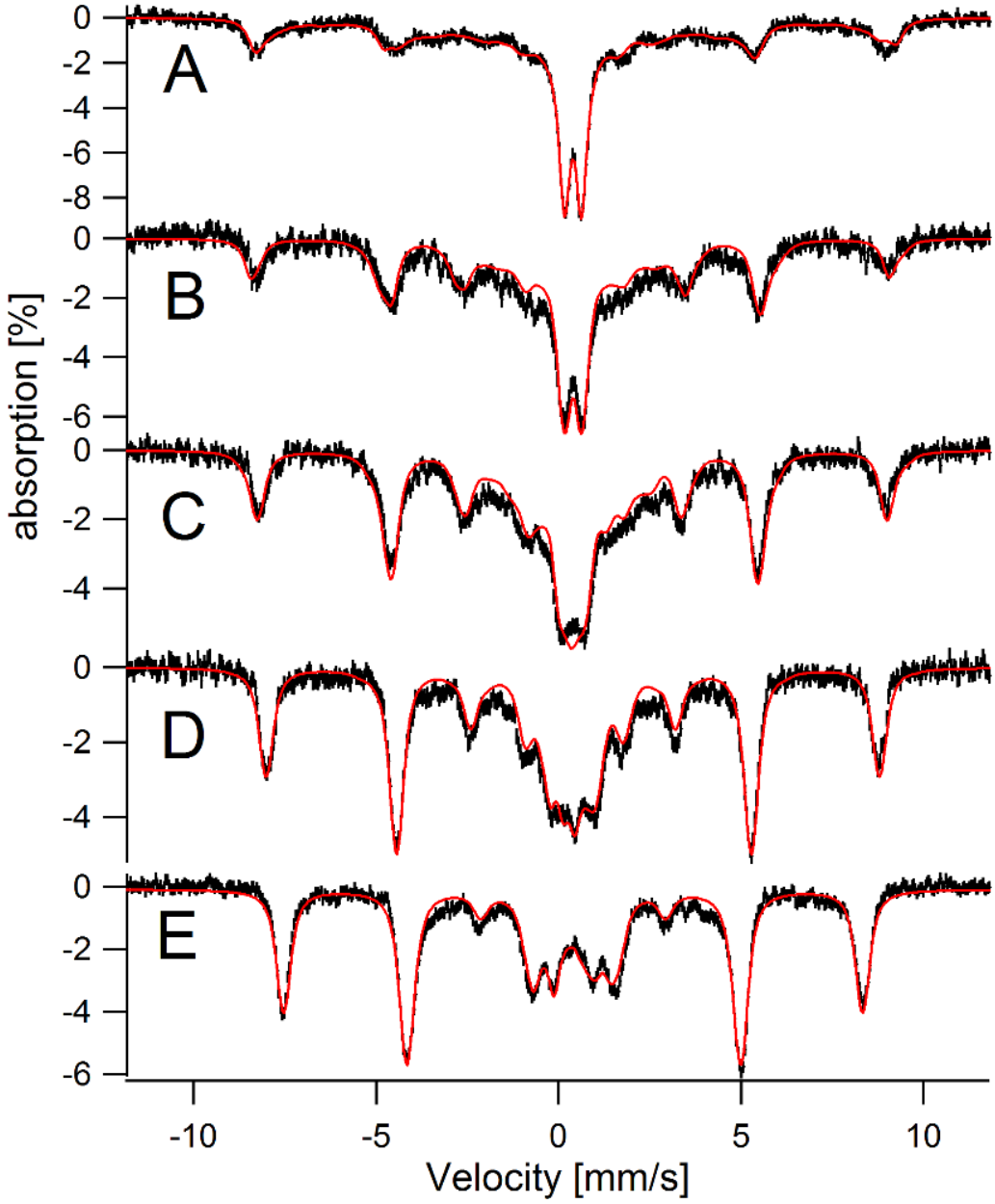

Figure 6.5: Variable-field 4.2 K Mössbauer spectra of 57Fe-loaded (water washed) cells. (A) 0; (B) 0.75; (C) 1.5; (D) 3.0, and (E) 6.0 (all in T). Fields were applied perpendicular to the gamma radiation. Overall simulations (red lines) were generated using the same model as in the Fig. 4 legend. The sample was the same as used in Fig. 1D and 4. The simulation in A assumed an applied field of 0.02 T.

At 4.2 K and 0.05 T, diamagnetic and superparamagnetic species could not be distinguished. Collectively they represented ca. 30% of spectral intensity. As the temperature was raised, the *shape* of the spectra changed but the intensity ratio of the sextet to the main doublet remained about the same. This suggested that any superparamagnetic Fe contribution associated with the doublet has a Blocking temperature $T_B \ll 4.2$ K. At high applied fields (e.g. Figure 5E), a superparamagnetic species will magnetically split depending on the hyperfine field, whereas diamagnetic species will not do this. Thus we assigned the ill-resolved region in the middle of the 4.2 K, 6T spectrum to diamagnetic species. Simulation of this region with an S = 0 Hamiltonian indicated that ca. 20% spectral intensity was due to diamagnetic species. This implies that the superparamagnetic species accounts for ca. 10% of spectral intensity. This low percentage, along with the broad distribution in hyperfine fields, made it impossible to reliably simulate the superparamagnetic species at high field. The sample was transferred from a Mössbauer cup to an EPR tube while maintaining it at or near liquid N_2 temperatures. The sample exhibited a g = 4.3 EPR signal due to the H.S Fe^{3+} species. The signal exhibited Curie-Law behavior in that the intensity of the product of signal intensity·temperature (S·T) was invariant between 10 K and 80 K (Figure 6). The broad g = 2 signal, which we assign to the superparamagnetic species, also seemed to exhibit Curie-Law behavior although there was a modest decrease in S·T at low T.

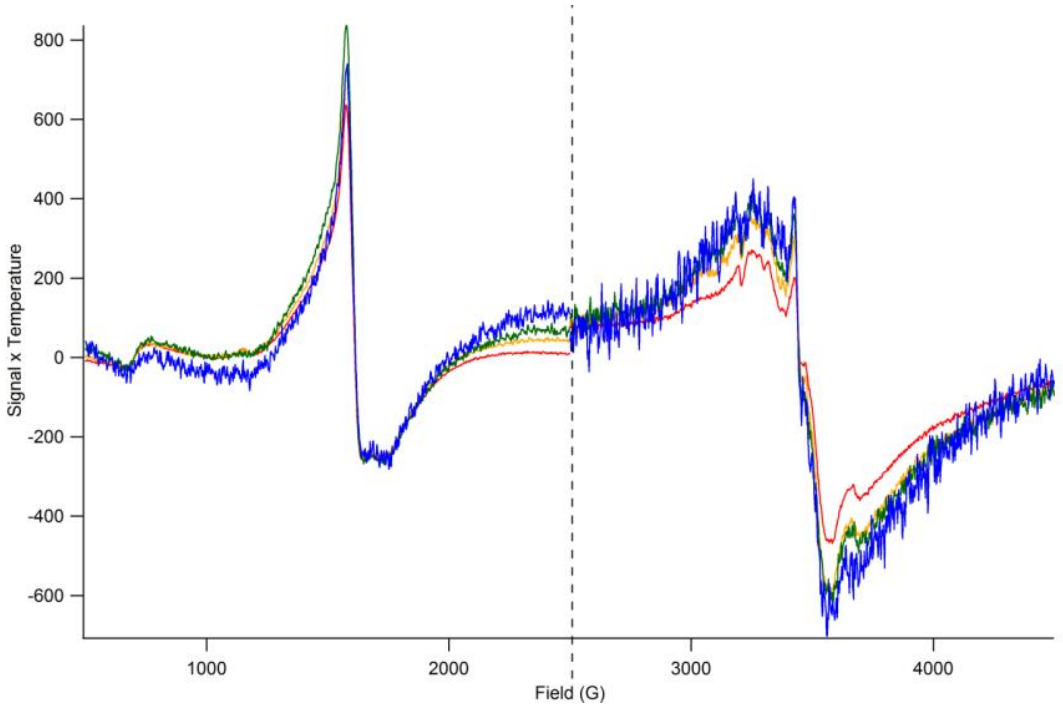

Figure 6.6: Temperature-dependent EPR spectra of 57Fe-loaded cells (water washed). Low-field spectra show the g = 4.3 signal while high-field spectra exhibit a broad g = 2 signal. Spectra were collected at 10 K (red line), 20 K (yellow), 40 K (green), and 80 K (blue). Signal intensities have been multiplied by temperature. The sample used was the same as in Fig. 1D, 4 and 5. Microwave power was 2 mW and 0.2 mW for the low- and high-field spectra, respectively. Other conditions were as in Fig. 2.

Compare the spectroscopic properties of the superparamagnetic nanoparticles to those of the 2 - 4 nm diameter nanoparticles in Yah1-depleted mitochondria **(15)**. In Yah1-depleted cells, the superparamagnetic doublet had $\delta = 0.52$ mm/s and $\Delta E_Q = 0.62$ mm/s at 5 K; here, $\delta = 0.38$ mm/s and $\Delta E_Q = 0.50$ mm/s. Like the current superparamagnetic species, Yah1-depleted nanoparticles had $T_B \ll 5$ K such that a superparamagnetic doublet was observed at all temperatures > 4.2 K. The EPR spectrum associated with nanoparticles from Yah1-depleted mitochondria also exhibited a broad g = 2 feature with anti-Curie-Law behavior. However, the inverse-temperature effect was

more dramatic for the nanoparticles of Yah1-depleted mitochondria than what we observed here.

Kinetics of cell wall iron release by chelation and enzymatic digestion

The experiments of Figure 1 show that CW Fe can be released under different wash conditions. To evaluate the *rate* of Fe release, we measured the concentration of cellular Fe as a function of time after treating Fe-loaded cells with water, EDTA at pH 8, or lyticase/EDTA at pH 8. We also monitored the concentration of Fe released into the medium. In all trials, we could account for > 90% of the released Fe. About 80% of CW Fe was removed by treating the cells with lyticase/EDTA for 1 hr (Figure 7, blue lines). The reaction was almost completed in 30 min. Equivalent treatment with EDTA alone (red lines) was less effective whereas treatment with water alone (black lines) was essentially *ineffective*. These results are qualitatively congruent with the MB/EPR experiments described above (however, the MB study suggests that EDTA is less effective in removing CW Fe, compared to EDTA/lyticase treatment, relative to the results of Figure 7). Similar results were obtained using EGTA rather than EDTA (data not shown). We estimate that *over half* of the CW Fe in dormant cells can be removed reasonably well by chelators such as EDTA at pH 8; this estimate assumes that all CW Fe is removed by enzymatic digestion.

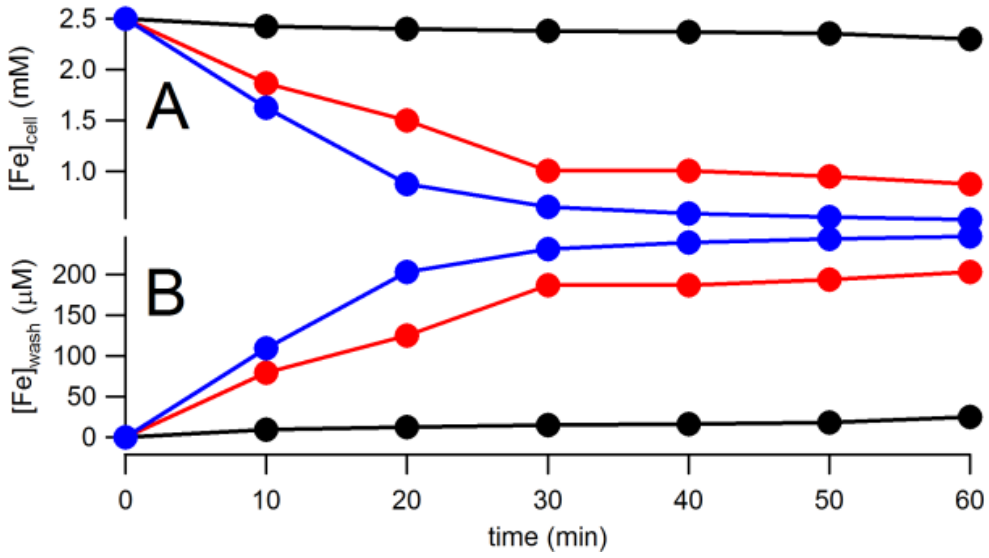

Figure 6.7: Iron concentrations in WT post-exponential cells and the corresponding washes after various treatments. (A) [Fe]cell; (B) [Fe]wash. Data are solid circles. Black, washed with water only; red, washed with EDTA only; blue, washed with lyticase and EDTA.

Metabolically Reactivated Fe-loaded cells grow using Fe mobilized from their internal stores AND from Fe in the medium, including trace levels of Fe in Fe-deficient medium

To evaluate whether cells can utilize their internal Fe stores for growth, we grew cells on $^{57}Fe_{40}B_0$ medium for 4 days (into stationary phase). After washing 3 times with 100 µM EDTA at pH 7, the resulting metabolically inactive ^{57}Fe-loaded cells contained 4.1 ± 0.4 mM Fe (n = 3) (less CW Fe is removed by EDTA at lower pH).

These ^{57}Fe-loaded cells were used to inoculate Fe-deficient Fe_0B_{30}medium, yielding $OD_{600} \approx 0.01$ at the start of the experiment. The 30 µM concentration of BPS in the medium was >30 times that required to coordinate all cellular Fe and endogenous Fe in

the medium. The ^{57}Fe-loaded cells in this experiment grew slowly, exhibiting a minimal doubling time (DT) of 4.8 hr (Figure 8A, solid circles). In contrast, cells growing on Fe-sufficient minimal medium replicate ~ every 2 hr **(128)**. After 3 - 4 days, the culture that had been inoculated with ^{57}Fe-loaded cells reached a final OD_{600} of 1.6 ± 0.3 (n = 2), slightly less than the final OD_{600}= 2 attained by cells grown in standard $Fe_{40}B_0$ medium. The stationary-state cells contained only 57 ± 7 μM Fe (n = 2). In contrast, cells on the Fe-sufficient medium and harvested under exponential growth conditions contain 300 - 400 μM Fe **(128)**.

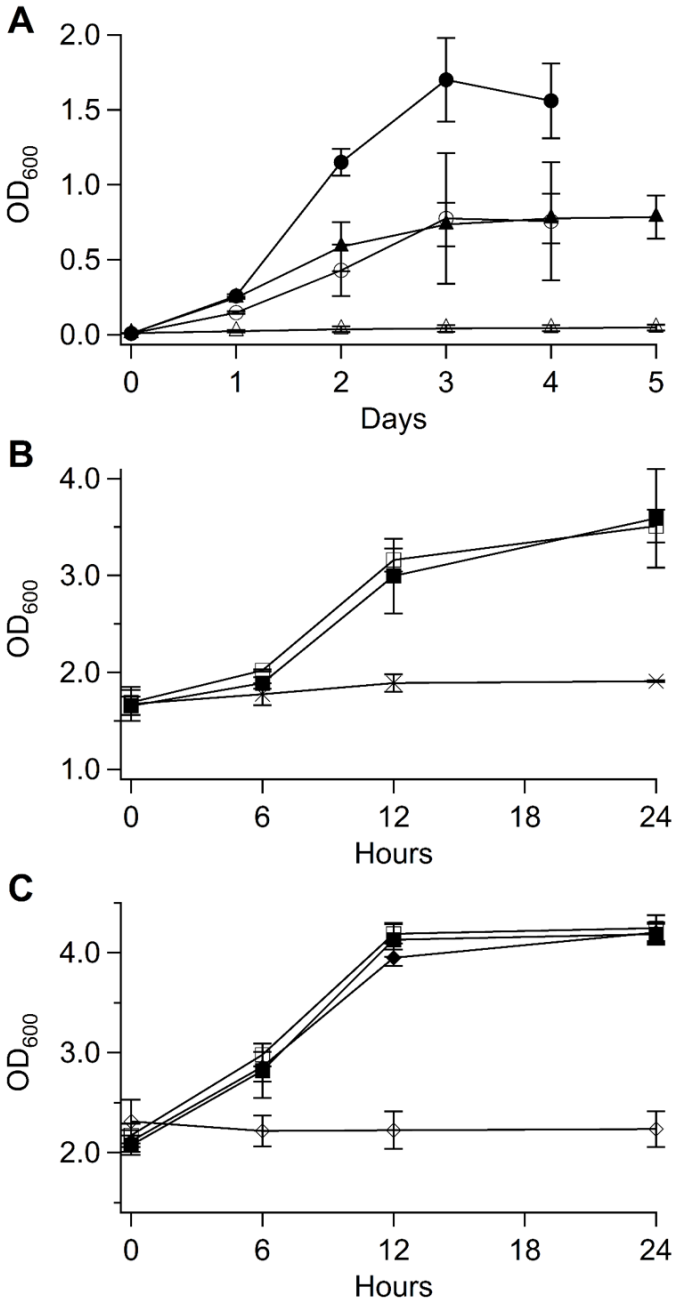

Figure 6.8: Growth of Fe-loaded or Fe-starved cells after transfer to various media. Solid circles, Fe-loaded cells transferred to Fe0B30 medium. Open circles, Fe-starved cells transferred to Fe0B30 medium. Solid triangles, Fe-loaded cells transferred to Fe0B100. Open triangles, Fe-starved cells transferred to Fe0B100 medium. Panel B, growth of Fe-loaded cells transferred to various media inoculated at conserved cell density. Solid squares, transferred to 57Fe40B0 medium. Open squares, transferred to Fe0B100 medium. Crosses, transferred to Fe0B100-NAB medium. Panel C, same as panel B, but a different experiment. Solid squares, transferred to 56Fe40B0 medium. Open squares, transferred to Fe0B100 medium. Solid diamonds, transferred to Fe0B0 medium. Open diamonds, transferred to DW.

Had the ^{57}Fe-loaded cells *exclusively* used their intracellular stores of ^{57}Fe for growth, and not import any ^{56}Fe from the Fe-deficient medium, they should have doubled 6 times and then stopped growing (4100μM ÷ $(2)^6 \approx 57$μM). The observed OD_{600} change indicates that they actually stopped growing after ~ 7 doublings (1.6 ÷ $(2)^7 \approx 0.01$). This implies that about half of the Fe used by these cells originated from their ^{57}Fe stores and half from the tiny amount of endogenous ^{56}Fe in the Fe_0B_{30} medium. This result was surprising because yeast cells are commonly thought to be unable to grow on Fe-deficient medium treated with BPS. If the endogenous Fe in BPS-treated medium is chelatable by (and kinetically accessible to) BPS, the tight-binding nature of the $Fe^{2+}(BPS)_3$ complex implies that virtually all endogenous Fe in the medium should have been chelated by BPS. Perhaps some fraction of the endogenous Fe is inaccessible to BPS yet can be imported and used by cells.

A second batch of ^{57}Fe-loaded cells with an [^{56}Fe]/[^{57}Fe] isotope ratio estimated at *ca*. 0.05 was transferred to Fe_0B_{30} medium, achieving an initial $OD_{600} = 0.01$. After 7 doublings the resulting ^{56}Fe/^{57}Fe ratio in the harvested cells was 1.0 (25 μM ^{56}Fe and 24 μM ^{57}Fe). The increase in cellular ^{56}Fe must have originated from the trace amounts of ^{56}Fe in the Fe_0B_{30} medium as there was no other source of ^{56}Fe in the experiment. In a third experiment, ^{56}Fe-loaded cells were used to inoculate Fe_0B_{30} medium. In this case, the final ^{56}Fe/^{57}Fe ratio in the harvested cells was 44 (62 μM ^{56}Fe and 1.4 μM ^{57}Fe), again consistent with the import of endogenous ^{56}Fe from Fe-deficient media. In both cases, the final [^{56}Fe]/[^{57}Fe] ratios in the harvested cells reflected the relative amounts of the Fe isotopes in the Fe-loaded cells and in the endogenous Fe in the medium. We

conclude that *Fe-loaded yeast cells can grow on their internal Fe stores AND on trace amounts of endogenous Fe present in Fe-deficient medium.*

Metabolically reactivated cells mobilize cell wall Fe^{3+} species

We wanted to identify the type of internal Fe stores that are used by Fe-loaded cells to grow on Fe-deficient medium. Our approach was to use MB spectroscopy. ^{57}Fe-loaded cells were transferred into 3 different media, namely $^{57}Fe_{40}B_0$ (the control for which Fe stores should not be used), Fe_0B_{100} (Fe-deficient, for which Fe stores should be used), and Fe_0B_{100}-NAB. The last medium was designed to prevent cells from growing in an iron-deficient environment, thereby eliminating the effects of cell growth and metabolic activity. In these experiments, the amount of Fe-loaded cells used to inoculate fresh media was much greater than in the first set of experiments, such that the OD_{600} immediately after inoculation was approximately equal to the OD_{600} when the Fe-loaded cells (used for that inoculation) had been previously harvested. This allowed MB spectroscopy (which requires large quantities of cells) to monitor changes in cellular Fe content.

The ^{57}Fe-loaded cells initially contained 4.9 ± 1.5 mM Fe (n = 2). Surprisingly, the cells grew equally well on $^{57}Fe_{40}B_0$ and Fe_0B_{100}media. Thus, cells that were loaded with Fe in their CWs and vacuoles grew as fast and to the same final extent in Fe-deficient media as they did in Fe-rich media; i.e. the absence of Fe in the medium did not limit the growth rate. The OD_{600} of these cultures increased from 1.7 at the time of

inoculation to 3.6 after 24 hr of growth (Figure 8B, solid and open squares, respectively).

Despite the same growth rate, the concentration of Fe in the resulting harvested cells was quite different. The cells harvested from the $^{57}Fe_{40}B_0$ medium contained 3.9 ± 0.9 mM Fe while those harvested from the Fe_0B_{100} medium contained 1.3 ± 0.4 mM Fe (n = 2 for each condition). If dilution due to cell growth was the only factor affecting these final cellular Fe concentrations (i.e. if Fe had not been imported from or exported to the environment), the $^{57}Fe_{40}B_0$–grown cells would have contained 2.3 mM Fe after the 24 hr incubation. The fact that they contained more Fe indicates that they (not surprisingly) imported Fe from Fe-rich $Fe_{40}B_0$medium. Thus, cells import environmental Fe even if they are not growth-limited by Fe.

The Fe concentration in the cells harvested from Fe_0B_{100} medium was 1.8-fold *less* than that expected if they had grown and divided exclusively using their own Fe stores. Where did the rest of their Fe stores go? The simplest interpretation is that the *Fe-loaded cells mobilized and released ~40% of their internal Fe stores when incubated in Fe-deficient medium for 24 hrs.* We will show below that some of the released Fe coordinated to BPS and that the resulting $Fe^{2+}(BPS)_3$ complexes adsorbed onto cell surfaces. Counting this absorbed Fe as part of the Fe that was mobilized suggests that these cells actually mobilized much more than 40% of their internal Fe stores during growth after dormancy. Some of the mobilized Fe remained in the growth medium, some coordinated to BPS, and some was reimported into the cell. Only this latter portion supported cell growth. We conclude that *a large portion of cellular Fe in post-*

exponential Fe-loaded (dormant) cells is rapidly mobilized when such cells are metabolically reactivated.

The ^{57}Fe-loaded cells that were transferred into Fe_0B_{100}-NAB medium barely grew during the same 24 hr period; the OD_{600} of the culture increased from 1.7 → 1.9 (Figure 8B, crosses) whereas the concentration of Fe in these cells declined to 2.9 ± 0.9 mM (n = 2). The extent of Fe loss was greater than could be explained by the effects of growth-associated dilution. Dilution would have caused the Fe concentration to decline only to ~ 4.3 mM. Thus, nearly 30% of the Fe in the Fe-loaded cells must have been released and used to support growth after those cells were transferred to Fe-deficient medium.

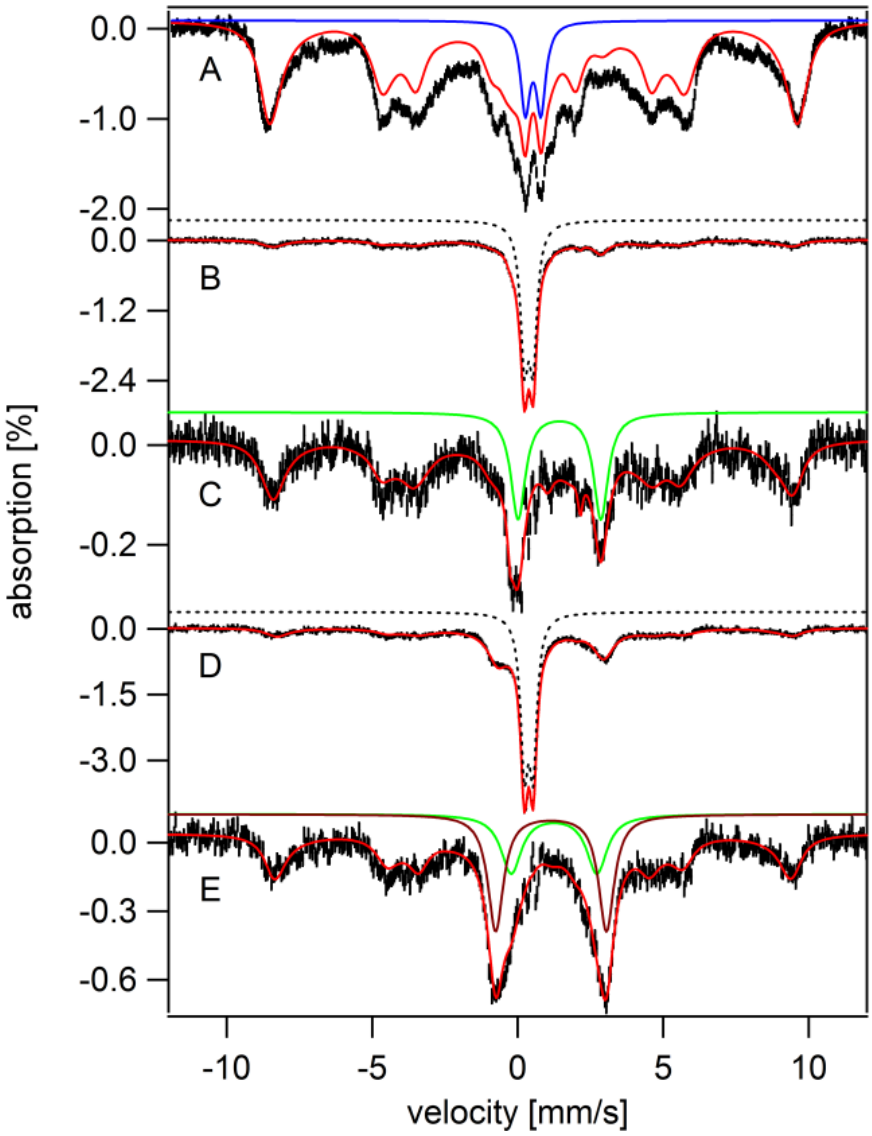

Figure 6.9: Mössbauer spectra (5 K, 0.05 T) of whole WT yeast cells before (A) and after (B–E) switching growth media. Results from this experiment are also presented in Fig. 8B. (A) Fe-loaded cells. The blue line is a simulation of Fe3+ nanoparticles (δ = 0.53 mm s_1; ΔEQ = 0.52mm s^{-1}; Γ = 0.45mm s^{-1}). The red line is a composite simulation including 20% absorption due to nanoparticles and 65% to NHHS Fe3+ (Aiso/gnbn = -235 kG; E/D = 0.33; D = 1.15 cm^{-1}; δ = 0.55mms^{-1}; ΔEQ = 0 mms^{-1}; Γ = 0.8mms^{-1}). (B) Fe-loaded cells 5 days after being transferred to Fe0B100. Red line is a composite simulation including NHHS Fe3+ and the quadrupole doublet due to 57Fe2+$(BPS)_3$. Simulation parameters are given in Table S3 (ESI†). (C) Same as B but after removing the quadrupole doublet due to 57Fe2+$(BPS)_3$. The green line is a simulation of the NHHS Fe2+ doublet and the red line is a composite simulation defined in Table S3 (ESI†). (D) Fe-loaded cells 1 day after being transferred to Fe0B100-NAB medium. Red line is a composite simulation. (E) Same as D but after removing the quadrupole doublet due to Fe2+$(BPS)_3$. Green and maroon lines are simulations of the two NHHS Fe2+ species described in the text. The red line is a composite simulation.

We then used MB spectroscopy to investigate the type(s) of Fe centers mobilized by Fe-loaded cells when such cells are grown on Fe-deficient media. The low-temperature low-field MB spectrum of ^{57}Fe-loaded cells (Figure 9A) was dominated by a sextet representing 65% of total spectral intensity. A similar feature is present in the spectra of Figure 1D and 4A which we have shown to be due to CW Fe. This sextet was similar to that arising from vacuolar Fe **(189)** which is why we previously assigned it as such **(128)**. Another 10% of the spectral intensity was due to a quadrupole doublet in the center of the spectrum (simulated by the blue line in Figure 9A). Both features are simulated collectively by the solid red line. The minor differences in simulation parameters relative to those used to fit the spectra of Figures 4 and 5 may reflect batch-to-batch variation as well as uncertainties caused by fitting overlapping spectral features. Some of the intensity of Figure 9Aappears to be due to broad, unresolved and poorly characterized magnetic features similar to those described previously **(128)**. MB parameters and total Fe concentrations for these samples are listed in Table S3.

The MB spectrum of ^{57}Fe-loaded cells that had grown for 24 hr on Fe_0B_{100} medium (Figure 9B) was dominated by a narrow quadrupole doublet arising from the $^{57}Fe^{2+}(BPS)_3$ complex. This doublet, which represented 60% of spectral intensity, was simulated by the dotted line with δ = 0.38 mm/s and ΔE_Q = 0.30 mm/s **(13)**. Another 27% of the intensity arose from a NHHS Fe^{3+}sextet, and another 10% from NHHS Fe^{2+} species (with δ = 1.3 mm/s and ΔE_Q = 3.0 mm/s). These two minor features are highlighted by removing the dominating $Fe^{2+}(BPS)_3$ doublet contribution (Figure 9C). The NHHS Fe^{2+} doublet is simulated by the green line. The sextet in the

spectrum of Figure 9C is only ~ 10% as intense as that in the spectrum of Fe-loaded cells (consistent with it originating from vacuolar NHHS Fe^{3+}). We conclude that *most (ca. 90%) of the Fe^{3+} species associated with the CW of Fe-loaded cells was mobilized. Some of this Fe helped cells grow on Fe-deficient Fe_0B_{100} medium, some formed a complex with BPS, and some remained in solution*.

The presence of the $^{57}Fe^{2+}(BPS)_3$ doublet in the spectrum of Figure 9B would be easily explained had the cells been grown on BPS medium containing ^{57}Fe. BPS is a membrane-impermeable Fe^{2+} chelator that turns cells pink due to the formation of $Fe^{2+}(BPS)_3$ on the CW and/or cell membrane surface (see SI of **(190)**). However, the cells used to generate the spectrum of Figure 9Bwere initially loaded with ^{57}Fe and then transferred to medium that was essentially devoid of Fe (virtually all of the trace endogenous Fe was ^{56}Fe). This demonstrates that *the ^{57}Fe used to generate the $^{57}Fe^{2+}(BPS)_3$ complex in this sample originated from ^{57}Fe that had been associated with the CW of ^{57}Fe-loaded cells* that were used to inoculate the Fe_0B_{100} culture. It also supports our earlier conclusion that Fe-loaded yeast cells can utilize their CW Fe for growth on Fe-deficient medium. Since BPS binds Fe^{2+} tightly, these results indicate that *mobilizing CW Fe^{3+} species involves reducing it to the Fe^{2+} state* prior to BPS coordination.

The Fe-loaded cells that barely grew on Fe_0B_{100}-NAB medium exhibited a MB spectrum (Figure 9D) that was similar to that of Fe-loaded cells that had been transferred to Fe_0B_{100} medium and harvested after 24 hr. Major spectral components were due to $Fe^{2+}(BPS)_3$ (48%), NHHS Fe^{3+} (24%), and two NHHS Fe^{2+} species (δ = 1.3 mm/s,

ΔE_Q = 3.0 mm/s, 10%; δ = 1.1 mm/s and ΔE_Q = 3.8 mm/s, 16%; green and maroon lines, respectively, in Figure 9E). The latter two doublets arise from a lack of adenine in the medium **(191)**. Under adenine-deficient conditions, ADE2 mutant strains such as the one used in this study turn pink and accumulate two types of NHHS Fe^{2+} species called Fe^{2+}_{ON} and Fe^{2+}_{ONS}. Since adenine was not supplemented in the Fe_0B_{100}-NAB medium, the spectra of these cells included these doublets.

MB spectra of Fe-loaded cells that had been incubated for 24 hr in Fe-deficient medium were dominated by the $Fe^{2+}(BPS)_3$ doublet. We suspect that this complex was adsorbed on the CW. Waste solutions obtained by washing such cells 3 times with EDTA-containing water and then 3 times in DW were pink due to the leaching of $Fe^{2+}(BPS)_3$ complex from the CW. We calculate that 30% – 40% of the CW Fe was washed away by these rinses. Additional washings were progressively less effective. The $Fe^{2+}(BPS)_3$ doublet observed in MB spectra arose from $Fe^{2+}(BPS)_3$complexes that remained on the CW after such washings.

Iron-starved cells can extract endogenous iron from Fe-deficient growth medium but their growth rate and extent of growth is diminished

Iron-starved cells should not grow as well on Fe-deficient medium as Fe-loaded cells since they lack Fe stores. To test this idea, Fe-starved cells were inoculated into $^{57}Fe_1B_{21}$ medium, which is essentially Fe-deficient medium but supplemented with a small amount of ^{57}Fe. The cells grew for 15 hr, achieving an $OD_{600} \approx 1.0$. They contained 130 ± 20 μM ^{57}Fe (n = 2) upon harvesting. Although this was a moderate

concentration of Fe, these cells were still "Fe-starved" relative to Fe-loaded cells which contain ≥ 4 mM Fe. Similar Fe concentrations have been observed previously in Fe-starved cells **(65)**. In the previous study, MB spectroscopy revealed that the Fe in these cells was mainly in the form of mitochondrial Fe-S clusters and heme centers, with some NHHS Fe^{2+} ions present but no vacuolar NHHS Fe^{3+} species. This makes sense because vacuolar Fe^{3+} is a storage form of Fe that is not essential for cell metabolism.

The Fe-starved cells were transferred to Fe_0B_{30} medium such that OD_{600} was ≈ 0.01 immediately after inoculation. They grew to a final OD_{600} of 0.8 ± 0.4 (Figure 8A, open circles) at which point they contained just 23 ± 2 μM Fe (Table S2) (n = 2), *the lowest cellular Fe concentrations reported for S. cerevisiae*. Since Fe-starved cells do not store Fe, these cells did not grow quickly or extensively under Fe-deficient conditions. Their minimal DT (5.7 hours) was longer than that of the Fe-loaded cells, and their ultimate cell density was *half* of that attained by Fe-loaded cells. The change of OD_{600} indicated that the Fe-starved cells doubled ~ 6 times after they were inoculated into Fe_0B_{30}, whereas the change of cellular Fe implied that the little Fe initially contained in these cells would only allow ~ 2.5 doublings. The Fe required for the additional ~ 3.5 doublings must have originated from the trace endogenous ^{56}Fe in the Fe_0B_{30} medium. In support of this, the $^{56}Fe/^{57}Fe$ ratio in ^{57}Fe-starved cells was 0.3 before inoculation and 4.4 after harvesting. This increase indicates that the cells imported much of their ^{56}Fe from the Fe_0B_{30} medium (virtually all of the endogenous Fe in that medium was ^{56}Fe). Each growth and division cycle appears to have been associated with the input of ~ 20 μM ^{56}Fe and ~ 3 μM ^{57}Fe (Appendix B, Electronic Supplementary Information).

This experiment again demonstrates that *yeast cells can grow using the tiny amount of Fe present in Fe-deficient BPS-treated medium.*

Effect of high concentrations of BPS on the growth of Fe-starved and Fe-loaded cells

To examine the effect of higher concentrations of BPS on cell growth, we prepared Fe-loaded and Fe-starved cells, and then transferred them to Fe_0B_{100} medium which contained 100 μM rather than 30 μM BPS. (We also standardized the incubation time to 5 days for both Fe-loaded and Fe-starved cells.) The Fe-starved cells barely grew on Fe_0B_{100} (minimal DT = 21 hours), attaining a final OD_{600} of only 0.05 ± 0.02 (Figure 8A, open triangles). The extent of growth implied just 2 doubling. Fe-starved cells that contained 130 ± 30 μM Fe at the time of transfer to Fe_0B_{100} should have contained just ~ 30 μM Fe after 2 doublings ***if*** they exclusively used their own Fe for growth. This estimate (we did not measure this concentration) is reasonable because it is similar to the minimum cellular Fe concentration of *S. cerevisiae* reported above.

The Fe-loaded cells grew on Fe_0B_{100} medium with a minimal DT (5.1 hours) similar to that of cells grown on Fe_0B_{30} medium. However, the final OD_{600} of the culture was only 0.79 ± 0.15 (Figure 8A, filled triangles), about half of that attained when Fe-loaded cells were grown on Fe_0B_{30} (Figure 8A, filled circles). Cells that began as Fe-loaded at the time of inoculation contained 110 ± 10 μM Fe after growing 5 days on Fe_0B_{100} medium. This is approximately *twice* the Fe concentration of equivalent cells that were transferred to Fe_0B_{30} medium and grown to approximately the same stage.

Thus, cells grown on a more extreme Fe-deficient medium grew to half the culture density and contained twice as much Fe as cells grown on less extreme Fe-deficient medium. Why? One could argue that they ran out of endogenous Fe sooner because there was less of it - but if that were the case why didn't they grow on their internal Fe stores?

We hypothesize that the *CW iron in Fe-loaded cells is in a form that cannot support growth directly; it must first be mobilized and released into the environment before it can be reimported and used by the cell.* Accordingly, BPS short-circuits this mobilization process by intercepting the mobilized Fe before it can be reimported into the cell, with higher concentrations of BPS in the medium more effective in doing this than lower concentrations. We further hypothesize that this Fe mobilization-reimport process requires metabolic energy, and that the cells stopped growing because they lacked the energy needed to drive mobilization. Thus, once CW Fe^{3+} is reduced, the Fe^{2+} becomes available for coordination to BPS for import into the cytosol. BPS at a higher concentration will react faster with mobilized Fe^{2+}, forming more $Fe^{2+}(BPS)_3$ which can no longer be reimported into the cytosol or used in metabolism. The metabolic activity of the Fe-starved cells gradually declines, preventing further growth.

Mobilized cell wall iron dissociates into the growth medium

To further assess whether mobilized CW Fe dissociates from the cell and moves into the growth medium, we directly measured Fe in three MM-based media (Fe_0B_{100},

Fe_0B_0, and $^{56}Fe_{40}B_0$) after each had been inoculated with ^{57}Fe-loaded cells. The first two media lacked added Fe; their endogenous ^{56}Fe and ^{57}Fe concentrations were measured to be 230 nM and 8 nM, respectively. The third medium contained 40 μM of added ^{56}Fe. We used DW as a fourth medium, which contained 43 nM ^{56}Fe and 2 nM ^{57}Fe prior to inoculation. ^{57}Fe-loaded cells were inoculated into each medium to about the same cell density as when they had been harvested. OD_{600} was then monitored for 24 hr, and then cells were harvested and analyzed by ICP-MS and MB spectroscopy. The concentration of Fe in the media itself was measured at different times during the incubations to obtain direct evidence that Fe dissociates from cells.

Cells in the first three media grew at similar rates and extents (Figure 8C, open squares, solid diamonds and solid squares, respectively), relative to each other and to cells grown in standard $^{57}Fe_{40}B_0$ medium (Figure 8B, solid squares). In the experiment of Figure 8C, OD_{600} increased regardless of media (n = 2 for $^{57}Fe_{40}B_0$; n = 3 for Fe_0B_{100} and n = 3 for Fe_0B_0). This indicated *one* cell doubling. The concentration of Fe in the Fe-loaded cells that were incubated in Fe_0B_{100} declined from 3.9 ± 0.7 mM before inoculation to 1.5 ± 0.2 mM thereafter (Table S2), similar to our previous results. There was a similar decline (to 1.2 ± 0.2 mM) in the Fe concentration of the cells incubated in Fe_0B_0. At face-value, these results suggest that the ^{57}Fe-loaded cells that were incubated in Fe_0B_{100} and Fe_0B_0 media respectively mobilized about 23% and 40% of their CW Fe into the media during the 24 hr period when they doubled. Cells actually mobilized more Fe because the $^{57}Fe^{2+}(BPS)_3$ that adhered to the CW (and was included in the measured cellular [Fe]) originated from Fe^{2+} that had also been mobilized.

The Fe concentration of ^{57}Fe-loaded cells after growth on $^{56}Fe_{40}B_0$ medium was 3.1 mM (Table S2, Figure 8C, solid squares), 21% lower than at the time of inoculation. However, since the OD_{600} doubled, the total amount of Fe in the entire population of cells must have increased by ~ 52% while the ^{57}Fe portion decreased by ~ 57%. This indicates that CW ^{57}Fe was mobilized and released as ^{56}Fe was simultaneously imported. Hence, *even under Fe-sufficient conditions, metabolically active cells mobilize and import CW Fe while they simultaneously reduce and import environmental Fe*.

Metabolically *inactive* cells placed in DW also lost Fe. The Fe concentration of ^{57}Fe-loaded cells placed in DW for 24 hr decreased by 46% ($\{^{Fe}3.9 \times {}^{OD}2.2 - {}^{Fe}2.1 \times {}^{OD}2.2\} \div \{^{Fe}3.9 \times {}^{OD}2.2\}$) even though the cells barely grew (Figure 8C, open diamonds). We regard this as Fe *leaching* from the CW rather than metabolic mobilization.

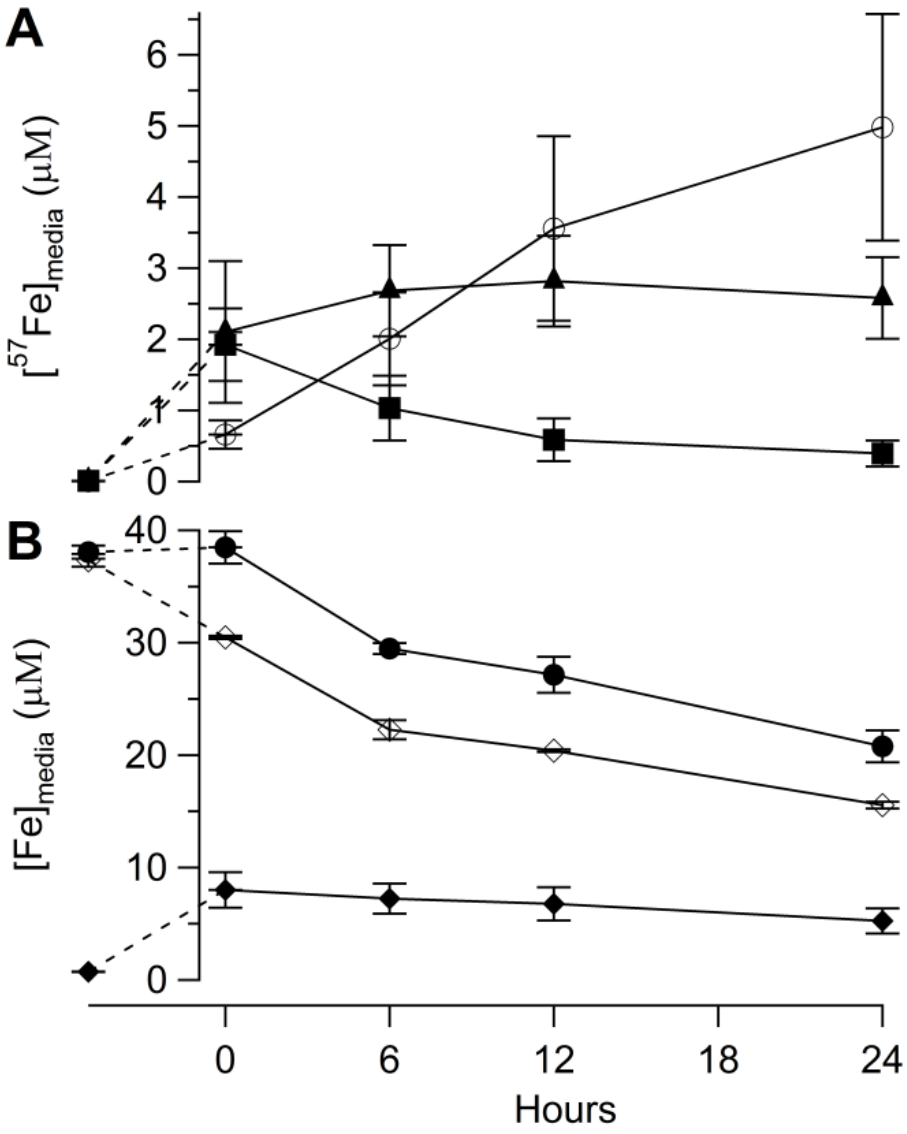

Figure 6.10: Iron concentrations in growth medium before and after inoculation with 57Fe-loaded cells. Other results of this experiment are presented in Fig. 1C. Panel A, 57Fe concentration in media: solid squares, medium before and after 57Fe-loaded cells were transferred to Fe0B100 medium. The datum at t o 0 was of medium prior to inoculation. Other data are of the medium 0, 6, 12 and 24 h after the transfer and after cells were removed by centrifugation. Solid triangles, same but for Fe0B0 medium. Blank circles, same but for DW. Panel B, Fe concentration in 56Fe40B0 medium: solid circles, total [Fe]; open diamonds, [56Fe]; solid diamonds [57Fe].

Loss of cellular Fe was confirmed by measuring the Fe concentration in media to which cells had been incubated. ^{57}Fe concentrations in Fe_0B_{100}, Fe_0B_0, and DW media at different times after ^{57}Fe-loaded cells were inoculated are shown in Figure 10A. Prior to incubation, the residual total Fe concentration in $Fe_0B_{100}$and Fe_0B_0 media was 0.24 μM (0.008 μM ^{57}Fe) while that in DW was 0.045 μM (0.002 μM ^{57}Fe). The OD_{600} was 2.1 immediately after ^{57}Fe-loaded cells were added. At different times, cells were removed by centrifugation and the Fe concentration in the medium was measured. Within 15 min of inoculation, the ^{57}Fe concentration in Fe_0B_{100} medium increased to 2 μM (Figure 10A, solid squares). Then the ^{57}Fe concentration decreased, reaching 0.4 μM at 24 hr. The concentration of ^{56}Fe in the medium dropped 0.12 μM over the first 12 hr (Figure 10B, open diamonds). A UV-vis spectrum of ^{57}Fe-loaded cells that had been incubated for 24 hr in Fe_0B_{100} medium showed strong absorption at 535 nm (Figure S1, B *vs*. A) that reflected $Fe^{2+}(BPS)_3$ complexes associated with these unwashed cells. A corresponding MB spectrum revealed that > 90% of Fe associated with these cells was $^{57}Fe^{2+}(BPS)_3$ (Figure 11D). Much of that $^{57}Fe^{2+}(BPS)_3$ complex was removed by washing at high pH (see below, Figure S1, C and D and Figure 11E). We conclude that *much of the CW Fe in Fe-loaded cells was mobilized and released into the Fe-deficient medium after which a significant portion bound BPS and adsorbed on the CW.*

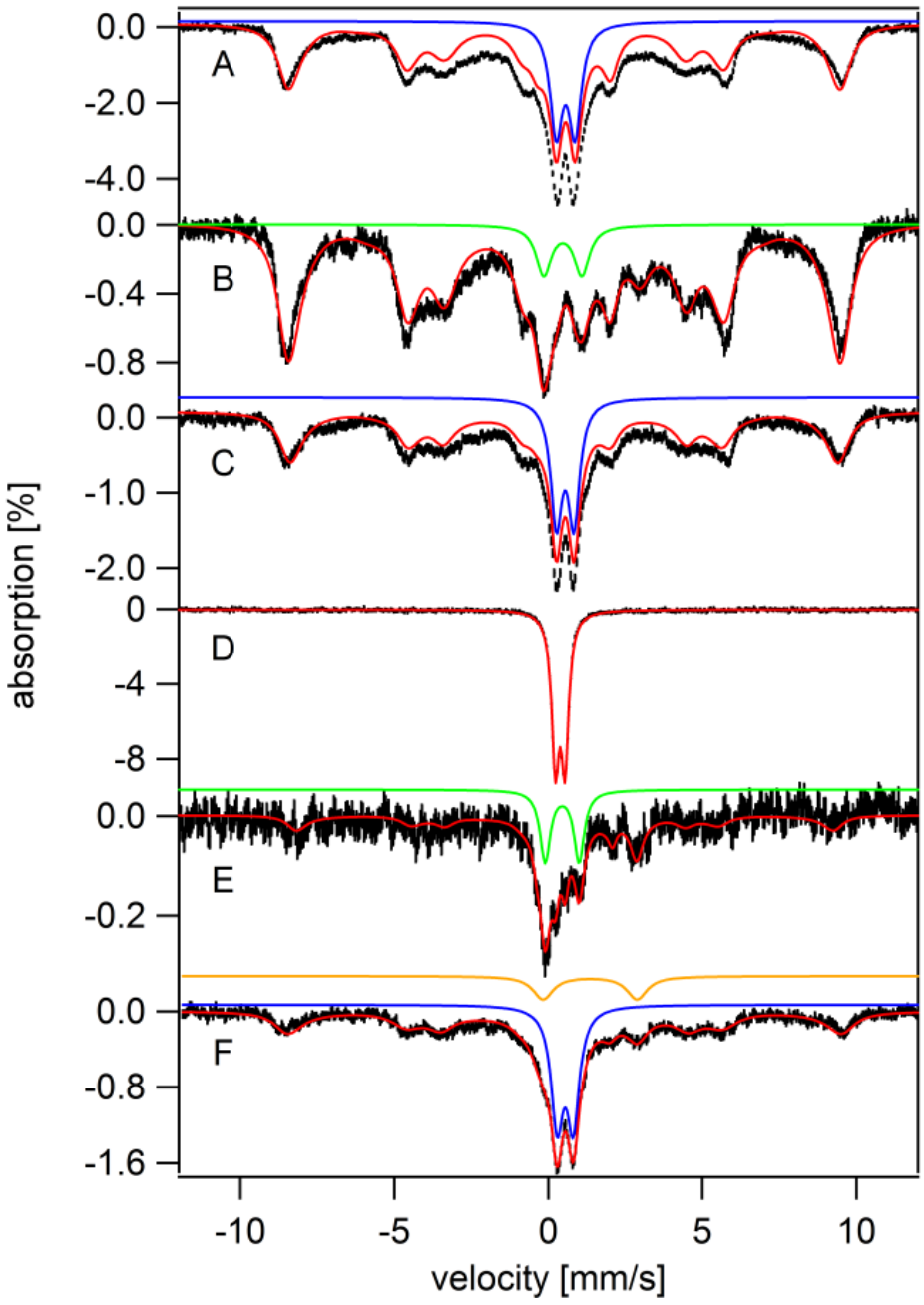

Figure 6.11: Whole-cell Mössbauer spectra (5 K, 0.05 T) obtained from the experiment of Fig. 8C. (A) 57Fe-loaded cells; (B–F) 57Fe-loaded cells after 1 day incubation in the following media: (B) Fe0B0; (C) DW; (D) Fe0B100; (E) same as D, but cells were rinsed with 100 mM Tris-HCl buffer (pH 9.4) three times prior to obtaining the spectrum; (F) 56Fe40B0. Red and blue lines in A and C are the same as in Fig. 9A. The green line in B simulates the Central Doublet (CD) while the red line is a composite simulation as defined in Table S3 (ESI†). The red line in D simulates the Fe2+(BPS)3 doublet, the green line in E simulates the CD, and the orange line in F simulates the NHHS Fe2+ doublet.

Whether the mobilized Fe^{2+} ions were "cleanly" released from the CW and then coordinated by BPS and readsorbed onto the CW, or whether BPS coordinated Fe^{2+} ions that remained *loosely* associated with the CW, is unknown. However, at least some of the mobilized Fe was released into the medium as evidenced by direct measurement. The kinetics of this experiment suggest an initial fast mobilization-and-release phase was followed by a slow-release phase that occurred as Fe was reimported into the cells.

For the experiment involving Fe_0B_0 medium, the concentration of ^{57}Fe in the medium increased to ~ 2 μM immediately after incubation (Figure 10A, solid triangles), similar to the experiment involving Fe_0B_{100} medium, but it then remained nearly invariant for 24 hr rather than decline. Why the difference? Fe_0B_0 medium lacks BPS, and so in this medium the exported ^{57}Fe stayed in solution rather than re-associate with the CW. Fe_0B_0–grown cells contained 1.2 mM Fe while Fe_0B_{100}-grown cells contained 1.5 mM Fe due to this association of $Fe^{2+}(BPS)_3$ with the CW. The 1.5 mM value might underestimate the magnitude of this effect because some $Fe^{2+}(BPS)_3$ complexes were removed from the CW during rinsing. In the absence of BPS, the mobilized ^{57}Fe ions must have been imported into the cytosol where they were used to support cell growth. The rates of these two processes (CW Fe mobilization and release vs. Fe import into the cytosol) appear to be similar since the concentration of Fe in the medium was largely invariant for 24 hr.

The low-temperature low-field MB spectrum of the corresponding cells after 24 hr incubation (Figure 11B) was dominated by an Fe^{3+}sextet along with significant intensity of the central quadrupole doublet that is primarily due to mitochondrial

respiratory complexes (green line). The MB spectrum of the original ^{57}Fe-loaded cells used in this experiment (Figure 11A) exhibited an intense sextet and doublet, features which were strongly diminished in spectra of the post-incubation cells. This indicates that ^{57}Fe-loaded cells exported nearly all of their CW Fe^{3+}. Some mobilized CW Fe was likely used to synthesize the Fe/S clusters and heme centers giving rise to the central doublet in Figure 11B.

Interpreting the effect of incubating Fe-loaded cells in DW proved to be difficult despite the absence of any cell-growth effects. Consistent with the decrease in cellular Fe, the ^{57}Fe concentration in DW increased gradually (Figure 10A, open circles), indicating that ^{57}Fe had exited the cells that had been placed in water. Consistent with that, the intensity of the corresponding MB spectrum declined (Figure 11C) to about half of that observed for Fe-loaded cells (Figure 11A). Curiously, the components in that spectrum and their relative percentages, before and after incubation in water, were nearly identical. Viewed naively, this would imply that all Fe in the metabolically inactive cells (not just CW Fe) was slowly released in proportion to the amount present. We conclude that *metabolically inactive cells "leach" CW Fe but they do not mobilize it* in contrast to metabolically reactivating cells.

The overall concentration of Fe in the cells incubated in $^{56}Fe_{40}B_0$decreased ~ 20% after 24 hr of incubation (3.9 mM → 3.1 mM) during which time the cells underwent a single doubling. The ^{56}Fe/^{57}Fe ratio changed from 0.03 to 2.6, indicating both mobilization and release of ^{57}Fe from the CW AND the import of ^{56}Fe from the medium. Initially, $[^{56}Fe]_1$ = 0.1 mM and $[^{57}Fe]_1$ = 3.8 mM (the subscript indicates the

generation number) whereas after doubling, $[^{56}Fe]_2$ = 2.2 mM and $[^{57}Fe]_2$ = 0.9 mM. Thus in one doubling the cells increased [^{56}Fe] by 2.1 mM and decreased [^{57}Fe] by 2.9 mM. This may seem like an extremely rapid rate of exchange, but the time required for that doubling event was far longer than takes place under standard exponential growth conditions (24 hr. vs. 2 hr.).

The overall concentration of Fe in the $^{56}Fe_{40}B_0$ medium declined during the 24 hr incubation (Figure 10B, solid circles), consistent with the import of ^{56}Fe into the cell and with the doubling of cellular content. In $^{56}Fe_{40}B_0$ medium, the concentration of ^{56}Fe (open diamonds) declined while that of ^{57}Fe (solid diamonds) increased during the initial 15 min, again consistent with the import of ^{56}Fe into the cell and the rapid loss of ^{57}Fe. The total Fe concentration in the medium was invariant during this period, indicating that cellular and environmental Fe ions exchange at roughly equal rates.

The MB spectrum of the ^{57}Fe-enriched cells that had been incubated for 24 hr in $^{56}Fe_{40}B_0$ medium (Figure 11F) displayed just the ^{57}Fe ions that were retained in the cells (imported ^{56}Fe was MB-invisible and any released ^{57}Fe was no longer associated with the cells). Consistent with a decrease in ^{57}Fe concentration (5.2 → 0.7 mM; Table S2), there was approximately a 5-fold decline in overall spectral intensity. Much of the lost Fe appears to have been CW Fe^{3+} species. The spectrum displayed an increase in the NHHS Fe^{2+} doublet (Figure 11F, orange line) which may represent the reduced form of the mobilized CW Fe^{3+} species.

$Fe^{2+}(BPS)_3$ desorption from the cell wall depends on pH

BPS is a negatively-charged chelator that should be unable to penetrate neutral or negatively charged cell membranes. This property is probably due to the large size of the molecule and to charge-charge repulsion involving negatively charged groups on the yeast CW (4). So why does $[Fe^{2+}(BPS)_3]^{4-}$ adhere to the CW? We hypothesize that it is actually neutral or positively charged at the pH of the medium, which would facilitate CW binding via hydrophobic or electrostatic interactions. The pH of $Fe_{40}B_0$ medium dropped from 4.6 to 3.1 during the 24 hr experiments. The pKa of the sulfonic acid groups on $Fe^{2+}(BPS)_3$ are 2.83 and 5.20 **(192)** which implies that a portion of the $Fe^{2+}(BPS)_3$ molecules should be neutral at the pH of the experiment.

Given these considerations, we endeavored to remove $Fe^{2+}(BPS)_3$from the CW by rinsing the pink cells with chilled 100 mM Tris at pH 9.4. At this pH, the complex should be negatively charged and, if our hypothesis is correct, no longer attracted to the CW or plasma membrane. Upon adding the high-pH buffer, the cells turned off-white and the washes turned an intense pink, indicating the large-scale release of the $Fe^{2+}(BPS)_3$ complex into the buffer (Figure S1, D). UV-vis spectra of the pink and off-white cells confirmed that $Fe^{2+}(BPS)_3$ had been removed (Figure S1, C vs. B). MB spectra of the equivalent cells showed that most of the $Fe^{2+}(BPS)_3$ complex was gone; the remaining Fe exhibited features commonly associated with normal yeast cells, such as the central doublet and HS $Fe^{2+/3+}$ features. However, these features were present at low levels (Figure 11 E vs. D, Table S2).

Nonheme high-spin Fe^{2+} forms transiently during initial stages of cell wall iron mobilization

To investigate the kinetics and mechanism of Fe mobilization from ^{57}Fe-loaded cells after being transferred into Fe_0B_{100} medium, we collected MB spectra of these cells 0, 0.5, 3 and 6 hr after transferring them into Fe_0B_{100} medium. The 0.5 hr spectrum (Figure 12B) exhibited features similar to those of original ^{57}Fe-loaded cells (Figure 12A), except that the NHHS Fe^{2+} doublet was three-times more intense (see arrow in Figure 12B; Table S3). At that time, the $Fe^{2+}(BPS)_3$ doublet had barely begun to form (Figure 12B, pink line). At longer times, NHHS Fe^{2+} and diamagnetic/superparamagnetic Fe^{3+} features diminished as the intensity of the $Fe^{2+}(BPS)_3$ doublet increased (Figures 12C and S2). The NHHS Fe^{3+} sextet also decreased, perhaps with a slight delay relative to the other processes (Figure S2, open squares *vs*. solid circles and squares). The $Fe^{2+}(BPS)_3$ doublet had reached ~ 50% of the total intensity by 6 hr (Figure 12D), eventually climbing to ~ 90% by 24 hr (Figure S2, solid circles). These results demonstrate that *an early step in CW Fe mobilization is the formation of NHHS Fe^{2+} from Fe^{3+} CW species, followed by BPS coordination.*

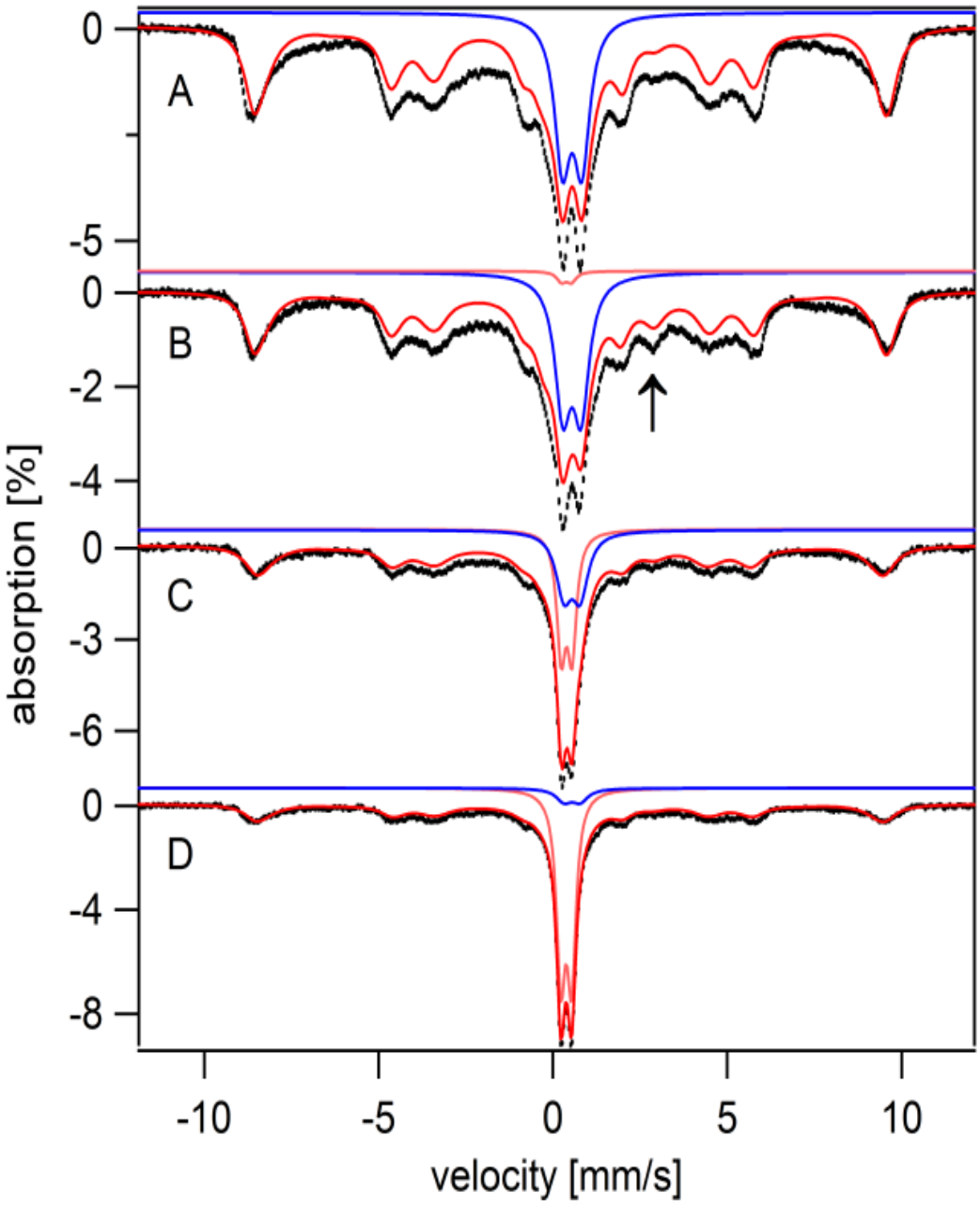

Figure 6.12: Mössbauer spectra (5 K, 0.05 T) of 57Fe-loaded cells before (A) and at increasing times after (B–D) transfer to Fe0B100 medium. Time after transfer: (B) 30 min; (C), 3 h; (D) 6 h. Blue and green lines are simulations of the Fe3+ nanoparticle and Fe2+(BPS)3 quadrupole doublets, respectively. The red lines are composite simulations as defined in Table S3 (ESI†). The arrow in B indicates the position of the high energy line of the NHHS Fe2+ doublet.

The Iron Regulon is not expressed during the accumulation of cell wall iron

We examined the level of Fet3p expression in various media and at different times. In cells grown on Fe_0B_{100}, Fet3p was expressed at all times (Figure 13, bottom panel). However, maximal expression was at 12 hr when the cells were growing exponentially (see Figure 8C). As cells entered stationary state, Fet3p expression declined to an extent similar to that observed previously **(128)**. This is consistent with the decreased need for Fe under stationary growth conditions. In the absence of BPS, Fet3p expression was reduced. In $^{56}Fe_{40}B_0$ medium, cells did not express much Fet3p because Fe was abundant in the medium. In *DW,* cells did not express Fet3p because they were metabolically inactive. These measurements suggest that *the Aft1/2-dependent iron regulon is not expressed under post-exponential conditions when the cell becomes dormant and Fe accumulates in the CW.* Iron regulon proteins probably promote CW Fe mobilization via the reductive Fe uptake system.

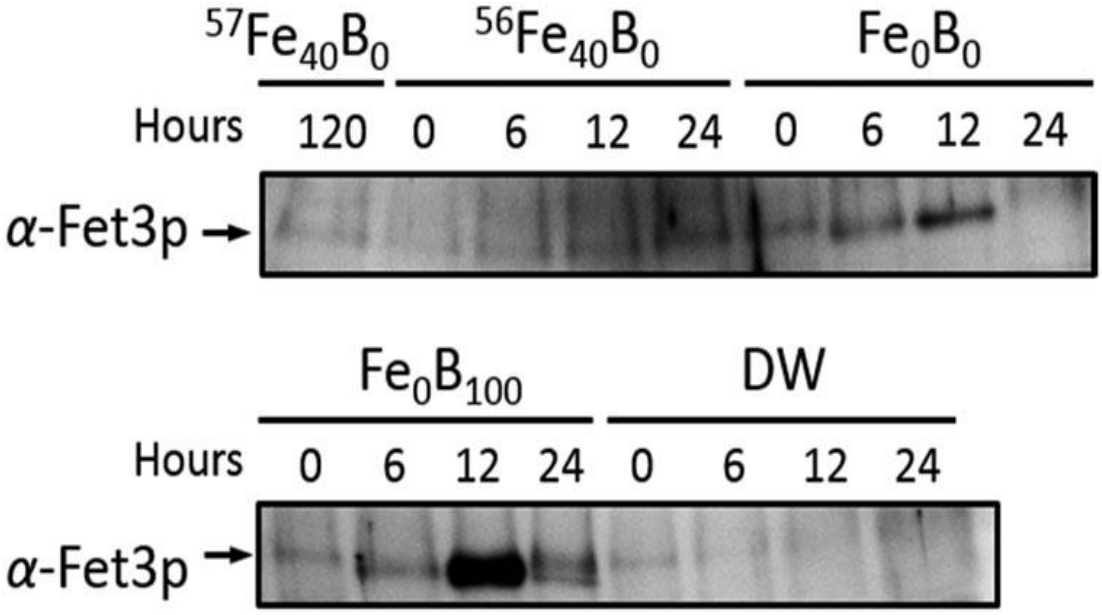

Figure 6.13: Western blot showing Fet3p expression levels in WT cells in various media. Top panel, Fe-loaded cells transferred to Fe40B0, 56Fe40B0, and Fe0B0 media and harvested at the indicated times (in h) after the transfer. Bottom panel, same as top panel but with cells transferred to Fe0B100 and DW media.

Conclusions

The major conclusions of this study are summarized in the model of Figure 14. Iron accumulates in the walls of yeast cells that are declining in metabolic activity (transitioning from exponential to post-exponential growth stages). This phenomenon is probably prompted by the lack of certain metabolites (possibly glucose) within the cell. Metal ion accumulation appears specific for Fe in that Cu, Mn, and Zn do not accumulate in the CW. In metabolically dormant cells, CW Fe accounts for ~ 90% of total cellular Fe; thus, the accumulation of CW Fe represents a *huge* perturbation of the Fe content of a yeast cell.

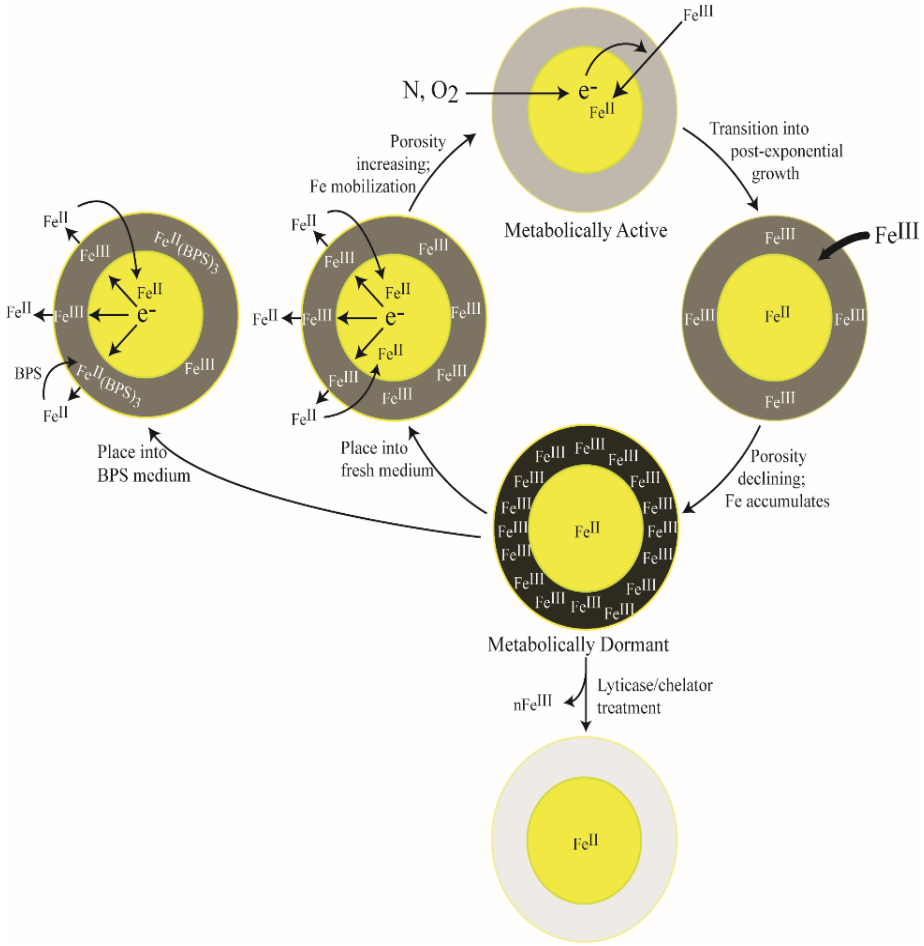

Figure 6.14: Model for iron accumulation into the cell wall. Metabolically active (exponentially-growing) cells do not accumulate Fe in their CWs; Fe3+ from the environment is reduced by metabolic processes in the cell and it enters the cell as Fe2+. As cells transition into a post-exponential (or dormant) state, Fe3+ begins to accumulate in the CW. CW Fe can be removed by chelation or CW digestion. When dormant cells become metabolically active (by placing them into fresh media), the CW Fe3+ becomes reductively mobilized to the Fe2+ state. The Fe2+ is released from the CW where it can: (a) dissociate from the cell and diffuse into the environment; (b) enter the cytosol to support cell growth; or (c) chelate with BPS (if BPS is in the medium). A significant portion of the neutral Fe2+(BPS)3 species adsorbs onto the CW.

Our results show that the majority of CW Fe (~70%) is present as mononuclear NHHS Fe^{3+} ions, with modest levels of diamagnetic Fe species (~ 20%) and even less superparamagnetic Fe^{3+}oxyhydroxide nanoparticles (~10%). It is tempting to speculate that Fe initially accumulates as magnetically isolated mononuclear Fe^{3+}species, then as Fe accumulates to a higher density, magnetic interactions develop that give rise to the diamagnetic and finally superparamagnetic species. The CW contains a large number of negatively charged phosphodiester bridges in both N- and O-carbohydrate side chains that anchor the protein to the CW **(193)**. Fe coordinates other phosphodiester species **(149)** suggesting this mode of binding. Fe^{3+} may bind to various sites in the CW **(194)**. Bound Fe may also serve to stabilize the CW structure.

When dormant cells reactivate, CW Fe^{3+} species become mobilized regardless of the Fe concentration in the growth medium. Mobilization involves reduction to the Fe^{2+} state probably via a reaction catalyzed by surface ferric reductases **(116)**. CW Fe may dissociate even when not reduced to Fe^{2+}, but this is a different phenomenon that we call *leaching*. The reducing equivalents used for mobilization must originate from the metabolic activity of the cell **(195)**. Mobilized Fe^{2+} is released from the CW; some is imported into the cytosol for cell growth and some remains in the environment. Thus, CW Fe becomes available as dormant cells awaken. If chelators such as BPS or EDTA are present in the environment, they will also coordinate mobilized Fe^{2+}. Metabolically active cells can also import trace amounts of endogenous forms of Fe in Fe-deficient (BPS-treated) growth media. The cell does not discriminate strongly in its source of imported Fe - it simultaneously imports mobilized CW Fe AND endogenous Fe from the

medium. Given the scarcity of bioavailable Fe in the environment, the CW Fe accumulation-mobilization-re-importation process would have provided a selective advantage during evolution.

Our results demonstrate that the CW should be regarded as a second storage compartment for Fe in *S. cerevisiae* and probably in other fungal cells. Its function in this regard is distinct from that of vacuoles; vacuolar Fe maintains intracellular homeostasis which allows metabolically active cells to survive in Fe-poor environments and it also sequesters potentially toxic forms of Fe. CW Fe helps reactivate dormant cells, by providing Fe regardless of the availability of Fe in the environment. Given the large extent of Fe accumulation, the CW should be regarded, along with mitochondria and vacuoles, as a major iron traffic "hub" in yeast.

During exponential growth, the reductive Fe uptake system controlled by the Aft1/2-dependent iron regulon may reduce bound Fe^{3+} such that the Fe could be imported and not accumulate in the CW. After the cell enters post-exponential growth, the iron regulon is shut down and CW bound Fe cannot be reductively mobilized; thus it accumulates. The Fit genes are part of the iron regulon, and so their expression should also decline. If the Fit proteins facilitate passage of Fe across the CW and into the cytosol, we would expect that Fe should accumulate during post-exponential growth, as is observed. Conflicting with this expectation is the observed *decline*in CW Fe in mutant strains lacking Fit proteins **(87)**. Further studies are needed to reconcile this situation. One practical ramification of our study is that researchers who measure Fe concentrations of whole fungal cells should not grow cells beyond exponential phase,

because the dominating contribution of CW Fe to the total cellular Fe could cause confusion. One should also be cautious in using BPS to generate Fe-deficient conditions. Doing so creates an Fe deficiency severe enough to turn-on the iron regulon **(196,197)** but not severe enough to fully abolish growth. Amazingly, yeast cells can import trace endogenous Fe from such media and use it for growth.

Other fungal cells besides *S. cerevisiae* have CWs, and some connections with iron metabolism have been reported. Vainshtein *et al.* identified Fe nanoparticles in the CW of the pathogenic fungus *Cryptococcus humicola* **(185)**. Cir1, the "master iron regulator" in the pathogen *Cryptococcus neoformans*, regulates CW biogenesis and other virulence factors **(198)**. The polysaccharide capsule of these cells is a major virulence factor, and capsule production is enhanced under Fe-limiting conditions **(83)**. In *Candida glabrata*, CW proteins CgCcw14 and CgMam3 are "pivotal virulence determinants" that are involved in iron metabolism **(199)**. CgCcw14 is a cysteine-rich glycosylphosphatidylinositol-linked CW protein while CgMam3 is a putative hemolysin. Ferric reductase Cfl1 in *Candida albicans* is involved in CW integrity, morphogenesis, virulence and invasion into host cells **(85)**. Mutant cells lacking Cfl1 overload with Fe, but whether the Fe accumulates in the CW or elsewhere was not investigated **(86)**. We suspect that the CW Fe accumulation phenomenon discovered here is a general property of fungi, and that it promotes their survival. If so, inhibiting CW Fe may diminish the ability of pathogenic fungi to survive in a host **(180)**. Deleting the Fet3 ferroxidases on the plasma membrane of pathogenic fungus *Colletotrichum graminicola* caused an 80% decline in chitin synthase and defects in the CW that reduced virulence. These proteins

are part of the reductive iron import system which is required for CW integrity/stability and pathogenic fungal virulence; indeed the ability to import Fe is considered a “key factor for pathogenicity”. Future studies should investigate whether pathogenicity is related to the ability of the CW to accumulate and/or mobilize Fe as such investigations may lead to improved treatments for fungal pathologies.

Acknowledgments

We thank Brad Pierce (University of Texas at Arlington) for kindly allowing us to use his EPR spectrometer, Andrew Dancis (University of Pennsylvania) for generously providing the Fet3 antibody, and Charles Johnson (University of Tennessee) for help in analyzing Mössbauer spectra. The National Institutes of Health (GM084266) and the Robert A. Welch Foundation (A1170) sponsored this study.

CHAPTER VII

CHARACTERIZATION OF THE LABILE IRON POOL IN *ESCHERICHIA COLI*, AND A "RESPIRATION SHIELD" THAT PROTECTS IT FROM O_2 DAMAGE[*]

Joshua D. Wofford[1], Naimah Bolaji[1], Nathaniel Dziuba[3], F. Wayne Outten[2], and Paul A. Lindahl[1,3*]

#1. Department of Chemistry, Texas A&M University, College Station, Texas USA 77843. #2. Department of Chemistry and Biochemistry, University of South Carolina, Columbia South Carolina 29208. #3. Department of Biochemistry and Biophysics, Texas A&M University, College Station Texas 77843.

Summary

The aim of this study was to better define the iron content of *E. coli* cells. Mössbauer and EPR spectra of cells prepared under different nutrient iron concentrations, carbon sources, growth modes, and O_2 concentrations were collected. Wild-type (WT) cells and those lacking Fur, FtnA, Bfr, and Dps were investigated. The iron content of exponentially growing cells was dominated by iron-sulfur clusters and variable amounts of nonheme high-spin Fe^{2+} species. An unassigned residual quadrupole doublet was also observed. The iron in stationary-phase cells was dominated by magnetically-ordered Fe^{3+} due to oxyhydroxide nanoparticles, not ferritins. Cytosolic

[*] This paper has been submitted to PNAS, is awaiting review, and has been done in collaboration with Naimah Bolaji and F. Wayne Outten at the University of South Carolina

extracts were isolated and analyzed using LC-ICP-MS. The low-molecular-mass Labile-Iron-Pool (LIP) consisted of two iron complexes with masses of ~500 (major) and ~1300 (minor) Da. They are probably high-spin Fe^{2+} species with mostly O ligands, few N, and probably no S ligands. The LIP in Δ*fur* cells was dysregulated. The iron content of *E. coli* and its reactivity with O_2 were remarkably similar to those of mitochondria. In both cases, a "respiratory shield" composed of membrane-bound iron-rich respiratory complexes appears to protect the LIP from reacting with O_2. When exponentially growing cells transition to stationary phase, the shield deactivates as metabolic activity declines. Given the universality of oxidative phosphorylation in aerobic biology, the iron content and respiratory shield effects in other aerobic prokaryotes may be similar to those of *E. coli* and mitochondria.

Introduction

Iron is critical for virtually all living systems, including *Escherichia coli*, arguably the most extensively studied organism on the planet. This redox-active transition metal is found at the active site of numerous metalloenzymes, in the form of hemes, iron-sulfur clusters (ISCs), diiron-oxo centers, and mononuclear iron centers **(203, 92)**. Certain forms of iron, especially mononuclear Fe^{2+} complexes, are dangerous to cells because they react with O_2 or O_2-derived species (e.g. H_2O_2) to generate highly reactive oxygen species (ROS) such as hydroxyl radicals **(204)**. Thus, iron import, trafficking, and regulation are especially critical in aerobic living systems so as to minimize the dangers of this essential transition metal **(205, 206)**.

The Ferric Uptake Repressor *Fur* is the "master regulator" of iron in *E. coli* and in many other bacteria **(207)**. This iron-sensitive transcription factor regulates the expression of > 100 genes involved in iron import, trafficking, and storage as well as iron-dependent enzyme catalysis and metabolism. When cellular concentrations of iron exceed metabolic requirements, Fe^{2+} binds Fur. The resulting Fe^{2+}-Fur dimers bind to promotor sites on the DNA called *Fur boxes*, which represses transcription of targeted genes. Under Fe-deficient conditions, Fur boxes are unbound which allows gene expression.

Under aerobic conditions, *E. coli* secretes high-affinity siderophores into the environment, which bind aqueous Fe^{3+} and re-enter the cell as iron chelates via specific membrane-bound receptors and the TonB-ExbB-ExbD complex **(89,208)**. Under anaerobic conditions, the *Feo* system imports Fe^{2+} ions **(208)**. The *Fec* system imports ferric citrate **(90)**; this form of ^{57}Fe was added to the growth medium in the current study. All iron import genes are regulated by Fur **(91)**.

E. coli cells contain three types of ferritins which store iron under iron-replete conditions, including ferritin FtnA, bacterioferritin Bfr, and miniferritin Dps **(92)**. The main iron storage protein is FtnA, a 24-subunit multimer that can bind thousands of iron ions as inert ferric aggregates. Fe^{2+}-Fur binding stimulates expression of FtnA and Bfr **(92)**; expression increases dramatically as cells transition from exponential growth to stationary state **(96)**.

Fur activation affects more than iron import and storage; it also promotes expression of several proteins involved in the TCA cycle and respiration. Fur regulates

anaerobic electron transport, heme biosynthesis, and cytochrome c maturation **(210)**. Fur regulates expression of enzymes that protect against ROS damage, and it controls peroxidase and catalase activities by regulating heme biosynthesis **(211, 212)**. Fur is induced during oxidative stress which represses iron uptake and limits Fenton chemistry **(213)**. Δ*fur* cells contain less iron than wild-type (WT) cells and are deficient in iron-containing proteins such as cytochrome c, ferritin, and ISC proteins **(210, 109)**. For these reasons, Δ*fur* cells cannot respire effectively **(214)**.

Gene expression in *E. coli* is also affected by oxygenation state. FNR is an O_2-sensing transcription factor that regulates the shift between aerobic and anaerobic metabolism **(97)**. It regulates >300 genes, and is sensitive to dissolved O_2 concentrations between 0 – 20 μM **(98)**. FNR contains a bridging Fe_4S_4 cluster that converts into two Fe_2S_2 clusters under oxidizing conditions; this conversion controls its DNA-binding activity. In the absence of O_2, [Fe_4S_4]-containing FNR along with ArcA increases expression of the *feo* iron uptake operon to increase cellular Fe^{2+} levels under O_2-limited conditions **(105)**.

Iron regulation and iron metalloprotein metalation in *E. coli* involves a poorly characterized *labile iron pool* (LIP) **(99,100,215)**. The LIP is presumed to be composed of one or more low-molecular-mass (LMM) non-proteinaceous Fe^{2+} complexes in the cytosol. The LIP is thought to enter cells via the *feo* system **(105)**. Estimates of the LIP concentration in WT cells are highly variable, with values of 1 **(216)**, 10 **(110, 217)**, 26 **(105)**, 15 – 30 μM **(103)** and 140 μM **(218)** reported for aerobic bacteria, and 177 μM under anaerobic conditions **(105)**. The size of the LIP increases under anaerobic

conditions due to altered regulation between Fe^{3+} and Fe^{2+} import into the cell **(105)**. The LIP concentration reportedly increases with increasing iron concentrations in the growth medium **(102)**.

The *fur* system regulates cellular iron by binding Fe^{2+} ions from the LIP. Aqueous Fe^{2+} ions bind Fur with reported K_D ~ 1 μM **(219, 102, 216)** and ~ 10 μM **(217)** for one-iron binding, and K_{D1} = 30 μM and K_{D2} = 280 μM for two-irons binding **(218)**. Imlay and coworkers reported LIP concentrations of 80 μM in Δ*fur* cells **(103)**, substantially higher than in WT cells.

The LIP is difficult to characterize because weakly coordinated ligands undergo fast ligand-exchange reactions making such complexes difficult to isolate and study biochemically. Böhnke and Matzanke **(100)** isolated and characterized a soluble nonproteinaceous negatively charged iron species from *E. coli* extracts that accounted for 40% of the LIP; they reported a mass of ~ 2.2 kDa and an association with a pentose or uronic acid, and possibly with sulfonate or phosphate esters.

Mössbauer (MB) spectroscopy has been used intermittently to study the iron content of *E. coli* cells. In 1980, Bauminger et al. reported that low-temperature MB spectra of *E. coli* exhibited a broad quadrupole doublet characteristic of magnetically-ordered Fe^{3+} ions **(106)**. Nine years later, Matzanke et al **(107)** identified a second doublet, representing 11% - 56% of spectral intensity, with parameters typical of nonheme high-spin (NHHS) Fe^{2+} complexes coordinated by O and N ligands. Hudson et al **(108)** recognized that the Fe^{2+} doublet was composed of two subcomponents. They found that isolated FtnA has a Blocking Temperature (T_B) of 19 - 22 K, which is higher

than that of magnetically-ordered Fe^{3+} species in *E. coli* whole cells. At temperatures below T_B, magnetically-ordered Fe^{3+} will exhibit a magnetic spectrum, whereas above T_B, they will exhibit a broad quadrupole doublet **(220)**. Because of this, these authors suggested that ferritin was not the source of the magnetically-ordered iron. However, a few years later, Abdul-Tehrani et al **(109)** concluded that the magnetically-ordered iron observed under stationary-state conditions indeed arose from FtnA. They also estimated the concentration of the Fe^{2+} species at ~ 200 μM, significantly higher than most estimates of the LIP in *E. coli*, and higher than implied by the Fe^{2+}-Fur dissociation constant. To explain this, they proposed that the Fe^{2+} species observed by MB represents a different pool than that used to bind Fur. Hristova et al. **(111)** reported a fourth doublet, representing ~ 60% of spectral intensity, that was attributed to a combination of $[Fe_4S_4]^{2+}$ and $[Fe_2S_2]^{2+}$ clusters, low-spin (LS) Fe^{2+} hemes, and possibly fast-relaxing high-spin (HS) Fe^{3+} species. Beilschmidt et al. **(112)** assigned the same doublet exclusively to ISCs.

In this paper, we probed the total iron content of WT *E. coli* and of genetic strains lacking Fur, FtnA, Bfr, and Dps. We used MB (and in some cases EPR) spectroscopy, and characterized the LIP in these cells using LC-ICP-MS. We found a dramatic change in the size of the LIP due to oxygenation state of the growth medium, and succeeded in isolating and partially characterizing the LIP. Our results impact the understanding of iron import and storage in *E. coli*, and suggest a reinterpretation of cellular iron homeostasis. They also reveal an unexpected connection to the iron content of mitochondria and other phylogenetically related aerobic prokaryotes.

Results

Our initial objective was to better define the iron *content* of *Escherichia coli* using MB spectroscopy (and EPR). The word *content* not only refers to the *concentrations* of iron in such cells but also to a description of the major iron species contained therein. To do this, we collected MB (and in some cases EPR) spectra of whole, intact *E. coli*. Cells were grown on minimal medium using either of two different carbon sources, any of three different nutrient iron concentrations, and variable levels of exposures to O_2. Some batches were harvested during exponential growth phase while others were harvested in stationary phase.

Table 7.1: Components assumed in simulating Mössbauer spectra of *E. coli* and the percentages of each component included in simulations.

Mössbauer Component	ISC	Residual	Fe^{2+}_{LMM}	Fe^{2+}_{RET}	Fe^{3+} nanoparticles	S = 5/2 Fe^{3+} sextet
δ (mm/s)	0.45 ± 0.01	0.47 ± 0.03	1.33 ± 0.01	1.17 ± 0.05	0.55 ± 0.1	.54±.01
ΔE_Q (mm/s)	1.15 ± 0.03	0.72 ± 0.13	3.47 ± 0.01	2.99 ± 0.05	0.55 ± 0.1	.39±.01
Γ (mm/s)	0.6 ± 0.1	0.6 ± 0.1	0.6 ± 0.3	0.7 ± 0.1	0.5 ± 0.1	.4±.01
Spectrum	%	%	%	%	%	%
Fig. 1A	22	36	07	29	0	05
Fig 1B (top)	28	38	11	18	0	05
Fig. 1B (bot)	31	42	0	34	0	05
Fig. 1C	0	0	0	0	0	05
Fig. 3A	17	0	40	45	0	0
Fig. 3B	11	0	30	54	0	0
Fig. 3C	19	18	37	27	0	0

Table 7.1 continued

Mössbauer Component	ISC	Residual	Fe^{2+}_{LMM}	Fe^{2+}_{RET}	Fe^{3+} nanoparticles	S = 5/2 Fe^{3+} sextet
Fig. 4A	32	0	62	12	0	0
Fig. 4B	05	20	32	44	0	0
Fig. 4C	05	16	30	39	0	0
Fig. 5A	10	29	15	44	0	0
Fig. 5B	13	0	0	10	61	0
Fig. 5C	30	32	09	15	0	10
Fig. 5D	26	39	06	15	0	06
Fig. 5E	13	0	0	10	76	0
Fig. 5F	23	12	35	18	11	0
Fig. 5G	31	15	13	37	0	0
Fig. 7A	17	20	29	21	16	0
Fig. 7B	17	20	16	21	29	0
Fig. 7C	0	0	-13	0	13	0
Fig. 8A	11	31	10	48	0	0
Fig. 8B	0	0	100	0	0	0
Fig. 8C	13	29	32	35	0	0
Fig. 8D	13	29	0	35	0	0

The iron concentration of *E. coli* cells grown on glucose and harvested under exponential growth conditions increased with increasing iron concentration in the growth medium. Cells grown in media supplemented with 1, 10, and 100 μM $^{57}Fe^{3+}$ citrate contained 400 ± 200, 500 ± 100, and 1000 ± 100 μM Fe, respectively (n = 2 for each condition). WT *E. coli* cells harvested during exponential phase using acetate as the carbon source and in media supplemented with 1, 10, and 100 μM $^{57}Fe^{3+}$ citrate contained 600 ± 200, 900 ± 500, and 1600 ± 400 μM Fe (n = 2), respectively. This is an average of ca. 1.6-times as much iron as in glucose-grown cells. See Table S1 for a compilation of selected metals and phosphorus concentrations in these and other samples.

Mössbauer spectra of exponentially growing cells:

Low-temperature low-field MB spectra of glucose-grown and exponentially harvested cells were similar regardless of nutrient iron concentration (Figure 1A and Figure S1, A and B). The doublet simulated by the solid blue line in Figure 1 and referred to as the *ISC doublet* had parameters typical of S = 0 $[Fe_4S_4]^{2+}$ clusters and low-spin Fe^{2+} hemes (the two cannot be resolved by MB). The ISC doublet represented as high as 30% of spectral intensity. The species simulated by the pink line in Figure 1 and referred to as the *Residual doublet* contributed to the dominant doublet in the spectrum; in some spectra it represented as much as 40% of the overall intensity (Table 1). The isomer shift δ associated with the Residual doublet was close to that of S = 0 $[Fe_4S_4]^{2+}$

clusters but the quadrupole splitting ΔE_Q was somewhat smaller than is typical; thus, we leave this species unassigned. The simulation of the dominant doublet, as it would appear at 6 T, was overlaid on the experimental 6 T spectrum in Figure S2. Although the spectrum was noisy, the fit provides evidence that both ISC and Residual doublets arose from diamagnetic S = 0 centers as expected for $[Fe_4S_4]^{2+}$ clusters and/or low-spin Fe^{2+} hemes.

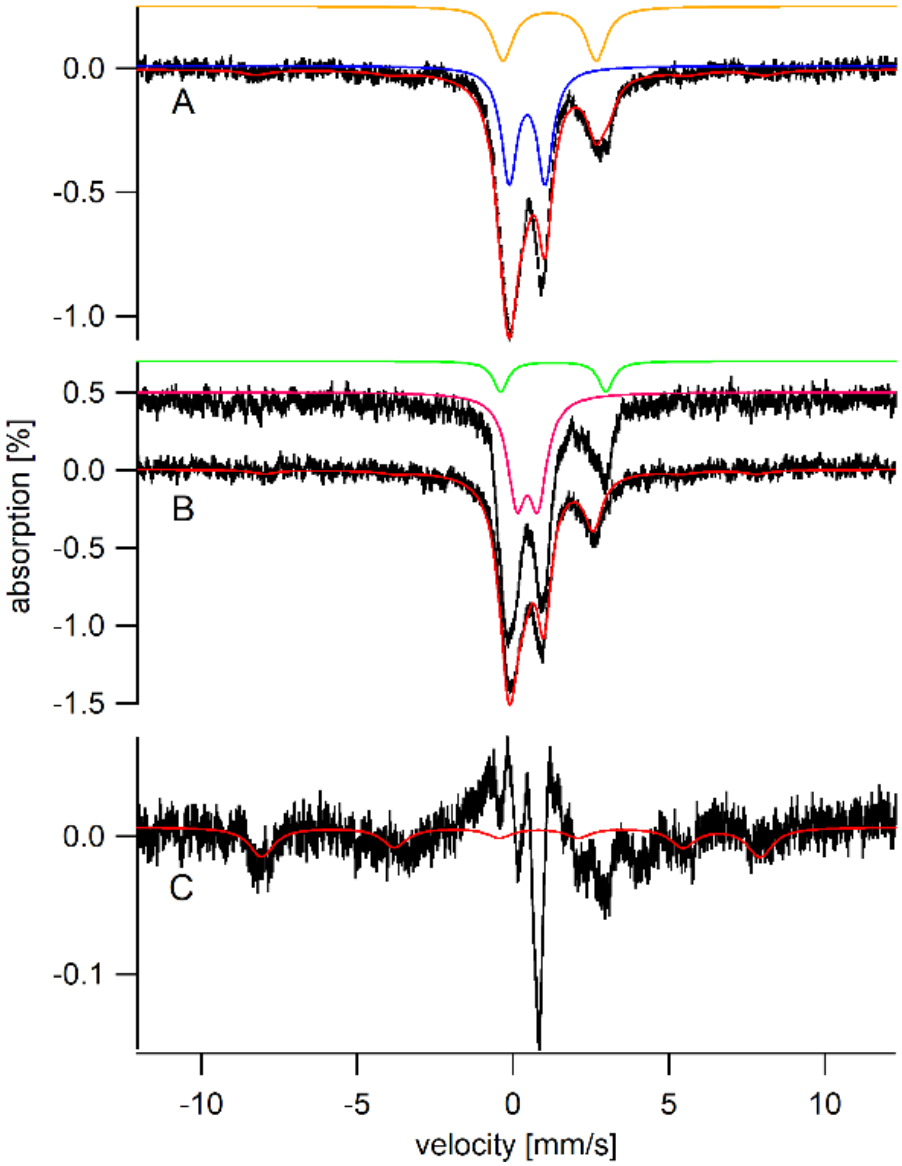

Figure 7.1. Low-temperature low-field (5 K, 0.05 T) Mössbauer spectra of WT *E. coli* harvested during exponential growth. A, glucose media supplemented with 100 μM 57Fe3+ citrate; B, acetate media supplemented with 1 (top) and 100 μM 57Fe3+ citrate (bottom); Gold, blue, green and pink lines simulate Fe2+RET, ISC, Fe2+LMM , and residual doublets, respectively. Simulation parameters are given in Table 1. Red lines in this and other figures are composite simulations assuming components and percentages given in Table 1. The presence of the Fe2+LMM doublet (20% intensity) in the spectrum from acetate-grown cells with 1 μM Fe added is evident from the shift in the high-energy line of the NHHS Fe2+ doublet. The spectrum in C is the sum of all six spectra in Figures 1 and S1, after removing contributions from the four major doublet. The red line in C is a simulation assuming parameters typical of S = 5/2 Fe3+ or ferritins (the two cannot be distinguished) with 5% of overall spectral intensity. Unless specified otherwise, the magnetic field was applied parallel to the gamma radiation.

The other major quadrupole doublet of Figure 1A had parameters typical of NHHS Fe^{2+} species in which Fe^{2+} is coordinated by 4 - 6 O and 0 - 2 N donor ligands (with few if any S donors). The doublet was broader than expected for a single species and so two subcomponents (Fe^{2+}_{RET} and Fe^{2+}_{LMM}) were used in simulations. The green and gold lines in Figure 1 simulates the two subcomponents, using parameters given in Table 1. Subscripts RET and LIP are explained below.

Acetate-grown and exponentially harvested cells exhibited the MB spectra shown in Figures 1B and S1, C and D. Relative to growth on glucose, cells grew less than half as fast on acetate as on glucose; the average exponential growth rate α was 0.40 ± 0.04 hr^{-1} for glucose-grown cells and 0.17 ± 0.03 hr^{-1} for acetate-grown cells (n = 3 for each). This is similar to a previous report which also found that both glucose- and acetate-grown cells consumed O_2 at about the same rate **(221)**. *E. coli* cells convert acetate directly to acetyl-CoA which is then sent to the TCA cycle without involving glycolysis. In contrast, cells first convert glucose to acetyl-CoA via glycolysis (and pyruvate dehydrogenase). Thus, acetate-grown cells *respire* exclusively whereas glucose-grown cells both respire and ferment for energy production.

MB spectra of acetate-grown cells were similar to those of glucose-grown cells, except that the ISC and Residual doublets were slightly more intense, consistent with the higher iron concentration in these cells. Acetate-grown cells, which are more respiratory metabolically, probably contain a somewhat higher concentration of iron-rich respiration-related proteins. We also observed a shift in the position of the Fe^{2+} doublet, depending on the iron concentration in the growth medium. For the sample grown with 1

μM $^{57}Fe^{3+}$ citrate added, the Fe^{2+}_{LMM} species represented 20% of the spectral intensity (Figure 1B, upper spectrum) whereas for the sample grown with 10 or 100 μM $^{57}Fe^{3+}$ citrate (Figure 1B, lower spectrum), no Fe^{3+}_{LMM} species was required to simulate the overall NHHS Fe^{2+} doublet.

We searched for low-intensity features emanating from the baselines of the "wings" associated with the two spectra of Figure 1 and the four spectra of Figure S1. Such features, if present, might arise from paramagnetic centers such as S = 5/2 Fe^{3+} hemes or from superparamagnetic centers such as ferritins (at temperatures below their T_B). To probe this, we *summed* the six spectra and removed the major spectral features described above. The resulting difference spectrum (Figure 1C) exhibited weak spectral absorption in the wings which could be simulated using parameters typical of either S = 5/2 Fe^{3+} hemes and nonheme species, or of ferritins (below their T_B). Magnetic features with S = ½ may have also been present, but they would be obscured by features in the central region of the spectra. Collectively, we estimate that magnetic features constituted roughly 5% of the overall spectral intensity. We include this estimate in the composite simulations of Figure 1, A and B.

***EPR Spectra**:*

Glucose- and acetate-grown whole cells exhibited EPR signals in the low- (g = 6 – 4) and high- (g ~ 2) field regions (Figure 2). Spectral decomposition identified three low- and three high-field signals (see Figure S2 for individual decomposed simulations). Low-field signals were typical of S = 5/2 hemes and nonheme Fe^{3+} species. High-field

signals included two g_{ave} = 1.94 type signals arising from reduced S = ½ $[Fe_4S_4]^{1+}$ and/or $[Fe_2S_4]^{1+}$ clusters, as well as an isotropic g = 2.00 signal arising from radical species. Similar spectra of whole *E. coli* cells have been reported **(210)** except that signals from $[Fe_3S_4]^{1+}$ centers were also observed in the previous study. Also the low-field signals in our spectra were more typical of those from dithionite-reduced cells in the previous study. All current signals except the radical were 2 - 10 times more intense in acetate-grown cells than in glucose-grown cells (the quantified intensity of the radical was similar in both spectra). The overall spin concentration in the g = 2 region was ca. 60 μM for the acetate-grown sample and 20 μM for the glucose-grown sample. We did not quantify the signals in the low-field region but expect concentrations of the same magnitude. Quantified spin concentrations suggest that these paramagnetic centers contribute 2% - 5% to the MB spectra in the central regions of the spectra and perhaps a similar percentage in the "wings". Although these are ballpark estimates, they are consistent with the very minor intensity associated with paramagnetic centers in the MB spectra of Figure 1C. Most ISCs in WT *E. coli* cells are diamagnetic and oxidized (i.e. $[Fe_2S_2]^{2+}$ and $[Fe_4S_4]^{2+}$ clusters).

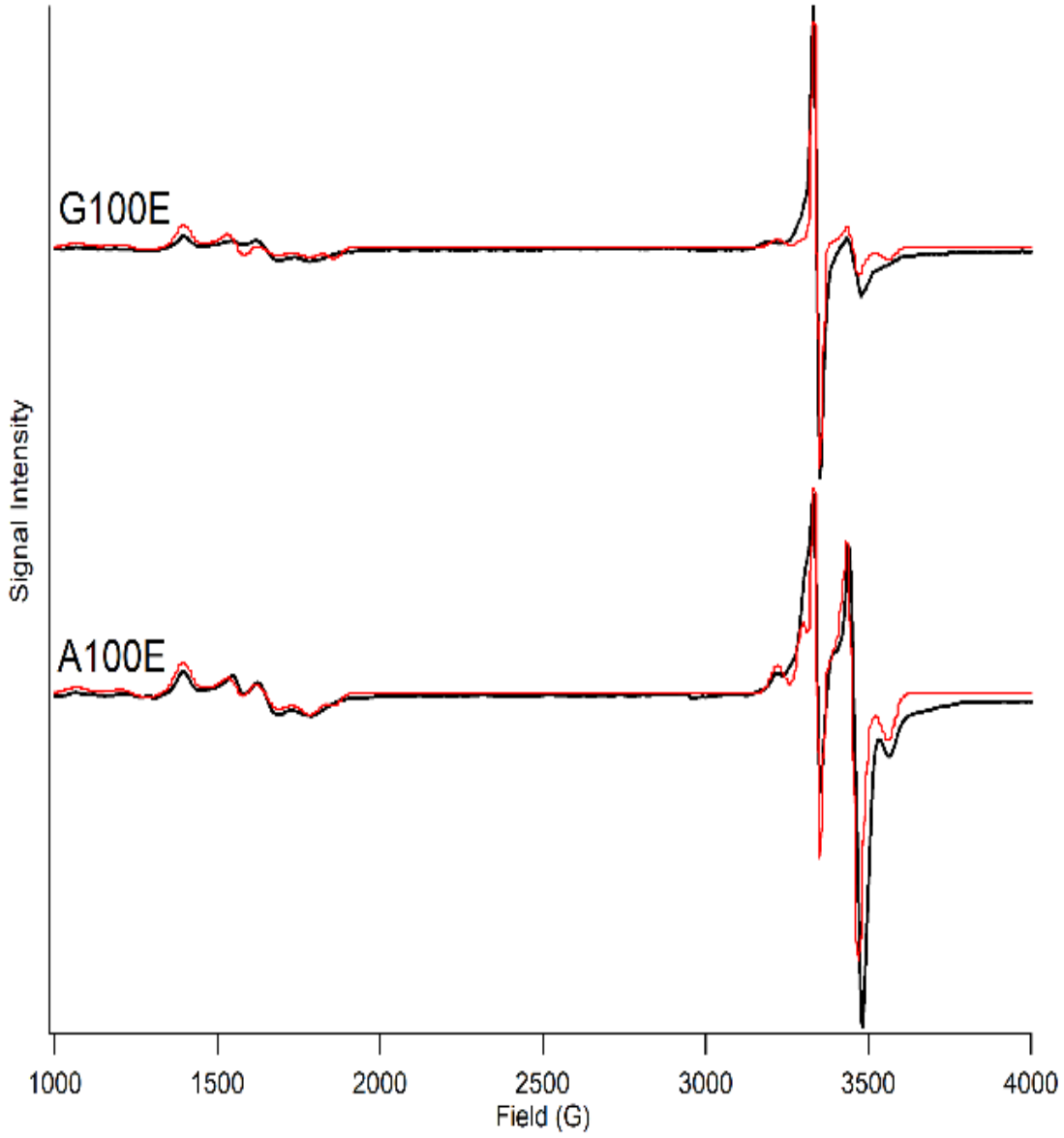

Figure 7.2: Low-temperature X-band EPR spectra of whole packed *E. coli* cells grown on glucose or acetate, and harvested under exponential growth conditions. Composite simulations are the red lines overlaying the data (black lines). Individual simulations are shown in Figure S2. Temperature, 10 K; microwave frequency, 9.38 GHz; microwave power, 0.2 mW; time constant 0.293 sec; modulation amplitude, 10 G.

Intensity of the NHHS Fe^{2+} doublets is correlated to O_2 levels during growth:

In some spectra, the NHHS Fe^{2+} doublets were significantly more intense than in Figure 1 – reaching as high as 85% of overall intensity for the MB spectra in Figure 3. This variation was puzzling because batches were grown on the same medium, using the same concentration of nutrient $^{57}Fe^{3+}$ citrate, and harvested in exponential phase at approximately the same OD_{600}. Like Beauchene et al. **(105)**, we found that the observed concentration of NHHS Fe^{2+} was strongly affected by the dissolved O_2 concentration in the growing culture. Subtle changes in aerobicity (e.g. caused by differences in rotation rates of the shaker, or in volume ratios of liquid culture to flask capacity) affected the intensity of the Fe^{2+} features. *Higher* concentrations of NHHS Fe^{2+} species correlated with *lower* O_2 concentrations.

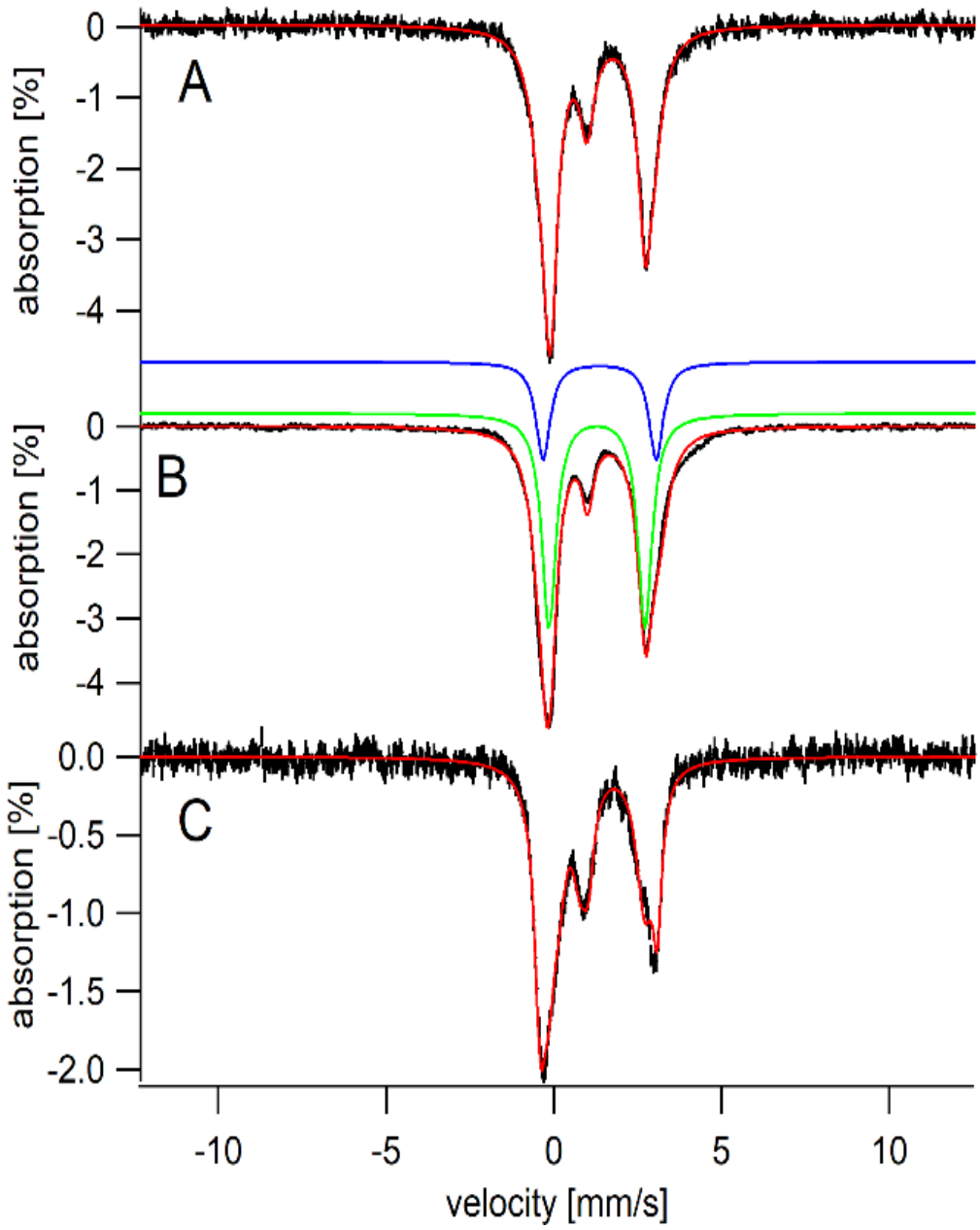

Figure 7.3: Mössbauer spectra (5 K, 0.05 T) of three separate batches of WT *E. coli* cells grown in glucose under reduced O_2 conditions. A, batch 1; B, batch 2; C, batch 3. Blue and green lines are simulations of the Fe^{2+}_{LMM} and Fe^{2+}_{RET} species, respectively.

Δfur cells have dysregulated Fe^{2+}_{LMM}:

We were surprised that modest changes in O_2 had a significant effect on the concentration of NHHS Fe^{2+} in WT cells; we had expected that Fe^{2+} concentrations would be tightly regulated by Fur. To investigate this further, Δ*fur* cells were grown on glucose media supplemented with 1, 10, and 100 μM $^{57}Fe^{3+}$ citrate. No trends were apparent in terms of cellular iron concentration; however, only one batch for each condition were examined and so we only report the average of the three batches, namely 400 ± 120 μM Fe. Like WT cells, Δ*fur* cells exhibited MB spectra dominated by NHHS Fe^{2+} and ISC doublets (Figure 4). However, overall spectral intensities were lower than in WT spectra, consistent with there being less iron in Δ*fur* cells. The most significant difference relative to WT spectra was the increased intensity of the Fe^{2+}_{LMM} doublet relative to other features as the concentration of nutrient iron increased. This effect was not observed in WT cells; it implies that the iron species giving rise to the Fe^{2+}_{LMM} doublet is not well regulated in Δ*fur* cells.

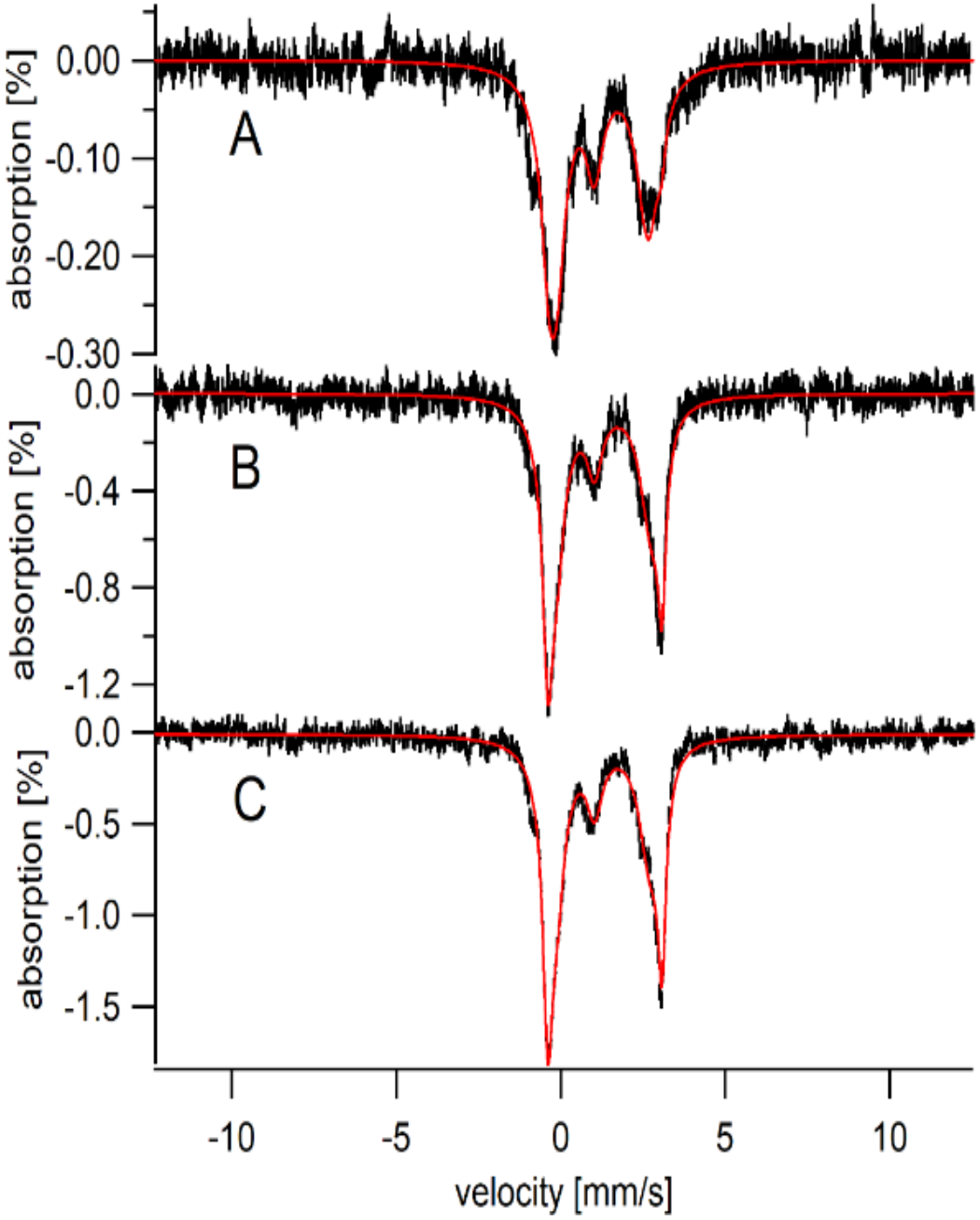

Figure 7.4: Mössbauer spectra (5 K, 0.05 T) of whole Δ*fur* cells grown on glucose media and harvested during exponential phase. The concentration of $^{57}Fe^{3+}$ citrate was: A, 1; B, 10, C, 100 µM.

Mössbauer spectra of cells harvested at stationary phase are dominated by magnetically-ordered Fe^{3+}:

WT cells harvested in stationary phase exhibited a broad quadrupole doublet with the parameters of magnetically-ordered Fe^{3+} (Figure 5B). This doublet was largely absent in spectra of cultures harvested during exponential growth (Figure 5A). The Fe^{2+} doublets were stronger in the spectra from exponentially growing cells, while the ISC and Residual doublets were comparable in both spectra. This suggests that species in the cell giving rise to these latter doublets are less susceptible than the cell's Fe^{2+} species to the metabolic deactivation associated with the exponential $\rightarrow$ stationary shift. The overall percent effect nearly doubled in the spectrum of stationary phase cells relative to that of exponentially growing cells. This implies that stationary phase cells import iron even when the cells are not dividing. We have observed a similar phenomenon in yeast **(128)**.

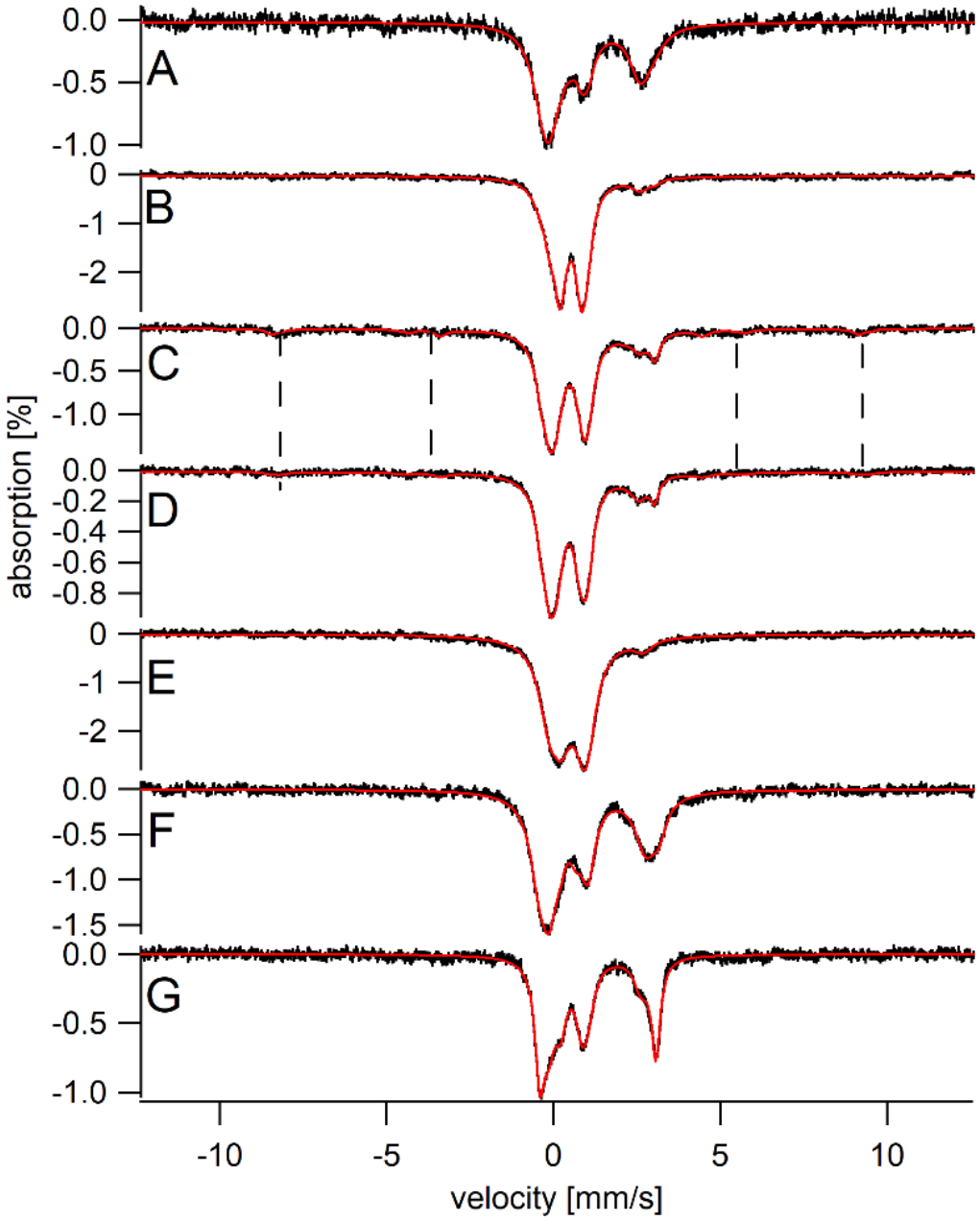

Figure 7.5: Mössbauer spectra (0.05 T) of whole *E. coli* cells grown on MM media, supplemented with 100 μM 57Fe citrate, and harvested during exponential growth and stationary state. A, WT cells harvested during exponential growth. B, same as A but cells were harvested in stationary state. C, Δ*ftnA* cells harvested during exponential growth. D, same as C except collected at 100 K. E, same as C and D except harvested in stationary phase. Vertical lines between C and D highlight the Fe3+ sextet extending slightly from the baseline. F, Δ*bfr*Δ*dps* cells harvested during exponential phase. G, same as F but harvested during stationary phase. Spectra A, B, C, E, F, and G were collected at 5 K.

We noticed that the magnetically-ordered Fe^{3+} doublet was similar to that arising from Fe^{3+} oxyhydroxide nanoparticles in mitochondria in which ISC assembly is impaired **(128, 145)** (see Figure S3B). Also, the high-field spectrum of the magnetically-ordered material in *E. coli* (Figure 5 of reference **222**) is remarkably similar to that of mitochondrial nanoparticles (**50, 223**). Thus, we assigned this spectral feature to Fe^{3+} oxyhydroxide nanoparticles.

Some past investigators assigned the magnetically-ordered Fe^{3+} material to iron bound in ferritin cores **(96, 99, 222)**; others were uncertain of this **(106, 107, 112, 223)**. To settle the issue, we repeated the above experiment using three genetic strains of *E. coli* (Δ*ftnA,* Δ*bfr*, and Δ*bfr*Δ*dps*) in which ferritin-related genes were deleted. As above, a portion of a growing culture was harvested during exponential phase, and the remainder was harvested later in stationary phase. In the experiments involving Δ*ftnA* and Δ*bfr*, samples harvested during exponential growth exhibited little if any intensity from the magnetically-ordered doublet (Figure 5C for Δ*ftnA* and Figure S4A for Δ*bfr*) whereas those harvested during stationary phase were dominated by this material (Figure 5E for Δ*ftnA* and Figure S4B for Δ*bfr*). The magnetically-ordered material in these spectra could not have originated from the major ferritin or bacterioferritin in *E. coli* since the corresponding genes had been deleted. The Δ*ftnA* 5 K spectral baseline in Figure 5C suggested a hint of magnetic material (~ 5% of total intensity) in the wings. We collected a spectrum at 100 K and found that ca. half of the intensity remained, suggesting that no more than ~3% of cellular iron could be due to ferritins. We cannot identify the species involved, but it cannot be FtnA. We suspect that this magnetic

material corresponds to the HS S = 5/2 Fe^{3+} hemes and nonhemes in these cells (consistent with the EPR). In summary, our results indicate that no more than ~ 3% of cellular iron is due to ferritins in any experiment performed in this study. The iron concentration of ΔFtnA cells increased from 1.2 mM → 2.0 mM as cells transitioned from exponential to stationary phase. The iron concentration of ΔBfr cells increased from 1.6 mM → 1.8 mM for the same transition. In WT cells, the iron concentration changed from 1.1 mM → 1.3 mM for the same transition. We estimate that no more than ca. 50 μM iron is bound to ferritins in cell harvested during exponential or stationary phases.

The results of two experiments with the Δ*bfr*Δ*dps* strain were qualitatively different from those of WT, Δ*ftnA* or Δ*bfr* cells. In both repeat experiments, the spectra of exponential and stationary phase were similar (Figure 5, F and G); nanoparticles did not form under stationary phase. These cells grew slowly and they may not have reached true stationary phase when they were harvested. The iron concentration of Δ*bfr*Δ*dps* cells changed less during the exponential → stationary transition (980 μM → 880 μM) compared to the other ferritin mutant strains.

The iron content in E. coli is similar to that in mitochondria:

We have studied mitochondria from yeast and human cells extensively using MB and EPR spectroscopies (e.g. **(51, 50, 224)**), and were surprised by the remarkable similarity to *E. coli*. MB spectra of *E. coli* cells harvested during exponential state were similar to those of mitochondria isolated from respiring cells (compare Figure 1 to

Figure S3A), whereas MB spectra of *E. coli* cells harvested in stationary phase were similar to those of mitochondria isolated from yeast cells possessing a defect in ISC assembly (compare Figure 5, spectra B and E, to Figure S3, spectrum B).

We have developed a chemical model that explains how nanoparticles form in mitochondria from ISC-defective mutants. Accordingly, nanoparticles in mitochondria are generated when a LMM complex called Fe_{580} reacts with O_2 (Figure 6, top panel) **(154, 10)**. Our model assumes that the matrix of the mitochondria is microaerophilic under WT healthy conditions, due to the ability of the iron-rich respiratory complexes on the inner membrane to hinder O_2 from diffusing into the matrix and reacting with Fe_{580}. In ISC-defective mutants, the respiratory complexes are less effective in this regard (due to incomplete metallation of these complexes). The O_2 that diffuses into the matrix of unhealthy mitochondria then reacts with Fe_{580} to generate nanoparticles.

The similar iron content of *E. coli* and mitochondria suggested a similar explanation for how nanoparticles are generated under stationary phase conditions. We hypothesize that the cytosol of exponentially growing *E. coli* cells is sufficiently reducing to maintain the Fe^{2+} state of a LMM complex called Fe_{500} (see below), and that this space is sufficiently oxidizing in stationary phase cells to support O_2-dependent oxidation of $Fe^{2+} \rightarrow Fe^{3+}$ oxyhydroxide nanoparticles.

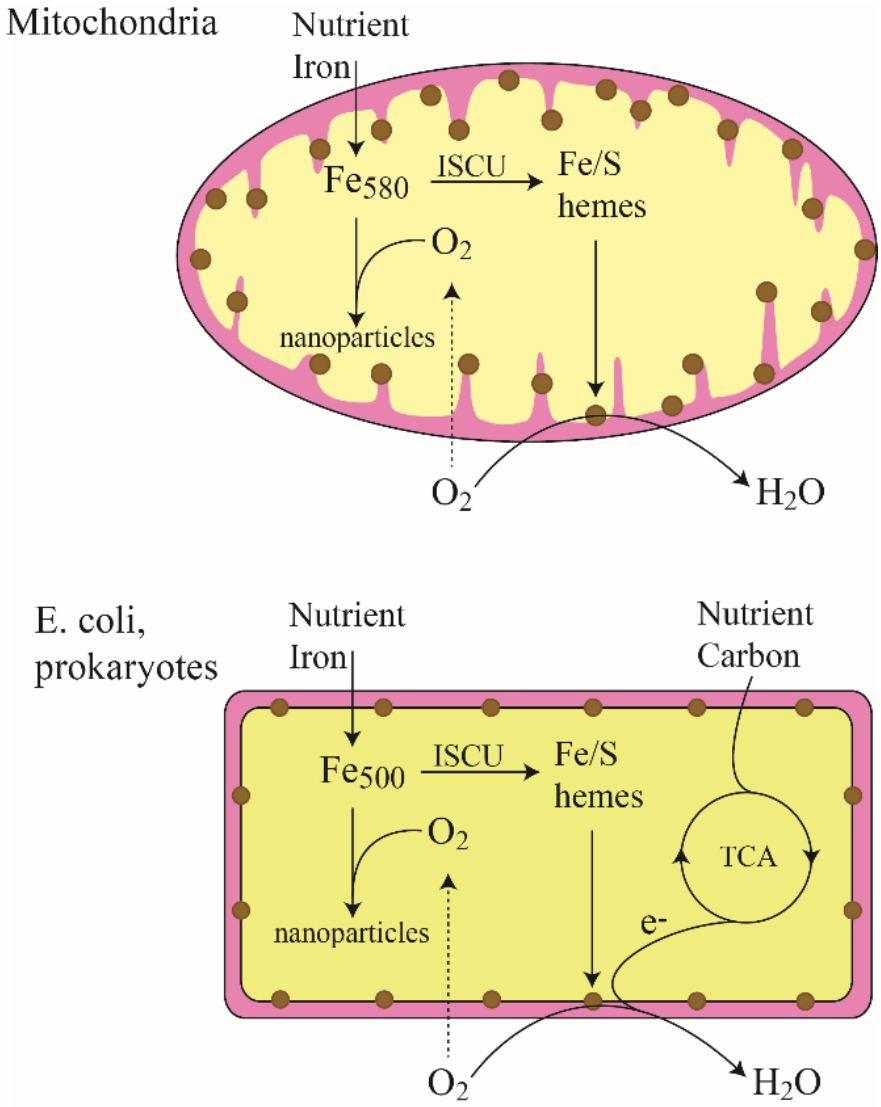

Figure 7.6: Respiratory Shield Model for Mitochondria (top), and for *E. coli* and other prokaryotes (bottom). The respiratory shield consists of the ISC- and heme-containing respiratory complexes located in the inner membrane of mitochondria and the cytoplasmic membrane of *E. coli* and other prokaryotes. The shield is operational when cells are metabolically active, oxidizing nutrient carbon and passing electrons through the respiratory electron-transfer chain and reducing much of the local O_2 diffusing by to water. With the shield operational, the cytosolic regions become microaerophilic. This protects the labile Fe^{2+} pool in the cell from reaction with O_2. When cells transition to stationary-state, they become metabolically less active, and the shield deactivates. Then, additional O_2 diffuses into cytosol where it reacts more rapidly with the labile Fe^{2+} pool forming Fe^{3+} oxyhydroxide nanoparticles. A similar deactivation of the shield occurs when respiratory complex IV is inhibited by cyanide. The same fundamental structure is proposed for all aerobic prokaryotes.

In the case of *E. coli* transitioning into stationary phase, the low activity of respiratory complexes is caused not by insufficient ISC or heme centers, but by low metabolic levels. The flow of electrons through iron-rich respiratory centers can be restricted by insufficient reducing equivalents as well as by insufficient iron centers. We suggest that the respiratory complexes on the periplasmic membrane of *E. coli* constitute a "shield" that partially blocks O_2 from crossing the membrane and penetrating the cytosol. This shield, when operational, maintains the cytosol in a microaerophilic (though not anaerobic) state. When exponentially growing cells transition to stationary phase, metabolic activity declines and the shield deactivates such that the cytosol becomes more fully oxygenated.

Inhibiting respiratory complex IV with cyanide generates nanoparticles in E. coli:

To test this hypothesis, we inhibited cytochrome c oxidase activity in exponentially growing cells by treating them with sodium cyanide, a known inhibitor of this respiratory complex. Cells were packed into MB cups before and after treatment. Prior to treatment, cells grew rapidly (exponential growth rate $\alpha = 0.26\ hr^{-1}$) and after treatment they immediately stopped growing ($\alpha \sim 0\ hr^{-1}$). After a 90 min incubation, 13% of the NHHS Fe^{2+} had converted to nanoparticles, as observed in the difference spectrum (Figure 7C). The parameters needed to simulate the observed NHHS Fe^{2+} doublet were those of $Fe^{2+}{}_{LMM}$. The other doublet was simulated using the parameters for the nanoparticle doublet (Table 1). That only the $Fe^{2+}{}_{LMM}$ doublet was affected suggests that the iron species giving rise to this doublet is particularly susceptible to oxidation by

O_2 or its ROS derivatives. In this experiment, cyanide might have also inhibited enzymes other than cytochrome c oxidase (e.g. catalases, peroxidases), and this may have contributed to the observed oxidation.

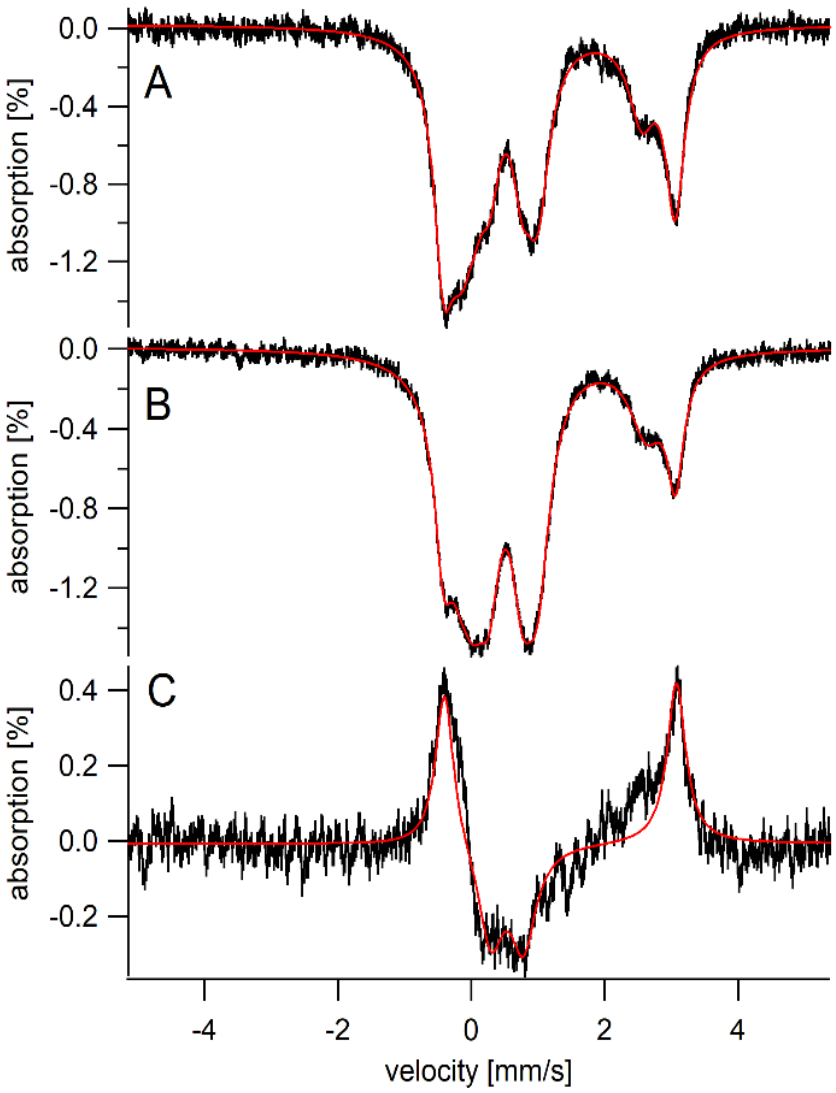

Figure 7.7: Mössbauer spectra (5 K, 0.05 T) of cyanide-treated E. coli cells. A, before treatment; B, after treatment. C is a difference spectrum of B – A. The solid red line in C is a simulation in which the $Fe^{2+}{}_{LMM}$ doublet in A is replaced by the nanoparticle doublet in B (13% of spectral intensity for each).

Mössbauer spectra of LMM flow-through solutions and retentate:

We wondered whether the NHHS Fe^{2+} species in *E coli* that give rise to the Fe^{2+}_{RET} and/or Fe^{2+}_{LMM} doublets were bound to Fe^{2+}-containing proteins or were non-proteinaceous LMM Fe^{2+} complexes. Such structural differences would suggest different physiological roles. Small Fe^{2+} complexes associated with the LIP have been suggested to be used in iron trafficking and regulation, Fenton chemistry, and as substrates for ISC/heme assembly **(109, 214, 105, 110, 103, 225, 226)**. Fe^{2+}-containing proteins are commonly metalloenzymes with catalytic roles. To distinguish these, three MB samples were brought into an anaerobic glove box after their spectra had been collected. The average spectrum of the three samples exhibited a strong NHHS Fe^{2+} doublet (Figure 8A) indicating a high concentration of the Fe^{2+} species. Samples were thawed, diluted with buffer, and lysed using glass beads. The supernatant fraction was passed through a 10 kD cutoff membrane. The retentate and flow-through solutions (FTSs) were collected, and each was transferred to a MB cup and frozen. The retentate should contain any soluble Fe-bound metalloproteins whereas the FTS should be largely protein free. The MB spectrum of the FTS (Figure 8B) exhibited a sharp NHHS Fe^{2+} doublet which was simulated using parameters of the Fe^{2+}_{LMM} doublet in whole-cell spectra (Table 1). This suggests that Fe^{2+}_{LMM} is a LMM Fe^{2+} complex (which explains our nomenclature). A MB spectrum of the FTS was also collected at 6 T and 4.2 K (Figure S1, B). Although noisy, it could be simulated using a high-spin Fe^{2+} S = 2 Hamiltonian.

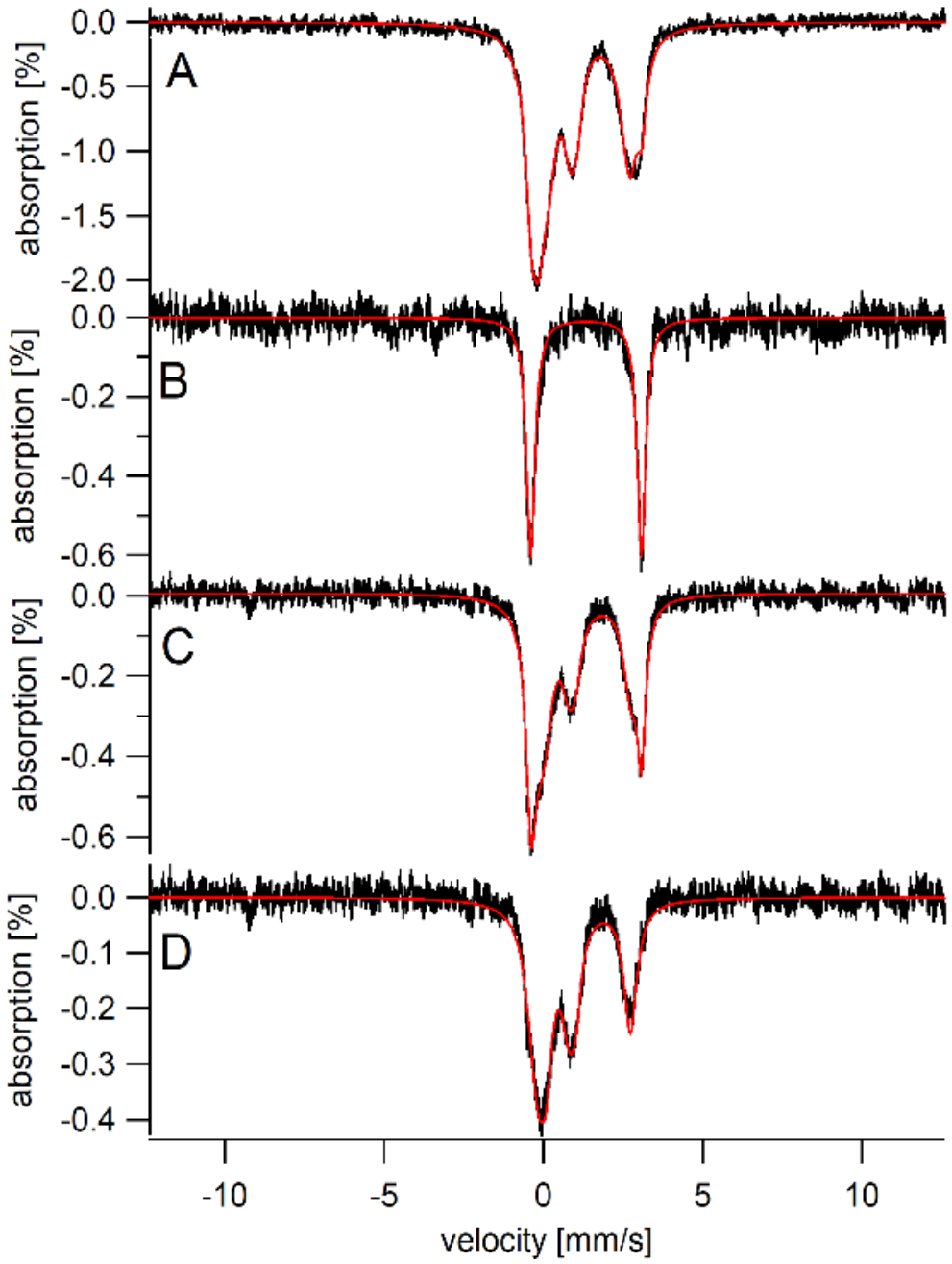

Figure 7.8: Mössbauer spectra (5 K, 0.05 T) of whole *E. coli* cells, and associated retentate and flow-through solutions. A, sum of the spectra obtained of the three samples used in the experiment; B, FTS; C, retentate; D, same as C except after removing the $Fe^{2+}{}_{LMM}$ contribution.

The low-field 5 K MB spectrum of the retentate (Figure 8C) also exhibited the Fe^{2+}_{LMM} doublet along with other features. The presence of the Fe^{2+}_{LMM} doublet in the retentate was expected because we did not wash this solution (e.g. by adding buffer and re-concentrating) such that Fe^{2+}_{LMM} would not have been removed. To highlight the other features in the retentate spectrum, we subtracted a simulation of the Fe^{2+}_{LMM} doublet. The Fe^{2+}_{RET} doublet was present in the resulting spectrum (Figure 8D) as was another broad doublet near the central region. This latter doublet was composed of the ISC and Residual doublets. The species giving rise to these doublets are high-molecular-mass and almost certainly protein-bound.

LC-ICP-MS chromatograms of flow-through-solutions reveal low-molecular-mass iron complexes:

In some samples, a portion of the FTS was analyzed for metal concentrations. For one sample in particular, the concentration of LMM iron within the cell was back-calculated from the iron concentration in the FTS. After multiplying by all dilution factors involved in obtaining the sample from whole cells, the concentration of LMM iron species within whole cells was calculated to be ~ 200 μM.

We then used liquid chromatography in conjunction with an online ICP-MS to detect Low-Molecular-Mass (LMM) iron species in soluble *E. coli* extracts, as a means of probing the LIP. FTSs from such extracts were passed through a size-exclusion column designed to resolve LMM peptides. The eluent flowed into an online ICP-MS.

Iron-detected chromatograms are shown in Figure 9; those of the other elements are presented in Figure S5.

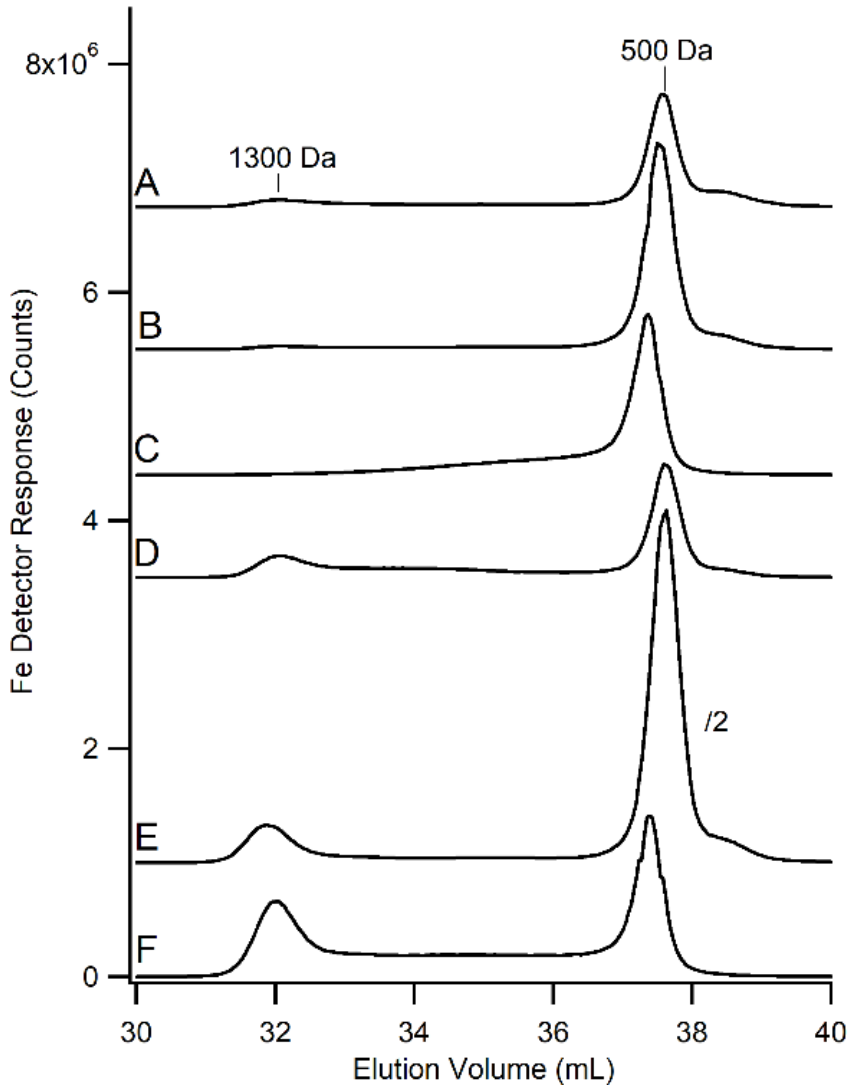

Figure 7.9: ^{57}Fe-detected LC-ICP-MS chromatograms of flow-through solutions from exponentially grown *E. coli* cells. A, B, and C were glucose-grown cells in which media were supplemented with 1, 10 and 100 μM $^{57}Fe^{3+}$ citrate, respectively. D, E, and F were the same iron concentrations for acetate-grown cells.

One major LMM iron species was detected in all chromatographs, with a mass of approximately 500 Da (to be referred to as Fe_{500}). A second LMM iron species at 1300 Da was evident as well, but was more intense in FTSs from acetate-grown cells. The intensities of Fe_{500} peaks did not vary systematically with the concentration of nutrient iron in cells grown on glucose, but in acetate-grown cells, the Fe_{1300} peak-intensity did increase with increasing nutrient iron levels. We do not understand the significance of these differences. In one experiment, the cells contained ~ 370 μM Fe (at a collective volume of 1.42 mL), whereas the FTS contained 230 μM Fe (volume of 600 μL). This suggests that ~ 26% of total cellular Fe should have been LMM; this compares nicely to the MB percentage of Fe^{2+}_{LMM} for this sample, namely 20%. We conclude that *Fe_{500} and Fe_{1300} collectively give rise to the Fe^{2+}_{LMM} doublet in the MB spectra of E. coli cells and constitute the LIP.*

Discussion

The Labile Iron Pool in E. coli:

In this study, we have isolated two low-molecular-mass Fe^{2+} complexes from *E. coli*, which we call Fe_{500} and Fe_{1300} (where subscripted numbers indicate approximate masses in Da). Fe_{500} was the primary component of the pool in all samples investigated. The concentration of Fe_{1300} was variable, with higher levels in samples grown on acetate as the carbon source and in samples grown under iron-replete conditions. The concentration of the LIP depended on the level of O_2 exposure during cell growth. Under

more aerobic conditions, the LIP concentration in WT *E. coli* cells was ~ 50 μM whereas under less aerobic conditions, the calculated LIP concentration exceeded 500 μM.

Our results suggest that these LMM Fe^{2+} complexes are not artifacts of isolation. Most importantly, the δ and ΔE_Q parameters for the $Fe^{2+}{}_{LMM}$ quadrupole doublet exhibited by whole intact *E. coli* cells were the same as those for the doublet observed in MB spectra of isolated FTS. We generated the FTS from whole cells rapidly in a refrigerated anaerobic glove box to avoid oxidation to the Fe^{3+} state and to slow ligand-exchange reactions. The intensity of the $Fe^{2+}{}_{LMM}$ doublet in whole cells varied with O_2 levels similar to the effect observed recently by Kiley and coworkers **(105)**. Other evidence arguing against the artifactual origin of these LMM species is that the FTS Fe^{2+} quadrupole doublet was sharper than would be expected for adventitious Fe^{2+} which is generally broadened due to heterogeneity. Finally, the simplicity of the LMM chromatograms, which reproducibly exhibited only peaks from Fe_{500} and Fe_{1300}, is inconsistent with chromatograms expected for adventitious iron which would likely afford variable results and multiple peaks. Aqueous Fe^{2+}/Fe^{3+} solutions, which would likely be a component of adventitious iron, adsorb on the columns used **(227)** whereas the LMM iron complexes observed here passed through the column. Considered collectively, we conclude that *we have isolated the physiological labile iron pool in E. coli*, and that it consists mainly of one NHHS Fe^{2+} complex with an approximate mass of 500 Da. A second species with a mass of ca. 1300 Da is also present. The low molecular mass of these complexes indicates that they are not iron-bound proteins. We don't know the function of Fe_{500} or Fe_{1300} but speculate that they are involved in iron trafficking,

sensing, and/or regulation. They might also serve as feedstock for building ISCs and/or hemes or for activating various metalloenzymes.

Comparing δ and ΔE_Q parameters for the $Fe^{2+}{}_{LMM}$ doublet (1.33 mm/s and 3.43 mm/s, respectively) to those from chemically defined high-spin Fe^{2+} complexes provides some insight into the coordination environment of Fe_{500}. An Fe^{2+} coordinated to four carboxylate oxygens and two ether oxygens in an octahedral environment yields a MB doublet with δ = 1.30 mm/s and ΔE_Q = 3.13 mm/s **(228)**. $[Fe(H_2O)_6](ClO_4)_2$ exhibits a doublet with δ = 1.34 mm/s and ΔE_Q = 3.4 mm/s **(229)**. The parameters for high-molecular-mass $Fe^{2+}{}_{RET}$ (δ = 1.19 mm/s and ΔE_Q = 2.99 mm/s) are closer to those of Fe^{2+} complexes with 5-6 N and O donor ligands. For example, an Fe^{2+} complex with N_3O_3 coordination exhibits a doublet with δ = 1.19 mm/s and ΔE_Q = 3.07 mm/s. Another complex with N_4O_1 ligation yields δ = 1.196 mm/s and ΔE_Q = 3.047 mm/s **(230)**. An Fe^{2+} complex with N_4O_2 ligation (including a tetraimidizole and an oxalate ligand) exhibits a doublet with δ = 1.195 mm/s and ΔE_Q = 3.131 mm/s **(231)**.

The role of Fur in iron regulation:

A popular notion is that only a small portion of cellular iron is present as labile Fe^{2+} - only to the extent required for regulatory sensing and trafficking. The idea is that the cell *minimizes* labile Fe^{2+} to limit Fenton Chemistry **(102, 99)**. Consequently, the LIP is generally thought to be buffered in the low μM range **(98, 128, 225, 232, 233).** This view is consistent with our results in which cells were grown under aerobic conditions. In these cases, the concentration of the LIP is ~ 50 μM (or less).

The situation is different under microaerophilic conditions in which the LIP concentration can exceed 500 μM. If K_D for binding of Fe^{2+} to Fur equals ~ 1 μM **(216, 102, 219)**, then > 98% of Fur would be bound with Fe^{2+} (at equilibrium) under all growth conditions. Under these conditions, how could Fur serve as a regulator? One possibility is that the K_D for Fe^{2+} binding to Fur may be weaker than 1 μM; higher values have been reported **(217, 218)**, including one as high as K_D = 280 μM **(218)**. There is more than one binding site on Fur, and perhaps sites that bind Fe^{2+} weakly (and have been largely ignored) may actually be physiologically relevant. Another possibility is that only certain Fe^{2+} complexes within the LIP bind Fur, and yet another possibility is that LIP levels in anaerobic/microaerophilic cells are not as tightly regulated as is generally assumed.

Beauchene et al. suggested that expression of the *feo* genes that control iron import under anaerobic conditions might be controlled more by FNR and ArcA than by Fur **(105)**. However, our results suggest that the concentration of Fe^{2+}_{LMM} is Fur-dependent. Its concentration in Δ*fur* cells was significantly affected by the concentration of iron in the medium whereas its concentration in WT cells were not affected in this way. Without Fur, Fe^{2+}_{LMM} does not seem to be well regulated.

Where is ferritin iron?

Abdul-Tehrani et al. **(109)** concluded from their MB study of iron-replete WT *E. coli* that *half* of the iron in cells harvested in stationary state was bound to the FtnA ferritin. They assumed that the magnetically-ordered Fe^{3+} material observed in MB

spectra of such cells arose from ferritin iron cores. During exponential growth, the concentration of iron in the cell was about half of what it was at stationary state due, they suggested, to the absence of the magnetically-ordered Fe^{3+} (i.e. FtnA-bound iron). This conclusion was reasonable because expression of FtnA increases 10-fold as exponentially growing cells transition to stationary state **(109, 234)**.

In contrast, we found virtually no evidence for iron-bound to ferritin in any *E. coli* sample studied, including iron-replete WT samples harvested at stationary state for which such iron ought to represent half of the iron in the sample. We observed an intense magnetically-ordered Fe^{3+} doublet in 5 K spectra of stationary-phase cells, and indeed this material represented over half of the iron in the samples. However, two aspects of our results establish that this material does not arise from FtnA-bound iron. First, the same doublet was observed in stationary-state cells lacking FtnA and Bft. The doublet had isomer shift and quadrupole splitting parameters typical of Fe^{3+} oxyhydroxide nanoparticles found in mitochondria. This assignment was reinforced by the Blocking temperature (T_B) of the doublet, which, like mitochondrial nanoparticles, is < 5 K. This explains why we observed (in *E. coli* spectra) a broad doublet at 5 K and another group observed magnetic interactions for the same material at 1.7 K **(109)**.

Abdul-Tehrani et al. **(109)** observed less magnetically-order iron in Δ*ftnA* cells than in WT cells when both were harvested at stationary phase. Under our growth conditions, we observed similar spectra from WT and mutant cells – e.g. Figure 5, B and D, and Figure S4, B and D. We noticed that Abdul-Tehrani et al. harvested cells after 18 hrs of growth which, according to plots in their article, were not fully in stationary

phase. One explanation that could reconcile the differences in our conclusions with theirs was that they harvested their Δ*ftnA* cells slightly sooner than WT cells, such that the Δ*ftnA* cells were transitioning to stationary phase whereas their WT cells were fully in stationary phase. The discrepancy could have been resolved had Abdul-Tehrani et al. reported spectra between 5 and 60 K. Magnetic features due to nanoparticles would collapse by 5 K whereas those due to FtnA would not collapse until ~ 30 K due to differences in T_B.

We also investigated whether ferritin iron could account for *any* iron in our spectra, and for this we searched the baseline. Although the baselines of our 5 K MB spectra were largely devoid of any features, some spectra exhibited very low-intensity features. The intensity of the baseline features represented less than ca. 5% of total cellular iron. Such features had characteristics (at 5 K and 0.05 T) of either ferritin-associated iron or high-spin Fe^{3+} heme or nonheme centers – these two possibilities could not be distinguished. However, similar features were evident in spectra of samples in which FtnA had been deleted; in these cases, such features could not have originated from the deleted ferritin. Also, EPR spectra of packed *E. coli* cells exhibited three low-field signals arising from S = 5/2 Fe^{3+} hemes and nonheme species. Such spin systems could certainly give rise to the MB spectral features emerging slightly from the baseline. Although we did not quantify the EPR signals, ballpark estimates were consistent with the tiny baseline intensities that we observed. The 100 K high-temperature MB spectra of *ΔftnA* cells exhibited similar magnetic features as observed at 5 K (but with reduced intensity). Collectively, *our results demonstrate that no more than half of these minor*

MB features, barely distinguishable from baseline, could arise from FtnA-bound iron; more likely is that they arise from high-spin Fe^{3+} hemes and nonheme species. We realize that our results and conclusions differ sharply from the well-documented view that ferritins play a major role in storing iron in *E. coli*, but we have been unable to find a flaw in our results or analysis.

***Connection to iron metabolism in mitochondria**:*

Chemiosmotic coupling is as ancient a process as transcription and translation, and it is universally employed to generate energy in living systems **(235)**. We propose that it has important consequences with regard to iron metabolism. Prior to the dramatic increase in atmospheric O_2 due to the evolution of photosynthetic organisms, early prokaryotes used molecules other than O_2 (e.g. NO_3^-, SO_4^{2-}) as terminal electron acceptors in chemiosmotic coupling. During that era, aqueous Fe^{2+} dominated the environment, and so these ancestral cells imported Fe^{2+} and trafficked it through the cytosol for use in ISC assembly followed by installation into various proteins - including respiratory complexes located on the periplasmic membrane. Once O_2 appeared in the environment, it replaced these other molecules as the terminal electron acceptor in chemiosmotic energy coupling. This improved the thermodynamics such that more ATP could be generated per electron transferred but it also had negative consequences for iron trafficking, regulation, and storage.

We hypothesize that the newly evolved OXPHOS process provided a "*respiratory shield"* for these early prokaryotes. The shield maintained the cytosol under

microaerophilic conditions even as the O_2 pressure in the atmosphere increased. This allowed cytosolic Fe^{2+} ions to continue to be used in trafficking and regulation because they were shielded from oxidation to the nearly insoluble Fe^{3+} state. Fe^{3+} complexes are less labile but also less useful in iron trafficking. Maintaining the shield simply required that the organisms metabolize nutrients fast enough to generate a rapid flow of electrons to the respiratory complexes which in turn reduces O_2 fast enough to limit its diffusion across the membrane and into the cytosol.

At a later stage in evolution, an ancestor of α-proteobacteria was engulfed by a proto-eukaryotic host, culminating in a symbiotic relationship in which mitochondria provided chemical energy to the host via OXPHOS **(236)**. Mitochondria and their bacterial ancestors share similar iron-rich respiration-related proteins as well as a suite of proteins involved in ISC biosynthesis **(237, 238-240).**

We report here that the iron content of *E coli* and mitochondria are remarkably similar, at least at the coarse-grain level probed by our methods. We have recently proposed that the mitochondrial matrix in healthy eukaryotic cells is microaerophilic, and that this provides a "safe space" for O_2-sensitive enzymes **(154, 10)**. This is especially important for ISC biosynthesis, an O_2-sensitive process that occurs in the matrix. The matrix contains a pool of labile LMM NHHS Fe^{2+} (called Fe_{580}) that gives rise to a quadrupole doublet in MB spectra (Figure S3, blue line) **(14)**. Fe_{580} in mitochondria and Fe_{500} in *E coli* may serve as feedstock for ISC biosynthesis and possibly for the iron insertion step of heme biosynthesis. Although the two LMM complexes have different names, we cannot exclude the possibility that they are the

same complex. Isolated mitochondria also exhibit an ISC doublet (Figure S3, green line) with parameters that are nearly identical to those of the ISC doublet in *E. coli* spectra. Previous results from the Lindahl lab suggest that nanoparticles form in mitochondria when O_2 penetrates the matrix and reacts with Fe_{580} **(10, 14)**, as illustrated in Figure 6, top. O_2 penetrates ISC-deficient mitochondria because the respiratory shield is disabled. Under these conditions, the respiratory complexes are probably not fully loaded with ISCs and heme centers, and are thus unable to transfer sufficient electrons from the TCA cycle to cytochrome c oxidase and then to O_2. In healthy mitochondria, most of the O_2 that diffuses to the IM is reduced to H_2O so that this diatomic molecule cannot overwhelm the matrix. We now propose an equivalent phenomenon in *E. coli* and other aerobic bacteria (Figure 6, bottom). Electrons generated by the metabolic activity of the cell are delivered to the inner membrane complexes and eventually to cytochrome c oxidase. This rapidly reduces much of the O_2 that would otherwise diffuse into the cytosol. When the metabolic activity of the organism declines, as when cells transition to stationary state, more O_2 penetrates the cytosol where it can react with Fe_{500} to form nanoparticles. The content and O_2-associated reactivity of iron in mitochondria and bacteria are similar largely because both have respiratory shields. Other studies also suggest the presence of a respiratory shield in aerobic bacteria. *Azotobacter vinelandii* uses such a shield to protect nitrogenase, an extremely O_2-sensitive enzyme **(239)**. In fact, the nitrogenase iron protein remains active when expressed in the mitochondrial matrix of yeast **(241)**.

Examining the iron content of all bacteria is not possible, but published MB spectra support a common iron content at least at the coarse-grain level. The MB spectra of *Pseudomonas ariginosa* whole cells (harvested after 44 hr of growth) exhibit the same features as observed for *E. coli* and mitochondria, namely a magnetically-ordered Fe^{3+} doublet, an ISC doublet, and a NHHS Fe^{2+} doublet **(242)**. The 82 K MB spectrum of *Proteus mirabilis* consists of a broad magnetically-ordered Fe^{3+} doublet as well as a NHHS Fe^{2+} doublet **(243).** MB spectra of *Erwinia chrysanthemi* (grown on glucose, harvested in stationary state) exhibit a magnetically-ordered Fe^{3+} doublet (67% of spectral intensity) and a NHHS Fe^{2+} doublet (33% of intensity) **(244)**.

To provide further examine for this notion, we examined the MB spectrum of Gram-positive *Bacillus subtilis* harvested under exponential growth conditions. As predicted, the spectrum (Figure S4) was similar to those of *E. coli* and mitochondria. The MB spectrum of *B. subtilis* exhibited more magnetic iron than in *E. coli* or mitochondria, but the difference was just one of degree. Viewed collectively, these results provide strong support for a *common coarse-grain iron content in aerobic prokaryotes and mitochondria*. We predict that the iron contents of anaerobic prokaryotes have a greater percentage of NHHS Fe^{2+} but are otherwise similar.

The respiratory shield might also serve to help regulate and store iron. Eukaryotes protect against Fenton chemistry by minimizing the concentration of Fe^{2+} in the cytosol, and by storing excess iron in ferritin (or in vacuoles, for fungi and plants). Iron stored in these ways is unable to engage in destructive ROS-generating chemistry. In ferritin cores, iron is stored as hematite, magnetite, and ferrihydrite **(245)**. In yeast

vacuoles, it is probably stored as Fe^{3+} polyphosphate **(149)**. In both cases, the mobilization of stored iron into the cytosol follows reduction to the Fe^{2+} state. It was reasonable to assume that *E. coli* and other prokaryotes use the same strategies. However, this does not appear to be the case. Metabolically-active *E. coli* grown under aerobic conditions do *not* store much iron, certainly not in ferritin cores. And under lower O_2 conditions, they do not minimize the concentration of labile Fe^{2+} species in the cytosol – in fact they might even store iron as labile Fe^{2+}. Thus, metabolically active *E. coli* avoid Fenton chemistry by a different strategy – by reducing the amount of O_2 that diffuses into the cytosol via the respiratory shield. As strange as it sounds, *E. coli* and other bacteria store iron *mainly as labile LMM* Fe^{2+} when they are metabolically active and as Fe^{3+} oxyhydroxide nanoparticles when they are metabolically dormant. Ferritins must play more specialized and limited roles in storing iron in stationary-state *E. coli* cells.

The concentration of O_2 in the mitochondrial matrix, *E. coli*, and other aerobic prokaryotes has not been measured directly and so estimates vary. Unden and coworkers measured O_2 consumption rates of bacterial cultures and calculated O_2 diffusion rates **(246, 247)**. They concluded that the O_2 concentration in the cytosol of bacteria is essentially the same as in external aerobic environments. This conclusion implies that the respiratory shield is weak and ineffective, and it supports the view that a multi-layered anti-oxidant system (involving SOD, catalases, peroxidases etc.) is continuously acting to prevent and repair ROS damage in healthy metabolically active cells. We do not claim that the respiratory shield is *completely* effective in preventing all O_2 from

entering the cytosol or matrix, and we recognize the critical importance of the anti-oxidant system; our dispute is one of degree. These protected spaces obviously contain *some* O_2 and O_2-derived ROS, as evidenced by enzymes (e.g. dioxygenases, superoxide dismutases, FNR) that are located in these spaces and use these molecules as substrates. We conclude that cells use both a respiratory "shield" and an anti-oxidant "sword" in their battle with O_2. By locating the respiratory shield near their peripheries, cells reap the energetic benefits of using O_2 in OXPHOS while minimizing its exposure to O_2-sensitive cytosolic species. We look forward to probing further this intriguing love-hate relationship – between aerobic cells and the molecule that they so desperately need but also poses an existential threat to their very existence.

Experimental Procedures

Cell Strains and Growth:

A single colony of WT MG1655 *E. coli* cells was inoculated into 50 mL of M9 minimal media that contained 0.2% (w/v) glucose and no added iron. Cultures were incubated overnight at 37 °C in an incubator shaker (Amerex Instuments SteadyShake 757 Gyromax) at ~200 rpm). For G1E, G10E, G100E, A1E, A10E, and A100E batches, cultures were used to inoculate 1 L of the same media (supplemented with 1, 10, or 100 μM $^{57}Fe^{3+}$ citrate) in 2.8 L baffled Fernbach flasks (Corning). Two 2 L of media were used for the cyanide-addition experiments and the exponential→stationary-phase experiments. For exponential growths, cultures were harvested at OD_{600} between 0.5 and 0.8. Stationary-phase samples were harvested at OD_{600} ~ 1.2. The same procedure was

used for cell grown on acetate except that the media contained 0.4% (w/v) sodium acetate rather than glucose. Cells were grown and harvested at USC under the same conditions except that 1 L cultures were grown in 2.0 L baffle flasks.

To prepare MB or EPR samples, harvested cells were centrifuged and washed once using 50 mL of 50 mM EDTA, 100 mM sodium oxalate, 100 mM NaCl, and 10 mM KCl. Washed cells were packed into either MB cups or EPR tubes (Wilmad Lab Glass, Suprasil precision quartz) and then frozen in liquid N_2. Low-field MB and EPR instruments have been described previously **(10)**. High field (6 T, 4.2 K) MB spectra were collected with a model LHe6T (See Co.) Instrument calibrated using α-Fe foil at room temperature. EPR spectra were simulated using SpinCount software (Michael Hendrich, Carnegie Mellon).

MG1655 Δ*fur::kan*^{R}, Δ*ftnA::kan*^{R}, Δ*bfr*, and Δ*bfr::kan*^{R}Δ*dps::cm*^{R} cells were grown as described above for WT cells. The Δ*fur::kan*^{R}, Δ*ftnA::kan*^{R}, and Δ*bfr::kan*^{R}Δ*dps::cm*^{R} mutations were constructed by replacing the indicated open reading frames in strain DY330 with kanamycin resistance cassette (*kan*^{R}) from pKD4 or chloramphenicol resistance cassette (*cm*^{R}) from pKD3 using the lambda RED system as described **(248)**. Mutations were moved by P1 transduction into the MG1655 or other strain backgrounds. MG1655 Δ*bfr* was generated by removal of the *kan*^{R} cassette from the MG1655 Δ*bfr::kan*^{R} strain using the pCP20 plasmid as described **(248)**. WT *B. subtilis* cells were grown in glucose-containing M9 media and prepared for MB analysis as described above.

***Cyanide addition experiments**:*

A single colony of WT *E. coli* cells was inoculated into 50 mL of media. Once grown, these were inoculated into 2 L of MM containing glucose and 100 μM Fe citrate in a 2.8 L baffled flask and placed in the incubator shaker at 37 C and 200 rpm. Cells were harvested during exponential phase (OD_{600} ~ 0.65). Half of the culture was use to prepare a MB sample. The other half was incubated with 3.0 mM KCN (final concentration), and then used to prepare a MB sample after 1.5 hr incubation.

***Metal analysis and LC-ICP-MS experiments**:*

MB samples were thawed and transferred to 4 cm long x 3 mm ID glass tubes which were packed by centrifugation. The volume of the pellet was determined by marking the pellet-height, removing the liquid above the pellet, quantitatively transferring the pellet to a 15 mL screw-top plastic tube (using 200 μL of distilled/dionized water), and determining the volume of water required to fill the tube to the mark. 300 μL of trace-metal-free grade nitric acid (Sigma Aldrich) was added. Samples were sealed with electrical tape and heated to 80 °C for ~ 24 hr. Solutions were passed through a 0.45 μm filter, and metal concentrations of the flow-through were determined by ICP-MS (Agilent 7700x) that had been calibrated using standard solutions of P, S, Cu, Mn, Zn, ^{56}Fe, ^{57}Fe, Co, Mo, and Ti (Inorganic Ventures). Instrument stability was verified using internal standards.

For LC-ICP-MS experiments, packed *E. coli* MB samples (~800 μL) were thawed in the glove box, and suspended in a 15 mL falcon tube containing 5.0 mL of 20

mM ammonium bicarbonate pH 8.5, ~100 mg lysozyme (Sigma Aldrich), and 2.0 mL of 0.1 mm diameter acid-washed glass beads (Sigma). The suspension was vortexed for 5 min, then placed in an ice bath for 5 min. This process was repeated twice. The lysate was then centrifuged for 15 min at 12,000×g (Sorvall Evolution RC centrifuge, GSA rotor). One mL of supernatant was mixed with 1.0 mL of 2% (v/v) Triton X-100 (Sigma), affording 1% final concentration of Triton, and the solution was vortexed for 30 min. (The remaining supernatant was frozen at – 80 °C.) The mixture was again vortexed, and spun at 12,000×g for 15 min. The resulting supernatant (~2 mL) was passed through an Ultracel 10 kDa ultrafiltration disc, regenerated cellulose (EMD Millipore) using an Amicon filtration system. 300 µL of the FTS was injected onto two Superdex Peptide 10/300 GL (GE Healthcare) columns connected in series, equilibrated in 20 mM ammonium bicarbonate pH 8.5. Additional details of the LC-ICP-MS system are described elsewhere **(227)**.

Acknowledgements: The National Institutes of Health (GM127021 to PAL and GM112919 to FWO) and the Robert A. Welch Foundation (A1170 to PAL) sponsored this study.

Supplemental Information

Table 7.S1: Selected metal and phosphorus concentrations in exponentially growing *E. coli* cells. Results for WT cells are the average (± Std. dev.) of two independent determinations. Values for Δ*fur* cells are the average of single determinations for batches grown with 1, 10, and 100 μM $^{57}Fe^{3+}$ citrate added to the media.

Sample	$[Fe]_{cell}$ (μM)	$[Mn]_{cell}$ (μM)	$[Zn]_{cell}$ (μM)	$[Cu]_{cell}$ (μM)	$[Co]_{cell}$ (μM)	$[Mo]_{cell}$ (μM)	$[P]_{cell}$ (mM)
Glucose 1 μM Fe	360 ± 160	16 ± 3	60 ± 20	10 ± 4	0.20 ± 0.08	0.4 ± 0.1	250 ± 10
Glucose 10 μM Fe	540 ± 60	06 ± 4	40 ± 30	21 ± 9	0.18 ± 0.06	0.3 ± 0.1	250 ± 10
Glucose 100 μM Fe	980 ± 20	09 ± 5	96 ± 4	40 ± 30	0.19 ± 0.01	1.1 ± 0.3	340 ± 40
Acetate 1 μM Fe	600 ± 200	12 ± 8	40 ± 30	20 ± 17	0.15 ± 0.01	0.4 ± 0.2	220 ± 10
Acetate 10 μM Fe	880 ± 540	09 ± 7	50 ± 40	08 ± 2	0.16 ± 0.05	0.5 ± 0.4	170 ± 50
Acetate 100 μM Fe	1600 ± 400	13 ± 4	82 ± 6	13 ± 2	0.26 ± 0.01	3 ± 2	260 ± 10
ΔFur 1, 10, 100 μM Fe ave.	400 ± 120	1.7 ± 0.5	9 ± 2	12 ± 4	0.2 ± 0.1	0.27 ± 0.05	170 ± 50

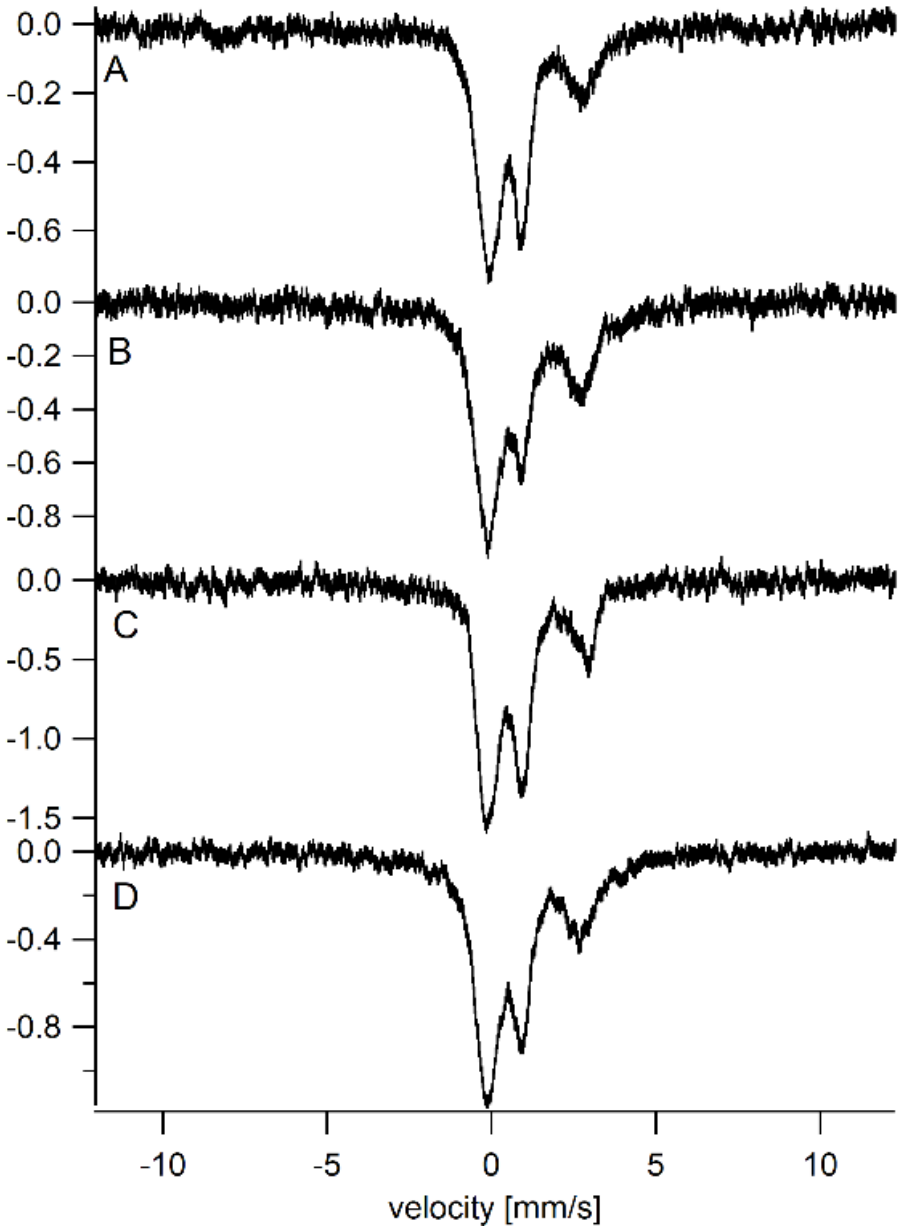

Figure 7.S1: Low-Field low-temperature (0.05 T, 5 K) Mössbauer spectra of *E. coli* whole cells grown in media containing glucose (A and B) and acetate (C and D). Samples used to generate A and C were supplemented with 1 μM $^{57}Fe^{3+}$ citrate while those used to generate B and D were supplemented with 10 μM $^{57}Fe^{3+}$ citrate.

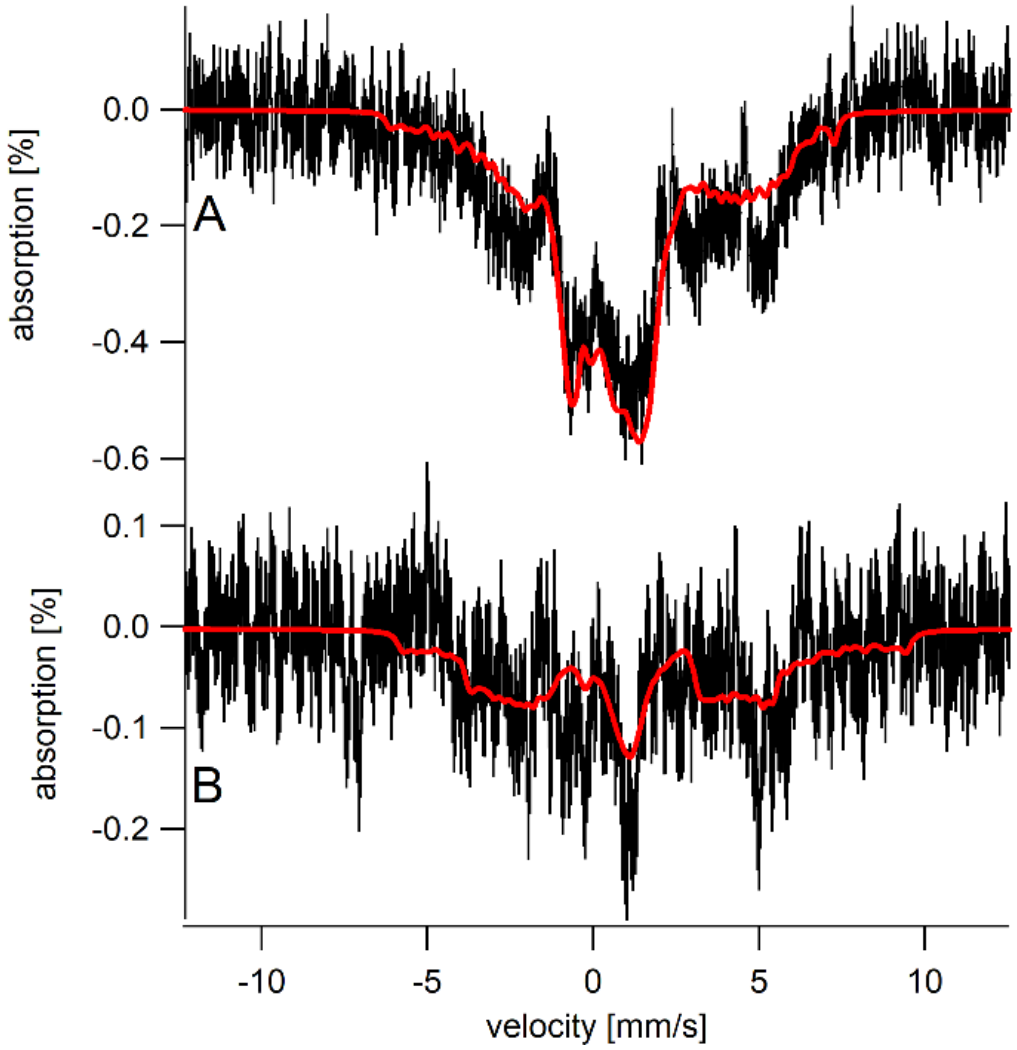

Figure 7.S2: High-Field low-temperature (6 T, 4.2 K) Mössbauer spectra of *E. coli* whole cells (A) and flow-through solution (B). The solid red line in A is a three-term simulation comprised of the ISC and Residual doublets (using parameters in Table 1), both assuming S=0, and an Fe^{2+} species assuming S = 2, D = 3.25 cm^{-1}, E/D = 0.27, ΔE_Q = 3.47 mm/s, η = 2, A_x = -285 kG, A_y = -65 kG, A_z = -325 kG, δ = 1.30 mm/s, and Γ = 0.3 mm/s. The solid red line in B is a simulation of only the S = 2 species. The parameters used for the S = 2 site are typical of Fe^{2+} sites, but do *not* represent a unique fit of the current data. The field was applied perpendicular to the gamma radiation. Each spectrum was collected for over 200 hr.

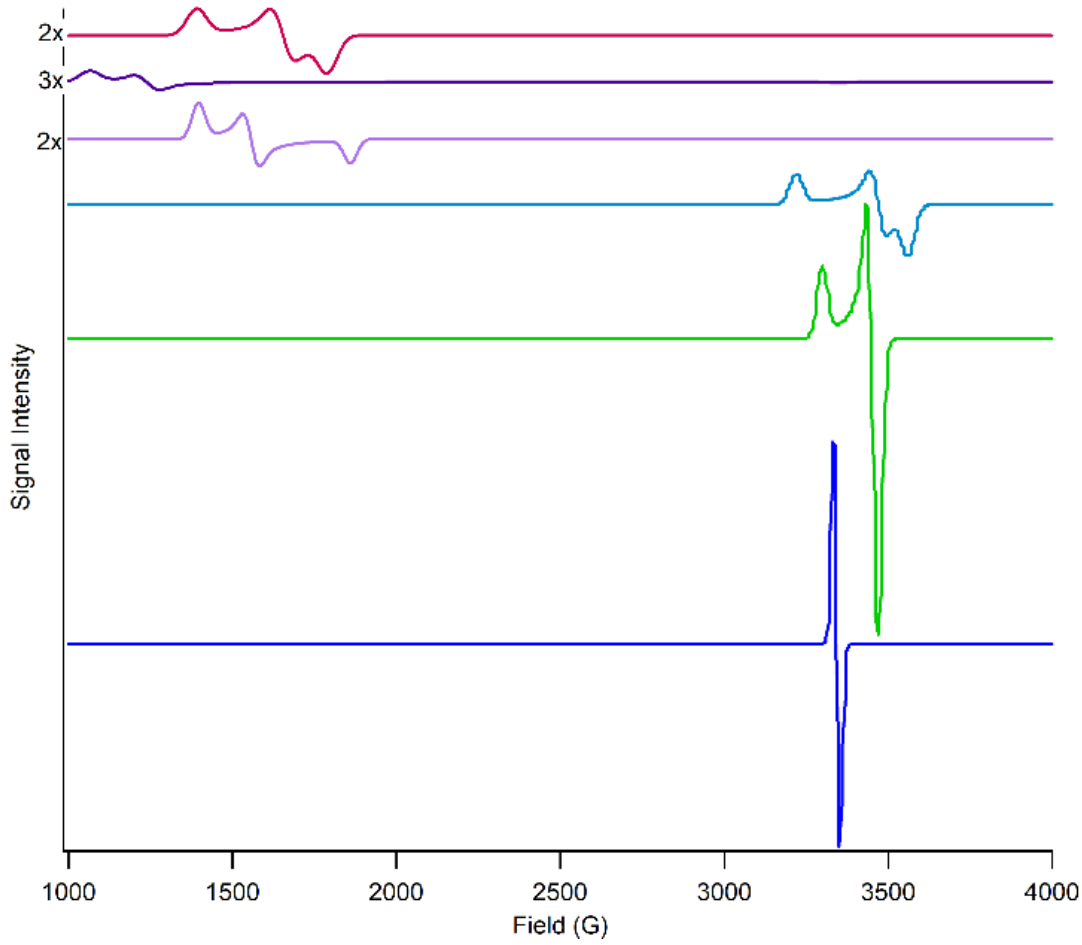

Figure 7.S3: Individual EPR simulations. Spectra in Figure 2 were decomposed into 6 signals with the following colored lines: magenta (g = 4.8, 4.0, 3.7), purple (g = 6.3, 5.4, 2.0), lavender (g = 4.8, 4.3, 3.6), turquoise (g = 2.08, 1.93, 1.88), green ($g_{\parallel}$ = 2.04, $g_{\perp}$ = 1.93), and blue (g_{iso} = 2.003). Other SpinCount parameters were: Field sweep, 4000 G; 1024 points; phi = 20; theta = 10; Deriv = 1; #Sig = 5; B1 = 90; Sym = 1.

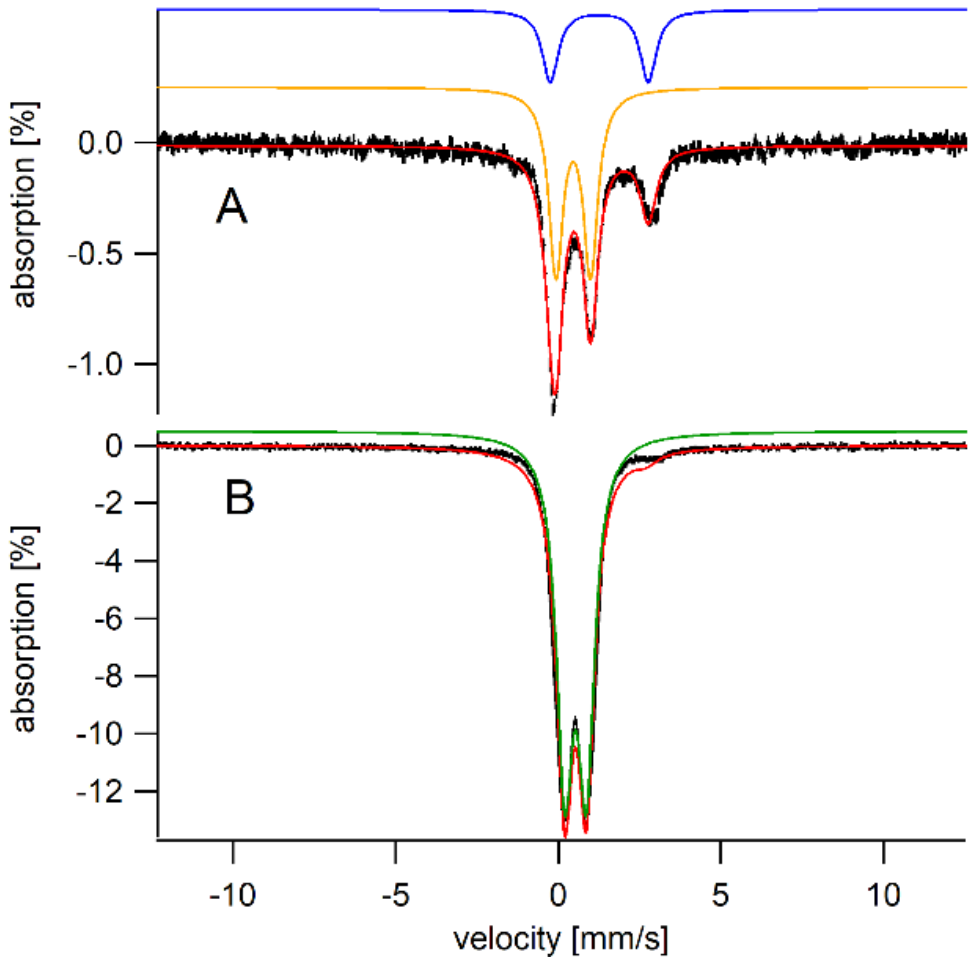

Figure 7.S4: Mössbauer spectra (5K, 0.05 T) of mitochondria isolated from yeast cells. A, mitochondria isolated from respiring WT yeast cells (prepared as in 48); B, mitochondria isolated from iron-dysregulated (Aft1-1up) yeast cells (from 44). The gold line is a simulation with the same parameters as for the ISC doublet given in Table 1. The blue line is a one-term simulation assuming parameters similar to those of Fe^{2+}_{LIP} and Fe^{2+}_{RET}. The green line is a simulation assuming the parameters of the Fe^{3+} nanoparticle doublet given in Table 1.

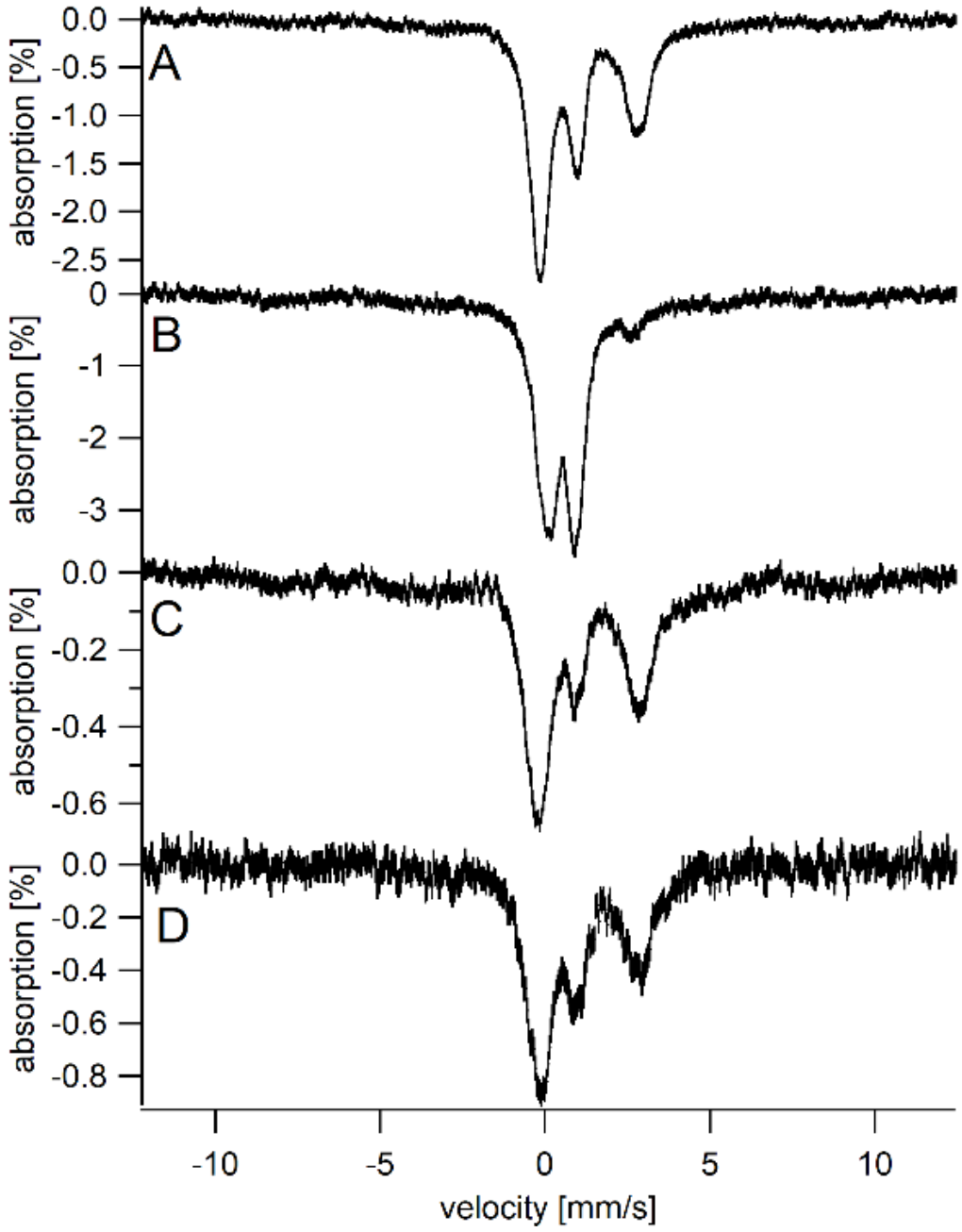

Figure 7.S5 Mössbauer (5 K, 0.05 T) spectra of whole *E. coli* mutant cells devoid of various ferritin genes. A, Δ*bfr*, exponential growth*;* B, Δ*bfr*, stationary state*;* C, Δ*bfr*Δ*dps*, exponential growth; D, Δ*bfr*Δ*dps*, stationary state. The Δ*bfr*Δ*dps* experiment was repeated, and resulting spectra are given in Figure 5, F and G.

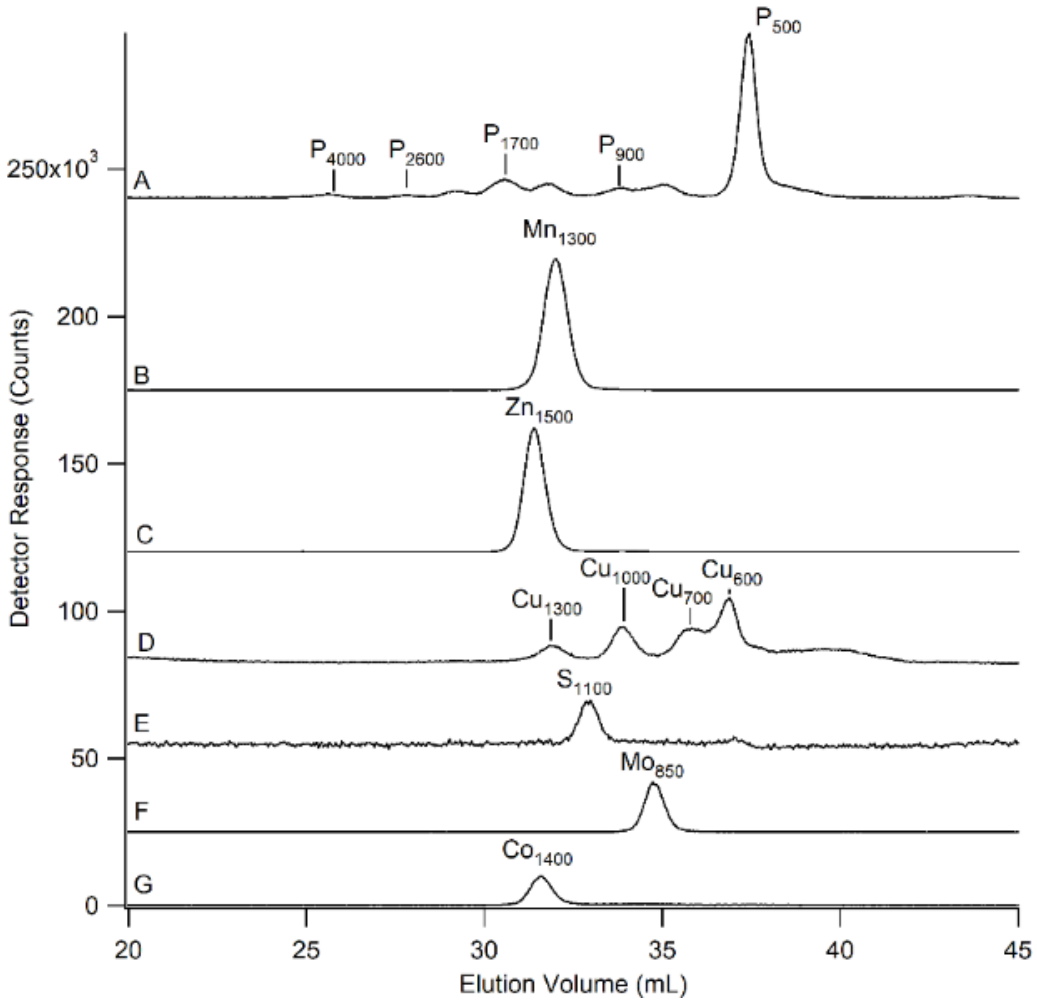

Figure 7.S6: LC-ICP-MS chromatograms of E. coli flow-through solutions detected by ^{31}P, Mn, Zn, Cu, S, Mo, and Co. Peaks are designated by the element detected and a subscript specifying the apparent molecular mass (in Da) associated with the peak. Apart from some variability in the copper peaks, the presented peaks were reproducible for the 6 traces examined.

.

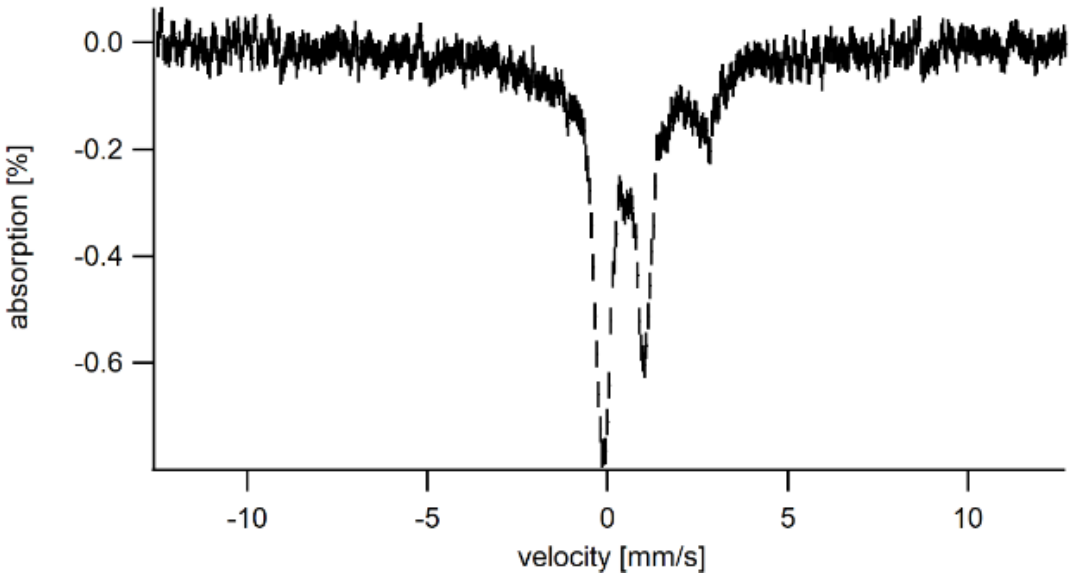

Figure 7.S7: Mössbauer spectra (5 K, 0.05 T) of WT *Bacillus subtilis* harvested during exponential growth conditions

CHAPTER VIII

CONCLUSIONS

Dual Regulation Model Characterization of WT and ISC mutants

My graduate studies began by working to determine what species are used in regulating systems' level Fe trafficking in S. cerevisiae. Using the mathematical model developed in Chapter III, the different proposed sensing mechanisms for regulation (cytosolic Fe, mitochondrial ISC assembly, or both in tandem) can be tested against data collected in the Lindahl lab. A cytosolic Fe sensing model appeared to fit WT data adequately, but it could not fit the ISC mutant behavior, as it could not sense the loss of FS assembly. On the other side, and an ISC sensed model could also fit WT behavior adequately, but it accumulated cytosolic Fe^{2+} to the same concentration of mitochondrial nanoparticles, contradicting the data that the Fe contents of ISC mutants were mostly nanoparticles, with only ~10% of the iron due to NHHS Fe^{2+}.

Our results suggest that *both* the concentration of cytosolic iron and mitochondrial ISC activity are important for cellular Fe regulation. Fe_{cyt} plays a role when healthy cells are grown in different media Fe conditions. In these conditions, ISC assembly is relatively constant, so that the import rates into the cytosol and mitochondria are constant. On the other hand, a lack of mitochondrial ISC assembly results in FS-based regulation controlling import rates. This dual regulation model has been suggested by Lill **(27)**, and other experimental data seems to support it.

Once the dual regulation model was established, it could then be used to attempt to reproduce data from other cell strains and conditions. Data were obtained from other studies in the lab and literature and can be found at table S1 in chapter III. It was found that the model could reproduce ~65% of cases studied, which was impressive given the relative simplicity of the model compared to the complexity of the Fe regulation and trafficking of the yeast cell.

Systems' level understanding of the recovery of ΔMrs3/4 mitochondrial iron and cell growth

The next study involved working with Dr. Moore to use Mössbauer spectroscopy to understand the systems' level changes in Fe regulation of the ΔΔMrs3/4 (ΔΔ) cells compared to WT. The recovery of growth of ΔΔ cells under high iron provided an interesting problem, which Mössbauer spectroscopy was able to assist in solving. By analyzing mitochondria from these mutants, it was found that nanoparticles were dominating at 1 μM Fe, while the central doublet (indicative of Fe_4S_4 clusters and hemes) was the dominant species in mitochondria grown in 40 μM Fe. As these cells were grown in respiring media, the appearance of Fe species present in respiratory clusters at high Fe indicated a restoration of respiration ability, and cell growth. The next problem to think about was the cause of the continued Fe dysregulation in these cells.

We then compared the concentrations of each Fe species present in ΔΔ compared to WT. The only Fe-containing species that we could observe at lower than WT concentration in mutant cells at Fe-sufficient conditions was the mitochondrial Fe^{2+} pool

(Fe_{580}) and mitochondrial heme centers. Fe_{580} could conceivably work with X-S in regulation, and is a candidate as the mitochondrial sensed species in this study. Nanoparticles, cytosolic Fe, and NHHS Fe^{3+} could be eliminated from consideration as the sensing species, as these were present in higher concentrations than WT cells.

Our results provide evidence that the mitochondrial Fe^{2+} pool in exponential growing cells is made up of Fe_{580}. The iron concentration associated with the Fe^{2+} pool in yeast mitochondria ranges from 60-200 uM, depending on strain and growth conditions. Fe_{580} was previously determined to be present at a concentration of approximately 100 uM **(14)**. Our current LC-ICP-MS results suggest that Fe_{580} is not associated with sulfur, and this is corroborated with the Mössbauer results, as the isomer shift and quadrupole splitting of the NHHS Fe^{2+} doublet is representative of an Fe center coordinated with O/N ligands **(155)**.

Multi-tiered modeling approach to transfer solutions from simpler tiers to more complex

When attempting to simulate the behaviors observed in the Mrs3/4 study (Chapter IV), the model presented in Chapter III was unable to simulate the ΔΔMrs3/4 phenotype and a new multi-tiered model was developed that could do this. Both models simulate iron import and trafficking in an exponentially growing yeast cell, with 3 regions of interest (cytosol, mitochondria, and vacuoles), and both involve the import of a single nutrient iron form N. The major differences lie in the complexity level, optimization method, and predictive power. The previous model included approximately

35 adjustable parameters, the current model has 23. Using the current model, the WT and ISC mutant behaviors were able to be simulated, as well as the Mrs3/4 behavior. The current model was used to simulate the recovery of mitochondrial Fe-S clusters and the loss of matrix O2 and mitochondrial nanoparticles, dubbed the waterfall.

The current model was solved at different levels of complexity. By solving the simpler variants first, and transferring these parameters to the more complex tiers, made for more reliable fitting, as more accurate data (like growth rates and cellular Fe concentrations) were available for the simpler tiers for fitting. Another strategic difference in modeling approaches was that we excluded all but one Reg function in the current model. This made the current model responsive to changing import parameters and allowed for better comprehension and interpretation of model behavior.

At the most complex tier, only four parameters differed between ΔΔ and WT simulations, $R_{cyt\text{-}max}$, k_{mit}, k_{vp}, and K_{α}. All other parameters were held constant between the simulations of these two genetic strains. The model's ability to reproduce ΔΔ and WT behavior with minimal changes is impressive. We can easily rationalize why half of these parameters should be different. A 4.6x reduction of k_{mit} for ΔΔ cells is reasonable because the high affinity transporters (Mrs3/4) are deleted. $R_{cyt\text{-}max}$ is 2x higher for ΔΔ cells because of the constitutive activation of the Fe regulon, leading to higher amounts of Fet3/Ftr1. K_{α} is a little more difficult to explain. This parameter is something like a K_m that reflects the sensitivity of the growth rate to changes in the nutrient iron concentration. So the 30x increase in K_{α} would reflect a 30 time less sensitive cell strain to changes in N relative to WT. Perhaps this reflects the slow flow of iron into the ΔΔ

mitochondria to support respiratory cell growth. The 2x increase in k_{vp} is even more difficult, because it would imply that the rate of VP formation is faster in ΔΔ vacuoles than WT. The actual mechanism of VP formation is more complicated than in represented in the current model, which has a simple order reaction mechanism. However, it is a credit to the model that is can simulate this effect as well, though further work is desired such that a more accurate "vacuole" can be simulated.

Mathematical models can inform experiment if they can make predictions about the system being studied. It is possible to over fit a reaction or system by using too many parameters such that a unique solution is not possible. We have attempted to give the model predictive power by grounding it in experiment and minimizing assumptions. This was challenging given the complexity of the system being investigated and limited amount of relevant data.

Our model can predict the effect of O_2 on iron metabolism in yeast cells. It predicts that the iron in mitochondria of ISC deficient cells that have been grown under microaerophilic conditions should be mostly made up of FM. A Yfh1-deficient strain is being examined with our biophysical and bioanalytical tools as a test of this model (in prep).

Finally, similar strategies could be applied to model import, trafficking, and regulation of any micronutrient. The concentration of the nutrient in question in whole cells and organelles should be known as should cellular growth rates. Obvious candidates are the biologically-involved transition metals, such as Cu, Mn, Zn, Mo, and

Co. The next logical candidate for modeling studies is Cu, as Cu and Fe work in concert, both in trafficking and in cellular respiration.

Cell Wall Fe accumulates as multiple forms, is chelatable, and used by cells during metabolic reactivation

Cells grown to stationary state accumulate Fe. This Fe is chelatable by EDTA, which is membrane impermeable, giving rise to a hypothesis that this accumulated Fe is located in the cell wall. This is further supported by the Fe levels further dropping with lyticase treatment to remove the cell wall. This lower Fe concentration in the remaining spheroplasts indicates that the accumulated Fe was located in the cell wall (CW Fe).To determine the chemical nature of this CW Fe, EPR and Mössbauer spectroscopy were employed. It was found that there were three species present, a diamagnetic species, a paramagnetic species, and a superparamagnetic species.

While cells were being grown, glucose levels (measured by Dr. Park), and oxygen levels were measured. Combined with OD_{600} data, a mathematical model was developed that described the metabolic deactivation and subsequent deactivation. This model describes the metabolic activation and reactivation as being glucose/oxygen dependent, with cells shifting to stationary state as their nutrient source ran low, and reactivating as glucose was reintroduced. Cells under exponential growth conditions are consuming nutrients and oxygen, and will shift to the dormant stationary state if nutrients become limiting.

E. coli possess similar Fe contents and the means to protect Fe relative to eukaryotic mitochondria

While the E. coli study in Chapter 7 is a departure from the studies of yeast and the integration of data into a system's level mathematical model, the results found could potentially be used to further research into mitochondrial iron, and the nature of the LMM complexes. As has been found in previous studies **(14)**, 2 LMM Fe species at 1100 and 580 Da (Fe_{1100}/Fe_{580}) appear to be conserved between yeast, murine, and human mitochondria. With this new study, it would appear that E. coli could be added to that list. With the similarities in molecular mass, and the closeness of Mössbauer fitting parameters to yeast mitochondria, it is reasonable to suggest that the LMM complexes close to 500 Da (Fe_{580}/Fe_{500}) might be the same complex, and that they might serve as a feedstock for ISC and heme assembly in both mitochondria and E. coli. Future work into characterizing this complex through techniques like ESI-MS and NMR is needed.

Similar to the vicious cycle of iron import and nanoparticle/ROS formation, we propose an equivalent event in E. coli and other aerobic bacteria. Electrons generated through metabolic activity are delivered to inner membrane complexes, then to cytochrome c oxidase. This allows for rapid reduction of O_2 threatening to diffuse into the cytosol. If the metabolic activity of the bacteria is disrupted, as what happens during the transition to stationary state or if cellular respiratory complexes are chemically inhibited (such as with cyanide), O_2 penetrates into the cytosol, reacting with Fe_{500} to form nanoparticles. Other studies also suggest a respiratory shield that protects O_2 sensitive materials in other bacteria. *Azotobacter vinelandii* possesses such a shield to

protect nitrogenase, an extremely O_2-sensitive enzyme **(231)**. Relating back to mitochondria, the nitrogenase protein is active if expressed in the mitochondria matrix of yeast **(234)**.

The respiratory shield might also help to regulate and store iron in addition to protecting it. Eukaryotes protect against Fenton chemistry by keeping the minimum amount of Fe^{2+} in the cytosol, storing the excess in ferritin/vacuoles in the Fe^{3+} state. In both cases, mobilization from these storage sites requires the reduction of Fe^{3+} to Fe^{2+}. Our results indicate that E. coli use a different strategy. We hypothesize that E. coli, and possibly bacteria in general, prevent oxidative damage through Fenton chemistry by utilizing the respiratory shield. This would allow for the strange phenomenon of storage of Fe in a labile form, and aggregation of nanoparticles in a metabolically dormant state. It would appear that ferritins play a more specialized, limited role in storing Fe in stationary-state E. coli.

This study has also been supplemented by studying another aerobic bacteria, B. subtilis, and Mössbauer spectra similar to E. coli were obtained. This provides evidence for a hypothesis that all bacteria could possess similar iron contents, and possible the same LMM complexes for trafficking within the cell.

Conclusions

Mössbauer spectroscopy and other biophysical methods provide invaluable information of Fe contents, regardless of organism. The obtained data are useful in assembling models of understanding Fe related phenomena. In other studies, these mechanistic models are summarized and presented using cartoons, pictures of the researcher's qualitative hypotheses. Mathematical models can be an improvement from these cartoons. These models provide a quantitative basis for testing the pathways proposed in the model, and could be used in the future as the summary figure that the cartoons typically serve as today.

In my graduate work, the mathematical modeling work has provided insight regarding an interesting phenomenon in the mitochondria of S. cerevisiae. The Fe-S clusters and hemes produced in the mitochondria consume oxygen in the respiration process. This keeps the matrix of the mitochondria relatively anaerobic, and provides a protective effect for the labile Fe^{2+} pool, that is used as a feedstock for Fe-S cluster and heme synthesis. However, if oxygen does come into the matrix, it can react with the labile pool, producing mitochondrial nanoparticles and ROS. This can become the dominating pathway if there are problems in Fe-S cluster assembly or in cellular respiration, which depletes this "respiratory shield". Our studies in E. coli show that this respiratory shield is also acting in these cells, and possibly in all aerobic prokaryotes.

REFERENCES

1. Lill, R., Hoffmann, B., Molik, S., Pierik, A. J., Rietzschel, N., Stehling, O., Uzarska, M.A, Webert, H., Wilbrecht, C., & Mühlenhoff, U. (2012). The role of mitochondria in cellular iron-sulfur protein biogenesis and iron metabolism. *Biochimica et Biophysica Acta - Molecular Cell Research*, *1823*(9), 1491–1508.
2. Guo, S., Frazer, D. M., & Anderson, G. J. (2016). Iron homeostasis. *Current Opinion in Clinical Nutrition and Metabolic Care*, *19*(4), 276–281.
3. Philpott, C. C., & Protchenko, O. (2008). Response to iron deprivation in Saccharomyces cerevisiae. *Eukaryotic Cell*, *7*(1), 20–27.
4. Craig D. Kaplan and Jerry Kaplan. (2009). Iron Acquisition and Transcriptional Regulation. *Chem. Rev.*, *109*(10), 4536–4552.
5. Kwok, E. Y., Severance, S., & Kosman, D. J. (2006). Evidence for Iron Channeling in the Fet3p − Ftr1p High-Affinity Iron Uptake Complex in the Yeast Plasma Membrane Evidence for Iron Channeling in the Fet3p-Ftr1p High-Affinity Iron Uptake Complex in the Yeast Plasma Membrane. *Biochemistry*, (45), 6317–6327.
6. Shatwell, K. P., Dancis, A., Gross, A. R., Klausner, R. D., & Segal, A. W. (1996). The FRE1 ferric reductase of Saccharomyces cerevisiae is a cytochrome b similar to that of NADPH oxidase. *Journal of Biological Chemistry*, *271*(24), 14240–14244.
7. Jensen, L. T., & Culotta, V. C. (2002). Regulation of Saccharomyces cerevisiae FET4 by Oxygen and Iron. *Journal of Molecular Biology*, (318), 251–260.

8. Zhang, Y., Lyver, E. R., Knight, S. A. B., Pain, D., Lesuisse, E., & Dancis, A. (2006). Mrs3p, Mrs4p, and frataxin provide iron for fe-s cluster synthesis in mitochondria. *Journal of Biological Chemistry*, *281*(32), 22493–22502.
9. Mühlenhoff, U., Stadler, J. A., Richhardt, N., Seubert, A., Eickhorst, T., Schweyen, R. J., Lill, R, & Wiesenberger, G. (2003). A Specific Role of the Yeast Mitochondrial Carriers Mrs3/4p in Mitochondrial Iron Acquisition under Iron-limiting Conditions. *Journal of Biological Chemistry*, *278*(42), 40612–40620.
10. Moore, M. J., Wofford, J. D., Dancis, A., & Lindahl, P. A. (2018). Recovery of mrs3Δmrs4Δ Saccharomyces cerevisiae Cells under Iron-Sufficient Conditions and the Role of Fe 580. *Biochemistry*, (57), 672–683.
11. Froschauer, E. M., Rietzschel, N., Hassler, M. R., Binder, M., Schweyen, R. J., Lill, R., Muhlenhoff, U., & Wiesenberger, G. (2013). The mitochondrial carrier Rim2 co-imports pyrimidine nucleotides and iron. *Biochemical Journal*, *455*(1), 57–65.
12. Yoon, H., Zhang, Y., Pain, J., Lyver, E. R., Lesuisse, E., Pain, D., & Dancis, A. (2011). Rim2, a pyrimidine nucleotide exchanger, is needed for iron utilization in mitochondria. *Biochemical Journal*, *440*(1), 137–146.
13. Holmes-Hampton, G. P., Miao, R., Garber Morales, J., Guo, Y., Münck, E., & Lindahl, P. A. (2010). A nonheme high-spin ferrous pool in mitochondria isolated from fermenting saccharomyces cerevisiae. *Biochemistry*, *49*(19), 4227–4234.

14. McCormick, S. P., Moore, M. J., & Lindahl, P. A. (2015). Detection of Labile Low-Molecular-Mass Transition Metal Complexes in Mitochondria. *Biochemistry*, *54*(22), 3442–3453.

15. Miao, R., Martinho, M., Morales, J. G., Kim, H., Ellis, E. A., Lill, R., Hendrich, M.P., Munck, E., & Lindahl, P. A. (2008). EPR and Mossbauer Spectroscopy of Intact Mitochondria Isolated from Yah1 Depleted S. cerevisiae. *Biochemistry*, (47), 9888–9899.

16. Babcock, M., de Silva, D., Oaks, R., Davis-Kaplan, S., Jiralerspong, S., Montermini, L., Pandolfo, M., Kaplan, J. (1997). Regulation of Mitochondrial Iron Accumulation by Yfh1p, a Putative Homolog of Frataxin. *Science*, *276*(5319), 1709–1712.

17. Ranatunga, W., Gakh, O., Galeano, B. K., Smith, D. Y., Söderberg, C. A. G., Al-Karadaghi, S., Thompson, J.R, & Isaya, G. (2016). Architecture of the yeast mitochondrial iron-sulfur cluster assembly machinery: The sub-complex formed by the iron donor, yfh1 protein, and the scaffold, ISU1 protein. *Journal of Biological Chemistry*, *291*(19), 10378–10398.

18. Pandey, A., Gordon, D. M., Pain, J., Stemmler, T. L., Dancis, A., & Pain, D. (2013). Frataxin directly stimulates mitochondrial cysteine desulfurase by exposing substrate-binding sites, and a mutant Fe-S cluster scaffold protein with frataxin-bypassing ability acts similarly. *Journal of Biological Chemistry*, *288*(52), 36773–36786.

19. https://www.ninds.nih.gov/Disorders/Patient-Caregiver-Education/Fact-Sheets/Friedreichs-Ataxia-Fact-Sheet last visited 5/14/2018

20. Klompmaker, S. H., Kohl, K., Fasel, N., & Mayer, A. (2017). Magnesium uptake by connecting fluid-phase endocytosis to an intracellular inorganic cation filter. *Nature Communications*, *8*(1879), 1–12.

21. Li, L., Chen, O. S., Ward, D. M., & Kaplan, J. (2001). CCC1 Is a Transporter That Mediates Vacuolar Iron Storage in Yeast. *Journal of Biological Chemistry*, *276*(31), 29515–29519.

22. Singh, A., Kaur, N., & Kosman, D. J. (2007). The metalloreductase Fre6p in Fe-efflux from the yeast vacuole. *Journal of Biological Chemistry*, *282*(39), 28619–28626.

23. Urbanowski, J. L., & Piper, R. C. (1999). The iron transporter Fth1p forms a complex with the Fet5 iron oxidase and resides on the vacuolar membrane. *Journal of Biological Chemistry*, *274*(53), 38061–38070.

24. Dodani, S. C., Leary, S. C., Cobine, P. A., Winge, D. R., & Chang, C. J. (2011). A targetable fluorescent sensor reveals that copper-deficient SCO1 and SCO2 patient cells prioritize mitochondrial copper homeostasis. *Journal of the American Chemical Society*, *133*(22), 8606–8616.

25. Chang, C. J., Gunnlaugsson, T., & James, T. D. (2015). Sensor targets. *Chemical Society Reviews*, *44*(13), 4176–4178.

26. Winterbourn, C. C. (1995). Toxicity of iron and hydrogen peroxide: the Fenton reaction. *Toxicology Letters*, *82–83*(C), 969–974.

27. Lill, R., Srinivasan, V., & Mühlenhoff, U. (2014). The role of mitochondria in cytosolic-nuclear iron-sulfur protein biogenesis and in cellular iron regulation. *Current Opinion in Microbiology*, *22*(Figure 1), 111–119.

28. Outten, C. E., & Albetel, A. N. (2013). Iron sensing and regulation in Saccharomyces cerevisiae: Ironing out the mechanistic details. *Current Opinion in Microbiology*, *16*(6), 662–668.

29. Martinez-Pastor, M., Vergara, S. V., Puig, S., & Thiele, D. J. (2013). Negative Feedback Regulation of the Yeast Cth1 and Cth2 mRNA Binding Proteins Is Required for Adaptation to Iron Deficiency and Iron Supplementation. *Molecular and Cellular Biology*, *33*(11), 2178–2187.

30. Csere, P., Lill, R., & Kispal, G. (1998). Identification of a human mitochondrial ABC transporter, the functional orthologue of yeast Atm1p. *FEBS Letters*, *441*(2), 266–270.

31. Maio, N., & Rouault, T. A. (2015). Iron-sulfur cluster biogenesis in mammalian cells: New insights into the molecular mechanisms of cluster delivery. *Biochimica et Biophysica Acta*, *1853*(6), 1493–512. https://doi.org/10.1016/j.bbamcr.2014.09.009

32. Campuzano, V., Montermini, L., Molto, M. D., Pianese, L., Cossee, M., Cavalcanti, F., Monros, E., Rodius, F, Duclos, F., Monticelli, A., Zara, F., Canizares, J., Koutnikova, H., Bidichandani, S.I., Gellera, C., Brice, A., Trouillas, P., De Michele, G., Filla, A., De Frutos, R., Palau, F., Patel, P.I., Di Donato, S., Mandel, J., Cocozza, S., Koenig, M., & Pandolfo, M. (1996).

Friedreich's Ataxia: Autosomal Recessive Disease Caused by an Intronic GAA Triplet Repeat Expansion. *Science*, *271*(5254), 1423–1427.

33. Mühlenhoff, U., Richhardt, N., Ristow, M., Kispal, G., & Lill, R. (2002). The yeast frataxin homolog Yfh1p plays a specific role in the maturation of cellular Fe/S proteins. *Human Molecular Genetics*, *11*(17), 2025–2036.
34. https://ghr.nlm.nih.gov/condition/beta-thalassemia, Last Accessed 5/11/2018
35. https://www.nhlbi.nih.gov/health-topics/hemochromatosis, Last Accessed 5/11/2018
36. Söderberg, C., Gillam, M. E., Ahlgren, E. C., Hunter, G. A., Gakh, O., Isaya, G., Ferreira, G.C., & Al-Karadaghi, S. (2016). The structure of the complex between yeast frataxin and ferrochelatase: Characterization and pre-steady state reaction of ferrous iron delivery and heme synthesis. *Journal of Biological Chemistry*, *291*(22), 11887–11898.
37. Lindahl, P. A., & Holmes-Hampton, G. P. (2011). Biophysical probes of iron metabolism in cells and organelles. *Current Opinion in Chemical Biology*, *15*(2), 342–346.
38. Mrinmoy Chakrabarti, Allison L. Cockrell, Jinkyu Park, Sean P. McCormick, L. S., & Lindahl, and P. A. L. (2015). Speciation of iron in mouse liver during development, iron deficiency, IRP2 deletion and inflammatory hepatitis. *Metallomics*, *7*(1), 520–529.

39. Holmes-Hampton, G. P., Chakrabarti, M., Cockrell, A. L., McCormick, S. P., Abbott, L. C., Lindahl, L. S., & Lindahl, P. a. (2012). Changing iron content of the mouse brain during development. *Metallomics*, *4*, 761.

40. Jhurry, N. D., Chakrabarti, M., McCormick, S. P., Gohil, V. M., & Lindahl, P. A. (2013). Mossbauer study and modeling of iron import and trafficking in human jurkat cells. *Biochemistry*, *52*(45), 7926–7942.

41. Park, J., McCormick, S. P., Chakrabarti, M., & Lindahl, P. A. (2013). Insights into the iron-ome and manganese-ome of Δmtm1 Saccharomyces cerevisiae mitochondria. Metallomics : Integrated Biometal Science, 5(6), 656–72.

42. Mossbauer, R. L. (2000). The discovery of the Mössbauer effect. *Hyperfine Interactions*, 126(1), 1–12.

43. Frauenfelder, H. (1963). The Mössbauer Effect. *Reports on Progress in Physics*, (25), 441–524.

44. Chakrabarti M, & Lindahl PA. The Utility of Mössbauer Spectroscopy in Eukaryotic Cell Biology and Animal Physiology in “Iron-Sulfur Clusters” (Tracey A. Rouault, Ed) Walter de Gruyter Publisher, Berlin Germany, 2014;4:49-75.

45. Sorin L.A., & Vlasova M.V. (1973) Electron Paramagnetic Resonance. In: Electron Spin Resonance of Paramagnetic Crystals. Springer, Boston, MA

46. Cotton, F.A., Wilkinson, G., Murillo, C.A., & Bochmann, M. (1999) Advanced Inorganic Chemistry: Sixth Edition, John Wiley & Sons, Inc., New York, NY

47. Crichton, R. (2001). 2 The Importance of Iron for Biological Systems. In *Inorganic Biochemistry of Iron Metabolism: From Molecular Mechanisms to Clinical Consequences. 2nd Edition* (Vol. 1, pp. 17–48).

48. Cabiscol, E., Piulats, E., Echave, P., Herrero, E., & Ros, J. (2000). Oxidative Stress Promotes Specific Protein Damage in Saccharomyces cerevisiae *. *Journal of Biological Chemistry*, *275*(35), 27393–27398.

49. Cabiscol, E., & Ros, J. (2000). Oxidative stress in bacteria and protein damage by reactive oxygen species. *International Microbiology*, *3*, 3–8.

50. Miao, R., Holmes-Hampton, G. P., & Lindahl, P. A. (2011). Biophysical investigation of the iron in Aft1-1 up and Gal-YAH1 saccharomyces cerevisiae. *Biochemistry*, *50*(13), 2660–2671.

51. Miao, R., Kim, H., Koppolu, U. M. K., Ellis, E. A., Scott, R. A., & Lindahl, P. A. (2009). Biophysical characterization of the iron in mitochondria from Atm1p-depleted Saccharomyces cerevisiae. *Biochemistry*, *48*(40), 9556–9568.

52. Theil, E. C. (2011). Ferritin protein nanocages use ion channels, catalytic sites, and nucleation channels to manage iron / oxygen chemistry. *Current Opinion in Chemical Biology*, *15*(2), 304–311.

53. Lindahl, P. A., & Moore, M. J. (2016). Labile Low-Molecular-Mass Metal Complexes in Mitochondria: Trials and Tribulations of a Burgeoning Field. *Biochemistry*, *55*(30), 4140–4153.

54. Chen, O. S., Crisp, R. J., Valachovic, M., Bard, M., Winge, D. R., & Kaplan, J. (2004) Transcription of the yeast iron regulon does not respond directly to iron but rather to iron-sulfur cluster biosynthesis. *J. Biol. Chem.* 279, 29513–29518

55. Li, L., Miao, R., Bertram, S., Jia, X., Ward, D. M., & Kaplan, J. (2012) A role for iron-sulfur clusters in the regulation of transcription factor yap5- dependent high iron transcriptional responses in yeast. *J. Biol. Chem.* 287, 35709–35721

56. Yamaguchi-Iwai, Y., Dancis, A., & Klausner, R. D. (1995) Aft1: a media-tor of iron-regulated transcriptional control in Saccharomyces cerevisiae. *EMBO J.* 14, 1231–1239

57. Yamaguchi-Iwai, Y., Stearman, R., Dancis, A., & Klausner, R. D. (1996) Iron-regulated DNA binding by the Aft1 protein controls the iron regulon in yeast. *EMBO J.* 15, 3377–3384

58. Li, L., Bagley, D., Ward, D. M., & Kaplan, J. (2008). Yap5 is an iron-responsive transcriptional activator that regulates vacuolar iron storage in yeast. *Molecular and Cellular Biology*, *28*(4), 1326–37. https://doi.org/10.1128/MCB.01219-07

59. Rietzschel, N., Pierik, A. J., Bill, E., Lill, R., & Mühlenhoff, U. (2015). The Basic Leucine Zipper Stress Response Regulator Yap5 Senses High-Iron Conditions by Coordination of [2Fe-2S] Clusters. *Molecular and Cellular Biology*, *35*(2), 370–8. https://doi.org/10.1128/MCB.01033-14

60. Srinivasan, V., Pierik, A. J., & Lill, R. (2014) Crystal structures of nucle- otide-free and glutathione-bound mitochondrial ABC transporter Atm1. *Science* 343, 1137–1140

61. Lee, J. Y., Yang, J. G., Zhitnitsky, D., Lewinson, O., and Rees, D. C. (2014) Structural basis for heavy metal detoxification by an Atm1-type ABC ex- porter. *Science* 343, 1133–1136

62. Mapolelo, D. T., Zhang, B., Randeniya, S., Albetel, A. N., Li, H., Couturier, J., Outten, C. E., Rouhier, N., & Johnson, M. K. (2013) Monothiol glu- taredoxins and A-type proteins: partners in Fe-S cluster trafficking. *Dalton Transactions* 42, 3107–3115

63. Ojeda, L., Keller, G.,Muhlenhoff, U., Rutherford, J. C., Lill, R., & Winge, D. R. (2006) Role of glutaredoxin-3 and glutaredoxin-4 in the iron regula- tion of the Aft1 transcriptional activator in Saccharomyces cerevisiae. *J. Biol. Chem.* 281, 17661–17669

64. Li, H., Mapolelo, D. T., Dingra, N. N., Naik, S. G., Lees, N. S., Hoffman, B. M., Riggs-Gelasco, P. J., Huynh, B. H., Johnson, M. K., & Outten, C. E. (2009) The yeast iron regulatory proteins Grx3/4 and Fra2 form heterodimeric complexes containing a [2Fe-2S] cluster with cysteinyl and histidyl ligation. *Biochemistry* 48, 9569–9581

65. Holmes-hampton, G. P., Jhurry, N. D., Mccormick, S. P., & Lindahl, P.A. (2013). Iron Content of Saccharomyces cerevisiae Cells Grown under Iron-Deficient and Iron-Overload Conditions. *Biochemistry*, *52*, 105–114.

66. Cockrell, A., McCormick, S. P., Moore, M. J., Chakrabarti, M., & Lindahl, P. A. (2014). Mössbauer, EPR, and modeling study of iron trafficking and regulation

in Δccc1 and CCC1-up saccharomyces cerevisiae. *Biochemistry, 53*(18), 2926–2940.

67. Lill, R., Dutkiewicz, R., Freibert, S. A., Heidenreich, T., Mascarenhas, J., Netz, D. J., Paul, V. D., Pierik, A. J., Richter, N., Stuempfig, M., Srinivasan, V., Stehling, O., & Mühlenhoff, U. (2015) The role of mitochondria and the CIA machinery in the maturation of cytosolic and nuclear iron-sulfur proteins. *Eur. J. Cell Biol.* 94, 280− 291
68. Mühlenhoff, U., Hoffmann, B., Richter, N., Rietzschel, N., Spantgar, F., Stehling, O., Uzarska, M. A., & Lill, R. (2015) Compartmentalization of iron between mitochondria and the cytosol and its regulation. *Eur. J. Cell Biol.* 94, 292−308.
69. Foury, F., & Roganti, T. (2002) Deletion of the mitochondrial carrier genes MRS3 and MRS4 suppresses mitochondrial iron accumulation in a yeast frataxin-deficient strain. *J. Biol. Chem.* 277, 24475−24483..
70. Li, L. T., & Kaplan, J. (2004) A mitochondrial-vacuolar signaling pathway in yeast that affects iron and copper metabolism. *J. Biol. Chem.* 279, 33653−33661
71. Zhang, Y., Lyver, E. R., Knight, S. A. B., Lesuisse, E., & Dancis,A. (2005) Frataxin and mitochondrial carrier proteins, Mrs3p and Mrs4p, cooperate in providing iron for heme synthesis. *J. Biol. Chem.* 280, 19794−19807.
72. Lin, H. L., Li, L. T., Jia, X. A., Ward, D. M., & Kaplan, J. (2011) Genetic and Biochemical Analysis of High Iron Toxicity in Yeast: iron toxicity is due to the

accumulation of cytosolic iron and occurs under both aerobic and anaerobic conditions. *J. Biol. Chem.* 286, 3851−3862. (25)

73. Li, L. T., Murdock, G., Bagley, D., Jia, X. A., Ward, D. M., & Kaplan, J. (2010) Genetic Dissection of a Mitochondria-Vacuole Signaling Pathway in Yeast Reveals a Link between Chronic Oxidative Stress and Vacuolar Iron Transport. *J. Biol. Chem.* 285, 10232−10242.
74. Muhlenhoff U, Richhardt N, Gerber J, & Lill R. (2002) Characterization of iron-sulfur protein assembly in isolated mitochondria - A requirement for ATP, NADH, and reduced iron. *J. Biol. Chem.,* 277, 29810-29816.
75. Gardner PR, Nguyen DD, & White CW. (1994) Aconitase is a sensitive and critical target of oxygen poisoning in cultured mammalian cells and in rat lungs. *Proc. Natl Acad. Sci. USA*, 91, 12248–12252.
76. Ollagnier-de Choudens S, Sanakis Y, Hewitson KS, Roach P, Baldwin JE, Münck E, & Fontecave M. (2000) Iron-Sulfur Center of Biotin Synthase and Lipoate Synthase. *Biochemistry*, 39, 4165-4173.
77. Lopez-Torrejon G, Jimenez-Vicente E, Buesa JM, Hernandez JA, Verma HK, & Rubio LM.(2016) Expression of a function oxygen-labile nitrogenase component in the mitochondrial matrix of aerobically grown yeast *Nature Commun*.,7, 1-6.
78. G. Lesage & H. Bussey (2006) Cell wall assembly in Saccharomyces cerevisiae, *Microbiol. Mol. Biol. Rev.* 70, 317–343.

79. J. G. De Nobel, F. M. Klis, J. Priem, T. Munnik & H. VanDenEnde, (1990) The gluconase-soluble mannoproteins limit cell wall porosity in Saccharomyces cerevisiae, *Yeast*, 6, 491–499.

80. P. W. J. DeGroot, A. F. Ram & F. M. Klis, (2005) Features and functions of covalently linked proteins in fungal cell walls, Fungal Genet. Biol., 42, 657–675.

81. F. M. Klis, M. de Jong, S. Brul & P. W. J. de Groot, (2007) Extraction of cell surface-associated proteins from living yeast cells, *Yeast*, 24, 253–258.

82. E. Albarouki &H. B. Deising, (2013) Infection structure-specific reductive iron assimilation is required for cell wall integrity and full virulence of the maize pathogen Colletotrichum graminicola, *Mol. Plant-Microbe Interact*., 26, 695–708.

83. S. E. Vartivarian, E. J. Anaissie, R. E. Cowart, H. A. Sprigg, M. J. Tingler & E. S. Jacobson, (1993) Regulation of cryptococcal capsular polysaccharide by iron, *J. Infect. Dis*., 167, 186–190.

84. V. K. Srivastava, K. J. Suneetha & R. Kaur, (2014) A systematic analysis reveals an essential role of high-affinity iron uptake system, haemolysin and CFEM domain-containing protein in iron homoeostasis and virulence in Candida glabrata, *Biochem. J.*, 463, 103–114.

85. Q. Yu,Y. Dong, N. Xu, K.Qian, Y. Chen,B.Zhang,L.Xing & M. Li, (2014) A novel role of the ferric reductase Cfl1 in cell wall integrity, mitochondrial function and invasion to host cells in Candida albicans, *FEMS Yeast Res*., 14, 1037–1047.

86. N. Xu, K. Qian, Y. Dong, Y. Chen, Q. Yu, B. Zhang, L. Xing & M. Li, (2014) Novel role of the Candida albicans ferric reductase gene CFL1 in iron acquisition, oxidative stress tolerance, mor- phogenesis and virulence, *Res. Microbiol*., 165, 252–261.

87. O. Protchenko, T. Ferea, J. Rashford, J. Tiedeman, P. O. Brown, D. Botstein & C. C. Philpott, (2001) Three cell wall mannoproteins facilitate the uptake of iron in Saccharomyces cerevisiae, *J. Biol. Chem*., 276, 49244–49250.

88. Saha, R., Saha, N., Donofrio, R.S., & Bestervelt, L.L. (2013) Microbial siderophores: a mini review. *J. Basic Microbiol.* 53, 303-317.

89. Miethke, M. (2013) Molecular strategies of microbial iron assimilation: from high-affinity complexes to cofactor assembly systems. *Metallomics* 5, 15-28.

90. Lau, C.K.Y, Krewulak, K.D., & Vogel, H.J. (2016) Bacterial ferrous ion transport: the Feo system. *FEMS Microbiol. Rev.* 40, 273-298

91. Mahren, S., Schnell, H., and Braun, V. (2005) Occurrence and regulation of the ferric citrate transport system in Escherichia coli B, Klebsiella pneumoniae, Enterobacter aerogenes, and Photorhabdus luminescens. *Archives Microbiol.* 184, 175-186.

92. Bradley, J.M., LeBrun, N.E., and Moore, G.R. (2016) Ferritins: furnishing proteins with iron. *J. Biol. Inorg. Chem.* 21, 13-28.

93. Arosio P., Elia, L., and Poli M. (2017) Ferritin, Cellular iron storage and regulation. *International Union of Biochemistry and Molecular Biology* 69, 414-422.

94. Bradley JM; Moore GR; Le Brun NE (2017) Diversity of Fe2+ entry and oxidation in ferritins *Current Opinion In Chemical Biology* 37, 122-128.

95. Chiancone E ; Ceci P (2010) The multifaceted capacity of Dps proteins to combat bacterial stress conditions: Detoxification of iron and hydrogen peroxide and DNA binding *Biochimica Et Biophysica Acta-General Subjects* 1800, 798-805.

96. Ferreira IGD; Rodrigues MM; Neto JFD; Mazzon, RR; Marques, MD (2016) Role and regulation of ferritin-like proteins in iron homeostasis and oxidative stress survival of Caulobacter crescentus *Biometals* 29:,851-862.

97. Kiley PJ; Beinert H (1998) Oxygen sensing by the global regulator, FNR: the role of the iron-sulfur cluster *FEMS Microbiology Reviews* 22, 341-352.

98. Escolar L, Perez-Martin J, De Lorenzo V (1999) Opening the iron box: Transcriptional metalloregulation by the fur protein *Journal Of Bacteriology* 181: 6223-6229

99. Fontecave and Pierre (1991) iron metabolism: the low-molecular-mass iron pool, *Biol. Metals* 4, 133-135.

100. Böhnke R; Matzanke BF (1995) The mobile ferrous iron pool in E coli is bound to a phosphorylated sugar derivative, *Biometals*, 8, 223-230.

101. Goodmansee AN; Imlay JA (2002) Quantitation of intracellular free iron by electron paramagnetic resonance spectroscopy *Methods in Enzymology* 349, 3-9.

102. Hohle TH; O'Brian, MR (2016) Metal-specific control of gene expression mediated by Bradyrhizobium japonicum Mur and Escherichia coli Fur is determined by the cellular context *Mol. Microbiol.* 101, 152-166.

103. Goodmansee AN; Imlay JA (2002) Reduced flavins promote oxidative DNA damage in non-respiring Escherichia coli by delivering electrons to intracellular free iron *Journal of Biol. Chem.*, 277, 34055-34066.

104. Imlay JA and Linn S (1988) DNA damage and oxygen radical toxicity, *Science* 240, 1302-1309.

105. Beauchene N.A., Mettert, E.L., Moore, L.J., Keles, S., Willey, E.R. and Kiley, P.J. (2017) O_2 availability impacts iron homeostasis in Escherichia coli. *Proc. Natl Acad Sci. USA* 114, 12261-12266.

106. Bauminger ER; Cohen SG, Dickson DPE, Levy A, Ofer S, Yarvis J (1980) Mossbauer spectroscopy of Escherichia coli and its iron storage protein, *Biochim. Biophys. Acta*, 623, 237-242.

107. Matzanke, B. F., Muller, G. I., Bill, E. & Trautwein, A. X. (1989) Iron metabolism of Escherichia coli studied by Mössbauer spectroscopy and biochemical methods. *Eur. J. Biochem.* 183, 371–379 (1989).

108. Hudson AJ, Andrews SC, Hawkins C, Williams JM, Izuhara, M, Meldrum FC, Mann S., Harrison PM; Guest JR (1993) Overproduction, purification and characterization of the Escherichia coli ferritin, *European Journal of Biochemistry*, 218, 985-995.

109. Abdul-Tehrani H, Hudson AJ, Chang YS, Timms AR, Hawkins C, Williams JM, Harrison PM, Guest, JR, Andrews SC (1999) Ferritin mutants of Escherichia coli are iron deficient and growth impaired, and fur mutants are iron deficient, *Journal of Bacteriology*, 181, 1415-1428

110. Keyer K, Imlay JA (1996) Superoxide accelerates DNA damage by elevating free-iron levels, *PNAS*, 93, 13635-13640

111. Hristova, D., Wu, C.H., Jiang, W., Krebs, C., Stubbe, J., (2008) Importance of the Maintainance pathway in the regulation of the activity of the Escherichia coli Ribonucleotide Reductase, *Biochemistry*, 47, 3989-3999.

112. Beilschmidt LK, de Choudens SO, Fournier M, Sanakis I, Hograindleur MA, Clemancey M, Blondin G, Schmucker S, Eisenmann A, Weiss A; Koebel P, Messaddeq N, Puccio H, Martelli A, (2017) ISCA1 is essential for mitochondrial Fe4S4 biogenesis in vivo, *Nature Communications* 8, 1-6.

113. Wofford, J. D., Chakrabarti, M., & Lindahl, P. A. (2017). Mössbauer Spectra of Mouse Hearts reveal age-dependent changes in mitochondrial and ferritin iron levels. *Journal of Biological Chemistry*, *292*(13), 5546–5554. https://doi.org/10.1074/jbc.M117.777201

114. Kuppuswamy, S., Wofford, J. D., Joseph, C., Xie, Z. L., Ali, A. K., Lynch, V. M., Lindahl, P.A., & Rose, M. J. (2017). Structures, Interconversions, and Spectroscopy of Iron Carbonyl Clusters with an Interstitial Carbide: Localized Metal Center Reduction by Overall Cluster Oxidation. *Inorganic Chemistry*, *56*(10), 5998–6012.

115. Kosman, D. J. (2013) Iron metabolism in aerobes: managing ferric iron hydrolysis and ferrous iron autoxidation. *Coord. Chem. Rev.* 257, 210 –217

116. Park, J., McCormick, S. P., Cockrell, A. L., Chakrabarti, M., & Lindahl, P.A. (2014) High-spin ferric ions in Saccharomyces cerevisiae vacuoles are reduced to the ferrous state during adenine-precursor detoxification. *Biochemistry* 53, 3940 –3951

117. Chen, O. S., & Kaplan, J. (2000) CCC1 suppresses mitochondrial damage in the yeast model of Friedreich's ataxia by limiting mitochondrial iron accumulation. *J. Biol. Chem.* 275, 7626 –7632

118. Rutherford, J. C., Jaron, S., Ray, E., Brown, P. O., & Winge, D. R. (2001) A second iron-regulatory system in yeast independent of Aft1p. *Proc. Natl. Acad. Sci. U.S.A.* 98, 14322–14327

119. Rutherford, J. C., Jaron, S., & Winge, D. R. (2003) Aft1p and Aft2p mediate iron-responsive gene expression in yeast through related promoter elements. *J. Biol. Chem.* 278, 27636 –27643

120. Courel, M., Lallet, S., Camadro, J. M., & Blaiseau, P. L. (2005) Direct activation of genes involved in intracellular iron use by the yeast iron- responsive transcription factor Aft2 without its paralog Aft1. *Mol. Cell. Biol.* 25, 6760 – 6771

121. Yamaguchi-Iwai, Y., Ueta, R., Fukunaka, A., & and Sasaki, R. (2002) Subcellular localization of Aft1 transcription factor responds to iron status in Saccharomyces cerevisiae. *J. Biol. Chem.* 277, 18914 –18918

122. Poor, C. B., Wegner, S. V., Li, H., Dlouhy, A. C., Schuermann, J. P., Sanishvili, R., Hinshaw, J. R., Riggs-Gelasco, P. J., Outten, C. E., & He, C. (2014) Molecular mechanism and structure of the Saccharomyces cerevi- siae iron regulator Aft2. *Proc. Natl. Acad. Sci. U.S.A.* 111, 4043– 4048

123. Chen, O. S., Hemenway, S., & Kaplan, J. (2002) Inhibition of Fe-S cluster biosynthesis decreases mitochondrial iron export: evidence that yfh1p affects Fe-S cluster synthesis. *Proc. Natl. Acad. Sci. U.S.A.* 99, 12321–12326

124. Schaedler, T. A., Thornton, J. D., Kruse, I., Schwarzlander, M., Meyer, A. J., van Veen, H. W., & Balk, J. (2014) A conserved mitochondrial ATP-binding cassette transporter exports glutathione polysulfide for cytosolic metal cofactor assembly. *J. Biol. Chem.* 289, 23264 –23274

125. Li, L., Jia, X., Ward, D. M., & Kaplan, J. (2011) Yap5 protein-regulated transcription of the TYW1 gene protects yeast from high iron toxicity., *J. Biol. Chem.* 286, 38488 –38497

126. Pedro-Segura, E., Vergara, S. V., Rodríguez-Navarro, S., Parker, R., Thiele, D. J., & Puig, S. (2008) The Cth2 ARE-binding protein recruits the Dhh1 helicase to promote the decay of succinate dehydrogenase SDH4 mRNA in response to iron deficiency. *J. Biol. Chem.* 283, 28527–28535

127. Robinson, A. J., & Kunji, E. R. (2006) Mitochondrial carriers in the cy-toplasmic state have a common substrate binding site. *Proc. Natl. Acad. Sci. U.S.A.* 103, 2617–2622

128. Park, J., McCormick, S. P., Chakrabarti, M., & Lindahl, P. A. (2013) The lack of synchronization between iron uptake and cell growth leads to iron overload in Saccharomyces cerevisiae during post-exponential growth modes. *Biochemistry* 52, 9413–9425

129. Koyama, T., Kinjo, M., & Araiso, T. (1989) Oxygen diffusion through mitochondrial membranes. In Oxygen Transport to Tissue XI (Rakusan, K., ed) pp. 763–767, Plenum Press, New York

130. Lill, R., & Muhlenhoff, U. (2006) Iron-sulfur protein biogenesis in eukaryotes: components and mechanisms. *Annu. Rev. Cell Dev. Biol.* 22, 457– 486

131. Brown, N. M., Kennedy, M. C., Antholine, W. E., Eisenstein, R. S., & Walden, W. E. (2002) Detection of a [3Fe-4S] cluster intermediate of cy- tosolic aconitase in yeast expressing iron regulatory protein 1: insights into the mechanism of Fe-S cluster cycling. *J. Biol. Chem.* 277, 7246 –7254

132. Cosper, M. M., Jameson, G. N., Eidsness, M. K., Huynh, B. H., & Johnson, M. K. (2002) Recombinant Escherichia coli biotin synthase is a [2Fe-2S]2+ protein in whole cells. *FEBS Lett.* 529, 332–336

133. Kriek, M., Peters, L., Takahashi, Y., & Roach, P. L. (2003) Effect of iron-sulfur cluster assembly proteins on the expression of Escherichia coli lipoic acid synthase. *Protein Expr. Purif.* 28, 241–245

134. Pandey, A., Pain, J., Ghosh, A. K., Dancis, A., & Pain, D. (2015) Fe-S cluster biogenesis in isolated mammalian mitochondria: coordinated use of

persulfide sulfur and iron and requirements for GTP, NADH, and ATP. *J. Biol. Chem*. 290, 640 – 657

135. Raguzzi, F., Lesuisse, E., & Crichton, R. R. (1988) Iron storage in Saccharomyces cerevisiae. *FEBS Lett.* 231, 253–258

136. Haurie, V., Boucherie, H., & Sagliocco, F. (2003) The snf1 protein kinase controls the induction of the genes of the iron uptake pathway at the diauxic shift in Saccharomyces cerevisiae. *J. Biol. Chem.* 278, 45391– 45396

137. Foster, A. W., Dainty, S. J., Patterson, C. J., Pohl, E., Blackburn, H., Wilson, C., Hess, C. R., Rutherford, J. C., Quaranta, L., Corran, A., & Robinson, N.J. (2014) A chemical potentiator of copper-accumulation used to inves- tigate the iron regulons of Saccharomyces cerevisiae. *Mol. Microbiol.* 93, 317–330

138. Shaw, G. C., Cope, J. J., Li, L. T., Corson, K., Hersey, C., Ackermann, G. E., Gwynn, B., Lambert, A. J., Wingert, R. A., Traver, D., Trede, N. S., Barut, B. A., Zhou, Y., Minet, E., Donovan, A., Brownlie, A., Balzan, R., Weiss, M. J., Peters, L. L., Kaplan, J., Zon, L. I., & Paw, B. H. (2006) Mitoferrin is essential for erythroid iron assimilation. *Nature* 440, 96−100. (9)

139. Paradkar, P. N., Zumbrennen, K. B., Paw, B. H., Ward, D. M., & Kaplan, J. (2009) Regulation of Mitochondrial Iron Import through Differential Turnover of Mitoferrin 1 and Mitoferrin 2. *Mol. Cell. Biol.* 29, 1007−1016.

140. Shvartsman, M., & Cabantchik, Z. I. (2012) Intracellular iron trafficking: role of cytosolic ligands., *BioMetals* 25, 711−723.

141. Robinson, A. J., Overy, C., & Kunji, E. R. S. (2008) The mechanism of transport by mitochondrial carriers based on analysis of symmetry. *Proc. Natl. Acad. Sci. U. S. A.* 105, 17766−17771.

142. Garber Morales, J., Holmes-Hampton, G. P., Miao, R., Guo, Y., Münck, E., & Lindahl, P. A. (2010) Biophysical characterization of iron in mitochondria isolated from respiring and fermenting yeast. *Biochemistry* 49, 5436−5444. (14)

143. Lutz, T., Westermann, B., Neupert, W., & Herrmann, J. M. (2001) The mitochondrial proteins Ssq1 and Jac1 are required for the assembly of iron sulfur clusters in mitochondria. *J. Mol. Biol.* 307, 815− 825.

144. Amutha, B., Gordon, D. M., Gu, Y. J., Lyver, E. R., Dancis, A., & Pain, D. (2008) GTP Is Required for Iron-Sulfur Cluster Biogenesis in Mitochondria. *J. Biol. Chem.* 283, 1362−1371.

145. Lesuisse, E., Santos, R., Matzanke, B. F., Knight, S. A. B., Camadro, J. M., & Dancis, A. (2003) Iron use for haeme synthesis is under control of the yeast frataxin homologue (Yfh1). *Hum. Mol. Genet.* 12, 879−889.

146. Lindahl, P. A., Morales, J. G., Miao, R., & Holmes-Hampton,G. P. (2009) Isolation of Saccharomyces cerevisiae mitochondria for Mössbauer, EPR, and electronic absorption spectroscopic analyses. *Methods Enzymol*. 456, 267−285.

147. Hudder, B. N., Morales, J. G., Stubna, A. A., Münck, A., Hendrich, M. P., & Lindahl, P. A. (2007) Electron paramagnetic resonance and Mössbauer spectroscopy of intact mitochondria from respiring Saccharomyces cerevisiae. *J. Biol. Inorg. Chem.* 12, 1029−1053.

148. Andreini, C., Banci, L., & Rosato, A. (2016) Exploiting bacterial operons to illuminate human iron-sulfur protein. *J. Proteome Research* 15, 1308−1322.

149. Cockrell, A. L., Holmes-Hampton, G. P., McCormick, S. P., Chakrabarti, M., & Lindahl, P. A. (2011) Mössbauer and EPR study of iron in vacuoles from fermenting Saccharomyces cerevisiae. *Biochemistry* 50, 10275−10283.

150. McNaughton, R. L., Reddi, A. R., Clement, M. H. S., Sharma, A., Barnese, K., Rosenfeld, L., Gralla, E. B., Valentine, J. S., Culotta, V. C., & Hoffman, B. M. (2010) Probing in vivo Mn2+ speciation and oxidative stress resistance in yeast cells with electron-nuclear double resonance spectroscopy. *Proc. Natl. Acad. Sci. U. S. A.* 107, 15335− 15339.

151. Atkinson, A., & Winge, D. R. (2009) Metal Acquisition and Availability in the Mitochondria. *Chem. Rev.* 109, 4708−4721.

152. Cobine, P. A., Ojeda, L. D., Rigby, K. M., & Winge, D. R. (2004) Yeast contain a non-proteinaceous pool of copper in the mitochondrial matrix. *J. Biol. Chem.* 279, 14447−14455.

153. Vest, K. E., Wang, J., Gammon, M. G., Maynard, M. K., White, O. L., Cobine, J. A., Mahone, W. K., & Cobine, P. A. (2016) Overlap of copper and iron uptake systems in mitochondria in Saccharomyces cerevisiae. *Open Biol.* 6, 150223.

154. Wofford, J. D., & Lindahl, P. A. (2015) Mitochondrial iron-sulfur-cluster activity and cytosolic iron regulate iron traffic in Saccharomyces cerevisiae. *J. Biol. Chem.* 290, 26968−26977.

155. Reisner, E., Telser, J., & Lippard, S. J. (2007) A planar carboxylate-rich tetrairon(II) complex and its conversion to linear triiron(II) and paddlewheel diiron(II) complexes. *Inorg. Chem.* 46, 10754−10770.

156. Brazzolotto, X., Pierrel, F., & Pelosi, L. (2014) Three conserved histidine residues contribute to mitochondrial iron transport through mitoferrins. *Biochem. J.* 460,79−89.

157. Sewell, C., Morgan, J. J., & Lindahl, P. A. (2002) Analysis of Protein Homeostatic Regulatory Mechanisms in Perturbed Environ- ments at Steady-State. *J. Theor. Biol.* 215, 151−167.

158. Yang, Q., Lindahl, P. A., & Morgan, J. J. (2003) Dynamic Responses of Protein Homeostatic Regulatory Mechanisms to Perturbations from Steady State. *J. Theor. Biol.* 222, 407−423.

159. Mo Chen WW, Niepel M, & Sorger PK. (2010) Classic and contemporary approaches to modeling biochemical reactions. *Genes & Development*, 24, 1861-1875.

160. Anbumathi P. (2014) Chemical Kinetics Based Modelling Approaches and Tools for Investigating Complex Biological Systems. *Asian J. Chem.*, 26, 2511-2517.

161. Mizera A, Czeizler E, & Petre I.(2011) Methods for biochemical model decomposition and quantitative submodel comparison. *Israel J. Chem.*, 51, 151-164.

162. Philpott CC, & Ryu MS.(2014) Special delivery: distributing iron in the cytosol of mammalian cells. *Frontiers in Pharmacology*, 5, 173

163. Omholt SW, & Kefang X, Andersen O, Plahte E.(1998) Description and Analysis of Switchlike Regulatory Networks Exemplified by a Model of Cellular Iron Homeostasis. *Journal of Theoretical Biology*, 195, 339–350,

164. Mobilia N, Donze A, Moulis JM, & Fanchon E. (2012) A model of the cellular iron homeostasis network using semi-formal methods for parameter space exploration, in E. Bartocci and L. Bortolussi (Eds) *EPTCS*, 92, 42-57.

165. Mobilia N, Donze A, Moulis JM, & Fanchon E. (2013) Producing a set of models for the iron homeostasis network. *EPTICS*, 125, 92-98.

166. Chifman J, Kniss A, Neupane P, Williams I, Leung B, Deng Z, Mendes, P., Hower, V., Torti FM., Akman SA, Torti SV, & Laubenbacher R. (2012) The core control system of intracellular iron homeostasis: A mathematical model. *Journal of Theoretical Biology*. 300, 91-99.

167. Chifman J, Arat S, Deng ZY, Lemler E, Pino JC, Harris LA, Kochen MA, Lopez CF, Akman SA, Torti FM, Torti SV, & Laubenbacher R. (2017) Activated Oncogenic Pathway Modifies Iron Network in Breast Epithelial Cells: A Dynamic Modeling Perspective. *PLoS Comput Biol*, 13, e1005352.

168. Mitchell S, & Mendes P. A (2013) A computational model of liver iron metabolism. *PLOS Computational Biology*, 9, e1003299.

169. Achcar F, Camadro JM, & Mestivier D. A (2011) Boolean probabilistic model of metabolic adaptation to oxygen in relation to iron homeostasis and oxidative stress. *BMC Syst Biol*, 5, 51.

170. Martelli A, & Puccio H. (2014) Dysregulation of cellular iron metabolism in Friedreich ataxia; from primary iron-sulfur cluster deficit to mitochondrial iron accumulation. *Frontiers in Pharmacology*, 5: article number 130.

171. Yamaguchi M, Namiki Y, Okada H, Mori Y, Furukawa H, Wang J, Ohkusu M, & Kawamoto (2011) S. Structome of *Saccharomyces cerevisiae* determined by freeze-substitution and serial ultrathin-sectioning electron microscopy. *J. Electron Microscopy*, 60, 337-351.

172. Wei DG, Jacobs S, Modla S, Zhang S, Young CL, Cirino R, Caplan J, & Czymmek K.(2012) High-resolution three-dimensional reconstruction of a whole yeast cell using focussed-ion beam scanning electron microscopy. *Biotechniques*, 53, 41-48

173. Chan YHM, Marshall WF. (2014) Organelle size scaling of the budding yeast vacuole is tuned by membrane trafficking rates. *Biophysical J*., 106, 1986-1996.

174. Stevens BJ. (1977) Variation in number and volume of mitochondria in yeast according to growth conditions: study based on serial sectioning and computer graphic reconstruction. *Biol. Cell.,* 28, 37-56.

175. Aras S, Bai M, Lee I, Springett R, Hüttemann M, Grossman L.I. (2015) MNRR1 (formerly CHCHD2) is a bi-organellar regulator of mitochondrial metabolism. *Mitochondrion*, 20, 43-51.

176. M Petrat F, deGroot H, Rauen U. (2001) Subcellular distribution of chelatable iron: a laser scanning microscopic study in isolated hepatocytes and liver endothelial cells. *Biochem. J.* 356, 61-69.

177. Krab K, Kempe H, Wikstrom M.(2011) Explaining the enigmatic K(M) for oxygen in cytochrome c oxidase: a kinetic model. *Biochim. Biophys. ACTA* ,1807,348-58.

178. P. W. J. DeGroot, C. Ruiz, C. R. Vazquez de Aldana, E. Euienas, V. J. Cid and F. Del Rey, et al., (2001) A genomic approach for the identification and classification of genes involved in cell wall formation and its regulation in Saccharomyces cerevisiae, *Comp. Funct. Genomics*, 2, 124–142.

179. F. M. Klis, A. Boorsma and P. W. J. DeGroot, (2006) Cell wall construction in Saccharomyces cerevisiae, *Yeast*, 23, 185–202.

180. E. Albarouki and H. B. Deising,(2013) Infection structure-specific reductive iron assimilation is required for cell wall integrity and full virulence of the maize pathogen Colletotrichum graminicola, *Mol. Plant-Microbe Interact*. 26, 695–708.

181. G. H. Fleet and H. J. Phaff,(1995) Ultrastructure of the Cell-Wall of Schizosaccharomyces pombe following treatment with various gluconases, *J. Struct. Biol.*, 114, 140–152.

182. E. Cabib, T. Drgon, J. Drgonova, R. A. Ford and R. Kollar, (1997) The yeast cell wall, a dynamic structure engaged in growth and morphogenesis, *Biochem. Soc. Trans*., 25, 200–204.

183. R. C. Goldman and A. Branstrom, (1999) Targeting cell wall synthesis and assembly in microbes: similarities and contrasts between bacteria and fungi, *Curr. Pharm. Des.* 5, 473–501

184. P. Orlean (1997) Biogenesis of yeast wall and surface components, in Themolecular and cellular biology of the yeast Saccharomyces Vol 3. Cell cycle and cell biology, ed. J. R. Pringle, J. R. Broach and E. W. Jones, Cold Spring Harbor Monograph series, vol. 21, pp. 229–362.

185. M. Vainshtein, N. Belova, T. Kulakovskaya, N. Suzina and V. Sorokin, (2014) Synthesis of magneto-sensitive iron-containing nanoparticle by yeasts, *J. Ind. Microbiol. Biotechnol.*, 41, 657–663.

186. J. H. Scott and R. Schekman (1980), Lyticase – endoglucanase and protease activities that act together in yeast cell lysis, *J. Bacteriol.*, 142, 414–423.

187. K. Chojnacka, (2010) Biosorption and bioaccumulation – the prospects for practical applications, *Environ. Int.*, 36, 299–307.

188. E. A. Preoteasa, G. Schianchi and D. C. Giori, EPR detection of possible superparamagnetic polyiron nanoparticles and free radicals in the blood serum of patients with homo- zygous b-thalassemia, *Appl. Magn. Reson.*, 2014, 45, 537–571.

189. A. L. Cockrell, G. P. Holmes-Hampton, S. P. McCormick, M. Chakrabarti and P. A. Lindahl (2011), Mössbauer and EPR study of iron in vacuoles from fermenting Saccharomyces cerevisiae, *Biochemistry*, 50, 10275–10283.

190. O. R. Homann, J. Dea, S. M. Noble and A. D. Johnson,(2009) A phenotypic profile of the Candida albicans regulatory net- work, *PLoS Genet.*, 5, 1–12.

191. J. Park, S. P. McCormick, A. L. Cockrell, M. Chakrabarti and P. A. Lindahl, (2014) High-spin ferric ions in Saccharomyces cerevisiae vacuoles are reduced to the ferrous state during adenine- precursor detoxification, *Biochemistry*, 53, 3940–3951.

192. D. Blair and H. Diehl, (1961) Bathophenanthrolinedisulphonic acid and bathocuproinedisulfphonic acid, water soluble reagents for iron and copper, *Talanta*, 7, 163–174.

193. J. C. Kapteyn, R. C. Montijn, E. Vink, J. delaCruz, A. Llobell, J. E. Douwes, H. Shimoi, P. N. Lipke and F. M. Klis, (1996) Retention of Saccharomyces cerevisiae cell wall proteins through a phosophodiester-linked beta-1,3-/beta-1,6-glucan hetero- polymer, *Glycobiology*, 6, 337–345.

194. E. Lesuisse, F. Raguzzi and R. R. Crichton, (1987) Iron uptake by the yeast Saccharomyces cerevisiae – involvement of a reduction step, *J. Gen. Microbiol.*, 133, 3229–3236

195. A. L. Hughes and D. E. Gottschling, (2012) An early age increase in vacuolar pH limits mitochondrial function and lifespan in yeast, *Nature*, 492, 261–265.

196. Y. Yamaguchi-Iwai, A. Dancis and R. D. Klausner, (1995) AFT1: a mediator of iron regulated transcriptional control in Saccharomyces cerevisiae, *EMBO J.*, 14, 1231–1239.

197. R. F. Hassett, A. M. Romeo and D. J. Kosman (1998) Regulation of high affinity iron uptake in the yeast Saccharomyces cerevisiae – role of dioxygen and Fe(II), *J. Biol. Chem.*, 1998, 273, 7628–7636.

198. J. W. Kronstad, G. Hu and W. H. Jung, (2013) An encapsulation of iron homeostasis and virulence in Cryptococcus neoformans, *Trends Microbiol.*, 21, 457–465.

199. V. K. Srivastava, K. J. Suneetha and R. Kaur,(2014) A systematic analysis reveals an essential role for high-affinity iron uptake system, haemolysin and CFEM domain-containing protein in iron homoeostasis and virulence in Candida glabrata, *Biochem. J.*, 463, 103–114.

200. E. Lesuisse, F. Raguzzi, R.R. Crichton, (1987) Iron uptake by the yeast Saccharomyces *cerevisiae* – involvement of a reduction step, *J. Gen. Microbiol.*, **133**, 3229-3236.

201. R.F. Hassett, A.M. Romeo, D.J. Kosman, (1998) Regulation of high affinity iron uptake in the yeast *Saccharomyces cerevisiae* – role of dioxygen and Fe(II), *J. Biol. Chem.*, **273**, 7628-7636.

202. J.W. Kronstad, G. Hu, W.H. Jung, (2013) An encapsulation of iron homeostasis and virulence in*Cryptococcus neoformans, Trends in Microbiol*., **21**, 457-465.

203. Blanc B, Gerez C, Ollagnier de Choudens S (2015) Assembly of Fe/S proteins in bacterial systems: biochemistry of the bacterial ISC system. *Biochim. Biophys. Acta* 1853: 1436-1447.

204. Outten FW (2015) Recent advances in the Suf Fe-S cluster biogenesis pathway: Beyond the Proteobacteria. *Biochim. Biophys. Acta* 1853, 1464-1469.

205. Outten FW, &Theil EC (2009) Iron-Based Redox Switches in Biology. *Antioxidants and Redox Signaling* 11, 1029-1046.

206. Mettert EL &Kiley PJ (2015) How is Fe-S cluster formation regulated? *Ann. Rev. Microbiol.* 69, 505-526.

207. Fillat MF (2014) The FUR (ferric uptake regulator) superfamily: Diversity and versatility of key transcriptional regulators. *Archives Biochemistry Biophysics* 546, 41-52.

208. Noinaj N, Guillier M, Barnard TJ, & Buchanan SK (2010) TonB-Dependent Transporters: Regulation, Structure, and Function. *Ann. Rev. Microbiol*. 64, 43-60.

209. Braun V. (2003) Iron uptake by Escherichia coli. *Frontiers in Biosciences* 8, s1409-1421

210. McHugh JP, Rodrıguez-Quinones R, Abdul-Tehrani H, Svistunenko DA, Poole RK, Cooper CE, Andrews SC (2003) Global Iron-dependent Gene

Regulation in *Escherichia coli*: A new mechanism for iron homeostasis. *J. Biol. Chem*. 278, 29478-29486.

211. Hamza I, Qi ZH, King ND, O'Brian MR (2000) Fur-independent regulation of iron metabolism by Irr in *Bradyrhizobium japonicum*. *Microbiology-SGM* 146, 669-676.

212. Benov L, & Sequeira F (2003) *Escherichia coli* Delta fur mutant displays low HPII catalase activity in stationary phase. *Redox Report* 8, 379-383.

213. Zheng M, Doan B, Schneider TD, & Storz G (1999) OxyR and SoxRS Regulation of fur. *J. Bacteriol.* 181, 4639-4643.

214. Jacques, J-F, Jang SJ, Prevost K et al. (2006) RyhB small RNA modulates the free intracellular iron pool and is essential for normal growth during iron limitation in *Escherichia coli*. *Mol. Microbiol*. 62, 1181-1190.

215. Woodmansee AN, & Imlay JA (2002) Quantitation of intracellular free iron by electron paramagnetic resonance spectroscopy. *Methods in Enzymology* 349, 3-9.

216. Ma Z, Faulkner MJ, Helmann JD (2012) Origins of specificity and cross-talk in metal ion sensing by Bacillus subtilis Fur. *Mol. Microbiol*. 86, 1144-1155.

217. Bagg A, & Neilands JB (1987) Ferric Uptake Regulation Protein Acts as a Repressor, Employing Iron(II) as a cofactor to bind the operator of an iron transport operon in *Escherichia coli*. Biochemistry, 26, 5471-5477.

218. Hamed, MY, Neilands JB & Huynh V (1993) Binding of the Ferric Uptake Regulation Repressor Protein (Fur) to Mn(II), Fe(II), Co(II), and Cu(II)

ions as co-repressors: electronic absorption, equilibrium, and ^{57}Fe Mössbauer studies. *J. Inorg. Biochem.* 15, 193-210.

219. Mills SA, Marletta MA (2005) Metal binding characteristics and role of iron oxidation in the ferric uptake regulator from *Escherichia coli*. *Biochemistry* 44, 13553-13559.

220. Papaefthymiou GC (2010) The Mössbauer and magnetic properties of ferritin cores. *Biochim. Biophys. Acta* 1800, 886-897.

221. Paalme T, Elken R, Kahru A, Vanatalu K, & Vilu R. (1997) The growth rate control in *Escherichia coli* at near to maximum growth rates: The A-stat approach. Antoine Van Leeuwenhoek International *Journal of General and Molecular Microbiology* 71: 217-230.

222. Popescu CV, Bates, DM, Beinert H, Münck, E. & Kiley, PJ (1998) Mössbauer spectroscopy as a tool for the study of activation/inactivation of the transcription regulator FNR in whole cells of Escherichia coli. *Proc. Natl., Acad. Sci USA* 95, 13431-13435.

223. Benda R, Bui BTS, Schünemann V, Florentin D, Marquet A, & Trautwein AX (2002) Iron-Sulfur Clusters of Biotin Synthase In Vivo: A Mössbauer Study. *Biochemistry* 41, 15000-15006

224. Jhurry ND, Chakrabarti M, McCormick SP, Holmes-Hampton GP, & Lindahl PA (2012) Biophysical Investigation of the Ironome of Human Jurkat Cells and Mitochondria *Biochemistry*, 51, 5276-5284.

225. Waldron KJ; Rutherford JC; Ford D; Robinson NJ (2009) Metalloproteins and metal sensing. *Nature* 460, 823-830.

226. Andrews, SC; Robinson, AK; Rodriguez-Quinones, F (2003) Bacterial iron homeostasis *FEMS Microbiol. Rev*. 27, 215-237

227. Dziuba N., Hardy J. & Lindahl PA (2018) Low-molecular-mass iron in healthy blood plasma is not predominately ferric citrate. *Metallomics*, in press.

228. Reisner E, Telser, J, Lippard SJ (2007) A Planar Carboxylate-Rich Tetrairon(II) Complex and Its Conversion to Linear Triiron(II) and Paddlewheel Diiron(II) Complexes. *Inorg. Chem*. 2007, 46, 10754-10770

229. Reiff WM, Frankel RB, Abeledo CR (1973) Orbital ground state inversion in [Fe(H2O)6](ClO4)2. *Chem. Phys. Lett* 22, 124-126.

230. Clemente-Juan JM, Mackiewicz C, Verelst M, Dahan F, Bousseksou A, Sanakis Y, & Tuchagues JP (2002) Synthesis, structure, and magnetic properties of tetranuclear cubane-like and chain-like iron(II) complexes based on the N4O pentadentate dinucleating ligand 1,5-Bis[2-pyridylmethyl)amino]pentan-3-ol. *Inorg. Chem*. 41, 1478-1491.

231. Lemercier G, Mulliez E, Brouca-Cabarrecq C, Dahan F, & Tuchagues JP (2004) Iron(II) Carboxylate Complexes Based on a Tetraimidazole Ligand as Models of the Photosynthetic Non-Heme Ferrous Sites: Synthesis, Crystal Structure, and Mössbauer and Magnetic Studies. *Inorg. Chem*. 43, 2105-2113

232. Guerra AJ and Giedroc DP (2012) Metal site occupancy and allosteric switching in bacterial metal sensor proteins. *Archives Biochem. Biophys*. 519, 210-222

233. Baichoo N, Wang T, Ye R, Helmann JD (2002) Global analysis of the *Bacillus subtilis* Fur regulon and the iron starvation stimulon. *Mol. Microbiol*. 45, 1613-1629.

234. Stephani K, Weichart D, Hengge R (2003). Dynamic control of Dps protein levels by ClpXP and ClpAP proteases in *Escherichia coli*. *Mol Microbiol*. 49,1605-14.

235. Lane N (2014) Bioenergetic constraints on the evolution of complex life. *Cold Spring Harb. Persp. Biol.* 6,a015982. 1-18.

236. Carvalho, DS; Andrade, RFS; Pinho, STR; Goes-Neto, A; Lobao, TCP; Bomfim, GC; El-Hani, CN (2015) What are the Evolutionary Origins of Mitochondria? A Complex Network Approach. *PLOS ONE*; 10, Article e0134988

237. Degli Esposti, M; Cortez, D; Lozano, L; Rasmussen, S; Nielsen, HB; Martinez Romero, E (2016) Alpha proteobacterial ancestry of the [Fe-Fe]-hydrogenases in anaerobic eukaryotes *Biology Direct* 11: Article 34;

238. Tachezy, J, Sanchez, LB, and Muller M. (2001) Mitochondrial type iron-sulfur cluster assembly in the amitochondriate eukaryotes *Trichomonas vaginalis* and *Giardia intestinalis*, as indicated by the phylogeny of IscS. *Mol. Biol. Evol*. 18: 1919-1928.

239. Poole, RK (1994) “Oxygen reactions with bacterial oxidases and globins: binding, reduction and regulation” *Antonie van Leeuwenhoek* 65: 289-310.

240. Al-Attar, S. & de Vries, S (2013) Energy transduction by respiratory metallo-enzymes: From molecular mechanism to cell physiology. *Coord. Chem. Rev.* 257: 64–80.

241. Lopez-Torrejon G., Jimenez-Vicente E., Buesa, J.M., Hernandez, J.A., Verma, H.K., and L.M. Rubio (2016) Expression of a functional oxygen-labile nitrogenase component in the mitochondrial matrix of aerobically grown yeast. *Nature Commun*. 7: article 11426

242. Kadir FH, Read NM, Dickson DP, Greenwood C, Thompson A, Moore GR (1991) Mössbauer spectroscopic studies of iron in *Pseudomonas Ariginosa*. *J. Inorg Biochem* 43: 753–758

243. Dickson DPE; Rottem S. (1979) Mössbauer spectroscopic studies of iron in *Proteus mirabilis Eur. J. Biochem*. 101: 291-295.

244. Boughammoura A; Matzanke BF; Bottger L; Reverchon S; Lesuisse E; Expert D; Franza T (2008) Differential Role of Ferritins in Iron Metabolism and Virulence of the Plant-Pathogenic Bacterium *Erwinia chrysanthemi 3937 J. Bacteriol*. 190: 1518–1530

245. Galvez, N., Fernandez, B., Sanchez, P, Cuesta R, Ceolın M, Clemente-Leon, M, Trasobares, S, Lopez-Haro M., Calvino JJ, Stephan O, and Domınguez-Vera, J.M. (2008) *J. Am. Chem. Soc*. 130, 8062-8068.

246. Unden G., Becker S., Bongaerts J, Holighaus G, Schirawski J, and Six S. (1995) 02-Sensing and O_2-dependent gene regulation in facultatively anaerobic bacteria. *Arch. Microbiol.* 164: 81-90.

247. Arras T, Schirawski J, and Unden G. (1998) Availability of O_2 as a substrate in the cytoplasm of bacteria under aerobic and microaerobic conditions. *J. Bacteriol*. 180: 2133-2136.

248. Datsenko KA, Wanner BL. (2000) One-step inactivation of chromosomal genes in *Escherichia coli* K-12 using PCR products. *Proc Natl Acad Sci U S A.* 97, 640-5.

249. Sanchis-Gomar, F., Perez-Quilis, C., Leischik, R., and Lucia, A. (2016) Epidemiology of coronary heart disease and acute coronary syndrome. *Ann. Transl. Med.* 4, 256

250. Theil, E. C., Tosha, T., and Behera, R. K. (2016) Solving biology's iron chemistry problem with ferritin nanocages. *Acc. Chem. Res.* 49, 784–791

251. Ferreira, C., Bucchini, D., Martin, M. E., Levi, S., Arosio, P., Grandchamp, B., and Beaumont, C. (2000) Early embryonic lethality of H ferritin gene deletion in mice. *J. Biol. Chem.* 275, 3021–3024

252. Ahmad, S., Moriconi, F., Naz, N., Sultan, S., Sheikh, N., Ramadori, G., and Malik, I. A. (2013) Ferritin L and ferritinHare differentially located within hepatic and extra hepatic organs under physiological and acute phase conditions. *Int. J. Clin. Exp. Pathol.* 6, 622–629

253. Kistler, M., Even, A., Wagner, S., Becker, C., Darshan, D., Vanoaica, L., Kuhn, L. C., and Schu ¨mann, K. (2014) Fe-59-distribution in conditional ferritin-H-deleted mice. *Exp. Hematol*. 42, 59–69

254. Omiya, S., Hikoso, S., Imanishi, Y., Saito, A., Yamaguchi, O., Takeda, T., Mizote, I., Oka, T., Taneike, M., Nakano, Y., Matsumura, Y., Nishida, K., Sawa, Y., Hori, M., and Otsu, K. (2009) Downregulation of ferritin heavy chain increases labile iron pool, oxidative stress and cell death in car- diomyocytes. *J. Mol. Cell. Cardiol.* 46, 59–66

255. Santambrogio, P., Biasiotto, G., Sanvito, F., Olivieri, S., Arosio, P., and Levi, S. (2007) Mitochondrial ferritin expression in adult mouse tissues. *J. Histochem. Cytochem.* 55, 1129–1137

256. Campanella, A., Rovelli, E., Santambrogio, P., Cozzi, A., Taroni, F., and Levi, S. (2009) Mitochondrial ferritin limits oxidative damage regulating mitochondrial iron availability: hypothesis for a protective role in Friedreich ataxia. *Hum. Mol. Genet.* 18, 1–11

257. Kohgo, Y., Ikuta, K., Ohtake, T., Torimoto, Y., and Kato, J. (2008) Body iron metabolism and pathophysiology of iron overload. *Int. J. Hematol.* 88, 7–15

258. Nam, H., Wang, C. Y., Zhang, L., Zhang, W., Hojyo, S., Fukada, T., and Knutson, M. D. (2013) ZIP14 and DMT1 in the liver, pancreas, and heart are differentially regulated by iron deficiency and overload: implications for tissue iron uptake in iron-related disorders. *Haematologica* 98, 1049–1057

259. Chua-anusorn, W., Tran, K. C., Webb, J., Macey, D. J., and St. Pierre, T. G. (2000) Chemical speciation of iron deposits in thalassemic heart tissue. *Inorg. Chim. Acta* 300, 932–936

260. Neves, J. V., Olsson, I. A., Porto, G., and Rodrigues, P. N. (2010) Hemochromatosis and pregnancy: iron stores in the HFE-/- mouse are not reduced by multiple pregnancies. *Am. J. Physiol. Gastrointest. Liver Physiol.* 298, G525-G529

261. Gutierrez, L., Quintana, C., Patino, C., Bueno, J., Coppin, H., Roth, M. P., and Lazaro, F. J. (2009) Iron speciation study in HFE knockout mice tissues: magnetic and ultrastructural characterization. *Biochim. Biophys. Acta* 1792, 541–547

262. Subramaniam, V. N., McDonald, C. J., Ostini, L., Lusby, P. E., Wockner, L. F., Ramm, G. A., and Wallace, D. F. (2012) Hepatic iron deposition does not predict iron loading in mouse models of hereditary hemochromatosis. *Am. J. Pathol*. 181, 1173–1179

263. St. Pierre, T. G., Tran, K. C., Webb, J., Macey, D. J., Pootrakul, P., and Dickson, D. P. (1992) Core structures of haemosiderins deposited in various organs in β-thalassemia hemoglobin E disease. *Hyperfine Interact*. 71, 1279–1282

264. Bell, S. H., Weir, M. P., Dickson, D. P., Gibson, J. F., Sharp, G. A., and Peters, T. J. (1984) Mossbauer spectroscopic studies of human haemo- siderin and ferritin. *Biochim. Biophys. Acta* 787, 227–236

265. Webb, J., Macey, D. J., Chua-anusorn, W., St. Pierre, T. G., Brooker, L. R., Rahman, I., and Noller, B. (1999) Iron biominerals in medicine and the environment. *Coord. Chem. Rev.* 190–192, 1199–1215

266. St Pierre, T. G., Tran, K. C., Webb, J., Macey, D. J., Heywood, B. R., Sparks, N. H., Wade, V. J., Mann, S., and Pootrakul, P. (1991) Organ-specific crystalline structures of ferritin cores in β-thalassemia hemoglobin *E*. *Biol.Met*. 4, 162–165

267. Kaufman, K. S., Papaefthymiou, G. C., Frankel, R. B., and Rosenthal, A. (1980) Nature of iron deposits on the cardiac walls in β-thalassemia by Mossbauer spectroscopy. *Biochim. Biophys. Acta* 629, 522–529

268. Perdomini, M., Belbellaa, B., Monassier, L., Reutenauer, L., Messaddeq, N., Cartier, N., Crystal, R. G., Aubourg, P., and Puccio, H. (2014) Prevention and reversal of severe mitochondrial cardiomyopathy by gene therapy in a mouse model of Friedreich's ataxia. *Nat. Med.* 20, 542–547

269. Michael, S., Petrocine, S. V., Qian, J., Lamarche, J. B., Knutson, M. D., Garrick, M. D., and Koeppen, A. H. (2006) Iron and iron-responsive pro- teins in the cardiomyopathy of Friedreich's ataxia. *Cerebellum* 5, 257–267

270. Payne, R. M. (2011) The heart in Friedreich's ataxia: basic findings and clinical implications. *Prog Pediatr. Cardiol.* 31, 103–109

271. Whitnall, M., Suryo Rahmanto, Y., Huang, M. L., Saletta, F., Lok, H. C., Gutierrez, L., Lazaro, F. J., Fleming, A. J., St Pierre, T. G., Mikhael, M. R., Ponka, P., and Richardson, D. R. (2012) Identification of nonferritin mito-

chondrial iron deposits in a mouse model of Friedreich ataxia. *Proc. Natl. Acad. Sci. U.S.A.*, 109, 20590–20595

272. Pousset, F., Legrand, L., Monin, M. L., Ewenczyk, C., Charles, P., Komajda, M., Brice, A., Pandolfo, M., Isnard, R., Tezenas du Montcel, S., and Durr, A. (2015) A 22-year follow-up study of long-term cardiac outcome and predictors of survival in Friedreich ataxia. *JAMA Neurol.* 72, 1334–1341

273. Whitnall, M., Suryo Rahmanto, Y., Sutak, R., Xu, X., Becker, E. M., Mikhael, M. R., Ponka, P., and Richardson, D. R. (2008) TheMCKmouse heart model of Friedreich's ataxia: Alterations in iron-regulated proteins and cardiac hypertrophy are limited by iron chelation. *Proc. Natl. Acad. Sci. U.S.A.* 105, 9757–9762

274. Puccio, H., Simon, D., Cossee, M., Criqui-Filipe, P., Tiziano, F., Melki, J., Hindelang, C., Matyas, R., Rustin, P., and Koenig,M.(2001) Mousemodels for Friedreich ataxia exhibit cardiomyopathy, sensory nerve defect and Fe-S enzyme deficiency followed by intramitochondrial iron deposits. *Nat. Genet.* 27, 181–186

275. Sutak, R., Xu, X., Whitnall, M., Kashem,M.A., Vyoral, D., and Richardson, D. R. (2008) Proteomic analysis of hearts from frataxin knockout mice: marked rearrangement of energy metabolism, a response to cellular stress and altered expression of proteins involved in cell structure, motility and metabolism. *Proteomics* 8, 1731–1741

276. Zhao, N., Sun, Z., Mao, Y., Hang, P., Jiang, X., Sun, L., Zhao, J., and Du, Z. (2010) Myocardial iron metabolism in the regulation of cardiovascular diseases in rats. *Cell. Physiol. Biochem.* 25, 587–594

277. Huang, M. L., Becker, E. M., Whitnall, M., Suryo Rahmanto, Y., Ponka, P., and Richardson, D. R. (2009) Elucidation of the mechanism of mitochondrial iron loading in Friedreich's ataxia by analysis of a mouse mutant. *Proc. Natl. Acad. Sci. U.S.A.* 106, 16381–16386

278. Schulz, T. J., Westermann, D., Isken, F., Voigt, A., Laube, B., Thierbach, R., Kuhlow, D., Zarse, K., Schomburg, L., Pfeiffer, A. F., Tschope, C., and Ristow, M. (2010) Activation of mitochondrial energy metabolism pro- tects against cardiac failure. *Aging* 2, 843–853

279. Elas, M., Bielanska, J., Pustelny, K., Plonka, P. M., Drelicharz, L., Skorka, T., Tyrankiewicz, U., Wozniak, M., Heinze-Paluchowska, S., Walski, M.,Wo- jnar, L., Fortin, D., Ventura-Clapier, R., and Chlopicki, S. (2008) Detection of mitochondrial dysfunction by EPR technique in mouse model of dilated cardiomyopathy. *Free Rad. Biol. Med.* 45, 321–328

280. Lesnefsky, E. J., Gudz, T. I., Migita, C. T., Ikeda-Saito, M., Hassan, M. O., Turkaly, P. J., and Hoppel, C. L. (2001) Ischemic injury to mitochondrial electron transport in the aging heart: damage to the iron-sulfur protein subunit of electron transport complex 3+. *Arch. Biochem. Biophys.* 385, 117–128

281. Zhang, D. L., Ghosh, M. C., and Rouault, T. A. (2014) The physiological functions of iron regulatory proteins in iron homeostasis: an update. *Front. Pharmacol*. 5, 124

282. Galy, B., Ferring, D., Minana, B., Bell, O., Janser, H. G., Muckenthaler, M., Schumann, K., and Hentze, M. W. (2005) Altered body iron distribution and microcytosis in mice deficient in iron regulatory protein 2 (IRP2). *Blood* 106, 2580–2589

283. Zumbrennen-Bullough, K. B., Becker, L., Garrett, L., Ho ¨lter, S. M., Calzada-Wack, J., Mossbrugger, I., Quintanilla-Fend, L., Racz, I., Rathkolb, B., Klopstock, T., Wurst, W., Zimmer, A., Wolf, E., Fuchs, H., Gailus-Durner, V., et al. (2014) Abnormal brain iron metabolism in IRP2 deficient mice is associated with mild neurological and behavioral impairments. *PLOS ONE* 9, e98072

284. Chakrabarti, M., Barlas, M. N., McCormick, S. P., Lindahl, L. S., and Lin- dahl, P. A. (2015) Kinetic of iron import into developing mouse organs determined by a pup-swapping method. *J. Biol. Chem.* 290, 520–528

285. Chua-anusorn, W, St. Pierre, T. G., Webb, J., Macey, D. J., Yansukon P., and Pootrakul, P. (1993) Mossbauer spectroscopic study of the forms of iron in normal liver and spleen tissue. *Hyperfine Interact.* 91, 905–910

286. Ramos, E., Ruchala, P., Goodnough, J. B., Kautz, L., Preza, G. C., Nem- eth, E., and Ganz, T. (2012) Minihepcidins prevent iron overload in a hepcidin-deficient mouse model of severe hemochromatosis. *Blood* 120, 3829–3836

287. Truksa, J., Gelbart, T., Peng, H., Beutler, E., Beutler, B., and Lee, P. (2009) Suppression of the hepcidin-encoding gene Hamp permits iron overload in mice lacking both hemojuvelin and matriptase-2/TMPRSS6. Br. *J. Haematol*. 147, 571–581

288. Wofford, J. D., Park, J., McCormick, S. P., Chakrabarti, M., & Lindahl, P. A. (2016). Ferric ions accumulate in the walls of metabolically inactivating Saccharomyces cerevisiae cells and are reductively mobilized during reactivation. *Metallomics, 8*(7), 692–708.

289. Ni, F.; Lee, C. C.; Hwang, C. S.; Hu, Y.; Ribbe, M. W.; Mckenna, C. E. (2013) Reduction of fluorinated cyclopropene by nitrogenase. *J. Am. Chem. Soc.* 135, 10346−10352.

290. Rebelein, J. G.; Hu, Y.; Ribbe, M. W. Differential reduction of CO2 by molybdenum and vanadium nitrogenases. (2014*) Angew. Chem., Int. Ed.*, 53, 11543−11546.

291. Spatzal, T.; Aksoyoglu, M.; Zhang, L.; Andrade, S. L. A.; Schleicher, E.; Weber, S.; Rees, D. C.; Einsle, O. (2011) Evidence for interstitial carbon in nitrogenase FeMo cofactor. *Science*, 334, 940.

292. Lancaster, K. M.; Roemelt, M.; Ettenhuber, P.; Hu, Y.; Ribbe, M. W.; Neese, F.; Bergmann, U.; Debeer, S. (2011) X-ray emission spectroscopy evidences a central carbon in the nitrogenase iron- molybdenum cofactor. *Science*, 334, 974−977.

293. Davis, J. H.; Beno, M. A.; Williams, J. M.; Zimmie, J.; Tachikawa, M.; Muetterties, E. L. (1981) Structure and chemistry of a metal cluster with a 4-coordinate carbide carbon-atom. *Proc. Natl. Acad. Sci. U. S. A.*, 78, 668−671.

294. Takemoto, S.; Matsuzaka, H. (2012) Recent advances in the chemistry of ruthenium carbido complexes. *Coord. Chem. Rev.*, 256, 574−588.

295. Muetterties, E. L.; Krause, M. J. (1983) Catalysis by molecular-metal complexes. *Angew. Chem., Int. Ed. Engl.*, 22, 135−148.

296. Čorić, I.; Holland, P. L. (2016) Insight into the iron−molybdenum cofactor of nitrogenase from synthetic iron complexes with sulfur, carbon, and hydride ligands. *J. Am. Chem. Soc.*, 138, 7200−7211.

297. Lopatin, V. E.; Varnek, V. A.; Bel'skii, V. K. (2002) Mössbauer spectroscopy study of the composition of carbido carbonyl clusters. *J. Struct. Chem.* 43, 608−614.

298. Shechter, H.; Ron, M. Niedzwiedz. (1966) Mössbauer spectrometer calibration using 57Fe enriched metallic iron. *Nucl. Instrum. Methods* 44, 268−272.

299. Bernhardt, E.; Bley, B.; Wartchow, R.; Willner, H.; Bill, E.; Kuhn, P.; Sham, I. H. T.; Bodenbinder, M.; Bröchler, R.; Aubke, F. (1999) Hexakis(carbonyl)iron(II)undecafluorodiantimonate(V), [Fe(CO)6]- [Sb2F11]2, and hexafluoroantimonate(V), [Fe(CO)6][SbF6]2, their syntheses, and spectroscopic and structural characterization by single crystal X-ray diffraction and normal coordinate analysis. *J. Am. Chem. Soc.* 121, 7188−7200.

300. Site 4 exhibits a quadrupole doublet (the high-energy line is at 3 mm s−1 at 0 T in Figure 7) with parameters typical of a high-spin Fe(II) ion with predominantly O/N ligand. The presence of this site is difficult to rationalize because the cluster is dominated by carbonyl ligands, which generally do not support such high oxidation states, and certainly not in high-spin configurations. The Fe(II) octahedral carbonyl complex [Fe(CO)6]2+ has been reported, but in this case the formally Fe(II) ion is low-spin and δ (−0.003 mm s−1) is far lower than that for site 4. Another indication that site 4 was an impurity was that the high-energy line of the site 4 doublet was substantially broader than the other spectral lines associated with the cluster

301. Que, L. (2000) Aspects of 57Fe Mössbauer spectroscopy. Physical Methods in Bioinorganic Chemistry; University Science Books: Sausalito, CA, pp 287−319.

302. Scott, A. D.; Pelmenschikov, V.; Guo, Y.; Yan, L.; Wang, H.; George, S. J.; Dapper, C. H.; Newton, W. E.; Yoda, Y.; Tanaka, Y.; Cramer, S. P. (2014) Structural characterization of CO-inhibited Mo- nitrogenase by combined application of nuclear resonance vibrational spectroscopy, extended X-ray absorption fine structure, and density functional theory: New insights into the effects of CO binding and the role of the interstitial atom. *J. Am. Chem. Soc.*, 136, 15942− 15954.

303. Creutz, S. E.; Peters, J. C. (2014) Catalytic reduction of N2 to NH3 by an Fe-N2 complex featuring a C-atom anchor. *J. Am. Chem. Soc.*, 136, 1105−1115.

304. Rao, L.; Xu, X.; Adamo, C. (2016) Theoretical investigation on the role of the central carbon atom and close protein environment on the nitrogen reduction in Mo nitrogenase. *ACS Catal.*, 6, 1567− 1577.

305. Danyal, K.; Dean, D. R.; Hoffman, B. M.; Seefeldt, L. C. (2011) Electron transfer within nitrogenase: Evidence for a deficit-spending mechanism. *Biochemistry*, 50, 9255−9263.

APPENDIX A

MÖSSBAUER SPECTRA OF MOUSE HEARTS REVEAL AGE-DEPENDENT CHANGES IN MITOCHONDRIAL AND FERRITIN IRON LEVELS*

Summary

Cardiac function requires continuous high levels of energy, and so iron, a critical player in mitochondrial respiration, is an important component of the heart. Hearts from ^{57}Fe-enriched mice were evaluated by Mössbauer spectroscopy. Spectra consisted of a sextet and two quadrupole doublets. One doublet was due to residual blood, whereas the other was due to $[Fe_4S_4]^{2+}$ clusters and low-spin Fe^{2+} hemes, most of which were associated with mitochondrial respiration. The sextet was due to ferritin; there was no evidence of hemosiderin, a ferritin decomposition product. Iron from ferritin was nearly absent in young hearts, but increased steadily with age. EPR spectra exhibited signals similar to those of brain, liver, and human cells. No age-dependent EPR trends were apparent. Hearts from *HFE*$^{-/-}$ mice with hemochromatosis contained slightly more iron overall than controls, including more ferritin and less mitochondrial iron; these differences typify slightly older hearts, perhaps reflecting the burden due to this disease. *HFE*$^{-/-}$ livers were overloaded with ferritin but had low mitochondrial iron levels. *IRP2*$^{-/-}$ hearts contained less ferritin than controls but normal levels of

---

* This work was originally published in the Journal of Biological Chemistry. Joshua D. Wofford, Mrinmoy Chakrabarti, and Paul A. Lindahl, Mössbauer Spectra of Mouse Hearts Reveal Age-Dependent Changes in Mitochondrial and Ferritin Iron Levels, 2017, Volume 292, 5546-5554, © The American Society for Biochemistry and Molecular Biology

mitochondrial iron. Hearts of young mice born to an iron-deficient mother contained normal levels of mitochondrial iron and no ferritin; the heart from the mother contained low ferritin and normal levels of mitochondrial iron. High-spin Fe^{2+} ions were nearly undetectable in heart samples; these were evident in brains, livers, and human cells. Previous Mössbauer spectra of unenriched diseased human hearts lacked mitochondrial and blood doublets and included hemosiderin features. This suggests degradation of iron-containing species during sample preparation.

Introduction

From an early stage of fetal development until the end of life, the heart functions unceasingly to pump blood throughout the body. This requires a high and sustained level of metabolic energy unrivaled by any other organ except perhaps the brain. Mitochondria, the organelle responsible for generating most of the chemical energy in cells, serve a critical role in cardiac function. Improving our understanding of cardiac physiology is important because heart disease is *the* most common cause of death in the Western world **(249)**. The preponderance of iron-containing centers in respiration-related mitochondrial proteins makes this metal a major player in cardiac physiology. Much of the iron that enters cardiomyocytes is used to build iron-sulfur clusters (ISCs) **(251)** and heme centers many of which are installed into mitochondrial respiratory complexes and respiration-related proteins. Excess cellular iron is generally stored within the core of cytosolic ferritin, a spherically shaped protein complex composed of variable ratios of H- and L-subunits **(250)**. H-ferritin is especially important in cardiac

function **(251,252)**. Besides storing iron, H-ferritin helps cells manage the metal **(253)**. H-ferritin levels are significantly lower in mice hearts after a myocardial infarct **(254)**. Such hearts contain spotty iron deposits and suffer from excessive oxidative stress. Deleting H-ferritin reduces the viability of cardiomyocytes and increases these deposits **(254)**. Excessive iron and increased oxidative stress damage cardiomyocytes and contribute to heart failure **(254)**. Mitochondrial ferritin (mt-ferritin) is highly expressed in heart mitochondria **(255)**. It functions to sequester Fe^{2+} in mitochondria and thus protect the organelle from iron-dependent oxidative damage **(256)**.

Cardiomyopathy is common in iron-overload diseases such as hereditary hemochromatosis (HH) **(257)**. HH initially impacts the liver, but eventually affects the heart, causing ROS damage especially to mitochondria **(258-260)**. The most common cause of HH is a mutation in the *HFE* gene. $HFE^{-/-}$ mutant livers contain 4–6 times more iron than controls, whereas the iron content of mutant hearts is slightly elevated **(261,262)**. Hemosiderin, a poorly defined iron-loaded breakdown product of ferritin **(263)**, accumulates along with ferritin in mutant livers but not in mutant hearts **(261,262)**. Hemosiderin is found in some iron-overloaded organs **(263-265)**.

Mössbauer (MB) spectroscopy has been used to investigate the iron content of hearts from patients with β-thalassemia, another iron-overload blood disease **(266-268)**. The average iron concentration in the β-thalassemia heart is nearly 3 times higher than normal **(259)**. MB spectra of β-thalassemia heart tissue exhibit features of ferritin, a high-spin Fe^{3+} species, and perhaps hemosiderin **(259,266)**. The control MB spectrum was too noisy to evaluate because the heart was neither overloaded nor enriched in ^{57}Fe.

Individuals with Friedreich's ataxia (FA) develop cardiomyopathy in conjunction with mitochondrial iron accumulation and ROS damage **(269-270)**. FA arises from a deficiency in frataxin, a mitochondrial protein involved in ISC assembly **(271)**. Eighty percent of FA patients die of cardiac disease **(272)**.

Mice in which frataxin was deleted in cardiac muscle exhibited the classical progression of FA **(268,272-274)**. At 7 weeks, mutant mice became deficient in ISCs, and at 9 weeks, the iron concentration in mutant hearts increased and respiratory activity declined **(275)**. At 10 weeks, the concentration of iron in mutant hearts contained nearly 10 times more iron than WT hearts, which contained about 1.3 mM iron **(274,276)**. The excess iron in the mutant cells flowed into mitochondria where it aggregated and generated ROS **(271,273,275,277)**.

MB spectroscopy was used to characterize the iron aggregates in hearts of 9-week frataxin KO mice **(271)**. The spectrum was noisy because mice were not enriched in ^{57}Fe. It exhibited a single quadrupole doublet due to Fe^{3+} oxyhydroxide nanoparticles **(271)**. The low-temperature MB spectrum of the liver from the same frataxin KO mice was dominated by a sextet due to ferritin **(259,271)**.

Cardiac failure is the most prevalent cause of death in the elderly and is commonly associated with impaired energy homeostasis **(278,279)**. Aged mitochondria often have respiratory defects **(280)**. Ischemia is associated with a decline in the EPR signal due to the Rieske ISC protein associated with respiratory complex 3+ **(280)**.

Iron-related proteins in mammals are primarily regulated by the IRP1/IRP2 system **(281)**. Under iron-deficient cellular conditions, IRP1/2 bind mRNA transcripts of

ferritin and TfR1. Doing so increases TfR1 expression and decrease ferritin levels. *IRP2*$^{-/-}$ mice accumulate large amounts of iron in the liver **(281,38,282,283)**, whereas *IRP2*$^{-/-}$ brains contain WT levels of iron and WT MB features **(38)**.

MB spectroscopy is the most powerful spectroscopic tool for probing the iron content of biological materials, but it has not been applied extensively to vertebrate animals **(44)**. MB is relatively insensitive and can only detect ^{57}Fe, which accounts for just 2% of naturally occurring iron. As a result, spectra of unenriched mammalian organs are noisy, even when iron overloaded. Enriching mammals in ^{57}Fe is inconvenient and costly. Nevertheless, we enriched mice with ^{57}Fe for this study. In earlier studies, we used MB spectroscopy to characterize the iron content of brain and liver **(38, 39, 284)**. Here we use MB to probe the iron content of healthy mouse hearts during development. We also investigate hearts from *HFE*$^{-/-}$ mice with hemochromatosis, hearts from *IRP2*$^{-/-}$ mice, and hearts from an iron-deficient mouse and her offspring.

Results

We wanted to characterize the iron content of healthy mammalian hearts at different developmental stages, and used MB spectroscopy as our primary tool. We enriched mice with ^{57}Fe to improve spectral quality. Analyses were augmented by EPR spectroscopy and ICP-MS analysis. Mice were euthanized at different ages and immediately imported into a refrigerated anaerobic glove box where blood was flushed extensively with Ringer's buffer. Hearts and other organs were removed by dissection, and frozen in MB cups for later analysis. Low-field MB spectra were collected on whole

intact hearts from elderly (Fig. 1), young (Fig. 2), and adult (Fig. 3) mice. For each group, multiple spectra are shown to help distinguish sample-to-sample variations from age-dependent changes. Distinguishing this is a challenge for studies like this in which only small numbers of animals can be investigated. After collecting spectra, samples were analyzed for metal concentrations. These results, and the MB parameters used in simulations are compiled in Table 1. EPR spectra were collected (Fig. 4) on different heart samples that had been homogenized and packed into EPR tubes by centrifugation.

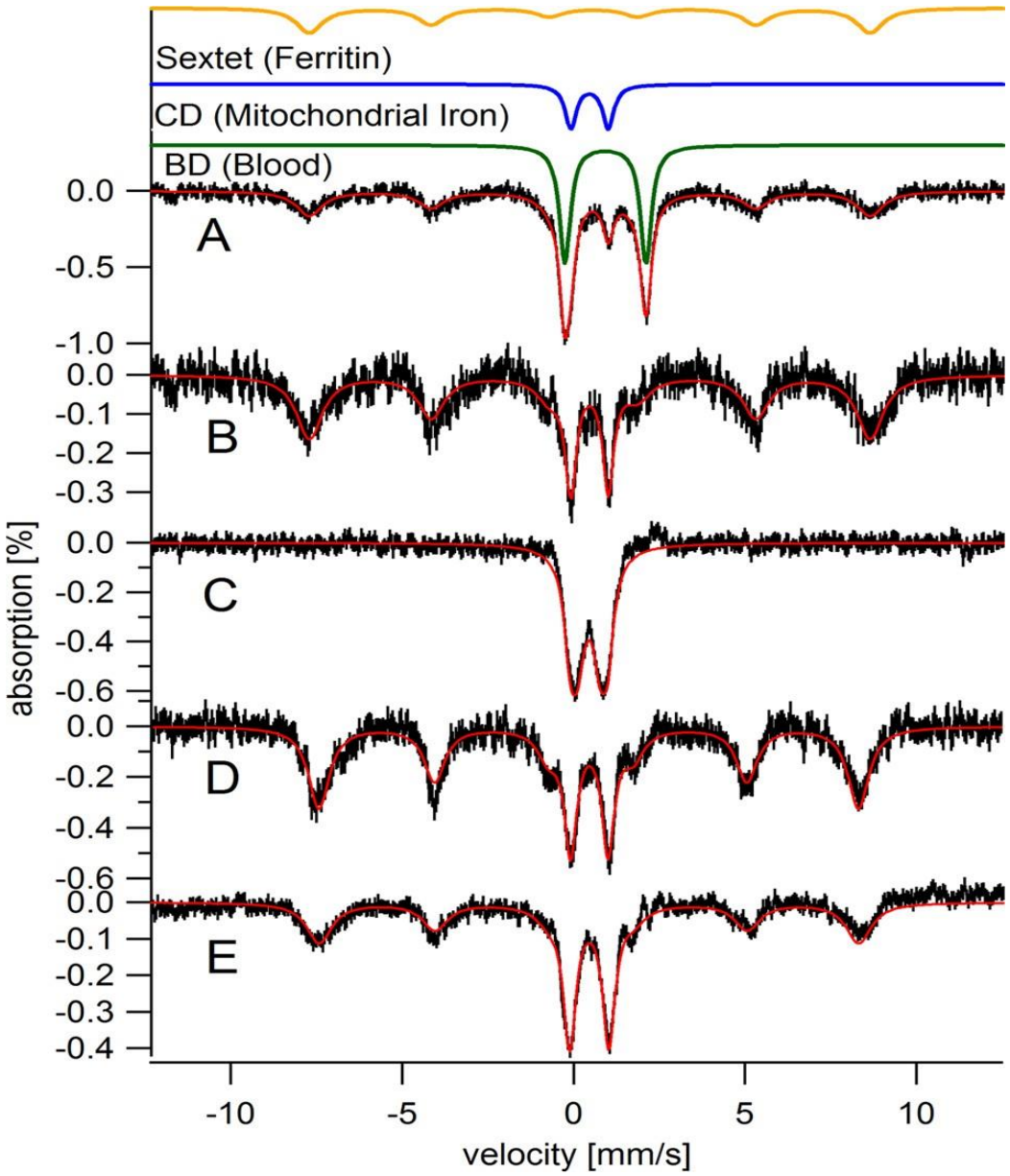

Figure A.1: Mössbauer spectra of hearts from elderly mice. All spectra presented in the text were collected at 5 K except for in *C*, which was collected at 100 K (and in Fig. 5*D*, which was collected at 70 K). In all MB spectra presented in the text, a 0.05 tesla magnetic field was applied parallel to the gamma rays. The *solid red lines* overlaying spectra in all MB figures are simulations using parameters listed in Table 1. *A*, C60, raw spectrum (all other spectra have the blood doublet removed). The *solid green*, *blue*, and *gold lines above* the data are simulations of the blood, CD, and ferritin components, respectively. *B*, C60 with contribution from blood removed; *C*, same as *B* but at 100 K; *D*, C52; *E*, I104.

MB spectra were composed of three major features, including a sextet and two quadrupole doublets (Fig. 1*A*). One doublet had parameters (Table 1) of high-spin Fe^{2+}hemoglobin. This doublet, simulated in *green* in Fig. 1, was assigned to residual blood. This so-called "blood doublet" (BD) was present in all raw spectra. The average relative intensity of the BD was 43%, with a standard deviation of just ±5% (n = 18). To view other spectral features better, we have removed the BD contribution from all spectra (except for that in Fig. 1*A*). The consistent high percentage of iron due to blood in our samples raises doubts that flushing by cardiac puncture is effective in removing blood from the heart itself. Nevertheless, knowing the percent contribution of the BD to the overall intensity of each spectrum and the absolute concentration of iron in each sample allowed us to calculate the concentration of iron within heart cells themselves for the first time. We have already done this for brain and liver; another group has done the same for liver and spleen (40). As such, the iron concentrations listed in Table 1 are probably the most accurate determinations for hearts from iron-sufficient mammals. The average iron concentration in the healthy heart samples (with blood excluded) was 400 ± 200 μM (n = 11), depending on age. The approximate concentration of iron in young, adult, and elderly hearts was 300, 450, and 700 μM, respectively.

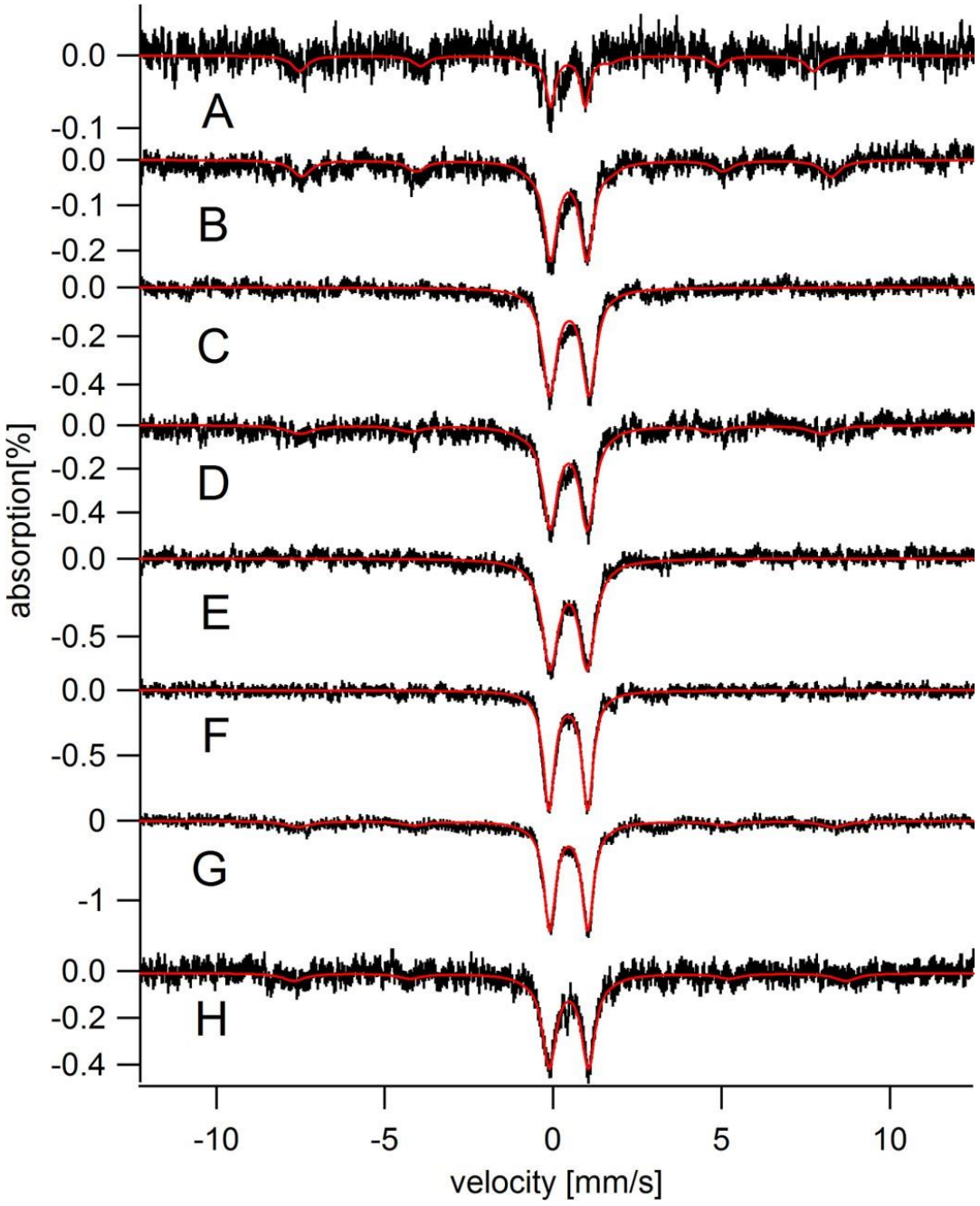

Figure A.2: Mössbauer spectra (5 K) of hearts from young mice. *A*, C00; *B*, C01; *C*, C02a; *D*, C02b; *E*, C03; *F*, C03D; *G*, C04a; *H*, C04b.

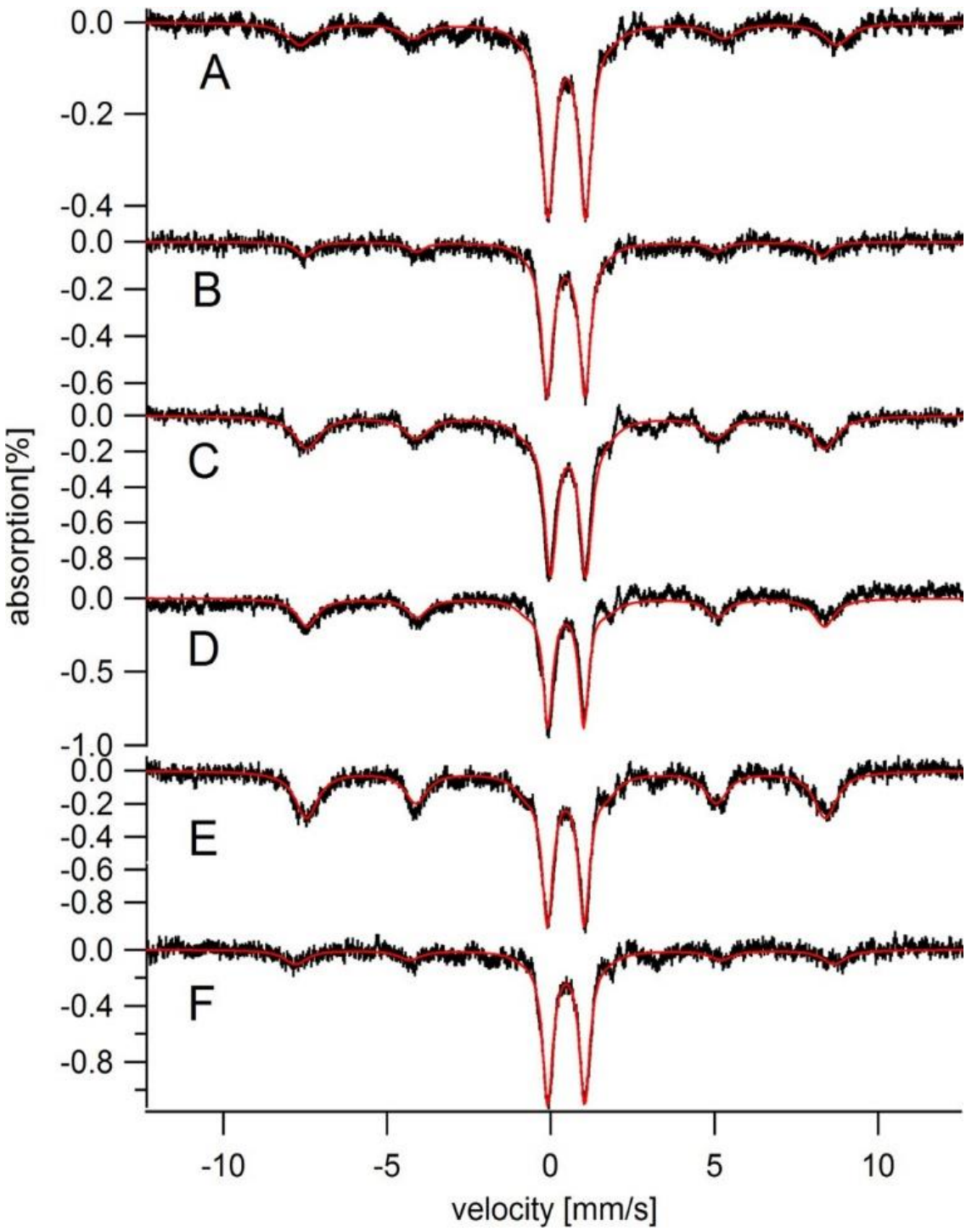

Figure A.3: Mössbauer spectra (5 K) of hearts from adult mice. *A*, C06; *B*, I08; *C*, C16; *D*, C24; *E*, C28; *F*, C28D

We assigned the sextet in heart MB spectra to Fe^{3+} aggregates in ferritin cores. The *gold line* above the data of Fig. 1*A* simulates the ferritin sextet using parameters in Table 1. To assess whether hemosiderin contributed to this absorption, we collected a 100 K spectrum of the C60 heart. The baseline was devoid of sextet features (Fig. 1*C*), suggesting the absence of this degradation product.

The other doublet in MB spectra of hearts, called the "central doublet" or CD, was simulated as the *blue line* in Fig. 1*A* using parameters in Table 1. The CD is due collectively to $[Fe_4S_4]^{2+}$ clusters and low-spin Fe^{2+} hemes; the two types of centers cannot be resolved by MB spectroscopy because they are diamagnetic and have similar δ and ΔE_Q values. The CD dominates the spectrum of mitochondria isolated from brain, liver, and human cells **(38,39,224)**, which allows us to assign this spectral feature to respiration-related complexes in that organelle. $[Fe_4S_4]^{2+}$ clusters and LS Fe^{2+} hemes are undoubtedly present in non-mitochondrial regions of the heart, but they are minor contributors to spectral intensity. We have quantified the intensity of the CD in the spectra of elderly hearts (Fig. 1) and find that it corresponds to 110–200 μM iron.

The CD dominated the MB spectra of young hearts (defined as newborn to 4 weeks) with an intensity that corresponded to 60–220 μM (Fig. 2 and Table 1). The intensity of the ferritin sextet was dramatically lower in spectra of young hearts than in those of elderly hearts; indeed the feature was absent in some spectra of young hearts. Adult hearts (Fig. 3, 6–28 weeks) exhibited even higher concentrations of the CD (220–350 μM iron) and intermediate levels of ferritin (55–320 μM iron).

EPR spectra of packed mouse heart homogenates of different ages are shown in Fig. 4. The g = 2 region consisted of numerous overlapping signals including a g_{ave} = 1.94 signal due to $[Fe_2S_2]^{1+}$ and/or $[Fe_4S_4]^{1+}$ clusters, a g_{ave} = 1.90 signal due to the $[Fe_2S_2]^{1+}$ cluster in the Rieske ISC protein, a radical signal at g = 2.00, and an unassigned resonance at g = 2.16. The same signals were observed in mouse brain and liver homogenates and in mitochondria isolated from these tissues **(38,39)**. No age-dependent EPR trends were apparent.

Table A.1: Metal concentrations in 57Fe-enriched mouse hearts (and livers), and associated Mössbauer parameters Metal concentrations are in μM, calculated by assuming a tissue density of 1.06 g/ml. Masses of hearts are in mg; uncertainties are ~1 mg. Values in parentheses refer to the number of hearts in the sample. If more than 1 heart was used, the mass refers to the average. Entry indicated with bold and italics is the collective mass of 4–7 hearts that had been combined. This mass, on a per-heart basis, is an outlier relative to the other samples. Sample designations C, H, and I refer to C57BL/6, *HFE*-/-, and *IRP2*-/- strains, respectively. The number that follows indicates the age of the mouse in weeks. Samples of the same age are distinguished with a and b. Samples from iron-deficient mice are distinguished by a subscript D. For ICP-MS analysis, each tissue was analyzed in triplicate; reported concentrations are averages; uncertainties are standard deviations. Cobalt and molybdenum concentrations were also determined but no age-dependent trends were apparent; average [Co] and [Mo] (n = 18) were 0.16 ± 0.11 μM and 0.05±0.02μM, respectively. Isomer shifts δ, quadrupole splittingsΔEQ, and line widths Γ (all in mm/s) used in simulations were: central doublet (0.45±0.01, 1.15±0.02, and 0.44±0.07); low-temperature ferritin (-0.10±0.05, 0.44±0.07, and 0.77±0.14) with Heff=490±6 kG; blood (0.91±0.06, 2.30±0.04, and 0.43±0.11); high-temperature ferritin (0.44, 0.70, and 0.55). Mössbauer spectra were calibrated against α-iron foil at room temperature. For convenience, the sum of the percent relative intensities for the three major MB components were forced to 100%; however, 10–15% of the actual spectral intensity cannot be accounted for by these three components.

Sample	Mass of Heart (mg)	[^{57}Fe]	[Fe_{tot}]	[Cu]	[Mn]	[Zn]	Central Doublet (%; μM)	Ferritin (%; μM)	Blood (%; μM)
C00 (1 day)	65 (1)	240 ± 3	300 ± 8	10 ± 1	1.6 ± 0.2	31 ± 7	20; 60	20; 60	60; 180
C01	14 (7)	350 ± 7	470 ± 10	33 ± 1	4.9 ± 0.1	43 ± 1	38; 180	17; 80	45; 210
C02a	180 (1)	240 ± 9	290 ± 10	12 ± 0.4	2.3 ± 0.1	26 ± 1	53; 150	00; 00	47; 140
C02b	59 (2)	170 ± 3	240 ± 9	19 ± 2	3.3 ± 0.1	26 ± 1	46; 110	13; 30	41; 100
C03	ND	ND	ND	ND	ND	ND	50; ND	0; ND	50; ND

Table A.1 Continued

Sample	Mass of Heart (mg)	[^{57}Fe]	[Fe_{tot}]	[Cu]	[Mn]	[Zn]	Central Doublet (%; µM)	Ferritin (%; µM)	Blood (%; µM)
C04a	98 (4)	600 ± 8	710 ± 9	29 ± 0.3	8.9 ± 0.2	46 ± 1	40; 280	10; 70	50; 360
C04b	61 (2)	570 ± 10	610 ± 10	48 ± 1	11 ± 0.2	45 ± 1	44; 270	12; 70	44; 270
C06	140 (1)	620 ± 1	670 ± 10	42 ± 1	8.1 ± 0.1	43 ± 1	36; 240	17; 110	47; 320
C12	150 (3)	63 ± 1	610 ± 10	38 ± 1	5.8 ± 0.1	37 ± 1	31; 190	32; 190	37; 230
C16	ND	ND	ND	ND	ND	ND	33; ND	28; ND	39; ND
C24	240 (2)	950 ± 8	1050 ± 8	45 ± 1	7.7±0.1	47 ± 1	30; 320	28; 290	42; 440
C28	140 (2)	740 ± 10	780 ± 10	36 ± 0.4	5.8 ± 0.1	34 ± 1	28; 220	36; 280	36; 280
C52	250 (2)	700 ± 10	1100 ± 20	39 ± 1	8.1 ± 0.1	48 ± 1	22; 240	48; 530	30; 330
C60	130 (1)	650 ± 30	960 ± 40	40 ± 10	3.4 ± 0.1	34 ± 1	16; 150	41; 390	43; 420

Table A.1 Continued

Sample	Mass of Heart (mg)	[^{57}Fe]	[Fe_{tot}]	[Cu]	[Mn]	[Zn]	Central Doublet (%; µM)	Ferritin (%; µM)	Blood (%; µM)
$C03_D$ (pups)	94 (4)	260 ± 10	310 ± 20	40 ± 2	24 ± 1	56 ± 2	54; 170	00; 000	46; 140
$C28_D$ (mom)	390 (1)	740 ± 5	850 ± 5	48 ± 0.3	8.8 ± 0.1	49 ± 1	35; 300	13; 110	52; 440
H12	160 (3)	58 ± 2	640 ± 20	58 ± 1	9.9 ± 0.2	60 ± 1	27; 170	37; 240	36; 230
H12 (liver)	1600 (1)	1200 ± 200	5600 ± 700	29 ± 4	14 ± 2	90 ± 2	0.5; 30	90; 5040	9.5; 530
C12 (liver)	1300 (1)	20 ± 90	960 ± 500	60 ± 30	14 ± 6	120 ± 70	18; 170	60; 580	22; 210
I08	95 (2)	520 ± 7	560 ± 7	35 ±2	7.0 ± 0.1	32 ± 1	38; 210	10; 60	52; 290
I104	200 (1)	600 ± 20	800 ± 30	36 ± 1	7.7 ± 0.3	32 ± 1	30; 240	34; 270	36; 290

MB spectra of *HFE*$^{-/-}$ hearts and matching controls are shown in Fig. 5, *A* and *B*, respectively. Spectra were noisy because the mice were enriched in ^{57}Fe for only 4 weeks. Relative to controls, the *HFE*$^{-/-}$ heart contained slightly more total iron, including more ferritin and less CD. In a qualitative sense, the *HFE*$^{-/-}$ heart appeared slightly older. The spectra of the *HFE*$^{-/-}$ liver and control (Fig. 5, *C* and *E*) were strikingly different, with only the *HFE*$^{-/-}$ liver overloaded with ferritin iron. The 70 K spectrum of the *HFE*$^{-/-}$ liver (Fig. 5*D*) was devoid of any sextet features in the baseline, confirming the absence of hemosiderin in this diseased liver. The *HFE*$^{-/-}$ liver contained significantly *less* CD than the control liver (notice the absence of spectral intensity between the two inner lines of the sextet of Fig. 5*C*), implying that the *HFE*$^{-/-}$ liver contains less mitochondria than WT livers. The MB spectrum of another diseased liver (Fig. 4*F* of Ref. **38**) also showed a deficiency of mitochondrial iron.

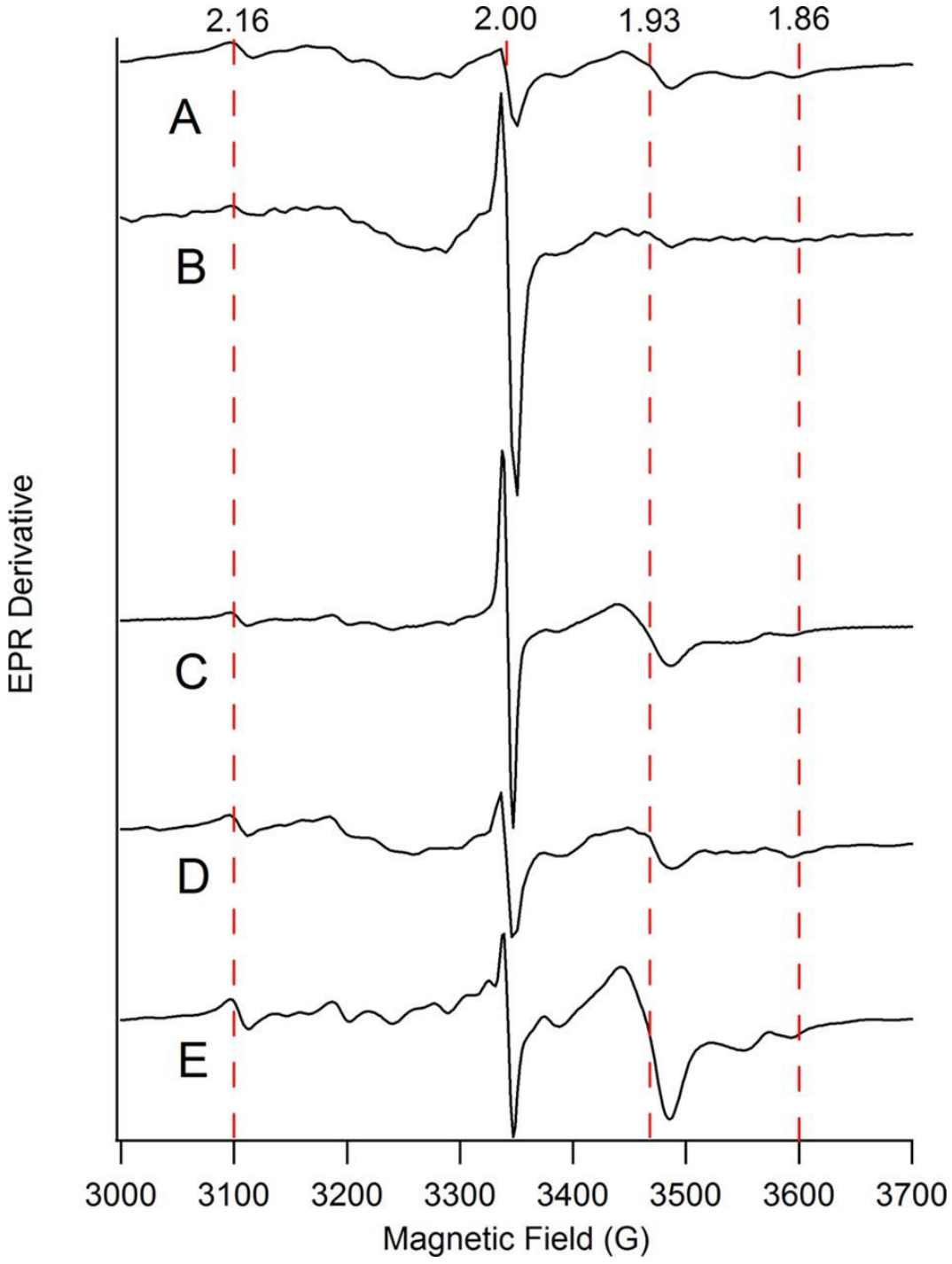

Figure A.4: X-band EPR spectra of heart homogenates from mice of different ages. *A*, 4 weeks; *B*, 12 weeks; *C*, 32 weeks; *D*, 52 weeks; *E*, 60 weeks. EPR conditions: temperature, 4 K; microwave frequency, 9.37 GHz; microwave power, 0.2 milliwatt (30 dB); modulation amplitude, 10 G. *Dashed vertical lines* indicate the fields corresponding to g values of 2.16, 2.00, 1.93, and 1.86.

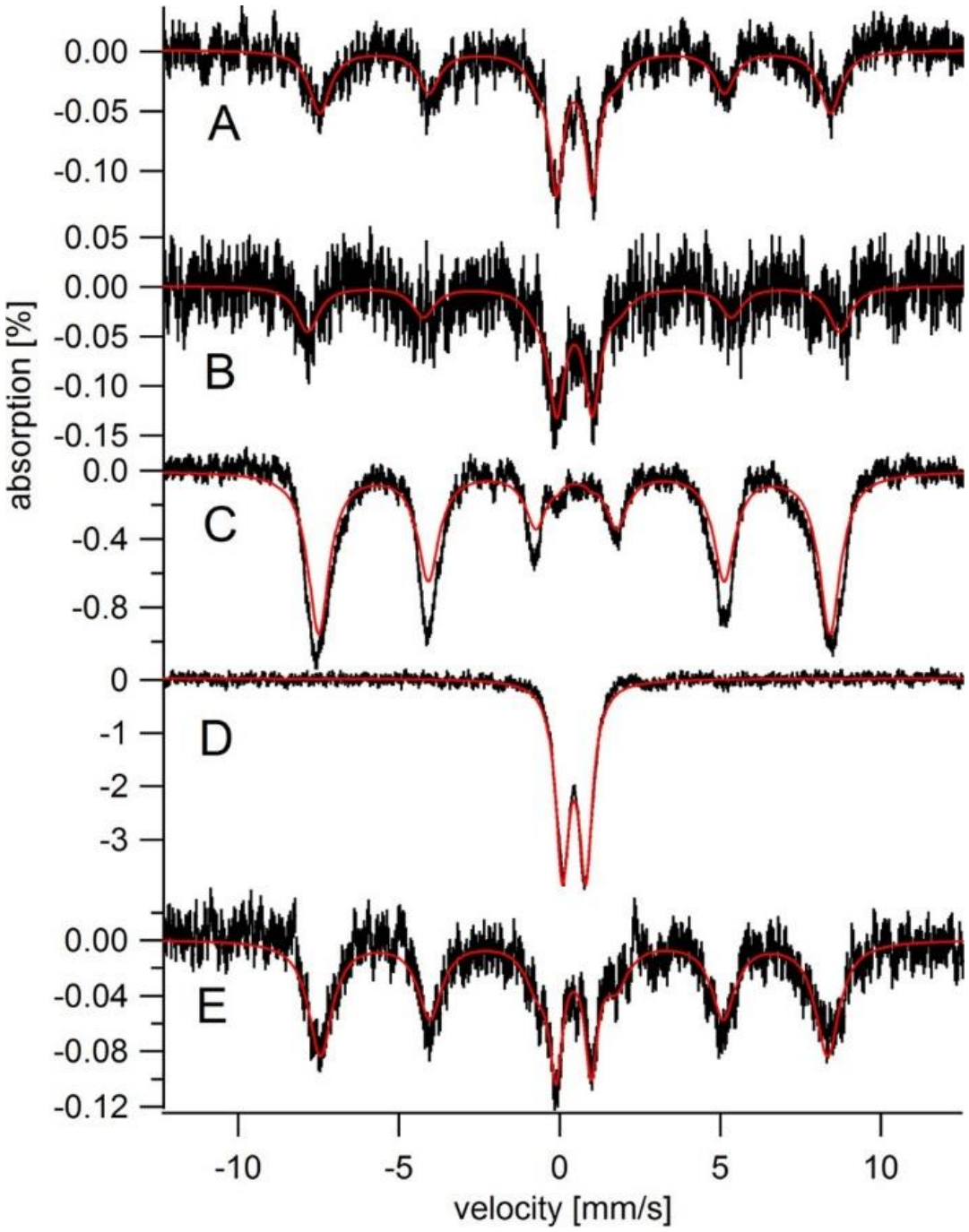

Figure A.5: Mössbauer spectra of 12 weeks *HFE*-/- hearts and livers *versus* controls. *A*, *HFE*-/- hearts; *B*, control hearts; *C* and *D*, *HFE*-/- livers; *E*, control livers. All spectra were collected at 5 K except for *D*, which was collected at 70 K.

Spectra of hearts from *IRP2*$^{-/-}$ mice (I08 in Fig. 3*B* and I104 in Fig. 1*E*) were similar to controls. The intensities of the ferritin sextets were slightly less in mutant spectra but the effect was modest. The intensities of the CD in the mutant spectra were comparable with (if not slightly stronger than) the same feature in the controls. The concentration of iron in I08 and I104 (Table 1) were slightly lower than in the controls. Like *HFE*$^{-/-}$ livers, *IRP2*$^{-/-}$ livers accumulated large amounts of ferritin iron; however, they contained more mitochondrial iron (see Fig. 4*E* of Ref. **38**) than did *HFE*$^{-/-}$ livers.

We fed a pregnant ^{57}Fe-enriched mouse an iron-deficient diet starting 1 week before she gave birth to 4 offspring, and then continued to feed her that diet until the pups were 3 weeks old. Mother and pups were then euthanized and their hearts were examined by MB spectroscopy. The MB spectrum of the pup hearts (Fig. 2*F*) exhibited standard features of young hearts, *i.e.* an intense CD and no ferritin sextet. The MB spectrum of the 28-week-old heart from the mother (Fig. 3*F*) exhibited less than half as much ferritin as a control heart of the same age (110 *versus* 280 μM). Surprisingly, the CD of the iron-deficient heart was *more* intense than the control (300 *versus* 220 μM).

Discussion

This is the first Mössbauer study of the iron content of *healthy* ^{57}Fe-enriched mammalian hearts. All previous MB studies have investigated *diseased human* hearts that were *overloaded* in iron. In those earlier studies, spectra from healthy controls could not be obtained because samples were not ^{57}Fe enriched and so spectral intensities would have been exceedingly weak.

One advantage of obtaining MB spectra of whole hearts is the ability to distinguish iron due to blood in vessels permeating the heart ($[Fe]_B$) from iron in the heart cells themselves ($[Fe]_H$). The total measured iron in whole hearts was $[Fe]_T = [Fe]_B + [Fe]_H$. Previous determinations of heart iron concentration probably overestimated $[Fe]_H$ by nearly a factor of 2 due to the large proportion of blood in the tissue. An exception is an earlier study from our group in which 40% of the iron in newborn to 6-week-old mice hearts was assumed to arise from blood; $[Fe]_H$ values between 450 and 720 μM iron were reported **(284)**. Another study reported that hearts from 12-week-old mice contained 1.4–1.6 mM iron **(286)** (millimolar units calculated from those reported). In another study, heart iron concentrations of 1.1–1.5 mM **(276)** were reported. If 43% of those concentrations were presumed to be due to blood, $[Fe]_H$ would be between 630 and 900 μM, reasonably similar to the concentrations we obtained. Comparing samples more precisely would require matching ages and the concentration of iron in the diet. In other studies, hearts from WT mice reportedly contained 4 **(262,287)**, 6 **(262)**, 7 **(271)**, and ~100 mM **(283)** iron. These values overestimated the actual heart iron concentrations by factors of 10–200.

Apart from blood, the two major forms of iron in heart tissues were ferritin and mitochondrial iron. Iron in hearts of young mice was mostly found in respiration-related ISCs and heme centers within mitochondria. The level of mitochondrial iron increased as young mice matured into adults, and then it stabilized or declined slightly in old age. As mice aged, their hearts accumulated increasing amounts of ferritin iron such that the iron content of elderly mice was dominated by this storage form of iron.

We used the overall concentration of iron in ^{57}Fe-enriched hearts and the percentage of CD and ferritin as determined by MB spectroscopy to calculate the absolute concentration of these two features (Table 1 and Fig. 6). Age-dependent mitochondrial iron concentrations ($[CD]_{age}$) were assessed by assuming the function in Equation 1.

$$[CD]_{age} = [CD]_{newborn} + \frac{[CD]_g \cdot age}{K_{CD} + age} \qquad [1]$$

A similar function was assumed to assess age-dependent ferritin iron concentrations, $[FN]_{age}$. In this case, parameters $[FN]_{newborn}$, $[FN]_g$, and K_{FN} were used. The optimized functions are given as the *solid lines* in Fig. 6. Total heart iron at any age (ignoring the blood contribution) was calculated as the sum of these two components, *i.e.* $[\text{Heart Fe}]_{age} = [CD]_{age} + [FN]_{age}$. The best-fit parameters suggest that the heart from a newborn should contain about 60 μM mitochondrial iron and little ferritin, as observed. Mitochondrial iron should increase during the first 6 weeks, maximizing at 280 μM. Ferritin iron levels should increase more slowly over the first 24 weeks, maximizing at 450 μM in adults and elderly.

These trends, illustrated qualitatively in Fig. 7, are easily rationalized given the requirement of the heart to function unceasingly from before birth until death. This high-energy requirement is satisfied by the high levels of mitochondria (and perhaps by not storing much iron). As hearts age, they store increasing amounts of ferritin iron.

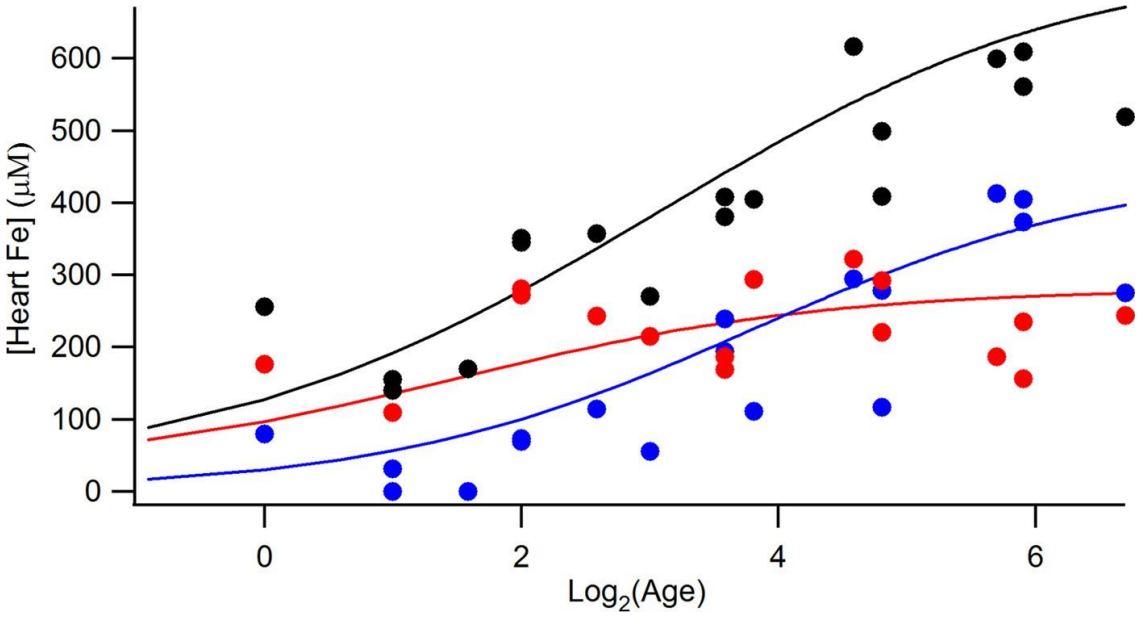

Figure A.6: Heart iron concentrations (excluding blood) as a function of age. *Black circle*, total iron; *blue circles*, ferritin; *red circles*, central doublet. Values were obtained from Table 1. The *solid red line* is the best-fit simulation generated assuming Equation 1. The *solid blue line* is the equivalent for ferritin. The *solid black line* is the sum of the *red and blue lines*. Simulations were optimized against the data by minimizing root mean square deviation. Best-fit parameters (concentrations in μM) were: [CD]newborn, 31; [CD]g, 250; KCD, 2.8 weeks; [FN]newborn, 0; [FN]g, 450; KFN, 14 weeks. Log2 numbers 0, 2, 4, and 6 refer to 1, 4, 16, and 64 weeks, respectively.

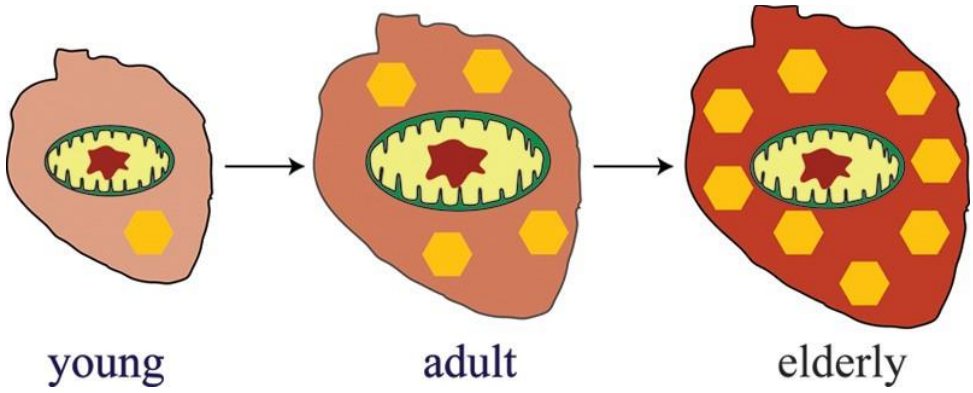

Figure A.7: Illustration of how iron content changes with age in healthy mouse hearts. The opacity of the background reflects the overall iron concentration in the heart. The size of the mitochondria reflects the concentration of iron present in that organelle. The number of *yellow hexagons* represents the concentration of iron present as ferritin.

These age-dependent changes differ from those occurring in the developing brain and liver **(38,39)**. The iron content of the newborn brain is dominated by ferritin iron, with modest levels of mitochondrial iron. This makes sense because the newborn does not use its brain extensively. Then, during the first few weeks of life, the animal opens its eyes, and begins to sense and interact with its environment, increasing its need for energy to drive brain function. To accommodate these needs, ferritin iron in the brain is *transformed* into mitochondrial iron. In fact, the overall iron concentration in the brain *declines* during the first few weeks of life, as the combined rate of mitochondriogenesis and brain volume growth outpaces the import rate of new iron **(284)**. Gradually, as the animal ages, the brain, like the heart, accumulates iron in the form of ferritin.

The changes in the iron content of the liver differ from those of brain and heart. The newborn liver contains very high concentrations of ferritin iron, much of which is exported from the liver during the first week of life **(38)**. This burst of exported iron is most likely used to help other organs develop (including the heart but perhaps not the brain). In healthy mice raised under iron-sufficient conditions, the liver accumulates a modest amount of iron as it ages, but not an excessive amount (this might depend on the iron concentration in the diet).

Another result that highlights an important difference between heart, brain, and liver is the absolute concentration of mitochondrial iron in these organs. The concentrations of mitochondrial iron in the developing brain and liver maximize at about 110 and 180 μM, respectively, whereas it maximizes at about 280 μM in the heart. These

differences may again reflect the high and sustained level of chemical energy required by the heart relative to these other organs.

Another difference between mouse hearts, brains, livers, and human Jurkat cells is the concentration of nonheme high-spin (NHHS) Fe^{2+} in these organs/cells. Jurkat cells are used for this comparison because they have been characterized by Mössbauer spectroscopy **(224,40)** and so the concentration of NHHS Fe^{2+} can be quantified. The concentration of such ions in the brain is 10 μM of 170 μM total iron **(39)**. Their concentration in the liver is 20–40 μM of 300–650 μM total iron **(38)**. In Jurkat cells, the concentration of NHHS Fe^{2+} is 40 μM of 400 μM total iron **(224)**. By contrast, we had difficulty detecting the NHHS Fe^{2+} doublet in most heart spectra. The heart contains high levels of mt-ferritin, which is thought to sequester Fe^{2+}. It is interesting to consider that the concentration of NHHS Fe^{2+} ions is so low in heart tissue because mt-ferritin sequesters these ions.

It is also interesting to compare the total iron concentrations in heart, brain, liver, and Jurkat cells (given above). Heart, liver, and Jurkat cells contain about 400 μM iron, whereas the brain contains less than *half* of that concentration. Perhaps the danger associated with Fenton chemistry has minimized the use of this metal in the most complicated and delicate of all organs.

Relative to age-matched controls, $HFE^{-/-}$ hearts contained slightly more total iron, including more ferritin and less mitochondrial iron; these differences were typical of somewhat older hearts, perhaps reflecting an increased burden on the heart due to hemochromatosis. The $HFE^{-/-}$ liver was iron-overloaded, as expected, but it also

contained lower than normal concentrations of mitochondrial iron, which was not expected. Given the literature suggesting that hemosiderin ought to be present in diseased livers, we were surprised not to detect it in our samples.

The lack of IRP2 in *IRP2*$^{-/-}$ mutant mice should allow ferritin transcripts to be translated and TfR1 transcripts to be degraded quickly under all nutrient iron conditions. Under iron-deficient conditions, the absence of IRP2 should lead to insufficient cellular iron, whereas under iron-excess conditions, the same absence should lead to excess cellular iron. In our study, mice were fed iron-sufficient chow (but just barely so) and so cellular iron would be expected to be near normal levels. Consistent with this, mutant hearts contained about 85% of the iron found in WT hearts, with an iron content similar to that of WT hearts. Similarly, spectra of the brains of *IRP2*$^{-/-}$ mice were virtually indistinguishable from controls **(38,39)**. By contrast, *IRP2*$^{-/-}$ livers were iron-overloaded with ferritin **(38)**. Perhaps the IRP1 system is sufficient to retain iron homeostasis in the mutant heart and brain, whereas the liver relies more on the IRP2 system for regulation, and so dysregulation was more severe. Interestingly, the level of mitochondrial iron in *IRP2*$^{-/-}$ livers was substantially higher than in the *HFE*$^{-/-}$ livers, even though both livers were overloaded with iron.

We also examined the effect of iron deficiency on a pregnant mouse and her offspring. As expected, the iron-deficient mother contained subnormal levels of ferritin iron, but normal levels of mitochondrial iron. A similar phenomenon was observed in spectra of iron-deficient brains **(39)**, in which the CD was actually *more intense* than it was in spectra of iron-sufficient brains. The hearts of the 3-week-old pups from the iron-

deficient mother contained normal levels of mitochondrial iron. This suggests that the iron-deficient mother does not limit the transfer of iron to her offspring during pregnancy or lactation. Interestingly, the iron-deficient mother also had a higher concentration of mitochondrial iron in the heart than did the iron-sufficient control.

Our study provides "control" spectra for the published MB spectrum of a frataxin KO mouse heart **(271)**. That spectrum contained only a doublet species due to Fe^{3+}oxyhydroxide nanoparticles (no ferritin or CD was observed). It should also be compared with the MB spectrum of human Jurkat cells in which frataxin expression was knocked-down by RNAi **(40)**. That spectrum also consisted of a nanoparticle doublet with parameters (δ = 0.48 mm/s, ΔE_Q = 0.57 mm/s) very near to those reported for the frataxin KO heart doublet. We conclude that the type of nanoparticles in both mouse hearts and human Jurkat cells must be similar.

Finally, we have pondered as to why previously published MB spectra of human hearts lacked the mitochondrial doublet and the blood doublet that we have observed with such strong intensities. Published spectra only exhibit features due to ferritin and hemosiderin. Our samples certainly contained ferritin, but none appeared to contain hemosiderin. Perhaps the iron associated with mitochondria and blood in published samples of human organs was converted into ferritin and/or hemosiderin iron during sample preparation. Few details of sample preparation were provided in those studies, but we suspect that the period between death and freezing samples for MB analysis was longer for human (days?) than mouse tissues (30 min). Also, embalming solutions and/or exposure to O_2 might alter the iron content of human tissues. In contrast, our mouse

tissues were dissected immediately in an anaerobic and refrigerated glove box. They were flushed with an isotonic aqueous buffer, and were frozen within 30 min of death. Clearly there are advantages to using non-human mammals in MB studies besides the ability to enrich them with ^{57}Fe. These advantages, along with the availability of many iron-related transgenic strains of mice, make these small mammals ideal for future MB investigations of iron-related diseases.

Experimental Procedures

All procedures involving mice were approved by the Animal Care and Use committee at Texas A&M University. The original C57BL/6 mice used in the study were a gift from Louise Abbott (Texas A&M University). *IRP2*$^{-/-}$ mice were a gift from Tracey Rouault (National Institutes of Health). C57BL/6 and *IRP2*$^{-/-}$ mice were bred as described **(39)**. They were fed iron-deficient chow (Harlan Teklad, Madison, WI; number 80396) to which 50 mg of $^{57}Fe^{3+}$ (Isoflex USA, San Francisco, CA) citrate per kg of chow was added. An iron-deficient pregnant mouse was raised similarly except that she was fed iron-deficient chow unenriched in ^{57}Fe for 1 month, starting a week before giving birth. Water was distilled and deionized. Three 8-week-old male *HFE*$^{-/-}$ (B6.129S6-Hfe<tm2Nca>/J; 017784) mice and matching C57BL/6 controls were purchased from The Jackson Laboratory. These mice were fed iron-deficient chow to which 200 mg of ^{57}Fe/kg of chow and 1.2 g of ascorbic acid/kg of chow were added. They were also given triple-distilled water to which 100 μM $^{57}Fe^{3+}$ citrate and 1 mM ascorbic acid had been added. These 6 mice were euthanized 1 month after arrival,

at 12 weeks of age. Mice were raised in iron-deficient cages, and euthanized with ketamine and xylazine, as described **(39)**. Immediately after death, carcasses were imported into a refrigerated (8 °C) nitrogen-atmosphere glove box (Mbraun Labmaster) containing <10 ppm O_2. Preparing samples anaerobically prevented any oxidation or degradation of iron centers in these samples. Animals older than 1 week were flushed by puncturing the heart with a needle, cutting the caudal vena cava, and flowing Ringer's buffer into the heart at 700 μl/min for 5 min per 10 g of animal mass. Organs were removed, weighed, transferred to MB cups, frozen, and removed from the box. EPR samples were prepared by thawing frozen samples anaerobically, adding ~5 ml of buffer, homogenizing using a tissue grinder, transferring to an EPR tube, capping the tube, removing it from the glove box, and spinning the tubes to pack the material. MB spectroscopy was performed as described **(39)**. Continuous-wave X-band EPR spectra were obtained using a Bruker Elexsys E500A spectrometer with a cryogen-free cooling system. After spectra were collected, samples were thawed and transferred quantitatively to 15-ml plastic tubes with screw-tops. An equal volume of concentrated trace metal-grade nitric acid was added to each sample, and sealed samples were heated to 90 °C overnight. Samples were diluted with 6.0 ml of distilled deionized water and analyzed by ICP-MS (Agilent 7700x).

Author Contributions

M. C. led in raising the mice, dissections, sample preparation, and early spectroscopy characterization. J. D. W. collected the remaining MB spectra, the EPR spectra, performed the metal analysis, prepared figures, and helped write the paper. P. A. L. designed the study, helped with all aspects of it, and wrote most of the paper. All authors approved the final version of the manuscript.

Acknowledgements

We thank current and former members of the Lindahl lab who helped raise and dissect the mice used in this study, including Allison L. Cockrell, Nathaniel M. Dziuba, Gregory P. Holmes-Hampton, Lora S. Lindahl, Cody Lupardus, Sean P. McCormick, Michael J. Moore, and Jinkyu Park.

Footnotes

This work was supported, in whole or in part, by National Institutes of Health Grant GM084266 (for the non-vertebrate animal portion) and Robert A. Welch Foundation Grant A1170. The authors declare that they have no conflicts of interest with the contents of this article. The content is solely the responsibility of the authors and does not necessarily represent the official views of the National Institutes of Health.

APPENDIX B

STRUCTURES, INTERCONVERSIONS, AND SPECTROSCOPY OF IRON CARBONYL CLUSTERS WITH AN INTERSTITIAL CARBIDE: LOCALIZED METAL CENTER REDUCTION BY OVERALL CLUSTER OXIDATION[*]

Introduction

Nitrogenase is an enzyme that catalyzes the six-electron reduction of dinitrogen to ammonia **(289-292)**. The FeMoco active site contains a carbide in the center of this hetero-metallic cluster **(291-292)**. Fe containing catalysts have become a recent synthetic target, with the goal of producing viable catalysts that are cheaper than existing counterparts that contain more expensive metals **(293-295)** There have been a number of attempts to synthetically model the FeMoco center of nitrogenase **(296)** as the interstitial carbide can provide stability to a synthetic cluster core to prevent fragmentation or other macroscale structural changes during catalytic turnover. Successful synthetic models of the FeMoco center could then provide cheap, long lasting catalysts.

---

[*] Reprinted in part with permission from Inorganic Chemistry. Subramaniam Kuppuswamy, Joshua D. Wofford, Chris Joseph, Zhu-Lin Xie, Azim K. Ali, Vincent M. Lynch, Paul A. Lindahl, and Michael J. Rose, Structures, Interconversions, and Spectroscopy of Iron Carbonyl Clusters with an Interstitial Carbide: Localized Metal Center Reduction by Overall Cluster Oxidation, 2017, Volume 56, 5998-6012.

Presented in this publication **(114)** is the synthesis of various hexa-iron clusters containing an interstitial carbide. These clusters were studied to provide precise X-ray structure data to dermie the nature and number of bridging carbonyls. Controlled oxidation of the negatively charged cluster with an otuer-sphere redox reagent provides a novel neutral-charge cluster. The various interconverted hexa- and penta- Fe clusters are studied with a number of spectroscopic methods to confirm

My part of this study involved utilizing Mössbauer spectroscopy to characterize a reduced Fe_6 cluster with an interstitial carbide and an oxidized produced (neutral charge overall) to determine the overall spin state of this cluster, as well as the nature of the Fe atoms present.

Physical Measurements

Mössbauer spectra were collected on a model MS4 WRC low field spectrometer and on a LHe6T spectrometer (SEE Co.; Edina, MN). Both instruments were calibrated using α-Fe foil at room temperature.

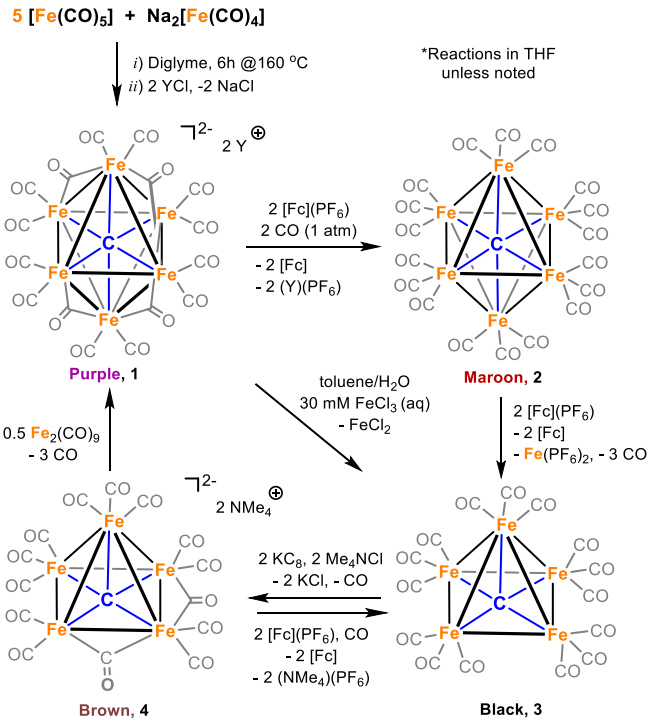

Scheme B.1: Synthesis of the starting $[Fe_6]^{2-}$ cluster 1 (top left), its neutral congener $[Fe_6]^0$ (2, top right), and the closed synthetic loop including the crystallographically defined five-iron clusters $[Fe_5]^n$ (n = 0 or 2–), shown at bottom. Shown here as an example of the clusters being studied in the Mössbauer studies below.

Results and Discussion

Mössbauer Spectroscopy for 1 and 2

A Mössbauer spectrum of the reduced cluster $(NMe_4)_2[Fe_6(\mu_6\text{-}C)(\mu_2\text{-}CO)_4(CO)_{12}]$ (1a) was collected at 5 K and 0.05 T (γ-rays parallel to the applied magnetic field). The spectrum (Figure 6) consisted of two partially overlapping quadrupole doublets. The solid red line is a simulation assuming the parameters delineated in Table 5. Sites 1 and 2 represented 2/6 and 4/6 of the spectral intensity, respectively. Within the context of the two axial Fe sites plus four equatorial Fe sites described in the X-ray section, site 1

corresponds to the two axial irons and site 2 to the four equatorial irons. The isomer shifts associated with both sites are similar, suggesting that the corresponding irons have the same or similar oxidation states. The Mössbauer spectrum of the same cluster at 295 K has been reported;**(297)** ΔE_Q was 0.57 mm s^{-1} and δ was −0.004 mm s^{-1}(we calibrated the reported value of δ = 0.22 mm s^{-1} vs sodium nitroprusside by subtracting 0.22 mm s^{-1}).**(298)** Minor differences observed between the δ and ΔE_Q values are probably due to temperature-dependent shifts.

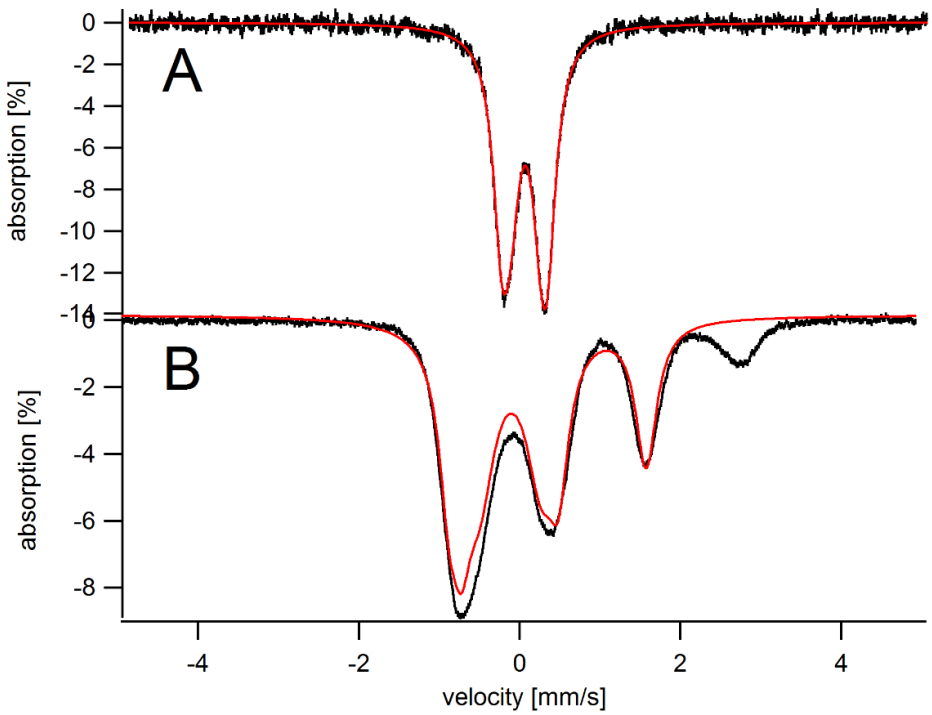

Figure B.1: Mössbauer spectrum of a solution of 1a (A) and 2 (B) in frozen THF. *Experiment conditions:* (5 K, 0.05 T).

Table B.1: Mössbauer and parameters for 1a and 2 derived from low field (0.05 T) measurements at 30 K, as well as DFT calculated charge parameters.

Mössbauer Parameters					DFT Charges
Cluster and Site	δ (mm/s)	ΔEQ (mm/s)	Γ (mm/s)	Area (%)	Mulliken
(NMe4)2 [Fe6(μ6-C)(CO)16] (1a)					
Site 1 (ax)	0.076	0.36	0.26	37	0.035 0.036
Site 2 (eq)	0.064	0.57	0.27	63	-0.080 -0.085 -0.081 -0.083
carbide	–	–	–	–	-1.7
[Fe6(μ6-C)(CO)18] (2)					
Site 1 (eq)	-0.18	1.35	0.29	22	-0.30 -0.32
Site 2 (eq)	-0.11	0.75	0.47	42	-0.20 -0.20
Site 3 (axial)	0.41	2.26	0.32	30	-0.0060 -0.0097
Site 4	1.2	2.8	.585	16	–
carbide	-	-	-	-	-1.7

Mössbauer spectrum of the oxidized cluster **2** was collected at 5 K (Figure 6B) and at 30 K (data not shown); the spectra were essentially indistinguishable. Both consisted of four quadrupole doublets, with parameters as listed in Table 5. The parameters for sites 1 and 2 are similar to those of trigonal bipyramidal $Fe(CO)_5$ (δ = −0.09 mm s^{-1} and ΔE_Q = 2.57 mm s^{-1}) and tetrahedral $[Fe(CO)_4]^{2-}$ (δ = −0.18 mm s^{-1} and ΔE_Q = 0 mm s^{-1}).**(299)** Thus, the isomer shift values for sites 1 and 2 suggest iron oxidation states between 0 and −2. Site 4 was not simulated in Figures 6 or 7, as it was ascribed to adventitious iron.

To further investigate the magnetic properties of **2**, Mössbauer spectra were collected at 4.2 K with applied fields ranging from 0–6 T (Figure 7). Spectra were fitted assuming that the spin state of the oxidized cluster was either S = 0 or S = 1. Site 4 was likely a paramagnetic contaminant,**(300,301)** so spectral intensity due to this site was ignored in the fitting. Simulations assumed two cluster sites, including one with δ and ΔE_Q values that were the average of those parameters for sites 1 and 2 (Figure 7, yellow line), and the other with δ and ΔE_Q values for site 3 (Figure 7, green line). The two sites represented 4/6 and 2/6 of the remaining spectral intensity, respectively. Simulations that assumed S = 0 (Figure 7, red lines) fit the spectra acceptably well at all applied fields, whereas those that assumed S = 1 did not. We conclude that the oxidized cluster is diamagnetic.

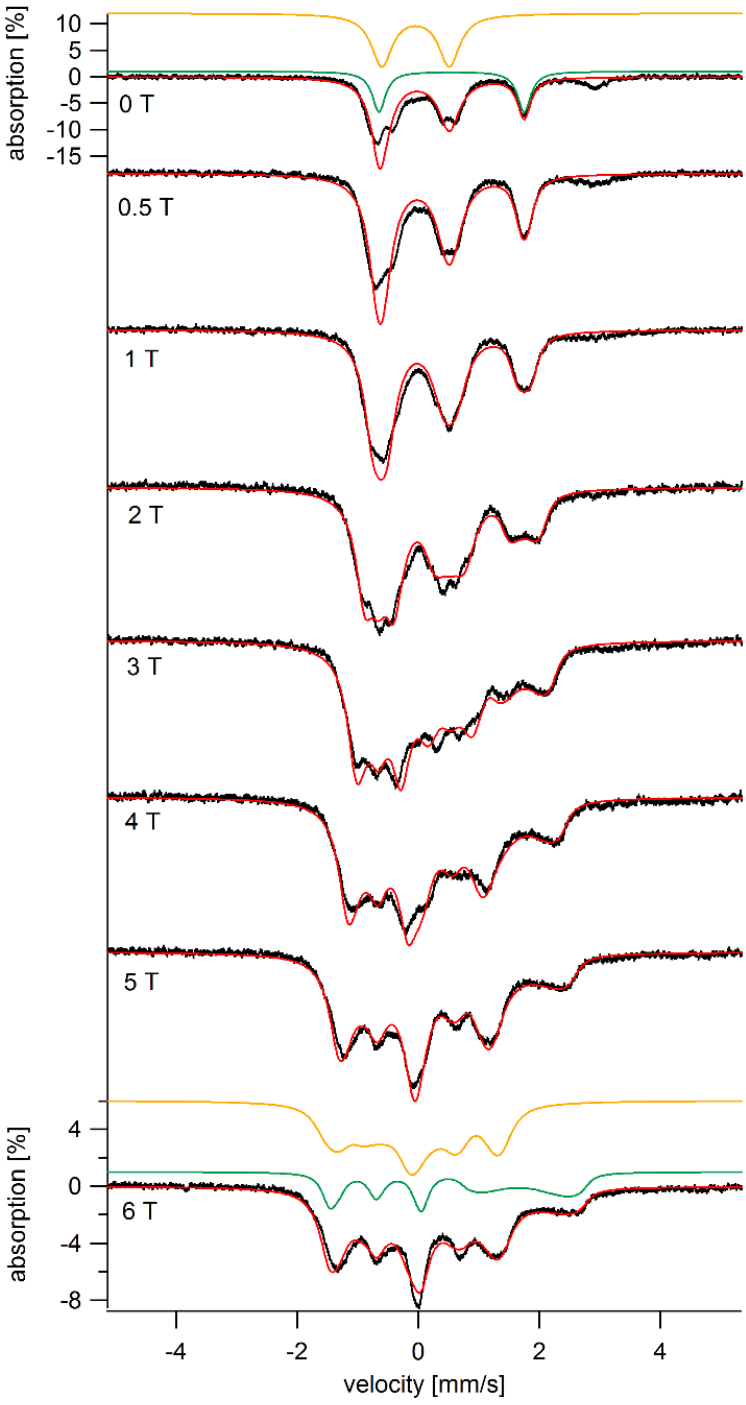

Figure B.2: Variable field Mössbauer spectra for a frozen solution of 2 in toluene. *Experiment conditions*: 4.2 K, 0→6 T fields, applied perpendicular to the γ radiation.

Conclusions

The interstitial carbide in the FeMoco active site of nitrogenase has been a topic of much study, and its actual function has yet to be determined. Proposed functions of the carbide ligand include allowing for structural changes upon substrate/inhibitor binding **(302)**, controlling the reactivity of the ligated iron center **(303)**, or that the hydrogen and nitrogen based substrates bind directly to the carbide, resulting in structural changes **(304)**.

The results presented in this study favor the notion that the carbide is uniquely positioned to control structural changes that occur during redox changes of the cluster. The concept of "deficit spending" proposed by Seefeldt, Hoffman, and Dean **(305)**, suggests that the P-clusters of nitrogenase donate elections to FeMoco then to the substrate, followed by a reduction that returns the P-cluster to its starting state. With the results presented here and in the full publication **(114)**, it's plausible that this mechanism would promote a redox-dependent disproportionation of election density in the cluster, reducing the Fe's at the N_2 or H_2 binding site while the other Fe's are oxidized. Through similar intracluster redox disproportionations (such as with product **2**), certain iron sites in the cofactor might become powerful nucleophiles/reductants, capable of binding N_2 and reducing the N-N triple bond in the presence of protons.

This study presents a novel, neutral hexa-Fe cluster produced from an outersphere oxidation of a negatively charged cluster using ferrocene. The formulation of this cluster is supported by interconversion among dianionic and neutral hexa- and penta- iron clusters using both outer-sphere and inner-sphere redox reagents. Substantial

context is provided by structural characterization of the 3 other iron-carbido-carbonyl clusters. From the collected Mössbauer spectra presented in this chapter, along with DFT calculations presented in the full article, it can be concluded that the overall spin state of the Fe_6 cluster presented in this study is diamagnetic, which agrees with other known studies of iron-carbido-carbonyl clusters.

The carbide is found to support an observation of unusual redox disproportionation within the cluster. While a narrow range of oxidation states (0.5 and 0) is favored in in the negatively charged hexa-Fe cluster, the diamagnetic cluster exhibits a wider range of 2+ and 0 while maintaining the core μ_6-C motif.